Degradable Polymersomes for Targeted Drug Delivery

A DISSERTATION
SUBMITTED TO THE FACULTY OF THE GRADUATE SCHOOL
OF THE UNIVERSITY OF MINNESOTA
BY

Matthew Alan Petersen

IN PARTIAL FULFILLMENT OF THE REQUIREMENTS
FOR THE DEGREE OF
DOCTOR OF PHILOSOPHY

Marc A. Hillmyer and Efrosini Kokkoli, Advisors

August 2013

Abstract

Chemotherapy today is often accompanied by major side effects due to delivery of toxic drugs to healthy tissue in addition to diseased cells. Targeted drug delivery offers the possibility of minimizing these side effects by specific delivery to cancer cells using targeted nanocarriers that enhance drug accumulation in tumors and facilitate target-specific cellular uptake. Polymersomes, vesicles self-assembled from polymeric amphiphiles, are an attractive targeted vehicle, as they are capable of encapsulating both hydrophobic and hydrophilic drugs, have lengthy circulation times *in vivo*, and can employ degradable functionality for triggered release of payload and clearance from the body.

This thesis reports on efforts to enhance the capabilities of degradable polymersomes for targeted delivery. First, targeting functionality is incorporated into polymersomes of the block copolymer poly(ethylene oxide)-*b*-poly(γ-methyl-ε-caprolactone) by incorporating the reactive vinyl sulfone group into the amphiphile's hydrophilic terminus, allowing site-selective reaction with cysteine-functionalized targeting peptides following self-assembly. The performance of targeted delivery using this polymersome is then evaluated *in vitro*. Binding and delivery to model cell lines for targeted and bystander cells is tracked using nontargeted polymersomes and compared to that for polymersomes using a high- or low-affinity ligand. Polymer degradation is also tracked both in simple media and during cellular delivery. Finally, a new monomer is developed incorporating acid-labile acetal functionality into a cyclic polyester. The polymerization of this monomer to two distinct polymers is also characterized and the degradation behavior of both polymers evaluated.

Table of Contents

List of Tables

List of Figures

1 Background

1.1 Introduction

Targeted Drug Delivery

Modern medicine has developed a plethora of compounds to kill cancerous cells. Many of these drugs offer high lethality to cancer cells using a minimal amount of drug, yet when taken from the lab to the clinic, many have significant drawbacks, including toxicity to healthy cells, major side effects that limit the amount of drug that can be used, and insufficient concentration of drug in the tumor itself for effective treatment. Tragically, though chemotherapeutics developed to date are often quite efficient for killing cancer cells in Petri dishes, they are often much less effective in the clinic due to the vicissitudes of the environment inside a living creature. This problem has been central to developing effective treatment strategies.

Ideally, drugs would segregate directly to the diseased site and have no interaction with healthy tissue elsewhere in the body. This idea is not new; over a century ago it was proposed as the 'magic bullet' by Paul Ehrlich.[1,2] The goal has been pursued by researchers and clinicians ever since, leading to the development of a wide variety of drug delivery systems leveraging many disparate approaches to bring treatment ever closer to Ehrlich's vision.

Current Clinical Cancer Treatment

Before discussing the specifics of targeted drug delivery, it is instructive to briefly review current cancer treatment options to better understand targeted delivery systems and

the ways they promise to change the field. Cancer therapies today are based upon stages of the disease, a systematic description of the state of the disease in a patient. A common approach is the 'TNM' system, which describes a case as ranging from local tumor invasion (T), to lymph node involvement (N), to metastasis (M), when the cancer has spread widely throughout the body.[3,4] It is on the basis of this staging system that current clinical treatment plans are often planned.[5]

As an example, colorectal cancer is typically detected in the early stages of the disease, at which point the clinical standard is surgical removal of the tumor followed by adjuvant treatment (chemotherapy) to destroy any remaining undetected or unremoved malignancy. By combining presurgical (neoadjuvant), surgical, and adjuvant care clinicians have the best chance to eradicate the cancer before it becomes widespread. With the addition of radiation therapy, they also can avoid many of the post-surgical recurrences that account for a significant portion of long-term morbidity. Today, this approach results in five year survival rates of 60-85% for colorectal cancer.[3,6,7]

The chemotherapy drugs used in these treatments using a range of approaches. Examples include antimetabolite pyrimidines,[8] DNA crosslinking cisplatin,[9–12] DNA intercalating doxorubicin, mitosis inhibiting paclitaxel, and gene damage promoting irinotecan.[13–15] New treatment plans utilizing combinations of these chemotherapeutics have produced dramatic gains in survival. In some cases, synergistic effects between drugs have been observed, suggesting that simultaneous delivery of multiple drugs may help overcome some forms of drug resistance.[16–20]

These results are heartening, yet many of these chemotherapeutics have significant side effects and inefficiencies that are a direct result of inadequately tumor-specific delivery. Due to interaction with healthy cells in addition to cancer cells, major side effects occur, particularly to faster-reproducing cells. The symptoms of nonspecific delivery of these toxic drugs include systemic toxicity, neutropenia (low white blood cell count), diarrhea, liver impairment, hypertension, bleeding, lack of wound healing, proteinuria due to kidney damage, arterial thrombosis, decreased liver regeneration, and neurotoxicity, among others.[21] Other commonly used drugs have been shown to clear completely from the bloodstream in a matter of hours, resulting in waste of drug and necessitating higher doses and repeated treatments.[22]

As a result of these limitations, chemotherapy is simultaneously less effective than it might be at fighting malignancy and more damaging to a patient's quality of life. The researcher's goals, therefore, are quite challenging: to increase the concentration of drug in the tumor while decreasing it everywhere else in the body.

Approaches to Drug Delivery Systems

Many systems have been devised to more efficiently deliver therapeutic agents to tumor sites while minimizing interactions with surrounding tissue. In general, they take advantage of one or more of the following approaches.[23,24]

1. Direct application: Rather than accumulating drug at the tumor following systemic injection, the drug is physically applied directly to the desired site.

2. Passive targeting: The drug is modified or encapsulated in a carrier with a size appropriate for preferential accumulation at the tumor site rather than in other tissue. Attached groups for active targeting may or may not be present.

3. Actively targeted delivery: Certain cell types, including cancers, express high levels of molecular markers which are rare elsewhere in the body. One or more targeting moieties for a cell type-specific marker are tethered to the delivery vehicle. By binding preferentially to cells with high expression, drug is taken up preferentially by the desired cell type.

4. External stimulus response: The carrier circulates until triggered to release its payload. Concentration of carriers at tumor sites *via* passive targeting is possible, but the release stimulus is from an external source. Examples of external stimuli include ultrasound, thermal cues, light, or magnetic fields.

5. Environmental stimulus response: the delivery vehicle circulates without releasing drug until triggered by some feature of the delivery site. Passive targeting may be used to concentrate the vehicle at the tumor and active targeting groups may be present. Common triggers include pH and temperature.

Some of these approaches have significant drawbacks. In many cases, the direct application of drug to tumor sites is of limited utility due to the difficulty of precisely injecting small tumors and a high degree of invasiveness for accessing certain areas of the body. In addition, an inability to locate all tumor sites, limited drug lifetimes following administration, and leakage into surrounding tissue. Similarly, problems arise when using external stimuli. In order to know where to aim the 'gun' providing the stimulus, the target must first be located and certain stimuli (e.g. temperature or light) can be difficult to target to deeper tissues. Both approaches rely on a time- and labor-intensive cycle of imaging, expert analysis, and repeated treatments due to the growth of previously unidentified sites.

A more desirable option, approaching the 'magic bullet' ideal would combine passive, active, and environmental targeting. This system would protect the drug while in circulation, passively localize to the tumor site, be taken up only by targeted cells, and release the drug only inside targeted cells. This project will pursue such a system to deliver the encapsulated drug in an efficient and highly specific manner.

1.2   General Concepts in Delivery

Passive Targeting

The enhanced permeation and retention (EPR) effect has proven to be a great boon for delivery of drugs to tumors *via* the bloodstream. The phenomenon, first reported by in 1986 by Maeda and coworkers,[22,25] relies upon the fact that a tumors' rapid, uncontrolled growth leads to vasculature (the blood vessel network) that is quite 'leaky' compared to that of healthy tissue. This network is rife with nanoscale fenestrations that allow nanoparticles to leave circulation for the tumors' interstitial space by diffusion through these pores. Given sufficient time for diffusion from the bloodstream into tumors, the results of the EPR effect can be dramatic, and intratumoral drug concentrations can increase by a factor of 10 to 100 relative to systemically-injected free drug.[24,26]

In order to take advantage of this effect, particles must be of the proper size to most effectively diffuse through pores in tumor vasculature while avoiding elimination elsewhere in the body. Many studies have addressed this issue, attempting to establish a cutoff for leveraging the EPR effect. Numerous optimum particle sizes have been reported, ranging from 200 to 600 nm.[27,28] Direct observations of extravasating, fluorescent nanoparticles from 60 to 400 nm in diameter found that intratumoral accumulation was

most effective for particles in the range of 100-200 nm.[29] This optimum size must be kept

in mind when designing nanoparticles to most effectively leave circulation at the desired

location. It is critical to note that the EPR effect is only used to concentrate nanoparticles

in the tumor interstitial space. The internalization of these particles into the cell, essential

for many drugs to function, must be achieved by some other means. This distinction, and

how to get nanoparticles into the desired cells, will be discussed below.
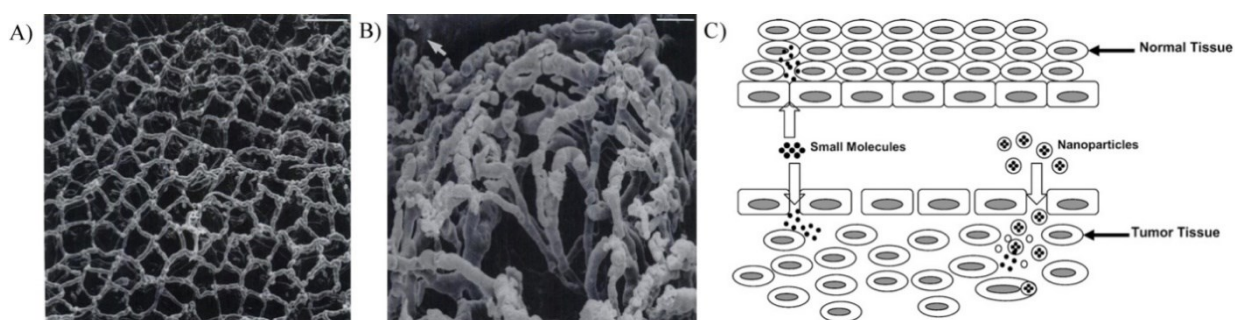
Figure 1-1: Source of the EPR effect. Scanning electron micrograph of A) normal rat colon with phenotypically healthy repeating honeycomb structure centered about the opening of mucosal glands and B) cancerous rat colon lacking honeycomb structure with poor uniformity in vessel walls. Scale bars 100 μm and 50 μm, respectively. C) Schematic illustration of the EPR effect. Appropriately-sized particles pass by healthy tissue due to well-formed vasculature but extravasate at the tumor site, increasing local concentration within the tumor interstitial space. From Skinner and Ganta.[24,30]

Size Effects

An unavoidable characteristic of the EPR effect is that it is slow. That is to say, the

rate of accumulation of nanoparticles after distant administration is estimated to take place

over the course of hours. As a result, prolonged systemic circulation is a necessity for

effective intratumoral accumulation, with circulation half-lives ($\tau_{1/2}$) in excess of roughly

six hours required.[31] Just as important as knowing how long the carrier is in circulation is

understanding how it leaves the body. Excretion in the urine, for example, leads to

decreased drug concentrations but little else in the way of adverse effects.

Additionally, nanoscale porosity is by no means a feature unique to tumors. A number of other organs and tissues in the body possess fenestrations that can allow extravasation of nanoparticles. In some cases, the removal of nanoparticles is a result of the body's natural filtration mechanisms. For example, particles of diameter 20-30 nm are eliminated by the kidney and excreted in the urine, while particles 150-300 nm in diameter tend to be accumulated in the organs of the reticuloendothelial (RES) system, which includes the liver and spleen, and are subsequently attacked by resident macrophages.[32–36] Nanoscale porosity can also lead to accumulation in healthy tissues and organs such as the bone marrow, heart, kidney, stomach, lung, cartilage, and muscle.[37–45] Inflamed tissues can also accumulate particles due to fenestrations on the nano- to microscale.[46] These size regimes offer opportunities for treatment in areas outside of cancer, as seen in studies leveraging size effects for delivery of therapeutic or imaging agents to noncancer targets such as cartilage and bone marrow, broadening the scope for passive targeting beyond chemotherapy.[44] However, they also underscore the need to create nanoparticles intended for chemotherapy with a precise size lest they be lost to diffusion through fenestrations found in these other tissues.
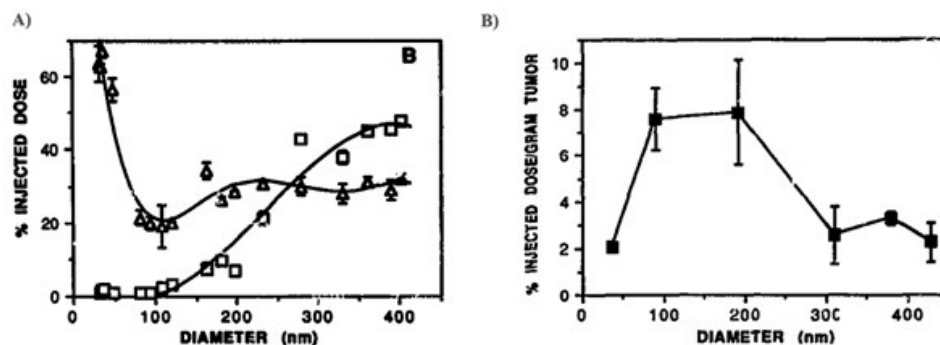
Figure 1-2: Size effects are essential for accumulation of nanoparticles in the tumor by passive targeting. Here the effect of size is explored for sterically stabilized lipid vesicles. A) Accumulation in the RES as determined by dose accumulated in the liver (Δ) and spleen (□) as a function of particle diameter. Diameters below 100 nm and above 200 nm both result in substantial accumulation in these organs, preventing them from reaching the tumor. B) By creating particles with diameters of 100-200 nm accumulation in the tumor is maximized. From Liu.[45]

Clearly, there are sizes that must be avoided to prolong circulation and enable maximum extravasation at the tumor site. Creating a particle larger than the size of the fenestrations of the tumor vasculature would be ineffective, since passage of such a particle into the tumor interstitial space is physically limited. Similarly, creating a very small particle in an effort to easily pass through the endothelial wall at the tumor site would also tend to enhance accumulation in a variety of other tissues. Such a small particle would tend to have a low circulation time, deliver potentially toxic drugs to sensitive and essential areas such as the liver and bone marrow, and achieve only middling concentrations of drug in the tumor itself. The general consensus is that the 'ideal' particle for cancer treatment is in the size range of 100-200 nm, as shown in Figure 1-2.[29,47,48]

Particle Shielding

Even in this 'ideal' size range, the particle will still be subject to removal from circulation by the RES *via* the liver and spleen. Without a means to avoid filtration and

removal by these organs a nanoparticle delivery system will not be effective. Upon injection into the bloodstream, the particle is immediately exposed to a multitude of proteins capable of adsorption. Gradually, the particle is covered in a proteinaceous mix rich in immunoglobulins and the blood serum proteins fibrinogen and albumin[49]. Opsonization, the term for this process, can result in a particle with a different size, surface charge, and binding profile than the originally injected particle. Size plays a role in this process as well, as the high surface curvature present at the surface of sub-200 nm particles has been shown to decrease the efficiency of the opsonization process.[50,51] Each of these opsonization-induced changes carries significant implications for the intended activity of the carrier in the body. The process of recognition, envelopment and destruction of foreign objects by scavenger macrophages is believed to be preceded by adsorption of opsonins that promote recognition by these specialized cells.[52]

The most important factors affecting circulation time are recognition by the immune system, hydrophilicity, and surface charge.[53] Immune system recognition can be triggered in many ways, including presentation of recognized binding sites, binding of antibodies, recognition by macrophages, and binding to receptors on scavenger cells. While in many cases this simply leads to inefficient delivery, also possible is a cascade of immune responses that enhances B cell activity, promotes the activation of dendritic cells and T cells and results in an intense allergic reaction and even anaphylactic shock.[54,55] Such responses must be avoided if there is to be any therapeutic value from the delivery system.

A number of studies have explored the effects of surface charge for purposes of delivery in the body. In general, a charged particle surface tends to have decreased

circulation time relative to one that is neutrally charged.[56–58] Opsonization of charged

particles occurs due to Coulombic interactions of serum proteins with the exposed ionic

groups present on many proteins.[59,60] In general, negatively charged surfaces result in

greater activation of the immune system than positively charged particles, though the latter

has been shown to activate the complement system as well.[61] In any case, it is typically

desirable to target a neutral, or at least modestly cationic, surface layer to most effectively

avoid clearance and maximize circulation time.[62–64]

PEO
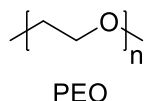
Figure 1-3: Repeat unit of poly(ethylene oxide) (PEO), the hydrophilic polymer most often
used to shield particles from opsonization *in vivo*.

Intuition suggests a hydrophilic particle surface should result in greater particle

compatibility with the aqueous milieu *in vivo.* Indeed, a more hydrophobic particle will

tend to be rapidly cleared from the body due to increased opsonization resulting from

hydrophobic interactions between proteins and the surface.[65,66] Polymeric modification of

the surface to impart hydrophilic character, most often by the polyether poly(ethylene

oxide) (PEO, Figure 1-3), has been shown to greatly reduce protein adsorption compared

to an unmodified surface.[67] PEO has been incorporated by a variety of means, including

physisorption of copolymer to a solid particle, covalent attachment to the particle surface,

modification of a bilayer-forming amphiphile, or as an integral part of an amphiphilic self-

assembled polymeric system. Such surface modification has led to substantially increased

circulation times and less particle accumulation in the spleen and liver.[52,68,69] In one

illustrative example, a 'bare' particle was 95% cleared from the bloodstream within 2

hours, while an otherwise similar particle shielded with PEO still had 10% of the injected

dose in circulation after 24 hours.[70,71] In another study, a PEO coating was shown to reduce

activation of the immune system and reduce uptake by macrophages.[72,73] Why is PEO such

an effective shielding molecule? As Allen observed, 'if you want to be invisible, look like

water.'[74] The ether oxygen has been suggested as a key factor in promoting hydrogen

bonding between the water surrounding the particle and the exterior layer of PEO, resulting

in a highly hydrated boundary layer with hydrogen bonding characteristics similar to that

of water itself. As a result, PEO chains are sheathed with solvent molecules and effectively

'camouflaged,' hiding the entire particle from opsonins.[66]

While hydrophilicity decreases hydrophobic opsonization, steric repulsion is also

crucial for deterring protein adsorption to the delivery vehicle. Attaching a shielding

polymer to the exterior of a nanoparticle, whatever the means, not only blocks attractive

interactions with opsonins by separating protein from the particle surface, the shield layer

also provides a mechanical impetus to repel proteins. A force is developed when a protein

impinges upon a shielding chain extended from the particle surface. Prior to impingement,

the chain is at its most high-entropy state and able to adopt a variety of conformations. In

the presence of a nearby protein, the number of conformations is limited by the constrained

chain and entropy is decreased. By creating a sufficiently dense layer of such shielding

chains, protein repulsion is sufficiently energetically favorable that protein adsorption can

be avoided.[75]

In summary, by combining careful control over particle size and surface chemistry

it is possible to leverage passive targeting *via* the EPR effect in order to concentrate drug

carriers at the tumor site. This process is an important first step in targeting, allowing more chemotherapeutics to be administered with decreased side effects compared to the free drugs that would distribute throughout the body and negatively affect healthy tissues as well as those afflicted with disease. However, this is only a first step, because in order to be effective, drugs must also be delivered to the interior of cancer cells and released. These considerations are addressed in the following sections.

1.3 Active Targeting

Delivery: The Final Step

Particle size and stealthiness are vital for enabling passage through the appropriate pores and the longevity in circulation to accumulate at the tumor site. However, the EPR effect is only effective in localizing the delivery system to the tumor interstitium, not for achieving internalization into the cell. Additionally, the fact that a nanoparticle is sufficiently stealthy to have evaded clearance and accumulate in the tumor interstitium does not bode well for efficient uptake into the desired cells *via* nonspecific interactions. Internalization is a crucial requirement, as many drugs function by interfering with intracellular processes. It is important to remember that active targeting groups do *not* enhance localization to the tumor, but do enhance internalization into targeted cells.[76]

Thus a final hurdle to improved treatment remains: attaining efficient, specific uptake of the delivery vehicle into the target cells. While many small molecules are capable of passive diffusion through the cell membrane, this can be a slow process that requires a high concentration gradient across the membrane, presupposes free drug is present in the extracellular environment (note that some drugs are hydrophobic or prone to degradation),

and lacks target selectivity. It is therefore necessary to take advantage of the cell's existing

uptake pathways for the most efficient delivery, an approach that may offer the additional

advantage of circumventing some modes of drug resistance.[12,77–85]
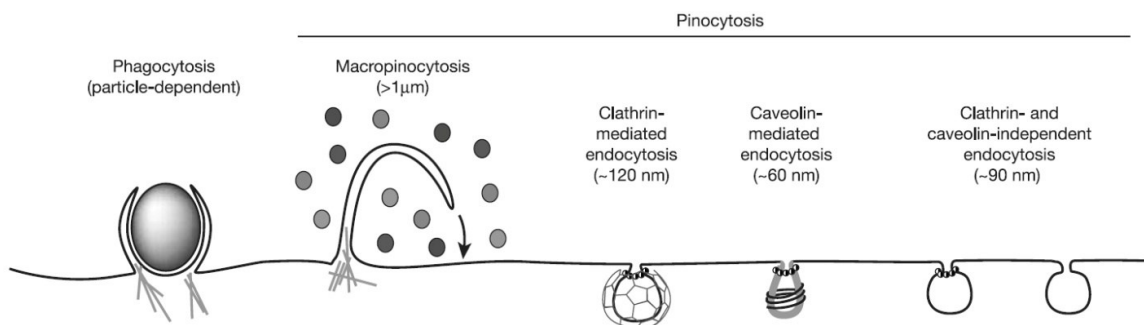
Figure 1-4: Endocytic modes of entry into mammalian cells. Phagocytosis is not observed in cancerous cells. Pinocytosis depicted here occurs in healthy and cancerous cells by at least the distinct four methods depicted here. The modes are distinguished by endocytic vesicle size, the nature of their cargo, and the means of vesicle formation. From Conner.[86]

Endocytosis

Cells take in material from the surrounding environment in several ways. Collectively referred to as endocytosis, these processes are essential for the transport of essential molecules into the cell *via* envelopment and internalization of the cargo in a lipid vesicle. Endocytosis as a whole is divided into two categories, phagocytosis ('cell eating') and pinocytosis ('cell drinking') as shown in Figure 1-4. Each of the possible modes of endocytosis are distinguished by cargo, receptor type and mechanism of internalization.

Most of these avenues of endocytosis are poorly suited for drug delivery. Phagocytosis is only observed in cells specialized for removal of large pathogens and debris and is therefore not present in cancer. Macropinocytosis is a mode of pinocytosis that does not invaginate around a particular cargo, but instead forms from ripples in the cell membrane that then encapsulate a large sample of the medium outside the cell, a

process not well suited to targeted delivery as concentrations may be low in this medium and specific targeting would be challenging. Caveolin-mediated endocytosis is very common in endothelial cells, but has small vesicle sizes (~60 nm) and a slow internalization time ($\tau_{1/2} > 20$ min). Additionally, its regulation is not as well-understood as that for other modes of endocytosis, hindering development of targeting groups.[86] Finally, clathrin- and caveolin-independent endocytosis are both modes encompassing a wide range of endocytosis routes that are not as well understood as the other modes of endocytosis and thus are very challenging to exploit for targeted delivery.

The remaining mode is clathrin-mediated endocytosis (CME), also known as receptor-mediated endocytosis, though this latter designation has fallen out of favor due to the discovery of receptor-mediated interactions in other modes of endocytosis. CME is essential for the uptake of nutrients, signal transduction, cellular development, and maintenance of homeostasis throughout the life of a cell. This mode of uptake is attractive for the internalization of drug delivery vehicles due to its mediation by ligand binding to specific, high-affinity receptors on the cell surface, and the size of vesicles created during CME are on the order of 120 nm, which is an excellent match for passively targeted nanoparticles.[87]

Generally speaking, CME occurs *via* the concentration of transmembrane proteins and their bound ligands into a clathrin-coated pit. The pit invaginates and pinches off to form a clathrin-coated vesicle. This coating is quickly removed and the vesicle rapidly matures to a late endosome, which can then fuse with other late endosomes or lysosomes. During this process, the receptor is released and recycled to the cell surface.[88] As

endosomes mature, the pH drops from the 'normal' extracellular pH of 7.4 (somewhat lower in tumors) to 5.0-6.5 in endosomes and 4.5 in lysozomes.[89] By taking advantage of this internalization mechanism, it is possible to increase intracellular concentrations of payload dramatically, by as much as three orders of magnitude.[90,91]

The decreasing pH following CME raises critical concerns for successful delivery of payload to the cellular cytosol. Some drugs are relatively fragile and may not survive the strongly acidic environment in the late endosomes or lysosome. Therefore, ensuring endosomal escape of payloads prior to maturation of endocytic vesicles and subsequent degradation of the drug is extremely important lest drug be destroyed at this late stage. This issue will be addressed below in the discussion of particular delivery systems.

Active Targeting

A major advantage of utilizing CME is it not only internalizes a particle, but it can do so in a highly specific manner. While receptors capable of activating endocytosis are ubiquitous in the body, the variety and quantity of receptors are heterogeneous between cell types. Further, they can be highly specific with regard to what ligand they will bind. This combination of heterogeneity between tissues and high specificity for a ligand is a boon to those seeking to specifically target cancer, as the particular overexpression patterns of many markers has been well studied for many forms of the disease. As a result, it is possible to tether targeting groups to a delivery vehicle that are appropriate for receptors overexpressed on the targeted cell, affording a route for selective internalization.[92]

It is important to choose a target receptor that is both plentiful (there are many on the target cell), and specific (it is rare elsewhere in the body). In this way, a targeting ligand will be functionally inert except when it encounters its target, whereupon it will bind tightly

and, along with its payload, undergo CME. Fortunately, there are a variety of such targets. In most cases the targeted feature is not wholly absent from 'normal' cells but is highly upregulated in cancerous cells. Examples from the literature utilized for this purpose include: the vascular endothelial growth factor (VEGF) receptor, the epidermal growth factor receptor, certain integrins, the transferrin receptor, matrix metalloproteinases, and various chemokines.[93,94]

Targeting Ligands

A variety of kinds of targeting ligands have been employed to specifically bind overexpressed cell surface markers. Monoclonal antibodies are perhaps the most established and well-studied, with a history of use in biology due to their specific, high affinity binding with diverse targets under biological conditions.[95,96] Because of this, they were among the first targeting groups employed. However, their large size (tens to hundreds of kg mol^{-1}) and nonhuman origin caused short circulation times which were insufficient for efficient accumulation in tumors, issues that also persisted for chimeric antibodies with sequences from multiple species.[97] Even when lower molar mass antibody fragments were created using only the active portion of the molecule, immunogenicity was still significant. Site-specific conjugation of antibody-based targeting groups to nanocarriers has proven difficult in practice, with poor control of ligand orientation resulting in less effective binding than predicted.[98,99] Nonetheless, the high binding affinities and proven capabilities of antibodies have set them apart as the 'gold standard' against which all other systems are judged.

Targeting using proteins bound to the nanocarrier is often accomplished by tethering directly to the ligand for a given receptor overexpressed on the target cell. For

example, the VEGF receptor is often targeted by conjugates to vascular endothelial growth factor itself. Typical targeting proteins tend to be far smaller than antibodies (EGF is approximately 6 kg mol^{-1}), yet some of the same limitations apply. These include a lack of overall particle stealthiness due to a bulky targeting group, difficulty in achieving the most effective orientation of binding sites on the protein and improper secondary structure due to misfolding caused by conjugation techniques used to couple the protein to the carrier.[100–102] Further, some conjugates have unexpectedly acted as superagonists, activating signaling cascades resulting in cell proliferation.[103]

Design of Targeting Peptides

In many cases, only a small region of the many amino acid residues present in a ligand protein are active in binding. While the remainder of the protein may be physiologically relevant, due to the decreased stealthiness of a large ligand and low areal density of active binding site, it is often not advantageous to utilize the entirety of even a highly active natural ligand. Peptide-based targeting groups pare unnecessary portions of the larger protein away, leaving only a minimal, highly effective sequence of amino acids. These peptide systems lack the immunogenicity of antibodies due to their synthetic origin and are a fraction of the size of antibody at only hundreds to low thousands of g mol^{-1}. In addition, the use of iterative and often automated solid phase synthesis techniques allows construction of peptides residue by residue and addition of useful functionality to the N-terminus.[104,105] These techniques allow fine control of molecular structure, allowing exact sequences to be used with precise control of orientation and connectivity.

One approach to development of targeting peptides is to screen libraries of candidates against a target. A number of methods exist for this approach, including phage

display, combinatorial libraries, affinity selection, and peptide nucleic acid microarrays.[106,107] Fundamentally, each approach relies on screening a large number of candidates for binding against the target and selecting the most effective. This has proven to be a useful approach to peptide design as it allows selection of novel sequences as well as, in some techniques, the introduction of non-natural amino acids and functional groups. This approach is especially applicable to targeting novel cellular features that lack the 'infrastructure' in the literature necessary to select, characterize and optimize a natural ligand.[108]

Integrin Targeting and Peptide Design

In contrast to library-based approaches, a 'rational design' approach to peptide selection modifies existing natural protein ligands to maximize activity while minimizing regions superfluous to binding. By this method it is possible to take advantage of the interactions already 'tested' by nature while omitting nonessential complexity.[109–111] An especially relevant example of rational design is the development of the fibronectin-mimetic peptide PR_b for bioactive surface modification and cell-specific targeting to integrins. These proteins are two part transmembrane receptors composed of one α and one β subunit that mediate cell adhesion to the extracellular matrix or other cells. Integrins have been implicated in a variety of processes from the essential, such as homeostasis and cell adhesion, to the harmful, such as autoimmune diseases and cancers of the skin, lung, prostate, colon and breast, among others.[112,113] In the body, these integrins function by binding extracellular matrix proteins such as fibronectin, fibrinogen or vitronectin to trigger a signal cascade promoting cell adhesion and spreading. Alternatively, the ligand for the integrin receptors and its coupled particle can be internalized via CME.[114]

The most ubiquitous integrin-targeting peptide in the literature today is the RGD sequence.[115–118] Derived from the 10th type III repeat of fibronectin, this sequence is composed of an arginine, a glycine, and an aspartic acid in series.[119,120] This ligand is capable of binding to certain activated receptors, allowing carriers bearing RGD sequences to be targeted towards the α_V-containing receptors, especially $\alpha_v\beta_3$, though RGD can also be recognized by $\alpha_v\beta_5$, $\alpha_v\beta_6$, $\alpha_{IIb}\beta_3$, $\alpha_1\beta_5$ and $\alpha_5\beta_1$.[121]

Specific Targeting of Integrin $\alpha_5\beta_1$

The last of these receptors, $\alpha_5\beta_1$, is a particularly attractive target due to its overexpression on tumor vasculature both in clinical cancer and in experimentally-induced models.[122] Highly expressed in embryos but only minimally expressed in healthy adult vasculature,[123] specific targeting of the $\alpha_5\beta_1$ integrin has been promising due to the integrin's overexpression in cancers of the breast, prostate, colon, skin, lung and rectum and low levels of expression elsewhere.[124–132] While the RGD sequence has proven quite effective in enhancing delivery to integrin $\alpha_5\beta_1$, it has the potential to bind a variety of integrins, hindering delivery specificity. To address this concern, past efforts have targeted the $\alpha_5\beta_1$ integrin specifically. As a result, specific targeting to this integrin using a high-affinity ligand has the potential to enhance treatment outcomes by binding specifically to diseased cells. In this manner, nonspecific delivery to 'bystander' cells can be minimized, reducing side effects due to off-target effects of toxic drugs.

To promote adhesion to this integrin, a variety of peptides have been synthesized incorporating both the PHSRN and RGD domains present on the integrin's native ligand, fibronectin. Maintaining the proper distance between PHSRN and RGD, 30-40 Å in fibronectin, has been shown to be essential for proper binding after a number of studies

were undertaken to design peptides using no linker, linkers of glycine amino acids or a PEO linker.[133–137] However, none managed to match the effectiveness of fibronectin alone. In contrast, the matching of both length and hydrophilicity of the region between RGD and PHSRN was shown to yield a peptide capable of encouraging cell spreading levels comparable to and even superior to fibronectin (sequence: KSSPHSRNSGSGSGSGSGRGDSP). This enhanced cell function was attributed to effective miming of fibronectin's engagement of both PHSRN synergy and RGD binding sites combined with the greater areal density achievable with a peptide than the much larger protein.[17] Named PR_b, the hydrophilically-matched spacer hypothesis was confirmed by systematic comparison to peptides incorporating hydrophobic or hydrophilic linkers.[16] Blocking experiments with antibodies have demonstrated that PR_b is a specific ligand for the $\alpha_5\beta_1$ integrin[138,139] and has a dissociation constant of 76.3 ± 6.3 nM,[140] recommending PR_b for enhancement binding and payload delivery when tethered to a delivery vehicle.[141–148] The development of such a specific and high-affinity ligand suggests a role for a versatile carrier capable of enhanced tumor accumulation *via* the EPR effect, specific internalization to the interior of cancer cells *via* binding between PR_b and the $\alpha_5\beta_1$ integrin and a clear means of release from nanoparticles. The range of such particles and their suitability for such a strategy is discussed in the next section.

1.4 *Drug Delivery Vehicles*

Types of Delivery Vehicles

The choice of the delivery system is critical, as it dictates characteristic advantages and drawbacks throughout the entire drug delivery process from initial injection to final

release. Many drug delivery approaches have been investigated. Some of the most common are depicted below in Figure 1-5.[24,85,94,149,150]

Unimolecular Systems

Dendrimer (~2-10nm)

Polymeric Nanoparticle (~20nm-1μm)

Self-Assembled Systems

Liposome (~50nm-10μm)

Micelle (~20-50nm)

Polymersome (~50nm-10μm)

Wormlike Micelle (~20-50 nm diameter)
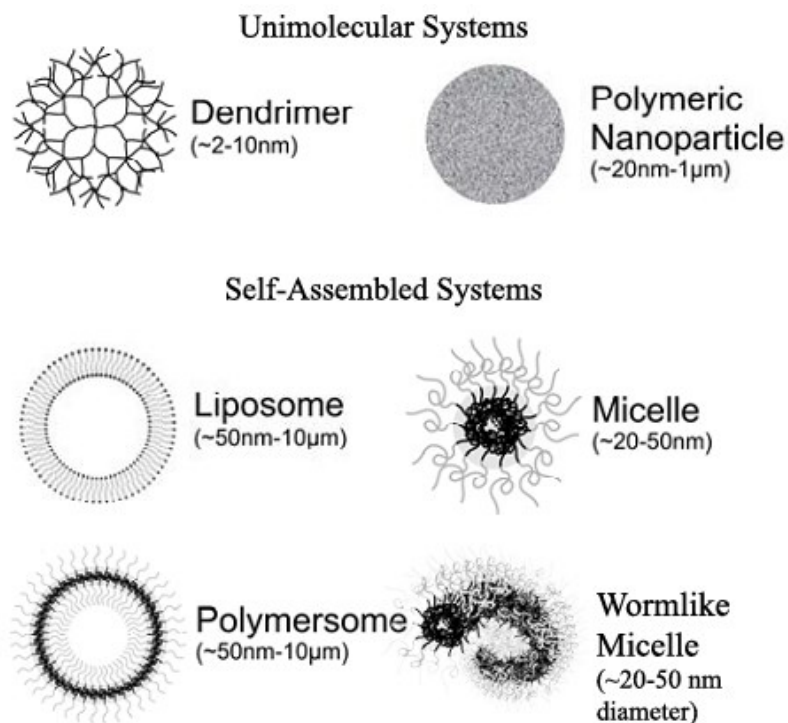
Figure 1-5: Delivery systems of current interest in the literature. From Pangburn.[149]

Perhaps the most classic nanoparticle is the simple one composed of a solid precipitate in which the payload is dissolved. These can be created using organic polymers, ceramics, proteins, carbon nanotubes, silica, gold or other inorganics, among others.[52,94,151,152] Such a particle is 'frozen,' trapped in a state wherein the constituent molecules are immobile. In comparison to the systems discussed below, the external chemical functionality of the particle can be difficult to control, making addition of shielding groups such as PEO or targeting moieties difficult to achieve with the level of control possible in other systems.

Dendrimers, in contrast, are exquisitely well controlled chemically. As a result, it is possible to create nearly monodisperse particle sizes with identical molecular architecture. However, there are inherent limits to this approach. First, as a result of molecular crowding, particle sizes are limited, keeping the ultimate size of typical dendrimers well below the 100-200 nm window desired to effectively leverage the EPR effect. In addition, payload can only be encapsulated in the interior space, which is composed of a single chemical environment. Thus it is necessary to tailor the dendrimer in such a way to encapsulate only a single class of payload (i.e. hydrophobes) at the expense of the other (i.e. hydrophiles). Finally, such particles are quite labor intensive to create due to the iterative nature of the synthesis process.[153–156]

Self-assembled amphiphilic systems have the potential to address some of these limitations of simple nanoparticles and dendrimers. Composed of many aggregated amphiphiles - molecules that possess distinct areas of hydrophilic and hydrophobic character on the same molecule - these systems are capable of self-assembly in water into various aggregates on the nano- to micro-scale. If carefully formulated, these systems can encapsulate both hydrophobic and hydrophilic cargo in a robust, chemically tailorable nanoparticle that is in many cases amenable to size adjustment by mechanical methods such as extrusion. Prior to discussing specific examples it is useful to review the concepts underlying amphiphilic self-assembly.

Amphiphiles and Self-Assembly

The current understanding of self-assembly in polymeric systems is greatly informed by systems composed of small molecule amphiphiles. In general, the structure of these lipidic amphiphiles is of the form RX, where R is a hydrophobic tail and X is a

hydrophilic head group. These groups can take a variety of chemical forms. For R groups, hydrocarbon chains are quite common, but unsaturation, branching, or aromatic rings are also possible. Hydrophilic head groups can be polar -sulfate, sulfonate, carboxylate and quaternary ammonium groups are common– or nonpolar, in which case a short chain of PEO is commonly employed. Under normal conditions, a familiar example being oil and water, close association of polar and nonpolar groups would be quite unfavorable; however, by chemically tethering these groups to one another interesting and useful phase behavior is possible.[157]

The energetically unfavorable association of hydrophobic regions with water is mitigated by micellization. During this process, amphiphiles that exist as unimers in dilute solution reach a sufficiently high concentration to form aggregates. This concentration is referred to as the critical micelle concentration (CMC) or critical aggregation concentration (CAC), and is accompanied by sharp transitions in phenomena such as conductivity, osmotic pressure and turbidity.[158] In water, this transition reflects a reordering of the surfactants in such a way as to concentrate hydrophobic tails 'inward' to form the core of the aggregate and hydrophilic groups 'outward' towards the solvent environment, resulting a global decrease in free energy relative to free unimers.

The driving force behind micellization was originally attributed to favorable enthalpic interactions between hydrophobic groups,[159] but this interaction has since been shown to make only a small contribution to the overall free energy decrease at the CMC.[160] Far more important is the entropic contribution from the solvent. Attractive forces between molecules of water are quite strong and tend to favor water interacting with itself. In order

to accommodate a nonpolar chain, it is necessary for water to adopt a highly ordered, cagelike conformation, which severely constrains the number of states that the solvent can explore. In contrast, the interactions between water and the head groups can be quite favorable. The tipping point comes at the CMC, when the global free energy becomes lower for clustering hydrophobic portions of surfactants together in aggregates rather than for forming solvent cages to accommodate free unimers. This phenomenon is known as the 'hydrophobic effect.'
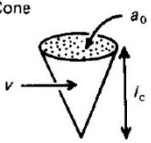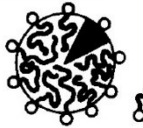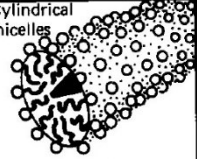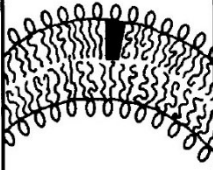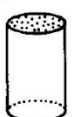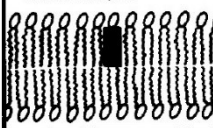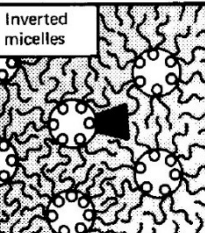
Critical packing parameter $v/a_0 l_c$	Critical packing shape	Structures formed
$< 1/3$	Cone	Spherical micelles
$1/3$-$1/2$	Truncated cone	Cylindrical micelles
$1/2$-1	Truncated cone	Flexible bilayers, vesicles
~ 1	Cylinder	Planar bilayers
> 1	Inverted truncated cone or wedge	Inverted micelles

Figure 1-6: The packing parameter of surfactants dictates the shape of self-assembled aggregates. From Israelachvili.[161]

The shape adopted by this aggregate is dictated by geometrical packing considerations as shown in Figure 1-6. This is quantified by the 'packing parameter,' which is defined as the ratio of the volume of the tail to the product of the liquid-state length of the tail and the area of the head group. By changing this parameter (for example, increasing

the tail volume by including two tails rather than one), it is possible to access the canonical series of aggregate morphologies depicted in Figure 1-6.[157,158]

Small molecule aggregates have played a pivotal role in the current understanding of targeted and stealthy drug delivery. Liposomes – lipid vesicles – have been investigated extensively to ascertain the effects of both targeting and shielding specifically for application to chemotherapy.[162] These nanocontainers have proven versatile as they permit delivery of both hydrophilic and limited quantities of hydrophobic drugs through loading of the aqueous core and hydrophobic shell, respectively. Reactive functionality on lipid head groups allows the installation of a wide variety of targeting moieties including antibodies,[98] antibody fragments,[99] peptides,[142,149] proteins,[100,101] and aptamers.[83,163–166] This same chemical functionality has allowed steric shielding by tethering PEO, resulting in circulation half-lives of 15 hours, a vast improvement over the 2 hour circulation times for unshielded liposomes.[167,168] Work on liposomes led to clinical treatment of cancer using sterically stabilized 'stealth' liposomes under the trade name Doxil for delivery of doxorubicin.[71,169] Due to this versatility and proven record, liposomes are the system to which all others are compared.

Macromolecular Self-Assembly.

Polymeric amphiphiles are composed of covalently connected macromolecular blocks of different chemical composition. These blocks are selected such that each has a different affinity for a selective solvent, i.e. a solvent that preferentially solvates one block and not the other. This term is more general than the more specific hydrophilic/hydrophobic terminology and can therefore encompass a variety of nonaqueous solvent systems, including other polymers. With that in mind, the solvent

system being considered here is aqueous due its intended biological application, and the terms 'hydrophobic' and 'hydrophilic' will be used for the sake of clarity.

Many of the same fundamental principles for small-molecule surfactants also apply for polymers, and above their CMC polymeric amphiphiles often adopt one of the 'standard' morphologies depicted in Figure 1-6. However, the much longer chain lengths employed in polymeric systems can yield extreme hydrophobicity. As a result, in addition to the canonical sphere-cylinder-bilayer continuum, many nonequilibrium structures have been observed that are kinetically 'trapped' and thus unable to alter their morphology.[170] Further, polymers need not be simple diblocks, and creative syntheses have yielded polymers composed that are triblocks, tetrablocks or more in a single chain and various branched configurations. [171–173] Aggregates composed of these newer architectures have been observed to self-assemble into a variety of exotic structures.[174–179]

Theoretical and experimental work to understand the routes by which these structures are generated has been extensive. While the arguments regarding self-assembly driven by global free energy minimization apply for both large and small molecules, the contribution from the stretching macromolecular amphiphiles' much longer chains plays a very significant role that cannot be excluded from the analysis. The balance of contributions to free energy are often quantified as: core chain stretching, corona chain repulsion and interfacial tension between core blocks and solvent.[180–182]

It is common to establish extrema for relative block lengths in self-assembled systems,[183,184] with 'starlike' or 'hairy' aggregates at one extreme and 'crew-cut' aggregates at the other. In starlike systems, corona chains are large relative to the core

blocks. The resulting crowding at the particle surface prevents polymers from developing their unperturbed conformation by 'squeezing' coronal chains outward radially. As a result, the contribution to the overall free energy from core chain stretching is comparatively small and aggregate behavior is dominated by coronal repulsion and core surface energy. Consequently, geometric constraints result in low aggregation numbers and predominantly, if not exclusively, spherical morphology.[185–188] It is in the crew-cut regime where the most variety is typically encountered in morphologies, including spheres, cylinders, bilayers, and a variety of more intricate structures. In these systems, the corona-forming block is small relative to the size of the core block. In contrast to starlike systems, the constraints imposed upon the corona blocks are small, resulting in a high surface area per corona chain, even to the extent of corona chains spreading across the core-solvent interface.[188] As a result of this lack of crowding, the corona stretching term no longer predominates and all three of energies must be considered, especially that of core chain stretching.[189]
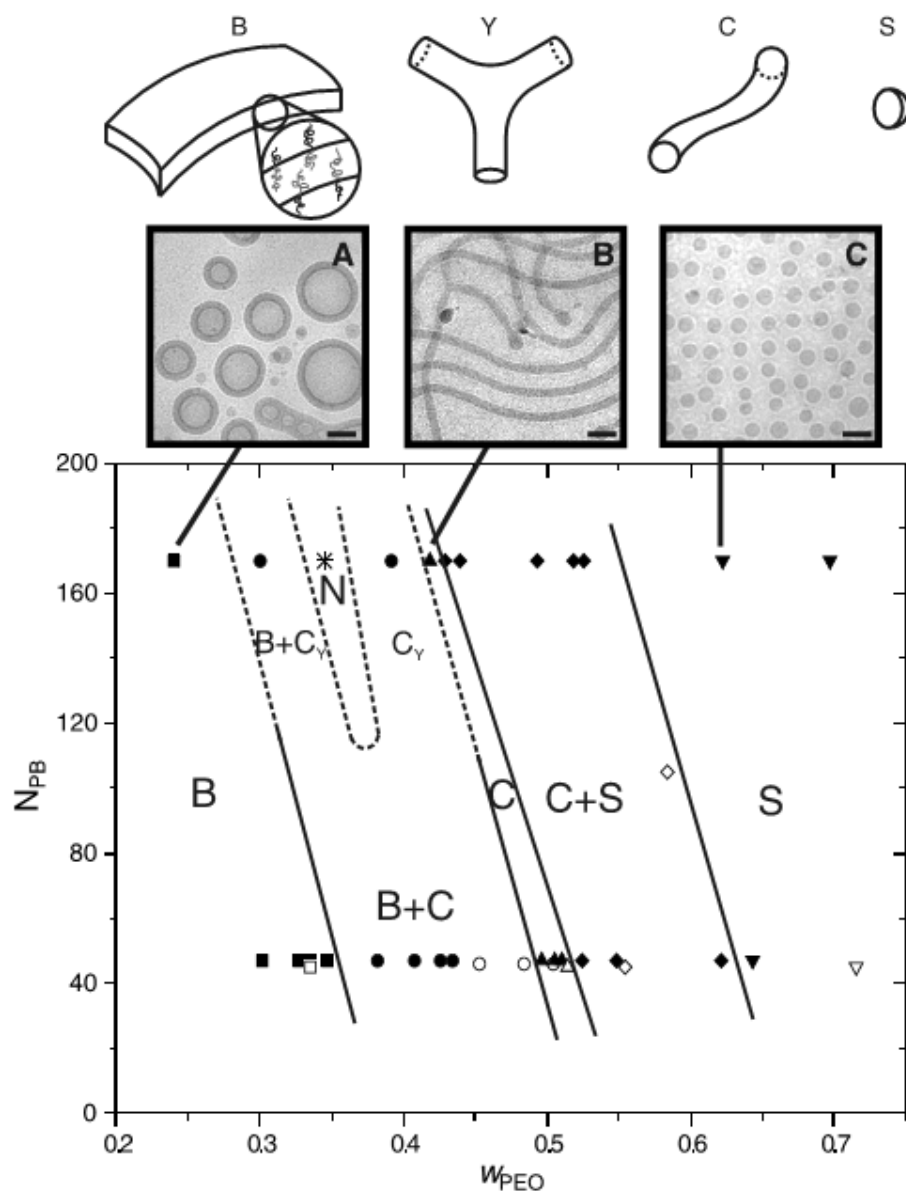
Figure 1-7: Observed morphologies following dispersal of different relative block sizes of PEO-*b*-poly(1,2-butadiene) (PB) copolymers in water. Vertical axis is degree of polymerization for PB. Horizontal axis is weight fraction of PEO in the diblocks copolymer. B = bilayer, C = cylindrical micelle, N = network, S = Sphere. From Jain.[190]

Crew-cut aggregates are of particular interest due to their adjustability, allowing straightforward experimental access to a variety of morphologies. The free energy parameters can be modified by a variety of means, including choice of polymer blocks,

solvent, temperature, additives, polydispersity, or relative length of each block.[191–193] This last consideration is particularly useful, as it allows targeting of self-assembled structures *via* well-understood synthetic means. An informative experiment holds the molar mass of one block constant while altering the molar mass of the other (see Figure 1-7). By these means it is possible to chart a transition from spheres to cylinders to bilayers as the ratio of soluble to insoluble blocks decreases.[190,194,195] Such free energy transitions can be understood intuitively by the same geometric packing arguments used above for small surfactants.

Morphology and Metastability

While appealing for charting transitions, plotting morphological phase diagrams for dispersed amphiphiles is quite challenging. In order to achieve the thermodynamic equilibrium implied by a phase diagram, substantial kinetic barriers to rearrangement must be overcome. In small molecule surfactants, this is typically achieved through means such as exchange of unimers or micellar fusion and fission.[196,197] In polymeric systems, however, the extremely low to immeasurably small CMC resulting from lengthy hydrophobic chains makes these processes extremely slow to nonexistent. In addition, the steric boundary of hydrophilic layers can have a strong repulsive effect and long core chains have been observed to relax in a way indicative of entanglements, further slowing equilibration.[198,199] Chain exchange dynamics have been estimated to proceed at nine to eleven orders of magnitude more slowly in polymeric systems than for small molecule surfactants. When compared *via* neutron scattering, little significant chain exchange was observed even over the course of weeks.[200,201]

Direct observation of dispersed solutions *via* cryogenic transmission electron microscopy (cryo-TEM) has revealed the coexistence of multiple morphologies, implying that a global energy minimum has not been achieved.[170,202] Polydispersity may play a role in these coexisting structures, but many studies report coexisting morphologies even in nearly monodisperse systems, suggesting that polydispersity-driven effects are not sufficient explanation.[203] Clearly, kinetics must play a role in the formation and coexistence of these metastable states, blurring the lines of morphological transition that are often quite sharp for small molecule surfactants. These coexisting systems can be quite stable, and dilute suspensions are often observed to be little changed following months at room temperature.[204,205]

In studies of phase behavior, it is common to use 'liquid-like' polymers with low glass transition temperatures for the core block. These allow dispersion and study of the transitions between morphologies due simply to changes in block length at room temperature without the need for cosolvents or high temperature as well as diffusional rearrangement within a given aggregate. These rearrangements are believed to result in a more thermodynamically favorable conformation and can result in the formation of a variety of highly curved surfaces without necessitating chain pullout. In this way it is believed that the energy penalty inherent in constraining the core block is minimized by allowing post-assembly assumption of conformations with high surface curvature.[190] Though rearrangement is often not immediate and the structures are not at a global thermodynamic energy minimum, the possibility for attaining curvature without overcoming the substantial kinetic barriers necessary for global energy minimization create

highly metastable structures. Such rearrangements have been reported to be sufficiently effective that core blocks are capable of adopting their unperturbed conformations.[199] Post-aggregation relaxation emphasizes the energetic benefits gained by rearrangements and has been observed in spherical, cylindrical, networked and bilayered aggregates.[206,207]

1.5 *Polymeric Delivery Vehicles*

Aggregate Morphologies

When compared to existing small molecule-based carriers such as liposomes, macromolecular systems can be much more physically robust. Further, these particles are fully synthetic and not limited to the natural chemical palette, affording great flexibility to tailor chemical and physical architectures. The morphologies discussed above – sphere, cylinder and vesicle – have all been investigated for delivery of drug and imaging agents.[208]

Spherical micelles are attractive for solubilizing and protecting hydrophobic agents in their central core.[209] These aggregates have been made from a very wide variety of polymers and have been shown to effectively deliver many agents to tumor sites. However, they inherently lack versatility due to an inability to natively encapsulate hydrophilic agents and are difficult to easily synthesize in the 100 – 200 nm diameter size range. Nonetheless, they enjoy the same variety of chemical compositions that any polymeric system can possess, and have been modified with a wealth of chemical functionalities including surface coatings, internal crosslinking, and targeting groups.[175,210–214]

Cylindrical micelles, also referred to as wormlike micelles or filomicelles, have recently been touted as drug delivery agents with unique advantages. These aggregates have been used as targetable vehicles for delivery of hydrophobic drugs.[215] They have also

been shown to exhibit a very high degree of stealthiness and biodegradability when formulated using PCL-*b*-PEO or poly(lactide)-*b*-PEO (PLA-*b*-PEO).[207,215–217] While these characteristics are shared by spherical systems, the high aspect ratio of these particles results in a variety of unusual and potentially useful phenomena. For example, filomicelles may be able to penetrate through the bulk of a porous tissue *via* reptation through its small pores, a route inaccessible to spheres with a similar radius of gyration.[217] In addition, hydrodynamic effects lead to greater drag along the length of the cylinder yielding longer circulation times. This longer circulation time has also been attributed to an inability for macrophages to take up more than a small section of a given filomicelle in a single phagocytic event.[218] While these advantages are compelling, like spherical micelles, wormlike micelles are also inherently limited in versatility due to the lack of a hydrophilic pocket. Nonetheless, they may prove to be highly effective carriers for hydrophobes and perhaps a useful alternative to spherical micelles.
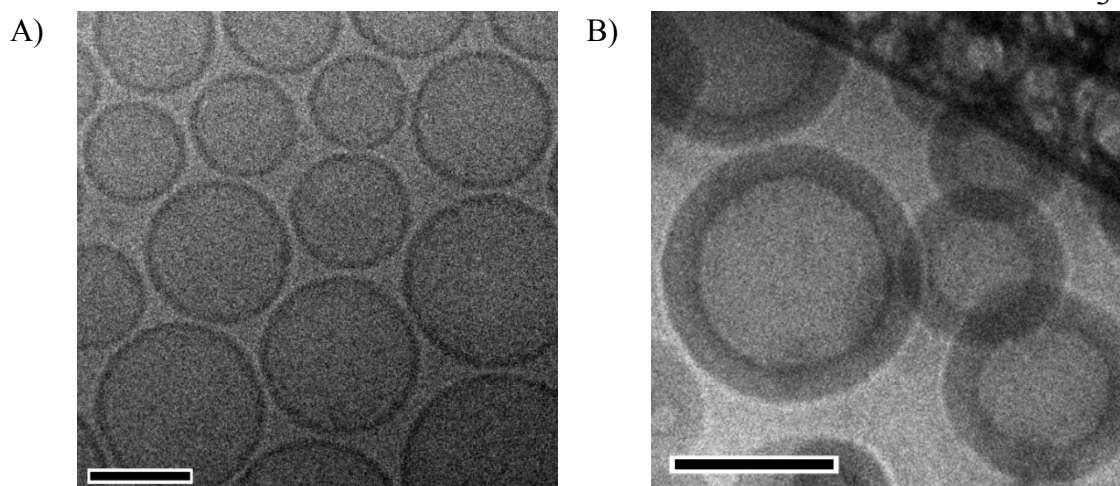
Figure 1-8: Cryogenic transmission electron micrographs of A) liposomes and B) polymersomes. Note the much thicker shell layers in polymersomes due to higher molecular weight hydrophobic blocks than the lipid tails in liposomes. Scale bars 100 nm. Liposomes were prepared by Maroof Adil and the image collected by Todd Pangburn (unpublished work) while polymersomes are from Demirgöz.[141]

Polymersomes

Of the morphologies that can be adopted by polymeric amphiphiles, vesicular structures are particularly compelling for medical imaging or drug delivery. These structures have come to be known as polymersomes by analogy with their lipid-based counterparts, liposomes (Figure 1-8).[219] Both are composed of a bilayer of amphiphiles and are capable of carrying both hydrophobic and hydrophilic payloads *via* their shell and core regions, respectively.[220] As a result, a single carrier system can be used for a wide variety of payloads. This may also have ramifications beyond the obvious, as synergistic effects have been observed during simultaneous dosing of complimentary drugs.[16–20] Conveniently, similar processing techniques to adjust size and purify unencapsulated drug can be used for both liposomes and polymersomes and the desired size of 100-200 nm is easily obtained *via* sonication, freeze-thaw cycling and extrusion through appropriately sized membranes.[141,143,221,222]

A number of advantages of polymersomes over existing systems have been reported that make them particularly attractive for use in the body. Perhaps the most immediately apparent advantage is the shielding layer. Typically liposomes are formulated with approximately 5-10 mol% of lipids derivatized with sterically stabilizing PEO.[74,223] However, the protective layer in the final liposome is often considerably sparser due to micellization of PEO-containing lipids that dissociate from the liposome to create more highly curved and energetically favorable spherical (starlike) micelles.[224,225] In comparison, there is complete coverage of the polymersome surface with PEO by the very nature of the constituent amphiphiles. The resulting shielding effect has been shown to be extremely effective, as injections of PEO-containing polymersomes remain in circulation twice as long as sterically shielded liposomes (polymersome $\tau_{1/2} > 24$ h) as a result of decreased clearance due to the lack of a 'handle' for opsonization.[226] It must be noted, however, that while substantially decreased, opsonization is still active for any particle due to the impossibility of wholly eliminating nonspecific interactions.

The chemical versatility of polymersomes is considerable. As a result of their fully synthetic nature, it is theoretically possible to 'build in' nearly any desired chemical functionality. This is especially relevant when attachment of targeting groups is desired. By creating end-functional polymers, it is possible to tether a wide variety of targeting moieties to the exterior of the vesicle by a variety of chemistries. Prominent examples include carbodiimide-mediated couplings, Michael additions, and the copper-catalyzed azide-alkyne 'click' reaction.[227–231] Reactive functionality can also be included with relative ease in the polymer backbone or at the hydrophobic terminus. By reacting these

groups, it is possible to introduce crosslinks within the bilayer itself to create a tough, rubbery particle, a process that would result in destruction of lipid bilayers.[232] Similarly, photo-induced crosslinking of core chain termini has been shown to increase stability of biodegradable polymersomes.[233]

Most striking, however, are the properties derived from the bilayer. Owing to the large molecules involved, the core layer of polymersomes are quite substantial, 8-21 nm, far thicker than the 3-5 nm typically observed in lipids.[199,200,234] This thickness has implications for the therapeutic versatility of polymersomes, particularly due to the increased volume available for hydrophobic shell loading as well as decreased 'leakiness' from the hydrophobic core *via* permeation of the membrane.[219]

To illustrate this point, solubilization of the hydrophobic chemotherapy drug paclitaxel in the shell layer is a necessary step for its successful delivery and for decreasing its side effects such as neurotoxicity; however, loading paclitaxel tends to destabilize liposomes.[235–237] In contrast, polymersomes have been demonstrated to successfully solubilize up to 10 mol/wt% of a series of large (1.4 - 5.4 nm at 700 - 5400 g mol^{-1}) fluorophores without a significant decrease in toughness. In contrast, liposomes could only load 1 mol/wt% of the smallest of these fluorophores prior to losing stability.[205] Similarly, it was possible to encapsulate both the dye Nile Red and quantum dots in a single PEO-PB vesicle with no appreciable change in mechanical or morphological properties.[221]

The strong driving force towards minimization of core block exposure to solvent also has mechanical benefits. Membranes, while not as stiff as lipid membranes, are much tougher. Using micropipette aspiration, polymersomal areal strains ($\Delta A/A_o$) were shown

to approach 50% prior to rupture, in stark contrast to the 5% rupture observed in lipid systems over a range of compositions.[199] Interestingly, relaxation was slow following aspiration, particularly as molar mass increased, consistent with frictive and entangling effects between chains.[206] These mechanical features may be quite useful in the challenging and often hostile environment *in vivo*.

Biodegradable Polymersomes

The polymers discussed thus far have largely been inert, typically a hydrophilic block of PEO and a hydrophobic block of biologically inert polymers. These polymers are well suited to uncovering the physics of aggregation, as they are not easily degraded and are typically made to narrow molar mass distributions.[238] However, if one is more concerned with medical therapies than with morphological theory, the very features that make these polymersomes so attractive, notably high resistance to breach of the vesicle wall, act in opposition to therapeutic goals. While a robust vesicle is extremely useful for getting the polymersome to the tumor site intact, it presents a problem following internalization. To wit, the payload generally must escape both the carrier and the endosome and then reach the cytoplasm, none of which is possible if the drug is trapped in an inert container. Thus delivery with polymers created to address questions of theory are inherently limited at the final stage by the very feature set that made them attractive theoretical systems.

Degradable polymersomes are a solution to problem. By including degradable linkages in the core block, it is possible to create a system that is responsive to its environment. These carriers offer the potential to behave much like inert systems prior to internalization – maintaining the advantageous features of stealth and tough membranes

capable of solubilizing a variety of payloads – while degrading and releasing their payloads following internalization. Early biodegradable polymersomes were composed of PEO hydrophilic blocks coupled to hydrophobic blocks of either polylactide (PLA), poly(ε-caprolactone) (PCL), or poly(trimethylene carbonate).[239] Later studies incorporated blends of these polymers and inert PEO-PB diblocks to reduce hydrolysis.[240] In recent years vesicles, composed solely of PEO-PCL have become more common in the literature due to advantages of this polymer in comparison to other polyesters including a lack of pH changes upon degradation, compatibility with other polymers, and slow degradation compared to PLA, poly(glycolic acid) and poly(lactic-*co*-glycolic acid).[241,242]

Degradation-induced effects also make polymersomes useful. In the Discher model for degradation, hydrolysis gradually results in a decrease in hydrophobic block length, with a resulting increase mass fraction of the hydrophilic portion of the molecule.[234] Using the arguments made above regarding surfactant self-assembly, this would favor the formation of highly curved surfaces such as spherical micelles. While this pathway is kinetically tractable and experimentally observable in wormlike micelles, which pinching off spheres, the same process is not possible in vesicles and results in energetically unfavorable stretching of core blocks.[243] This unfavorable energetic state is ameliorated by the gradual accumulation of short-tail polymers to create highly curved pores in the vesicle wall, allowing release of the hydrophilic payload encapsulated in the aqueous lumen.[240] Poration is also a promising route for endosomal escape, a critical limitation of many systems. Following endocytosis there is a large nanoparticle concentration in the endosome. As pH drops, vesicles degrade, creating a high concentration of copolymers

with a shortened hydrophobic block. In these high-concentration situations, it is possible for the diblock to interact with endosomal lipids and accumulate in the endosomal wall. As in the vesicle poration case, these amphiphiles favor high-curvature conformations, resulting in the formation of holes in the endosomal wall, allowing release of drug into the cytoplasm.[244] The end result is a vehicle capable of selectively releasing its payload following endocytosis, resulting in more effective treatment of tumors than that observed using inert polymersomes.[245,246]

Dispersal and Biocompatibility

Self-assembled aggregates are often formed by dispersing the copolymer into the aqueous phase from a good organic solvent for both blocks. Following dispersal, this solvent is removed by dialysis, evaporation or other means to leave behind polymersomes or other self-assembled aggregates.[247,248] While this is a rapid approach suitable for some laboratory studies, in systems intended for dispersal in the human body, the inherent uncertainty concerning complete removal of hazardous solvents make such an approach unsuitable. Further, the use of high temperatures for dispersal of polymers excludes promising therapeutics due to conditions unsuitable for encapsulation of sensitive molecules.[249]

It is therefore essential that systems intended for human use be able to self-assemble in water without the use of organic solvents. Candidate techniques include direct dissolution or thin film hydration, each of which requires a polymer that is liquid-like at room temperature. For studies of phase behavior systems such as PEO-*b*-poly(ethyl ethylene), PEO-*b*-PB, and PEO-*b*-poly(isoprene) have all been investigated as amphiphile capable of self-assembly under these conditions.[141,202,205,250] However, these polymers are

biologically inert and incapable of the pH sensitivity desired in a responsive system and polymers must be capable of both organic solvent-free dispersal at ambient temperature and pH-sensitive degradation.

PEO-PMCL
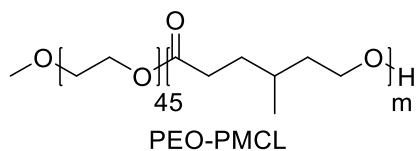
Figure 1-9: Diblock copolymer poly(ethylene oxide)-*b*-poly(γ-methyl-ε-caprolactone) used to form self-assembled aggregates, including polymersomes,[194] by thin film hydration at room temperature.

Systems using polyester hydrophobic blocks have been proven in numerous studies to be extremely effective and versatile delivery systems for a variety of applications. Unfortunately, FDA-approved PCL is semicrystalline, with a $T_m \approx 60\ °C$, making room temperature dispersal in water impossible without the aid of organic cosolvents or high temperature. Another approach, and one that is explored in this thesis, is the use of a modified PCL that eliminates crystallinity, making it compatible with bio-friendly dispersion techniques. Work by Trollsas and coworkers provided a route to modify the CL monomer by substitution of a methyl group in the γ position of the caprolactone ring to create γ-methyl-ε-caprolactone (MCL).[251] This modification disrupts chain packing, resulting in an amorphous polymer with a glass transition temperature of -60 °C. This monomer has since been utilized to create PEO-*b*-poly(γ-methyl-ε-caprolactone) diblock copolymers (Figure 1-9) that are dispersable by simple thin-film hydration[247,252] and form the full range of canonical aggregates in water at room temperature in a manner comparable to PCL.[194,249] This system has also been investigated for deep-tissue imaging, encapsulating fluorescent agents for diagnosis.[253,254] By utilizing PEO-PMCL it is possible

to obtain highly stable nanoparticles that behave much like known systems yet are dispersible by bio-friendly techniques.

1.6   Summary

Cancer remains one of the greatest challenges in modern medicine, proving capable of withstanding the extremely diverse treatment strategies currently employed. Chemotherapy is among the most widely used treatment options, but a hallmark of chemotherapy is the infliction of a wide range of side effects that negatively affect a patient's quality of life and often dictate the tolerable dosages that can be administered, limiting therapeutic efficacy. Many approaches have been investigated to decrease these side effects while preserving the therapeutic effects of chemotherapy drugs. A promising avenue has been the development of nanoparticle systems that take advantage of the leaky blood vessel network often present in the vicinity of fast-growing tumors to preferentially accumulate nanoparticles carrying drug at the tumor site for eventual release of a toxic drug.

Liposomes are the most common of these nanoparticle carriers and have been modified to include targeting functionalities that greatly enhance uptake into target cells that overexpress specific cell-surface receptors. These carriers, however, tend to have limited circulation times due to their limited steric repulsion layer and while effective at encapsulating hydrophilic drugs, have limited capacity for loading of hydrophobes. Polymersomes, the macromolecular analogs of liposomes, have the potential to increase treatment efficacy by enhancing intratumoral accumulation due to the extended circulation time afforded by their dense hydrophilic brush layer, encapsulation of both hydrophilic and

hydrophobic payloads, tough shell layer, and synthetic flexibility. However, most polymersomes have been composed of nondegradable polymers that slow release and eventual clearance from the body, or have lacked targeting functionality, hindering binding and uptake into targeted cells.

The primary purpose of this work was to develop polymersomes combining degradable, polymersome-forming amphiphiles with functionality for site-specifically tethering a targeting peptide to enable specific binding to targeted cells. The goal is to enhance the specificity of delivery of chemotherapeutic drugs and consequently incur fewer negative side effects during chemotherapy. Towards this end, methods were developed to synthesize well-defined polymersome-forming amphiphiles capable of rapid reaction with cancer-targeting peptides while preserving peptide orientation. The behavior of these targeting polymersomes was then investigated both in simple solution and *in vitro* in the presence of targeted and untargeted cells. Following these investigations, a novel polymer system was designed to integrate an acid-labile moiety into the polymer backbone. By this means it is hoped that it will be possible in the future to create polymers with more rapid degradation and release when subjected to the lower pH present in the vicinity of tumors and following uptake into targeted cells and enhance the specificity of delivery and minimize the deleterious side effects of chemotherapy.

2 Synthesis and Characterization of Reactive PEO-PMCL Polymersomes[*]

2.1 Introduction

This chapter describes the synthesis and molecular characterization of a polymersome-forming block copolymer of poly(ethylene oxide) (PEO), a hydrophilic polymer, and poly(γ-methyl-ε-caprolactone (PMCL), a hydrophobic polymer, that integrates chemistry such that following self-assembly site-specific tethering of a targeting peptide is possible. In addition, this chapter includes verification of the self-assembly of the PEO-PMCL amphiphiles, characterization of the solution morphology of the aggregates, both before and after tethering of a targeting peptide, and characterization of the extent of the conjugate addition of the model targeting peptide.

This work was motivated by a desire to combine the potential advances in payload diversity, circulation time, and synthetic flexibility afforded by use of polymersomes compared to other delivery mechanisms with the need to integrate a means of tethering a targeting peptide capable of binding to receptors overexpressed on targeted cancer cells. By doing so it is hoped that the specificity of delivery can be enhanced. To maintain vesicular morphology independent of the peptide used for targeting, it is essential that the chemistry used to tether the targeting peptide be capable of reacting relatively rapidly and in high yield after the self-assembly of polymersomes. While examples exist of

---

[*] Reproduced in part from Petersen, M.A., Yin, L., Kokkoli, E., *Polymer Chemistry* 1, 1281-1290. Copyright 2010 Royal Society of Chemistry.

polymersome morphology being maintained when peptides are attached prior to self-assembly[141], the potential for the emergence of novel, highly-complex morphologies has also been demonstrated[255] and complicates the prospect of developing a versatile, modular drug delivery vehicle that are best avoided. A vinyl sulfone group is particularly attractive for this approach, as it will react selectively with thiols (easily introduced into peptides by addition of a cysteine residue) *via* conjugate addition in mild aqueous conditions and is relatively stable with regards to hydrolysis. The alkyne-azide 'click' reaction has also been used for a similar purpose,[139,147] but has the drawback of requiring a potentially toxic copper catalyst for the reaction to proceed in most conventional formulations.[256,257]

While polymersomes have previously been formed using PEO-PMCL,[194] they have lacked suitable reactivity on the PEO block to enable tethering of a targeting peptide. Similarly, while self-assembling amphiphiles have been synthesized that were capable of tethering a targeting peptide (while maintaining peptide orientation), these have been in nondegradable systems. In these cases the chemically robust polymers used allowed for relatively harsh reaction conditions without the risk of undesired side reactions (e.g. transesterification, backbiting reactions, etc.) that affect the integrity of the polymer chain, alter molar mass distributions, and impact the final morphology adopted by aggregates of these polymers.[139,147,255] Examples of such systems are shown in Figure 2-1.
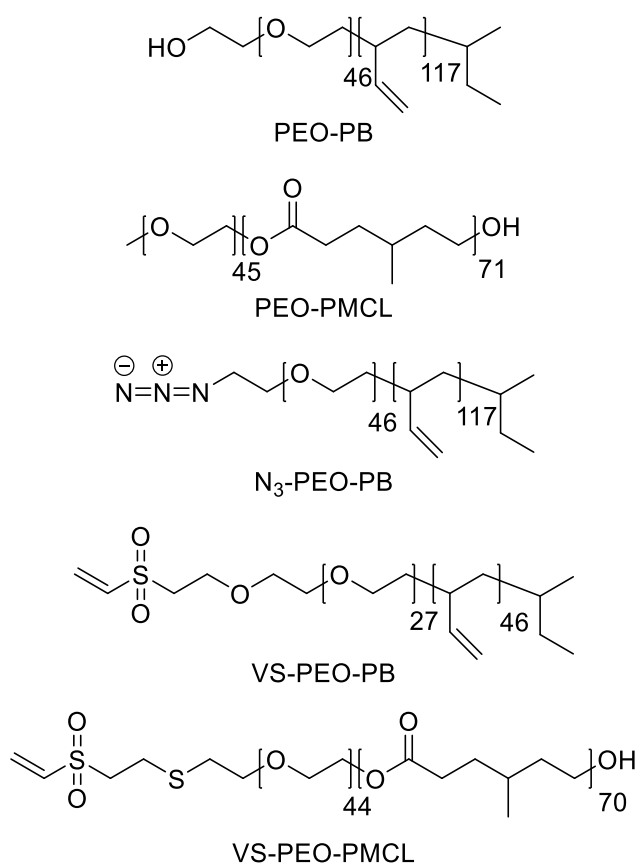
Figure 2-1: Several polymer systems have been developed *en route* to degradable targeted polymersomes. All have factored significantly in this work. Early efforts predominantly used PEO-PB.[141,219,222] PEO-PMCL was developed as a degradable system also capable of adopting the range of canonical aggregates.[194,247,252] PEO-PB was later modified with either azide[139,147] or vinyl sulfone[255] functionality using synthesis techniques not readily amenable to use with a degradable block suck as PMCL to enable the tethering of targeting peptides functionalized with alkynes or thiols, respectively. The current work develops a method to integrate the vinyl sulfone reactive end group into PEO-PMCL.

Due to the need for installation of a reactive group onto a degradable chain that could be substantially degraded by exposure to harsh conditions, it was necessary to develop a route to install a reactive group prior to polymerization of the degradable PMCL block. To achieve this goal, a related procedure by Bae *et al. was* initially followed to preferentially modify one end of PEO diol with divinyl sulfone (VS).[37] This could then be used to initiate polymerization of PMCL from the remaining hydroxyl groups. This resulted

in a mixture of VS-PEO-VS homopolymer, VS-PEO-PMCL diblock copolymer, and PMCL-PEO-PMCL triblock copolymer, from which the desired diblock could be isolated. Following isolation of the desired end-functional diblock copolymer (VS-PEO-PMCL), the polymer self-assembled in aqueous solution to form polymersomes analogous to those observed in unfunctionalized PEO-PMCL systems. These polymersomes were modified after self-assembly with thiol-containing peptides by site-specific attachment to the vinyl sulfone groups in the vesicle corona. Following peptide attachment the vesicle morphology was unchanged.

2.2 *Experimental*

Materials

All chemicals were obtained from Sigma-Aldrich (St. Louis, MO) and used as received unless otherwise noted. Water was obtained from a Milli-Q water system purified to a resistivity of 18.2 MΩ cm. Peptides were synthesized by the Oligonucleotide and Peptide Synthesis Facility at the University of Minnesota and their molar masses were confirmed by Matrix Assisted Laser Desorption Ionization Mass Spectrometry (MALDI-MS). ^{1}H NMR spectra were acquired using a Varian VAC-300 spectrometer at room temperature, all polymer samples were dissolved in CDCl$_3$ at approximately 1 wt/vol % and chemical shifts were referenced to tetramethylsilane and integrations reported relative to 2.0 kg mol^{-1} PEO (180 methylene protons per chain). Size exclusion chromatography (GPC) was performed and polydispersity indices (Đ) were determined using a Hewlett-Packard series 1100 liquid chromatography system equipped with a Hewlett-Packard 1047A RI detector and three PLgel 5 μm MIXED-C columns (Polymer Laboratories) with

chloroform as the mobile phase (35 °C, 1 mL/min) and calibrated using polystyrene standards (Polymer Laboratories). All phosphate buffered saline (PBS) was 100 mM and pH 7.5 with 5 mM ethylenediaminetetraacetic acid (EDTA). Dialysis bags were regenerated cellulose and purchased from Spectrum Labs. Fluorescence readings were acquired using a Varian Cary Eclipse fluorescence spectrophotometer.

Mass Spectrometry

Electrospray Ionization Mass Spectrometry (ESI-MS) samples were dissolved at approximately 1 w/v% in 50:50 MeOH:H_2O doped with approximately 0.1 w/v% KCl and measurements obtained using a Bruker Biotof II instrument in reflectron mode. MALDI-MS samples were dissolved at approximately 1 w/v% in THF containing 10 w/v% 2-(4-hydroxyphenyl-azo)-benzoic acid (HABA) and 1 w/v% NaCl as a cationizing agent followed by spotting of 0.7 μL of the solution on a MALDI target. Measurements were acquired using a Bruker Reflex III instrument in reflectron mode. Analysis and predictions for all mass spectrometry data was performed using Bruker DataAnalysis software.
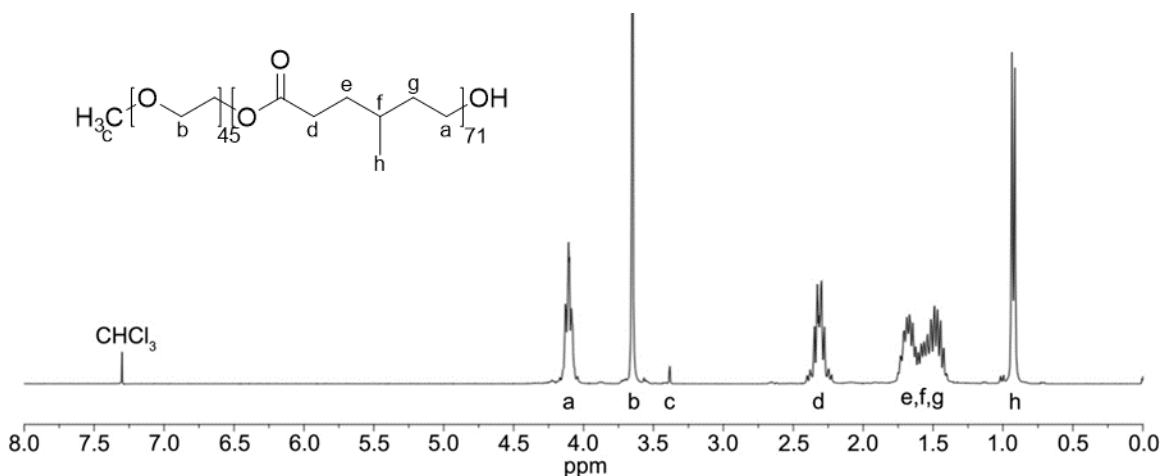
Figure 2-2: ^{1}H NMR spectrum and assignments for nonreactive PEO-PMCL.
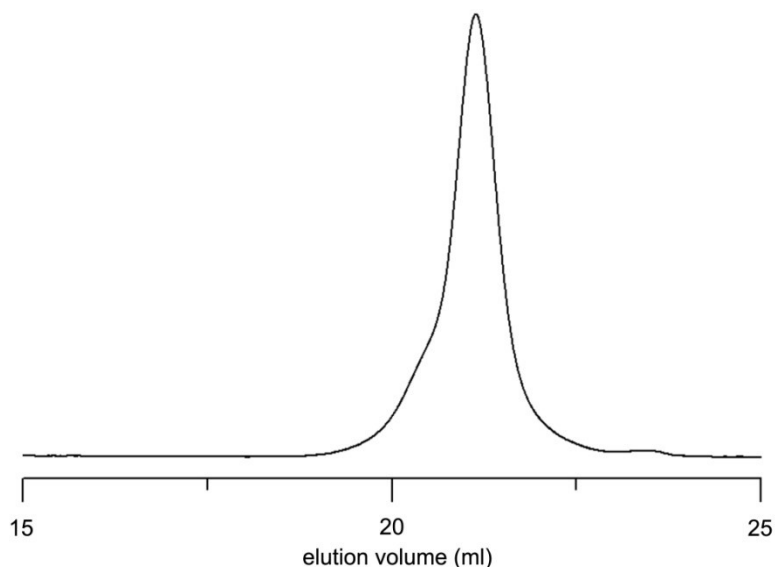
Figure 2-3: GPC trace for nonreactive PEO-PMCL.

Synthesis of Non-Reactive PEO-PMCL

MCL was prepared by Baeyer-Villiger oxidation of 4-methyl cyclohexanone using *m*-chloroperoxybenzoic acid (mCPBA) and 4-methyl cyclohexanone as described elsewhere.[24-25, 41] PEO-PMCL was synthesized by tin octoate-catalyzed ring opening polymerization of MCL from a 2.0 kg mol^{-1} PEO methyl ether (MePEO) macroinitiator. In a sample reaction, MePEO (550 mg, 0.28 mmol) and a Teflon-coated stir bar were added to a previously flame-dried reaction vessel, heated under vacuum to 110 °C for 2 h, sealed and cooled to room temperature. In a dry box under inert atmosphere MCL (3.0 g, 23 mmol) and SnOct$_2$ (12 µL, 37 µmol) were added to the reaction vessel. It was sealed, transferred to an oil bath and allowed to react at 110 °C for 1.5 h under mixing. The vessel, now containing a clear, viscous liquid, was cooled to room temperature. The mixture was dissolved in CH$_2$Cl$_2$ and precipitated twice into hexanes. ^{1}H NMR (CDCl$_3$): δ 4.10 (m, 142H, -C(O)-O-C*H*$_2$-), 3.65 (s, 180H, -O-C*H*$_2$-C*H*$_2$-O-), 3.38 (s, 3H, C*H*$_3$-O-), 2.30 (m, 142H, -C*H*$_2$-C(O)-O-), 1.75-1.35 (m, 355H, -C*H*$_2$-CH(CH$_3$)-CH$_2$-, -CH$_2$-C*H*(CH$_3$)-CH$_2$-,

and –CH$_2$-CH(CH$_3$)-C*H$_2$*-), 0.92 (d, 213H, -CH$_2$-CH(C*H$_3$*)-CH$_3$-). M$_n$ 24.0 kg/mol, Đ 1.19 (GPC).

Synthesis of VS-PEO-PMCL

VS-PEO-PMCL synthesis was based on that of Bae.[37] We have made significant modifications to enhance yields and provide precision characterization of the intermediates. The details are described below.
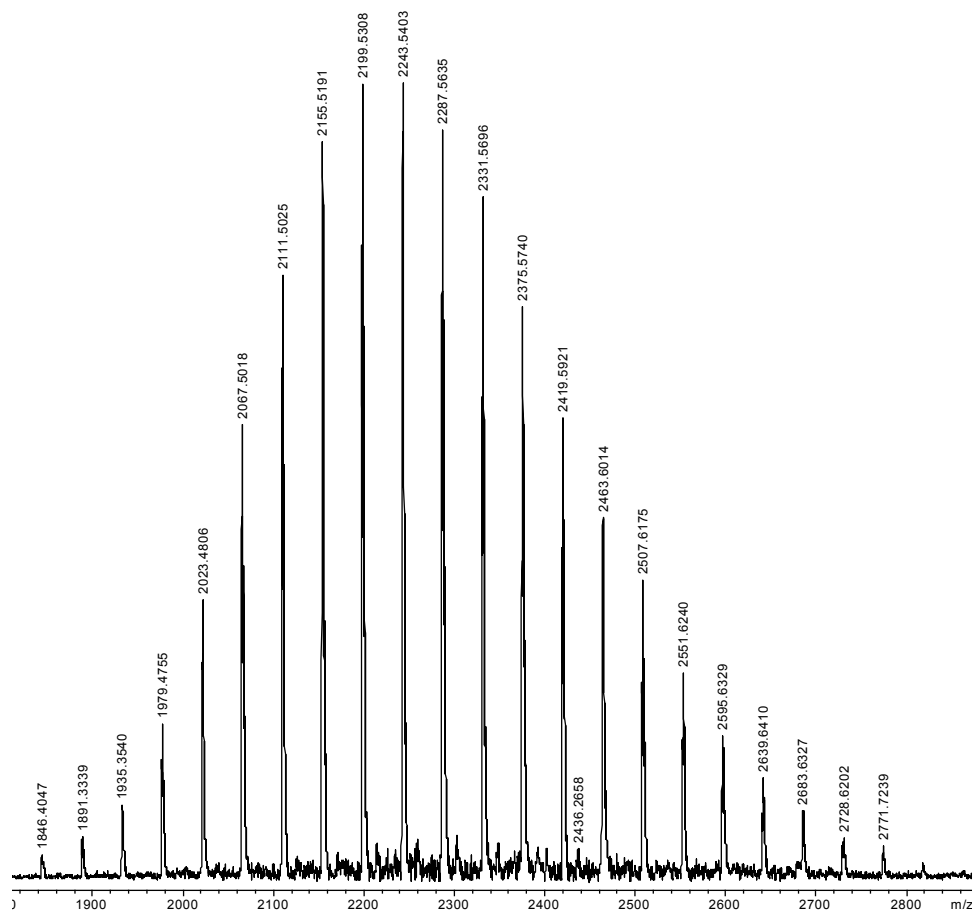
Figure 2-4: MALDI-MS of unmodified PEO. Here HABA was used as a matrix and NaCl dopant as a cationizing agent. This mass spectrum was used to aid comparison to unknown mixtures of polymers synthesized *en route* to VS-PEO-PMCL.

(a) Tosylation of PEO: In a representative reaction, bis(hydroxyl) terminated PEO with molar mass of 2 kg/mol (10 g, 5 mmol) was dissolved in 200 mL dry CH$_2$Cl$_2$ and

chilled to 0 °C. Ag$_2$O (1.75 g, 7.5 mmol) was synthesized from aqueous NaOH and AgNO$_3$[42] and added to the chilled PEO under vigorous stirring followed by KI (0.6 g, 3.6mmol) and *p*-toluenesulfonyl chloride (1.5 g, 7.8 mmol). The reaction mixture was stirred rapidly for 2 h at 0 °C, filtered over Celite, and reduced under vacuum to a white solid. The solid was then dissolved in 75 mL H$_2$O, filtered, extracted into 3 x 50 mL CH$_2$Cl$_2$, dried over MgSO$_4$, and precipitated into ice-cold diethyl ether. Residual solvent was removed from the resulting white solid under vacuum. Yield 95%, 85% tosylation by integration of methylene protons at 4.16 ppm and comparison to the PEO backbone peak at 3.65 ppm; ^{1}H NMR (CDCl$_3$): δ 7.80 (d, 1.7H, Ar), 7.35 (d, 1.7H, Ar), 4.16 (t, 1.7H, TsO-C*H$_2$*-), 3.65 (b, 180H, -O-C*H$_2$*-C*H$_2$*-O-), 2.45 (s, 2.6H, -Ar-C*H$_3$*); ESI-MS (Figure 2-5 and Figure 2-6): m/z unmodified PEO [M+K$^+$] calculated 2126.207 observed 2126.114, Ts-PEO [M+K$^+$] calculated 2148.137 observed 2148.141, Ts-PEO-Ts [M+K$^+$] calculated 2126.041 observed 2126.114. M$_n$ 3.86 kg/mol, Đ 1.05 (GPC). In order to ease characterization of mixed intermediates prepared above, bis(tosyl) PEO was also prepared wherein all hydroxyl groups were reacted with tosyl chloride, allowing direct comparison between known bis(tosyl) PEO and unknown intermediates. To prepare bis(tosyl) PEO, approximately 5 g of polymer was dissolved in approximately 100 mL of CH$_2$Cl$_2$. Approximately 1 mL triethylamine was added followed by a 1.1 molar excess of tosyl chloride with respect to polymer. The solution was allowed to react under stirring for 18 h and polymer isolated by multiple precipitations into ice-cold diethyl ether followed by drying under vacuum. The expanded mass spectrum of the product of this reaction can be seen in Figure 2-5.
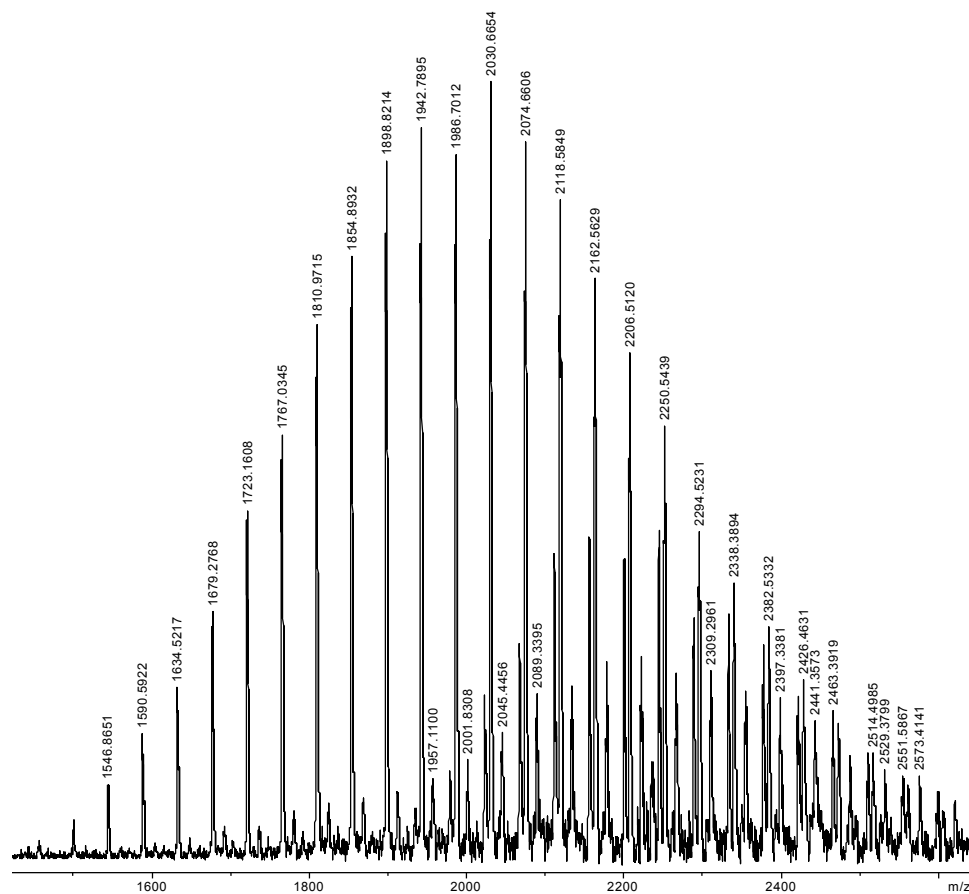
Figure 2-5: Expanded view of MALDI-MS of tosylated PEO. Here MALDI-MS was used for initial characterization but ESI-MS (detail in Figure 2-6) was used for detailed analysis due to enhanced resolution.
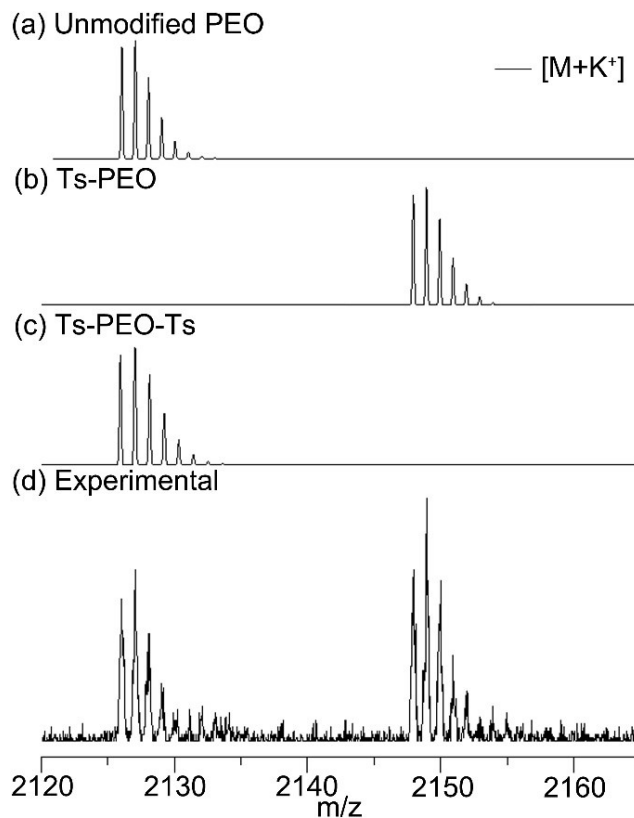
Figure 2-6: Detail of ESI-MS characterization data for PEO tosylated using Ag_2O. ESI-MS was used to minimize potential loss of tosyl substituents during ionization. Predicted data are depicted in (a)-(c) while (d) shows experimental mass spectrum. While Ts-PEO is clearly distinguishable, masses corresponding to Ts-PEO-Ts and unmodified PEO overlap and cannot be distinguished.
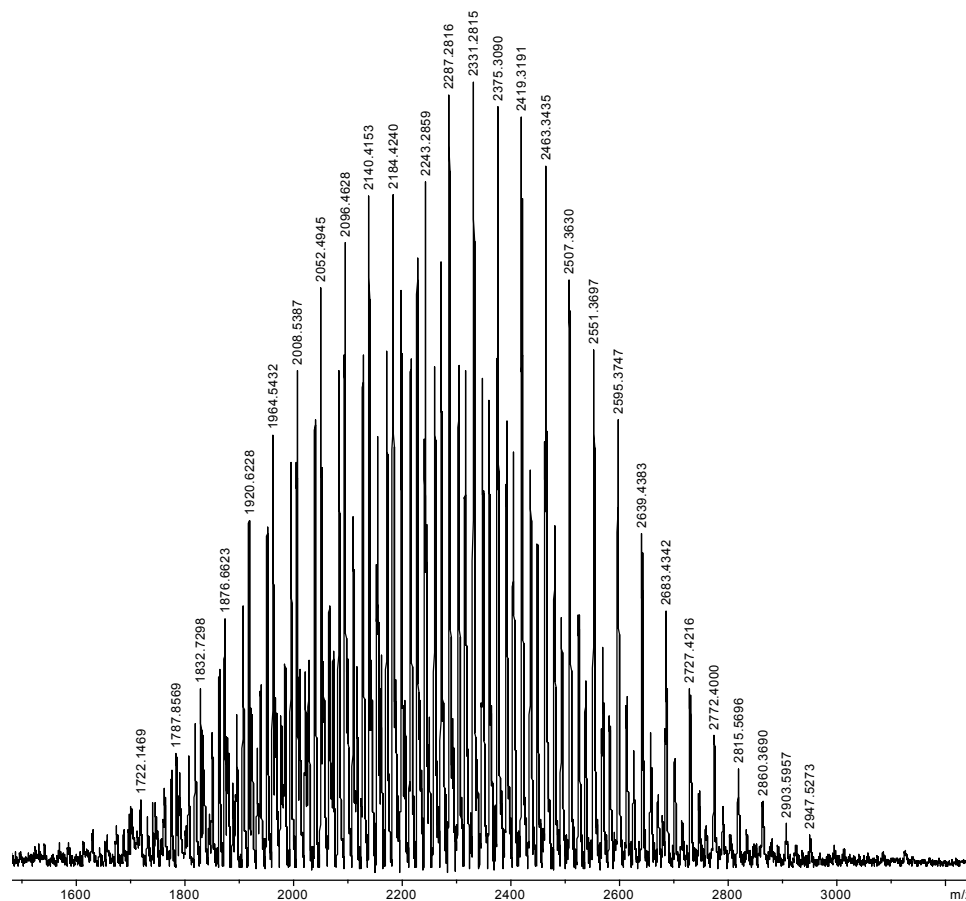
Figure 2-7: MALDI-MS of bis(tosyl) PEO prepared in analysis of mixed tosylates used in synthesis of VS-PEO-PMCL.

(b) Displacement with thioacetate: Potassium thioacetate (5.1 g, 50 mmol) was

dissolved in 125 mL of dry N,N-dimethylformamide (DMF) and the mixture was added to

the mixed PEO tosylates from the previous reaction (9.5 g, 4.75 mmol) and stirred until no

solids were visible. The mixture was degassed by three freeze-pump-thaw cycles,

backfilled with nitrogen, and allowed to react under stirring for three days at 35 °C. DMF

was removed by vacuum distillation. The solid was dissolved in 200 mL of H_2O, filtered,

extracted with 3 x 60 mL CH_2Cl_2 and then dried over $MgSO_4$. Volume was reduced under

vacuum and the polymer precipitated into ice cold diethyl ether followed by solvent

removal under reduced pressure. Yield 90%, 85% thioacetate modification was calculated

by integration of methylene protons at 3.09 ppm and comparison to the PEO backbone peak at 3.65 ppm. ^{1}H NMR (CDCl$_3$): δ 3.65 (b, 180H, -O-CH_2-CH_2-O-), 3.09 (t, 1.7H, -S-CH_2-CH$_2$-), 2.34 (s, 2.6H, -S-C(O)-CH_3); MALDI-MS (Figure 2-8 and Figure 2-9): m/z unmodified PEO [M+Na$^+$] calculated 2110.23 observed 2110.13, [M+K$^+$] calculated 2126.21 observed 2126.20, AcS-PEO [M+Na$^+$] calculated 2124.20 observed 2124.13, [M+K$^+$] calculated 2140.17 observed 2140.10, AcS-PEO-AcS [M+Na$^+$] calculated 2138.16 observed 2138.11, [M+K$^+$] calculated 2110.10 observed 2110.13. M$_n$ 3.23 kg/mol, Đ 1.07 (GPC).

It should be noted that use of a wash bottle of bleach on all surfaces in contact with thioacetate and derivatives as well as proper personal protective equipment is highly recommended due to their strong odors.
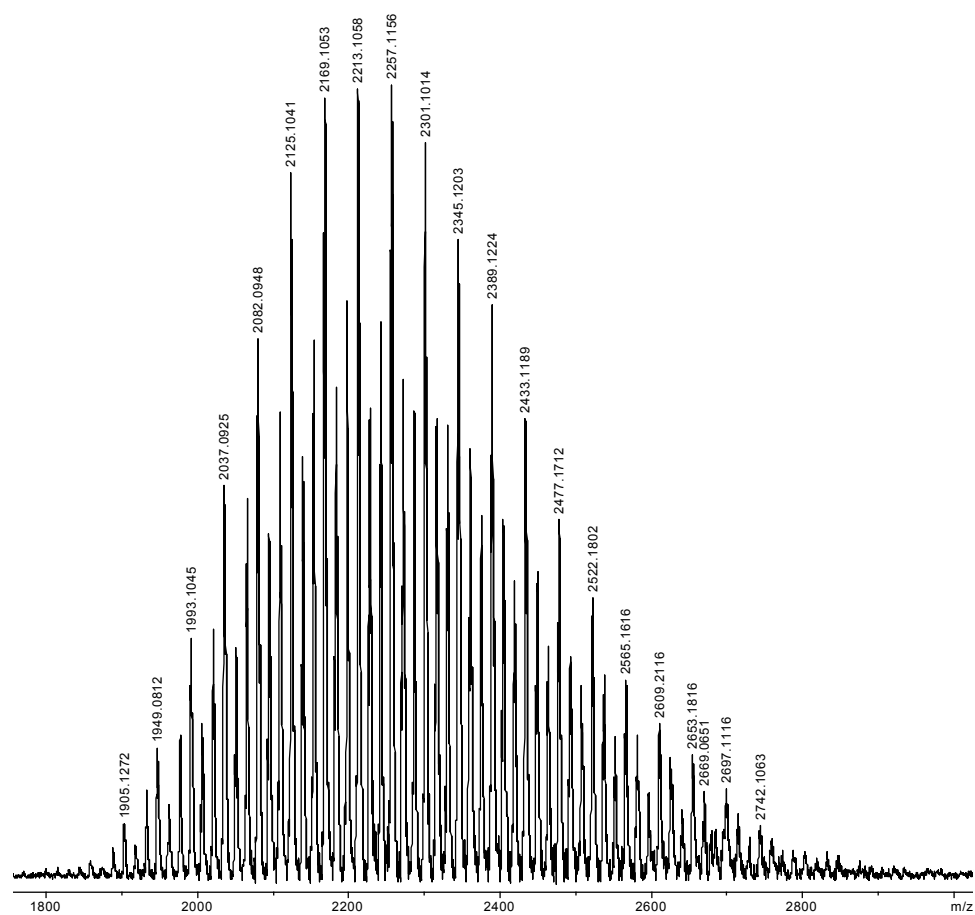
Figure 2-8: Expanded view of MALDI-MS used to characterize PEO thioacetate.
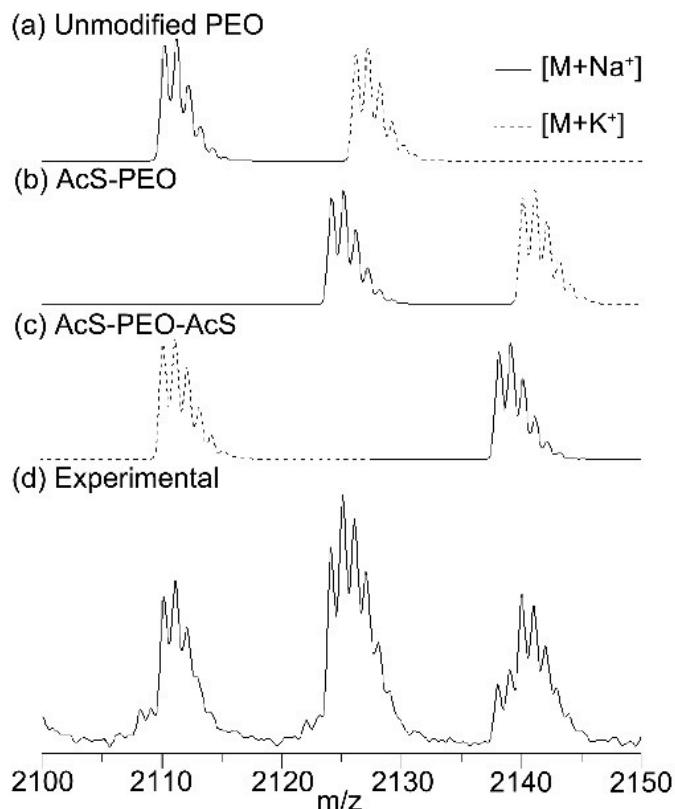
Figure 2-9: Detail view of MALDI-MS data for a combination of unmodified PEO, AcS-PEO and AcS-PEO-AcS. Predicted peaks are depicted in (a)-(c) and experimental data in (d). Observations in experimental measurements were consistent with a mixture of these three forms of PEO.

(c) Deprotection to thiol: PEO thioacetate (8.5 g, 4.25 mmol) was dissolved in 150 mL methanol containing 150 mM potassium methoxide and stirred at room temperature for 1.5 h. The mixture was subsequently neutralized with HCl, filtered, and solvent removed under vacuum. To reduce disulfide bonds, the solid was dissolved in 300 mL 0.1 M aqueous sodium bicarbonate to which was then slowly added sodium borohydride to 0.1 M (1.13 g, 29 mmol) followed by stirring under a nitrogen atmosphere.[43] The solution was acidified to pH 3 by dropwise addition of HCl, extracted into 3 x 50 mL CH_2Cl_2, dried over $MgSO_4$, volume reduced under vacuum, and finally precipitated into ice cold diethyl ether.

The reduction-precipitation step was performed twice to yield a light-yellow solid. Yield 75%, 85% thiol modification as calculated by integration of methylene protons at 2.70 ppm and comparison to the PEO backbone peak at 3.65 ppm. ^{1}H NMR (CDCl$_3$): δ 3.65 (b, 180H, -O-CH_2-CH_2-O-), 2.70 (q, 1.7H, -CH_2-S-), 1.60 (t, 0.85H, -SH); MALDI-MS (Figure 2-10 and Figure 2-11): m/z unmodified PEO [M+Na$^+$] calculated 2110.23 observed 2110.18, [M+K$^+$] calculated 2126.21 observed 2126.23, HS-PEO [M+Na$^+$] calculated 2126.21 observed 2126.23, [M+K$^+$] calculated 2142.18 observed 2142.11, HS-PEO-SH [M+Na$^+$] calculated 2142.19 observed 2142.11, [M+K$^+$] calculated 2114.14 observed 2114.19. M$_n$ 3.43 kg/mol, Đ 1.08 (GPC).
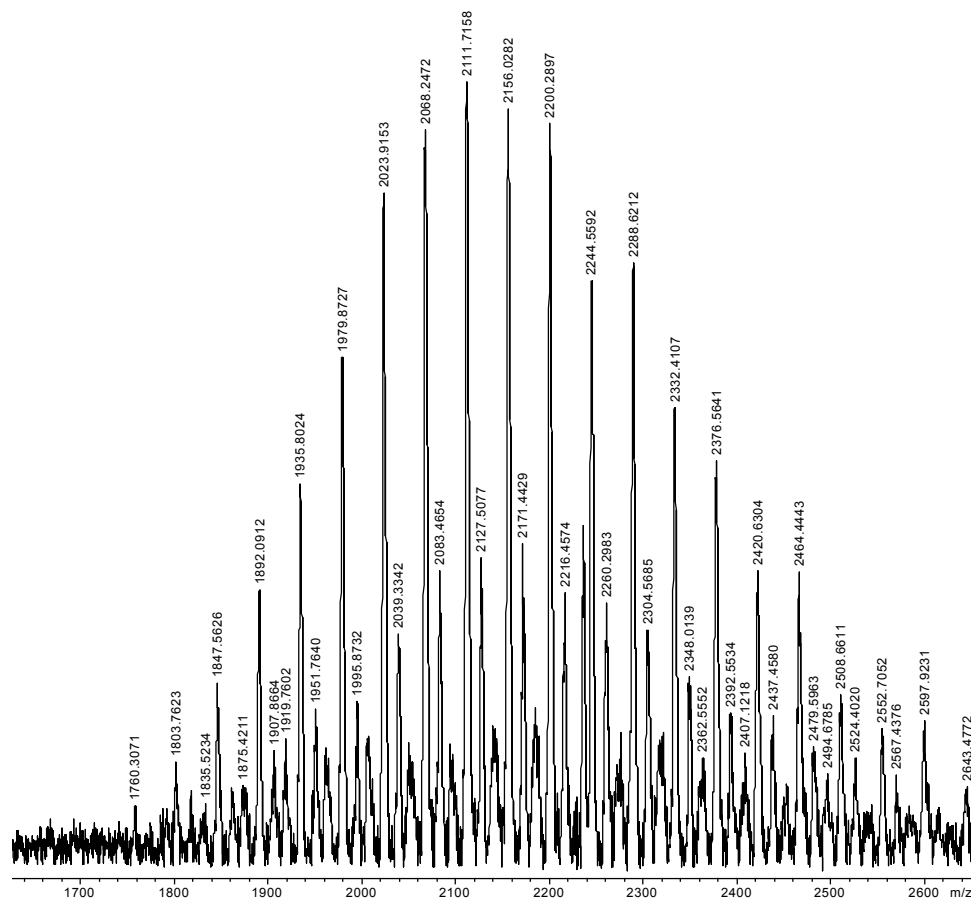
Figure 2-10: Expanded view of MALDI-MS data used to characterize mixed PEO thiolates generated following cleavage of thioacetate.
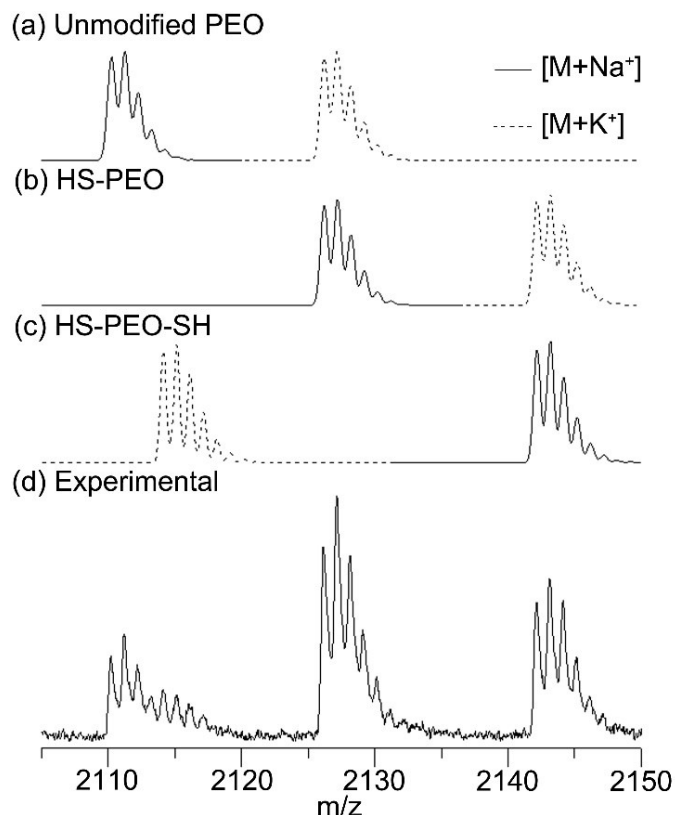
Figure 2-11: Detail view of MALDI-MS characterization data for thiol-modified PEO. Predicted data are depicted in (a)-(c) while (d) shows experimental mass spectra.

(d) Divinyl sulfone attachment: Thiol-terminated PEO (2.0 g, 1 mmol) was dissolved in 50 mL tetrahydrofuran (THF) containing triethylamine (700 μL, 5 mmol) and degassed by three freeze-pump-thaw cycles. A small amount of dithiothreitol (DTT) (38 mg, 0.25 mmol) was added under nitrogen atmosphere to reduce any residual disulfide bonds and the reaction was allowed to stir for 1 h. Divinyl sulfone (DVS) (5 mL, 50 mmol) was rapidly added under vigorous stirring. The reaction vessel was capped and allowed to react for 18 h at room temperature. The solution was reduced in volume under vacuum, precipitated three times into ice-cold diethyl ether and remaining solvent removed under vacuum. Yield 80%, 85% DVS modification was calculated by integration of methylene protons at 2.94 ppm and comparison to the PEO backbone peak at 3.65 ppm. ^{1}H NMR

(CDCl$_3$): δ 6.71 (dd, 0.85H, CH$_2$=C*H*-SO$_2$-), 6.46 (d, 0.85H, C*H$_2$*=CH-SO$_2$-), 6.22 (d, 0.85H, C*H$_2$*=CH-SO$_2$-), 3.65 (b, 180H, -O-C*H$_2$*-C*H$_2$*-O-), 3.31 (m, 1.7H, -SO$_2$-CH$_2$-C*H$_2$*-S-), 2.94 (m, 1.7H, -S-C*H$_2$*-CH$_2$-O-), 2.74 (t, 1.7H, -SO$_2$-C*H$_2$*-), 2.53 (bs, 1.3H, -O*H*); MALDI-MS (Figure 2-12 and Figure 2-13): m/z unmodified PEO [M+Na$^+$] calculated 2110.23 observed 2110.24, [M+K$^+$] calculated 2126.21 observed 2126.22, VS-PEO [M+Na$^+$] calculated 2112.14 observed 2112.18, [M+K$^+$] calculated 2128.11 observed 2128.08, VS-PEO-VS [M+Na$^+$] calculated 2114.05 observed 2114.04, [M+K$^+$] calculated 2130.02 observed 2130.02. M$_n$ 4.05 kg/mol, Đ 1.13 (GPC).

To aid in characterization of mixed intermediates, bis(vinyl sulfone) PEO was prepared. To synthesize bis(vinyl sulfone) PEO, a similar procedure was followed to that employed by Zupancich using PEO-PB.[255] In short, approximately 5 g of PEO diol homopolymer was added to a pressure vessel with a side-mounted stopcock. Sufficient toluene (~25 mL) was added to fully dissolve the polymer. This solution was then frozen in liquid nitrogen and vacuum applied until all toluene had been removed. The polymer was dissolved in ~30 mL dry CH$_2$Cl$_2$. Under nitrogen, a 10-fold excess of sodium hydride was added, followed by a 25-fold excess of divinyl sulfone with respect to the hydroxyl groups. The vessel was sealed and allowed to react at 40 °C for 3.5 days. Sodium hydride was neutralized by dropwise addition of acetic acid. The resulting salts were then filtered and the polymer isolated by multiple precipitations into ice-cold diethyl ether. The final polymer was dried under vacuum and quantitative end-substitution with vinyl sulfone was verified by ^{1}H NMR. MALDI-MS can be found in Figure 2-14.
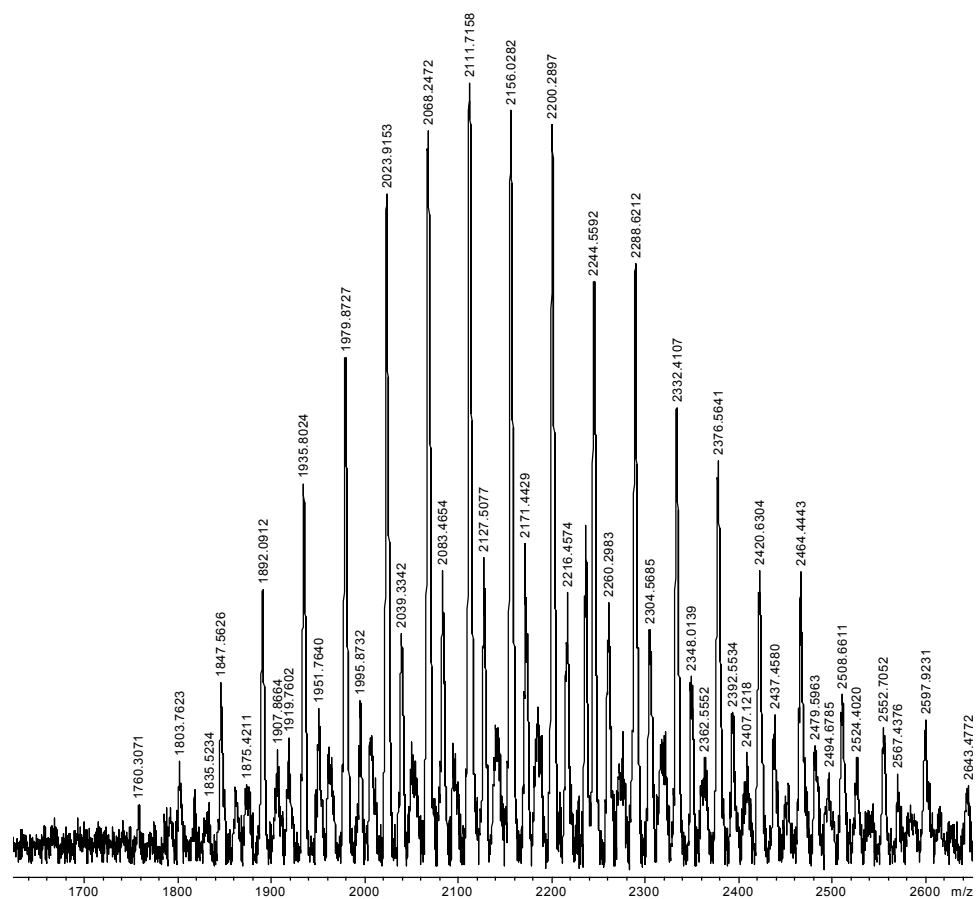
Figure 2-12: Expanded view of MALDI-MS of VS-PEO product following reaction of thiolated PEO with excess vinyl sulfone.NaCl-doped HABA was used as a matrix.
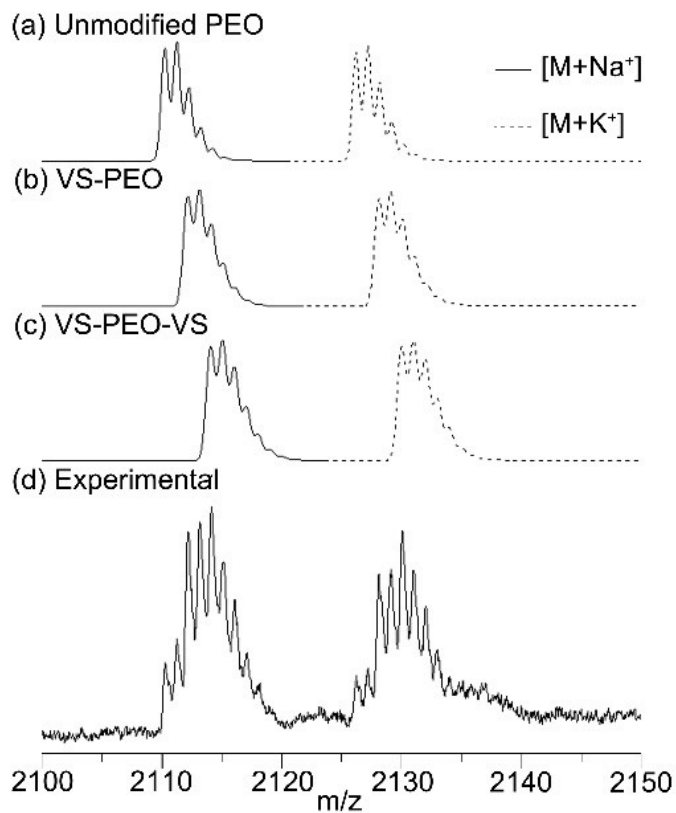
Figure 2-13: MALDI-MS data for a combination of unmodified PEO, VS-PEO and VS-PEO-VS. Predicted peaks are depicted in (a)-(c) and experimental peak in (d). The predicted peaks and those observed in experimental measurements are consistent with a mixture of these three forms of PEO.
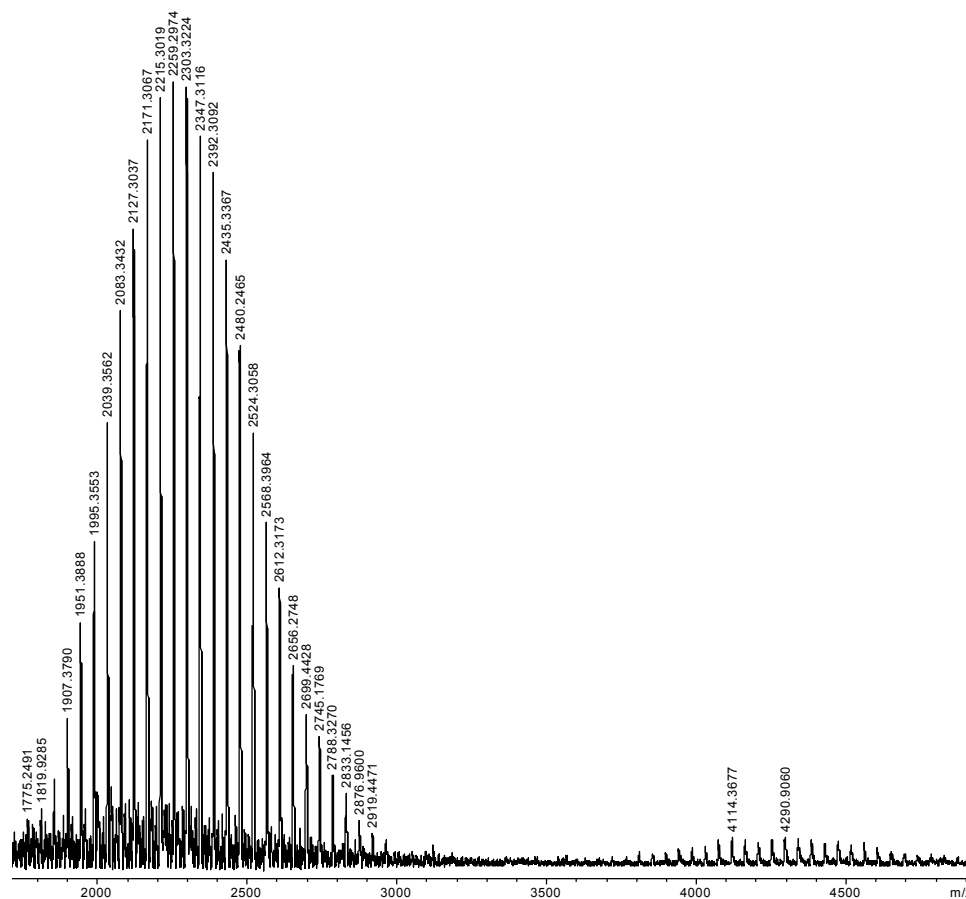
Figure 2-14: MALDI-MS of bis(VS)-PEO used to verify m/z values for VS-PEO. The polymer was prepared by reacting unmodified PEO diol with vinyl sulfone. High m/z peaks are attributed to a minority of coupled polymer chains.

(e) Polymerization of MCL: VS-PEO (1.5 g, 0.75 mmol) was added to a flame dried reaction vessel, dried under vacuum to baseline and back filled with argon. In a glove box, MCL (11.6 g, 91 mmol) and SnOct$_2$ (30 µL, 92 µmol) were added and mixed thoroughly. The reaction vessel was sealed and heated to 110 °C for 1.5 h to yield a viscous liquid. The vessel was then cooled to room temperature, the product dissolved in CH$_2$Cl$_2$, and precipitated twice into hexanes followed by solvent removal under vacuum. ^{1}H NMR (CDCl$_3$): δ 6.71 (dd, 0.85H, CH$_2$=CH-SO$_2$-), 6.46 (d, 0.85H, CH_2=CH-SO$_2$-), 6.22 (d, 0.85H, CH_2=CH-SO$_2$-), 4.10 (m, 140H, -C(O)-O-CH_2-), 3.65 (b, 180H, -O-CH_2-CH_2-O-),

3.31 (m, 1.7H, -SO$_2$-CH$_2$-CH_2-S-), 2.94 (m, 1.7H, -S-CH_2-CH$_2$-O-), 2.74 (t, 1.7H, -SO$_2$-CH_2-), 2.30 (m, 140H, -CH_2-C(O)-O-), 1.75-1.35 (m, 350H, -CH_2-CH(CH$_3$)-CH$_2$-, -CH$_2$-CH(CH$_3$)-CH$_2$-, and –CH$_2$-CH(CH$_3$)-CH_2-), .92 (d, 210H, -CH$_2$-CH(CH_3)-CH$_3$-). M$_n$ 29.3 kg/mol, Đ 1.35 (GPC).

(f) Isolation of purified VS-PEO-PMCL: The product of the previous step was dissolved in 30 mL CH$_2$Cl$_2$ and transferred to glass centrifuge tubes. Methanol was added dropwise until a cloudy solution was observed. The mixture was then heated until clear, allowed to cool to room temperature, and centrifuged for 10 minutes at 1500g. The supernatant was carefully decanted into a fresh centrifuge tube and the pellet collected. The process was repeated until no triblock (PMCL-PEO-PMCL) peak was apparent in the supernatant GPC trace. Solvent was removed under vacuum and the viscous colorless liquid dissolved in 25 mL THF and added to 75 mL H$_2$O. The resulting cloudy mixture was then transferred to a hydrated dialysis bag (MWCO 10 kDa), dialyzed against 10 two liter volumes of water over 7 days at room temperature and lyophilized. ^{1}H NMR (CDCl$_3$): δ 6.71 (dd, 0.8H, CH$_2$=CH-SO$_2$-), 6.46 (d, 0.8H, CH_2=CH-SO$_2$-), 6.22 (d, 0.8H, CH_2=CH-SO$_2$-), 4.10 (m, 140H, -C(O)-O-CH_2-), 3.65 (b, 180H, -O-CH_2-CH_2-O-), 3.31 (m, 2H, -SO$_2$-CH$_2$-CH_2-S-), 2.94 (m, 2H, -S-CH_2-CH$_2$-O-), 2.74 (t, 2H, -SO$_2$-CH_2-), 2.30 (m, 140H, -CH_2-C(O)-O-), 1.75-1.35 (m, 350H, -CH_2-CH(CH$_3$)-CH$_2$-, -CH$_2$-CH(CH$_3$)-CH$_2$-, and –CH$_2$-CH(CH$_3$)-CH_2-), 0.92 (d, 210H, -CH$_2$-CH(CH_3)-CH$_3$-, 210H). M$_n$ 24.7 kg/mol, Đ 1.11 (GPC).
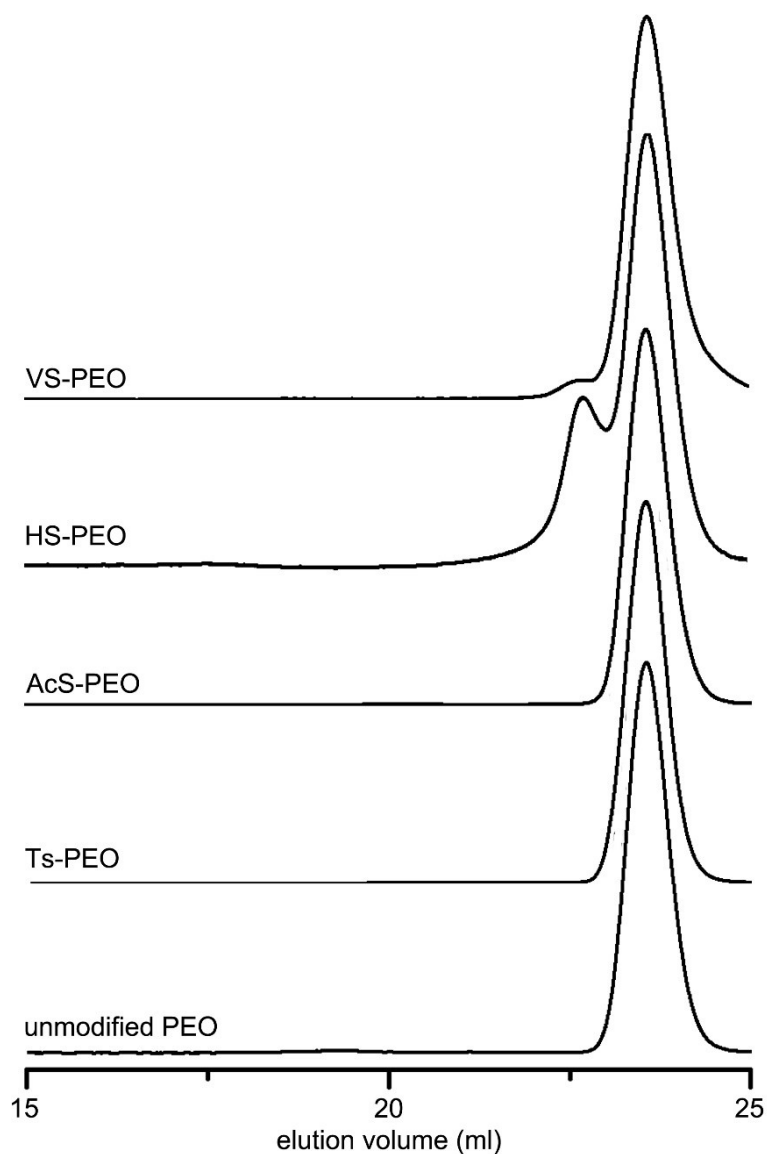
Figure 2-15: GPC traces for each form of modified PEO.

Preparation of Dispersions

All dispersions were prepared by thin film hydration. Polymer was dissolved in CH$_2$Cl$_2$ and added to a vial of known mass. Solvent was evaporated under a nitrogen stream to create a thin film which was dried under vacuum overnight at 45 °C. PBS was then added to the sample to reach 1 wt/vol % polymer. A Teflon-coated stir bar was added, the vial sealed, and the solution stirred at room temperature for 1 week.

Peptide Attachment

  Dispersions used for peptide attachment assays were prepared as described above and extruded through polycarbonate membranes of first 400 nm then 200 nm. Peptides were prepared as a stock solution in PBS. 1100 μl of dispersed polymer was transferred to a vial containing a Teflon-coated stir bar. The desired amount of peptide was added from a stock solution followed by buffer to reach a total volume of 1300 μL. Samples were allowed to react at room temperature for 18 h while stirring. Unincorporated peptide was removed by dialysis against 3 x 3 liter volumes of PBS using dialysis membranes with a molecular weight cutoff (MWCO) of 3.5 kDa over 72 h. The amount of attached peptide was determined by rapid injection and immediate, vigorous mixing of 60 μL of fluorescamine (10 mg mL^{-1} in acetone) into each purified sample. Resulting fluorescence was measured using $\lambda_{ex} = 390$ nm and $\lambda_{em} = 500$ nm at a 90° angle relative to the excitation signal and comparing data to a calibration curve of known peptide concentrations. Data collected for samples not reacted with peptide were used to determine background fluorescence and subtracted from peptide-containing samples. All reported fluorescence data is the average of ten measurements (n=10). Each experiment was performed in triplicate.
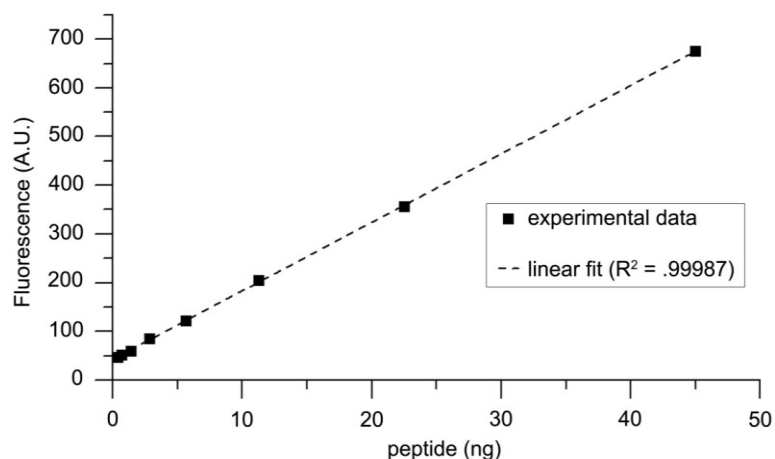
Figure 2-16: Calibration curve used to quantify attached peptide using fluorescamine.

Microscopy

Cryo-TEM imaging was performed by Ligeng Yin. Samples to be imaged by cryogenic transmission electron microscopy (cryo-TEM) were prepared using a home-built controlled environment vitrification system (CEVS) at room temperature.[44] An aliquot of micelle solution (typically 8 μL) was loaded onto a lacey carbon support film (Ted Pella), which was held by a pair of tweezers in the water vapor saturated CEVS. Excess solution was blotted away using a piece of filter paper to form a thin film spanning the holes of lacey carbon with thickness of approximately 100–300 nm. About 15 seconds of waiting time was allowed to relax possible deformations formed during blotting. The grid was then quickly plunged into melting ethane (at ~90K) cooled by surrounding liquid nitrogen. The vitrified sample was transferred into a Gatan 626 cryogenic sample holder, and examined at about −177 °C in a JEOL 1210 TEM with accelerating voltage of 120 kV. Images were collected using a Gatan 724 multiscan CCD and processed with Digital Micrograph version 3.3.1. Phase contrast was enhanced by utilizing a 3–20 μm underfocus.

2.3 Results and Discussion

Modification of PEO

Installation of a selectively reactive end group on the hydrophilic terminus of a diblock copolymer capable of forming polymersomes has been undertaken in the past using vinyl sulfone and azide groups. In these cases, the end group was installed after polymerization of both blocks was complete and under relatively harsh reaction conditions.[139,147,255] However, the harsh reaction conditions employed to install the vinyl sulfone moiety are not applicable to PMCL systems due to the susceptibility of this aliphatic polyester to degradation and transesterification that would not be significant factors for nondegradable polymers. Due to this fact it was necessary to devise a synthetic route to install the vinyl sulfone moiety prior to polymerization of PMCL and verify that it was maintained following polymerization and purification. The key step of such a synthesis is selective end-modification of a precursor PEO diol to allow installation of vinyl sulfone on one end of the molecule while maintaining the hydroxyl group necessary to initiate ring-opening polymerization of MCL. The synthetic route to vinyl-sulfone modified PEO is shown in Figure 2-17.
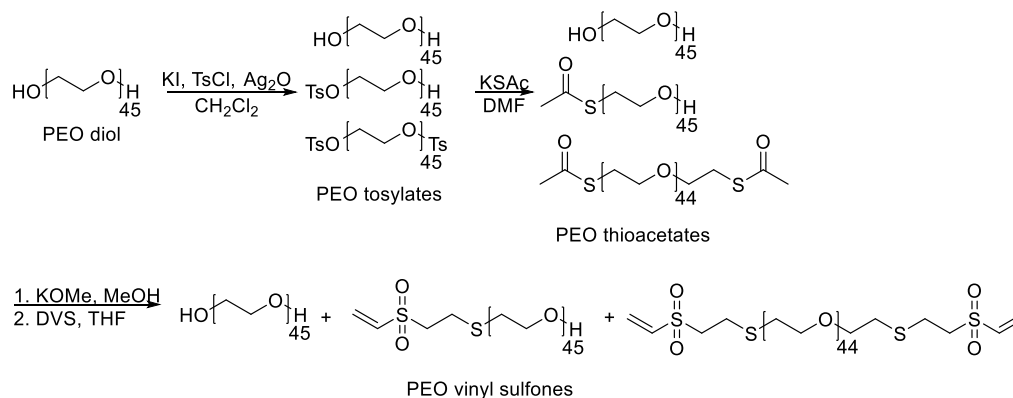
Figure 2-17: Synthetic route to vinyl-sulfone modified PEO (VS-PEO) from PEO diol. Alcohols were first tosylated in methylene chloride using Ag$_2$O which was then displaced with sodium thioacetate in DMF to install a protected thiol functionality. Following isolation, thioacetates were cleaved in alkaline conditions to thiols which were reacted with an excess of divinyl sulfone. Following isolation, the remaining hydroxyl groups could be used to initiate polymerization of PMCL.

Bouzide and Sauvé developed an approach using silver(I) oxide to selectively monotosylate a variety of diols, among them oligo(ethylene glycols).[258] The authors reported 85% monotosylation of hexaethylene glycol in the presence of a stoichiometric amount of tosyl chloride. This is a far more selective result than that obtained using a simple base-catalyzed reaction with a stoichiometric amount of tosyl chloride, which would be expected to yield a statistical 1:2:1 mixture of unmodified diol, the desired monotosylate and the bistosylate, respectively. Bouzide and Sauvé noted that as the length of polymer chain between end groups increased the selectivity of monotosylation decreased.[258] This method of selective end-modification has since been applied to PEO with as many as 80 repeat units (3.5 kg/mol),[258,259] yet no quantification was performed with regard to selectivity in such large molecules.
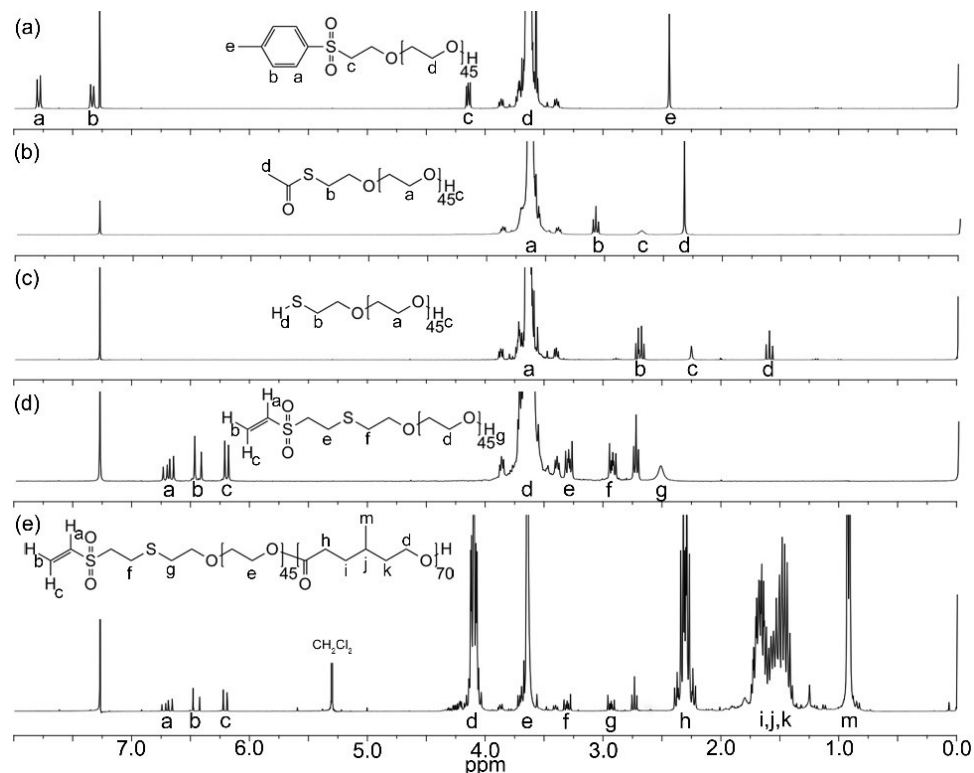
Figure 2-18: ^{1}H NMR spectra (CDCl$_3$) of PEO derivatives. (a) PEO tosylates (b) PEO thioacetates (c) PEO thiolates (d) PEO vinyl sulfonates (e) VS-PEO-PMCL.

After silver(I) oxide-mediated tosylation of PEO, the resulting white solid was analyzed by ^{1}H NMR spectroscopy, and it was determined that, on average, 85% of PEO chains had a tosyl group installed (Figure 2-18a). ESI-MS measurements (Figure 2-5 and Figure 2-6) were consistent with the presence of the desired monotosylate (Ts-PEO). Overlapping peaks for unmodified PEO and the bistosylate (Ts-PEO-Ts, Figure 2-7) confirmed that at least one was present but made it impossible to confirm the presence of both of these polymers. The entire mixture of tosylated polymers was reacted with an excess of potassium thioacetate in DMF to replace the tosyl groups with thioacetates. ^{1}H NMR analysis confirmed that tosyl groups were displaced to form the thioacetate (Figure 2-18b). MALDI-MS (Figure 2-8 and Figure 2-9) was used to confirm that this

transformation had taken place and comparison to predicted results indicated that all three expected forms of PEO were present (AcS-PEO-SAc, AcS-PEO-OH, and HO-PEO-OH). Molar masses and isotopic abundances were consistent with theoretical predictions, confirming the coexistence of these PEO derivatives along with the desired heterotelechelic form of the polymer (AcS-PEO-OH).

The mixture of thioacetates was deprotected to the corresponding thiols by dissolution in methanol containing potassium methoxide. The GPC trace of the products was multimodal (Figure 2-19a) due to the formation of disulfide bonds between thiol-functionalized chains. Two cycles of reduction with aqueous sodium borohydride[43] followed by extraction into an organic phase and precipitation into cold diethyl ether effectively reduced disulfide bonds, resulting in a nearly monomodal GPC trace (Figure 2-19b). Following reduction, MALDI-MS was consistent with theoretical predictions for HS-PEO, PEO and the HS-PEO-SH, with distinct peaks apparent for each molecule (Figure 2-10 and Figure 2-11), while ^{1}H NMR spectroscopy confirmed complete conversion to the thiol (Figure 2-18c). Reoxidation was also reversible, as the multimodal GPC trace attributed to formation of disulfide bonds could be recovered by bubbling air through the sample (Figure 2-19c).
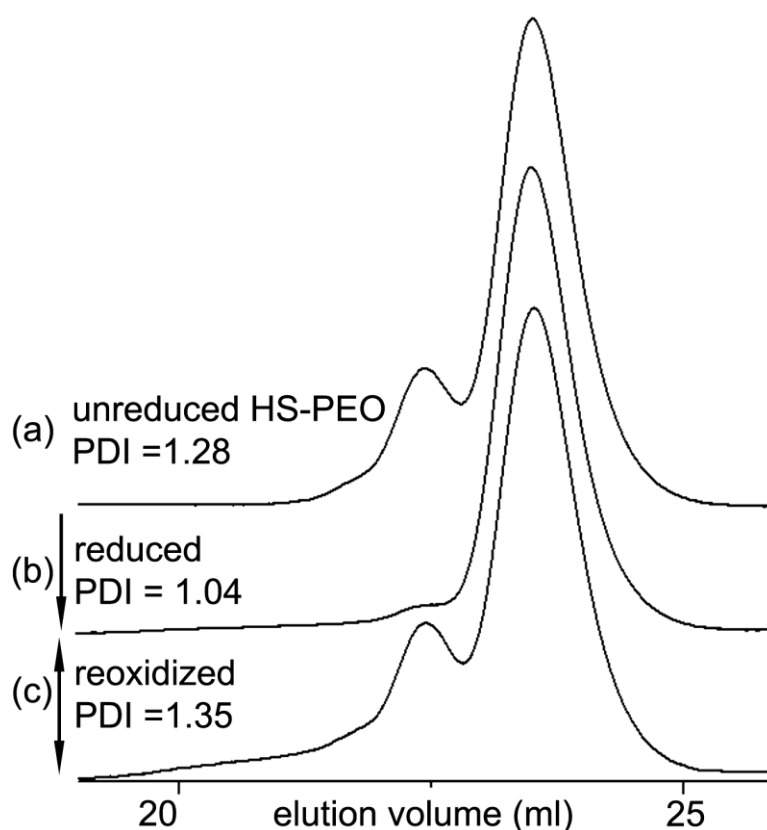
Figure 2-19: GPC traces of thiol-modified PEO demonstrating that this polymer is prone to oxidation to form disulfide bonds chains at thiol-modified end groups. Cleavage of these disulfide bonds is essential both for purification and to ensure thiols are available for reaction with divinyl sulfone. (a) Following cleavage of the thioacetate many PEO chains are linked via disulfide bonds, leading to a high Đ value. (b) Following reduction only minimal low elution volume peak is visible and the polydispersity index is much lower, consistent uncoupled free chains. (c) Disulfide bonds can be reintroduced by bubbling air through the sample.

Divinyl sulfone was added to thiol-modified end groups by conjugate addition between thiols and vinyl sulfone. To minimize disulfide bond formation all solvent was thoroughly degassed and reactions were performed under nitrogen atmosphere. After dissolution of polymer, a small amount of dithiothreitol was added to reduce any fortuitously-formed disulfide bonds. In early experiments the commonly-used disulfide

reducing agent tris(2-carboxyethyl) phosphine (TCEP) was used, but use of this reagent was discontinued following very low yields due to apparent reaction with divinyl sulfone.

Following reduction, divinyl sulfone was added rapidly under vigorous stirring at large excess to minimize chain-chain coupling. Following reaction, repeated precipitation into ice-cold diethyl ether yielded a white solid free of unattached divinyl sulfone with quantitative reaction of thiol groups as determined by ^{1}H NMR spectroscopy (Figure 2-18d). A small peak at low elution volume was detected by GPC and was unaffected by the addition of reductants, implying some divinyl sulfone mediated chain-chain coupling. Experimental MALDI-MS data was consistent with simulated predictions of VS-PEO, PEO, and VS-PEO-VS (Figure 2-12, Figure 2-13, and Figure 2-14). To verify that no reaction would occur between hydroxyl groups and vinyl sulfone, unmodified PEO was mixed with divinyl sulfone under identical conditions to those used to install vinyl sulfone on the thiol-terminated system. Following precipitation into cold diethyl ether, no evidence of divinyl sulfone was observed in the ^{1}H NMR spectrum, confirming minimal reactivity with hydroxyl groups under these conditions.
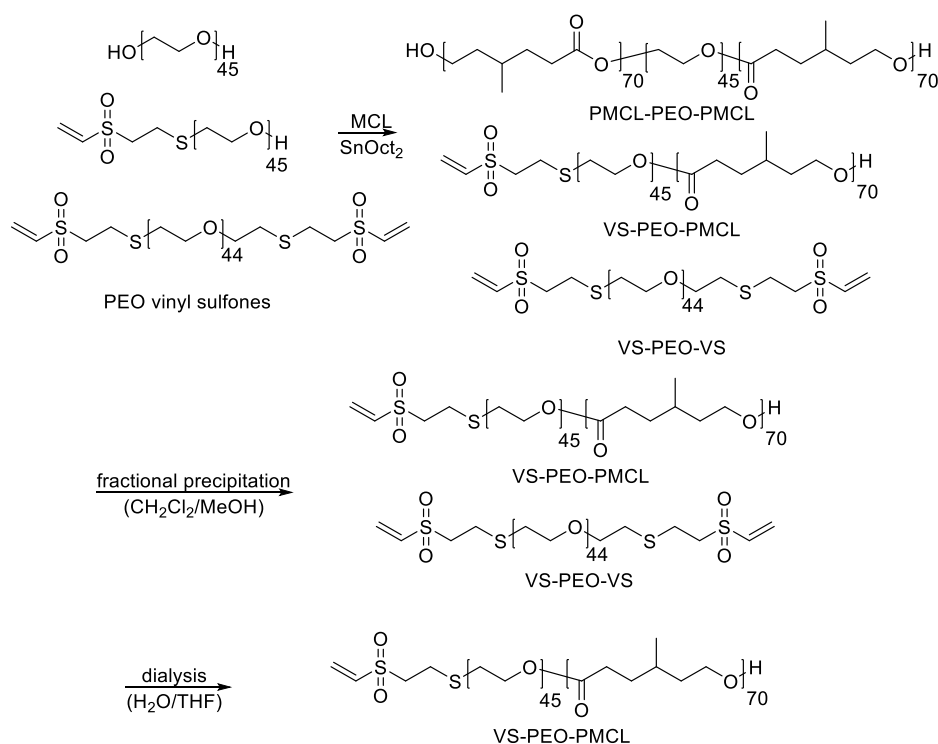
Scheme 2-1: Polymerization of MCL from crude VS-PEO macroinitiator and purification used to isolate VS-PEO-PMCL diblock.

Polymerization of MCL

After installation of vinyl sulfone, the remaining hydroxyl end groups were used as initiation sites for polymerization of MCL. In past studies, PEO-PMCL has primarily been prepared in organic solvent using aluminum alkoxides and PEO monomethyl ether as the initiating system.[23-25] Initial experiments using these conditions and vinyl-sulfone modified PEO (VS-PEO) resulted in loss of vinyl sulfone groups. To address this concern, SnOct$_2$ was employed as the catalyst and no solvent was used. No loss of vinyl sulfone was detectable by ^{1}H NMR spectroscopy under these conditions. In all cases a diblock of approximately 11 kg/mol was targeted (i.e., PEO 2 kg/mol, PMCL 9 kg/mol), a molar mass similar to that shown to form vesicles in studies of unreactive PEO-PMCL.[25]

When PEO methyl ether was used to initiate polymerization it was possible to obtain the unreactive diblock polymer PEO-PMCL while maintaining Đ values below 1.2 as long as the polymerizations were not allowed to proceed to full conversion. When vinyl-sulfone modified PEO was used to initiate polymerization, polymerization proceeded from all available hydroxyl groups as shown in the GPC data presented in Figure 2-20. Based on these data we concluded that VS-PEO formed the desired vinyl sulfone-functionalized block polymer VS-PEO-PMCL. However, initiation also occurred at both ends of residual unmodified PEO to yield PMCL-PEO-PMCL (low elution volume). VS-PEO-VS remained as well (evident at high elution volumes). The agreement between predicted and experimental mass spectra for modified PEO above clearly suggested that a mixture of singly-, doubly- and unmodified PEO was present; however, quantification of the relative populations of each product by MALDI-MS is challenging[47-49] and necessitated quantification by other means. Using ^{1}H NMR data following polymerization of MCL supplemented by comparison of relative peak heights in the GPC trace of the combined polymers (Figure 2-20) we estimated that the mixture was composed of approximately 10 mol% VS-PEO-VS (2270 g/mol), 70 mol% VS-PEO-PMCL (11 kg/mol) and 20 mol% PMCL-PEO-PMCL (ca. 20 kg/mol), demonstrating only mild selectivity compared to the stoichiometric mixture that would be expected for more conventional approaches to end-modification.

Following MCL polymerization, fractional precipitation was used to isolate the target VS-PEO-PMCL diblock, taking advantage of the relatively greater hydrophobicity of the triblock PMCL-PEO-PMCL. By slow addition of methanol to a dichloromethane

solution of the crude mixture until the point of cloudiness and centrifuging the mixture it was possible to gradually adjust solvent quality to be incompatible with triblock polymer while leaving most of the diblock and nearly all of the VS-PEO-VS in solution (Figure 2-20b). By formulating similar arguments to those used in to estimate the quantity of each polymer following MCL polymerization it was possible to estimate that after fractional precipitation 60 mol% of the remaining mixture of VS-PEO-PMCL and VS-PEO-VS was comprised of the VS-PEO-PMCL diblock. Dialysis against water was used to remove residual VS-PEO-VS. Following dialysis and lyophilization no degradation of the polymer chain was detectable by GPC (Figure 2-20c) and only a small degree of vinyl sulfone loss was detectable by ^{1}H NMR spectroscopy (~10%, Figure 2-18e), yielding the desired diblock as a viscous, transparent liquid.
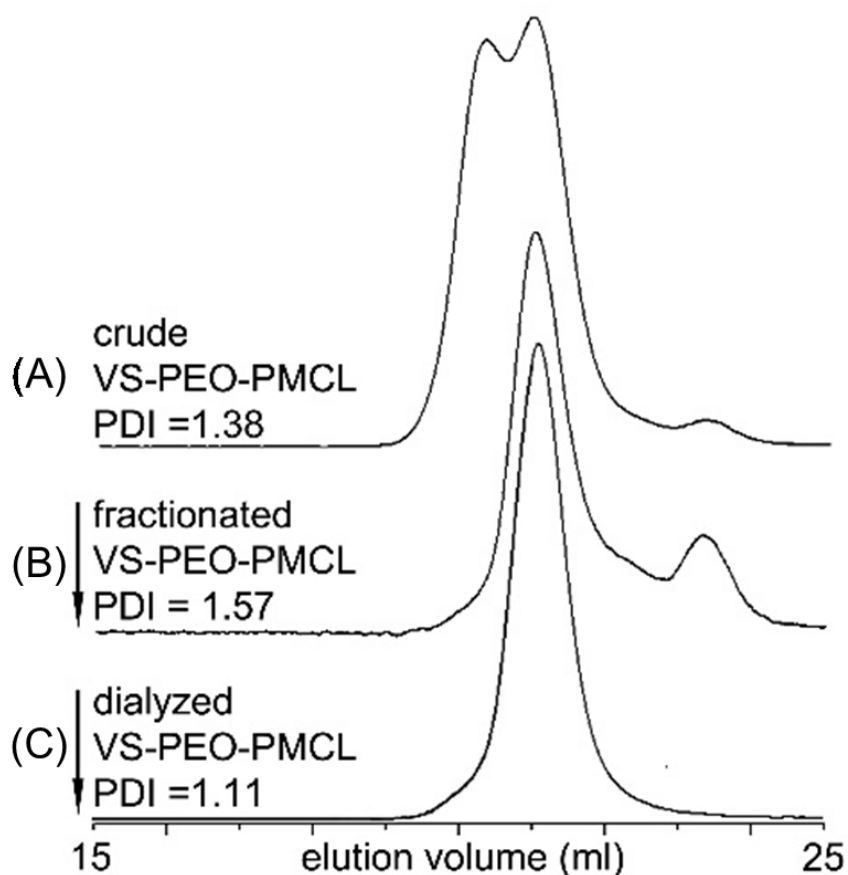
Figure 2-20: GPC elugrams showing the purification of VS-PEO-PMCL diblock. (A) Polymerization initiated from hydroxyl groups on vinyl sulfone modified PEO. Unmodified PEO formed the triblock PMCL-PEO-PMCL at low elution volumes, VS-PEO formed the diblock VS-PEO-PMCL and comprises the middle peak and VS-PEO-VS initiated no polymerization of MCL and was eluted last. (B) Following precipitation from CH_2Cl_2 to remove PMCL-PEO-PMCL, the diblock VS-PEO-PMCL remained, as did VS-PEO-VS. (C) After dialysis, only the desired VS-PEO-PMCL diblock remained.

Aggregate Morphology and Peptide Attachment

To verify that aggregate morphology was unaffected by vinyl sulfone groups and attached peptide, cryo-TEM was used to compare the solution morphology of VS-PEO-PMCL without peptide (VS-0) and samples densely grafted with peptide (VS-100) to the control sample of unreactive PEO-PMCL. In the nonreactive system (Figure 2-21) vesicles were the primary morphology observed. Some wormlike micelles were also present,

consistent with coexisting morphologies observed in a number of self-assembled polymer systems, including PEO-PMCL.[25, 50-51] When vinyl sulfone groups were present but no peptide had been conjugated to the reactive end groups (sample VS-0, Figure 2-21), there was little discernable difference in morphology from that expected in the absence of a reactive group and only vesicles were observed.
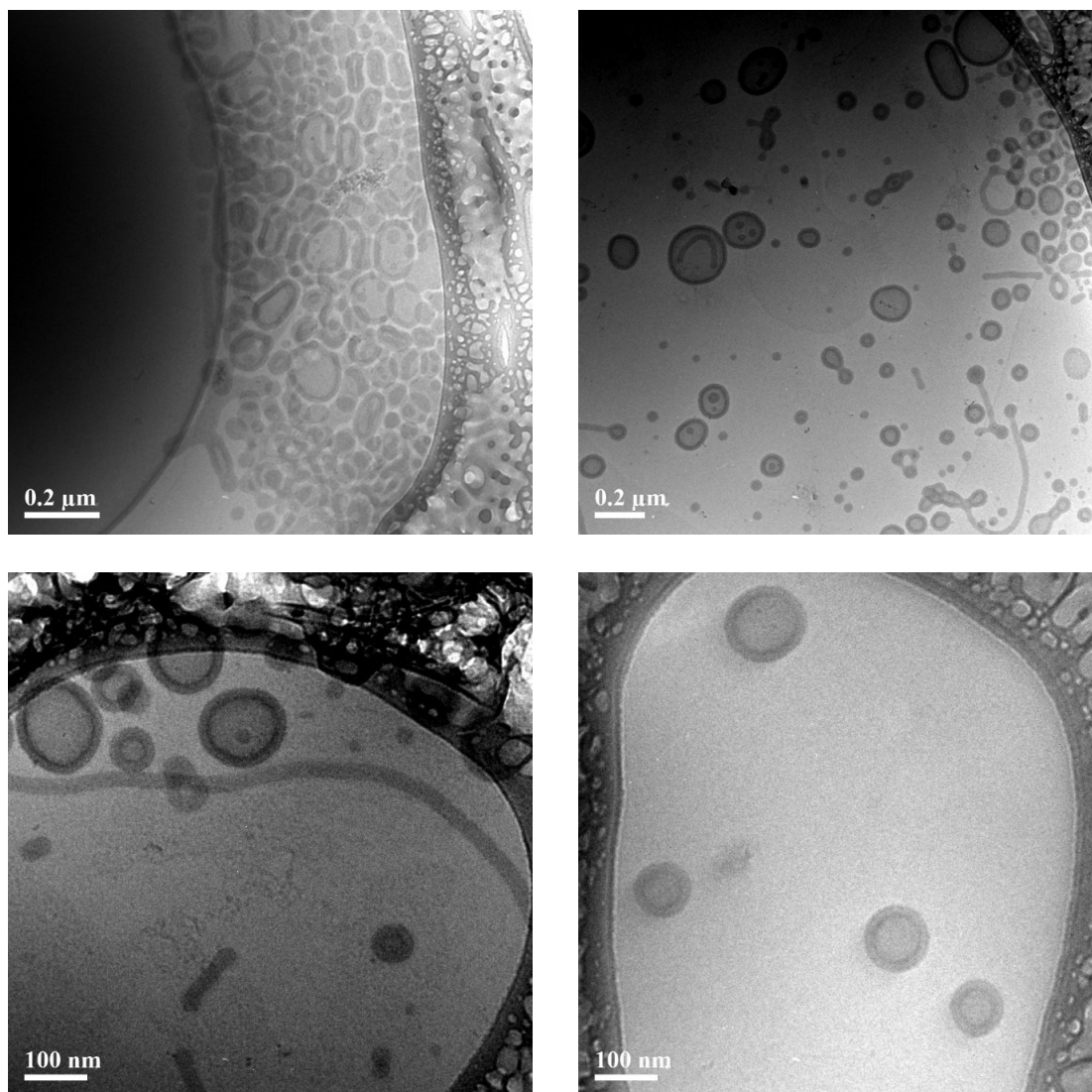
Figure 2-21: Cryo-TEM of nonreactive PEO-PMCL diblock copolymer (sample O-0 in Table 2-1) following thin-film hydration. Vesicles were the predominant morphology with some coexisting wormlike micelles, consistent with prior studies of this system.[194] Large black structures on the periphery of images are the lacey carbon used to suspend samples for vitrification. Images by Ligeng Yin.
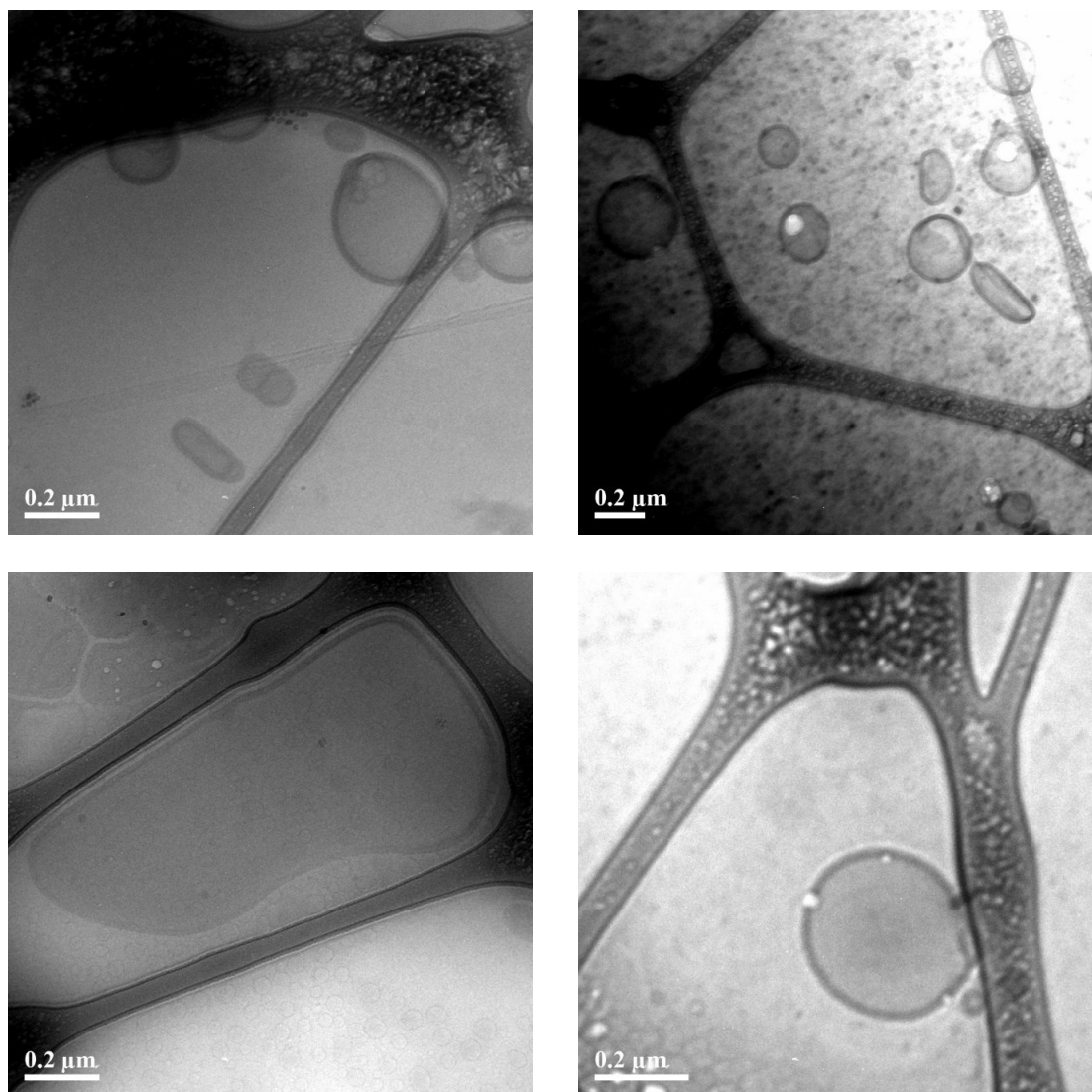
Figure 2-22: Cryo-TEM of reactive VS-PEO-PMCL diblock copolymer without peptide (sample VS-0 in Table 2-1) following thin-film hydration. Vesicles were again the predominant morphology and the reactive group did not appear to have a significant effect on morphology. Large black structures on the periphery of images are the lacey carbon used to suspend samples for vitrification. Images by Ligeng Yin.

To probe the capacity of this vinyl-sulfone functional polymer to attach peptides, dispersions of either nonreactive PEO-PMCL (9100 g/mol PMCL, 18 wt% PEO, Đ 1.19) or reactive VS-PEO-PMCL (8900 g/mol PMCL, 18 wt% PEO, Đ 1.11) were formed at 1 wt/vol% in PBS (pH 7.5). Following extrusion to 200 nm, the desired amount of peptide (CGRGDS or GRGDS) was added to the polymersome solution and allowed to react for 18 hours. Then the solution was dialyzed against pure water to remove unreacted peptide. To determine the amount of peptide attached to polymersomes, the fluorescamine assay was used.[52] A fluorescence-based assay was chosen due to the fact that the more common colorimetric assays rely on measures of absorbance to quantify peptide concentrations. In the case of polymersomes, solutions are not necessarily clear even prior to the addition of assay reagents and as a result, absorbance measurements are particularly susceptible to interference from the dispersion itself. The superior selectivity of the fluorescence-based assay (minimal fluorescence unless fluorescamine reacts with peptide amines) and 90° detection angle should decrease interference relative to absorbance-based assays even if the solution scatters light. In the present study, any interference from the solution would result in an underestimation of attached peptide, whereas an absorbance-based assay would overestimate this quantity. As a result, if the values reported here are inaccurate, it is more likely to be due to underestimation of peptide conjugation than overestimation.

Fluorescence values obtained for VS-PEO-PMCL dispersions without peptide were used as a measure of background (sample VS-0) and peptide amounts determined by comparison to fluorescence of calibration curves containing known amounts of peptide (Figure 2-16). The results of this assay are presented in Table 2-1. When peptides contained

a thiol-bearing cysteine residue, even low concentrations of peptide were highly reactive, and nearly all of the peptide coupled to vinyl sulfone groups on the surface of vesicles. As the amount of peptide was increased relative to the total vinyl sulfone groups present on both the exterior and interior interface, the amount of coupled peptide increased then gradually plateaued at slightly over 40% of all vinyl sulfone groups. This is consistent with only outwardly-oriented vinyl sulfone groups being available for reaction with thiols, as approximately half of the polymer chains on a given aggregate are situated on the inner surface of the polymersome and thus inaccessible to peptides. As approximately 10% of the vinyl sulfone groups were hydrolyzed during dialysis purification, the measured level of peptide attachment is consistent with saturation or near-saturation of the remaining reactive sites. Any residual unreacted vinyl sulfones on the vesicle's exterior interface in high peptide-concentration samples (VS-100 and VS-500) may be the result of dense crowding following peptide attachment resulting in steric restraints hindering the addition of further peptides.

Table 2-1: Results of peptide attachment to polymersomes. All 'VS-' samples were composed of VS-PEO-PMCL while all 'O-' samples were composed of PEO-PMCL. Experiments were performed in triplicate and experimental uncertainty was calculated as one standard deviation from the mean of these data.

sample	peptide sequence	introduced peptide[a]	attached peptide[a]
VS-15	CGRGDS	15	14±2.1
VS-40	CGRGDS	40	37±3.3
VS-75	CGRGDS	75	38±7.5
VS-100	CGRGDS	100	40±1.8
VS-500	CGRGDS	500	42±3.7
VS-100R	GRGDS	100	.25±.45
O-0	-	0	.04±.40
O-100	CGRGDS	100	.25±.64

[a]Mole % versus polymer.

To ensure proper function of targeting groups it is essential that the attachment of ligands not only proceed to high reaction conversions but also be site-specific, as simply tethering a targeting group without regard for orientation will result in decreased ligand activity.[260,261] Here, presentation of the peptide with a specific orientation is facilitated by attachment solely due to reaction between the thiol on a cysteine residue at the N-terminus of the peptide and a vinyl sulfone group in the vesicle corona. Of particular concern is that amines can act as donors in conjugate additions. To ensure that peptide attachment was not due to the reaction of amines GRGDS peptide, which lacks a cysteine residue but contains a terminal amine, was reacted with VS-PEO-PMCL vesicles. Following dialysis only a small amount of peptide was detected (0.25 mol% ± 0.45%), suggesting that if peptide amines do react with vinyl sulfone groups, this reaction occurs much less readily than is the case for thiols, a finding consistent with prior reports about the relative reactivity of each functional group in conjugate addition.[55] When cysteine-containing peptides were mixed with polymersomes lacking the vinyl sulfone groups (O-100) minimal peptide was detected (0.25 mol% ± 0.64%), implying that both a vinyl sulfone group and a thiol are required for peptide attachment. These results suggest that site selective attachment of targeting groups is indeed possible in this system, as the vast majority of attachment will occur between a vinyl sulfone group in the polymersome corona and a peptide's N-terminal thiol. No change in morphology was observed following the near-saturation of the vesicle surface with peptide (sample VS-100, Figure 2-23).
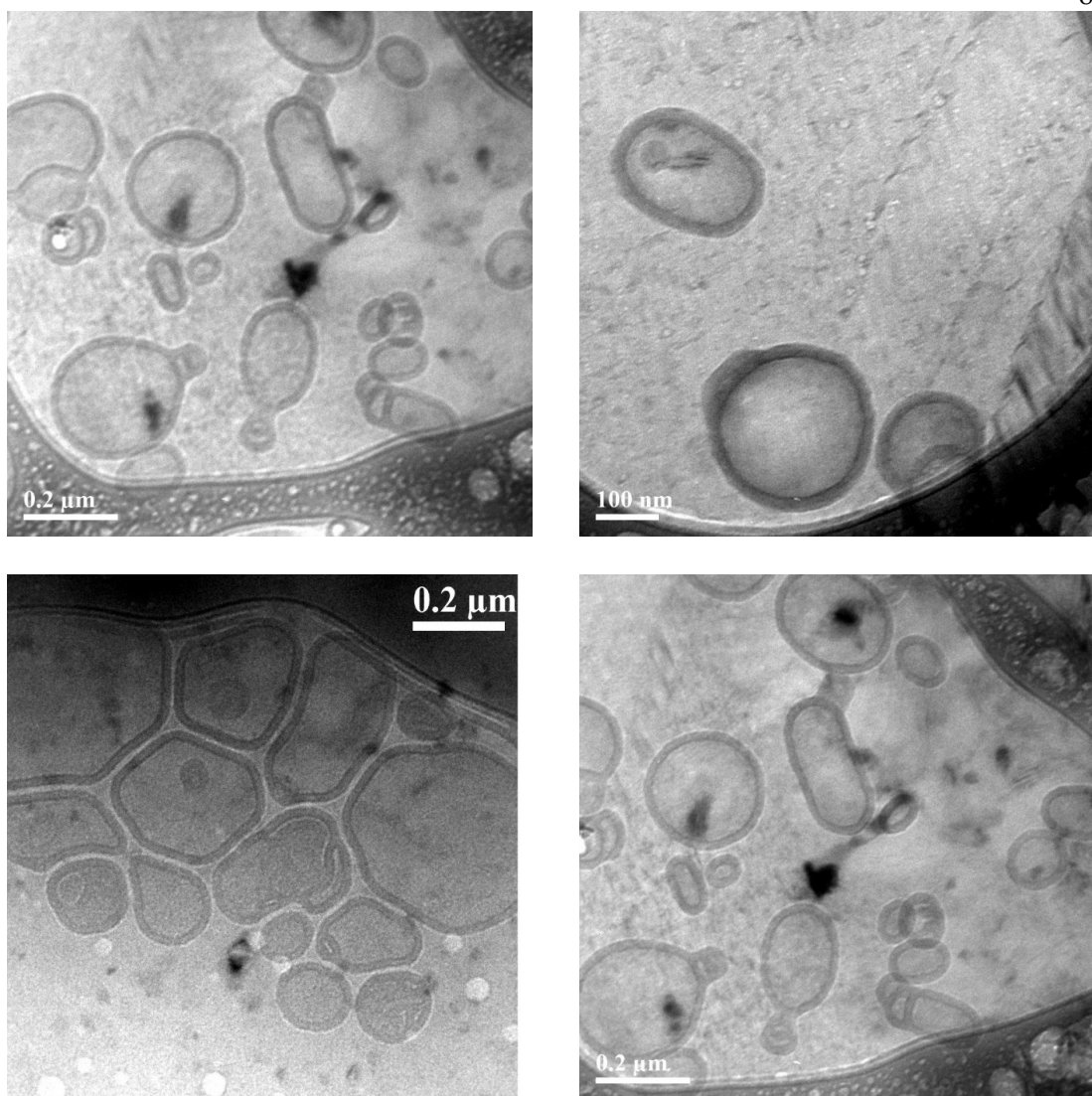
Figure 2-23: Cryo-TEM of peptide-saturated VS-PEO-PMCL diblock copolymer (sample VS-100 in Table 2-1) following thin-film hydration and then peptide conjugation. Here approximately 40 mol% of all vinyl sulfone groups (both exterior- and interior-facing) are tethered to the thiol-bearing peptide CGRGDS. This limited reaction is likely due to near-saturation of exterior reactive groups only, since interior-facing groups are not accessible to the peptide. No apparent change in morphology is observed upon tethering of this nearly 600 g/mol targeting moiety. Large black structures on the periphery of images are the lacey carbon used to suspend samples for vitrification. Images by Ligeng Yin.

2.4   Conclusions

To develop a degradable, targeted drug delivery system the vesicle-forming block polymer VS-PEO-PMCL was developed. This amphiphile self-assembled in water to form vesicles with reactive vinyl sulfone groups at the terminus of the corona-forming PEO block. These groups were capable of tethering high concentrations of a thiol-containing targeting peptide after self-assembly of vesicles in mild conditions without the need for catalyst. Attachment of thiol-containing targeting peptides proceeded to high conversion while maintaining the orientation of the peptide (CGRGDS) while peptides lacking a thiol group (GRGDS) underwent minimal attachment.

Following targeting peptide attachment, no change was observed in aggregate morphology. In biological systems, even low concentrations of surface-bound ligand dramatically enhance binding and endocytosis in cells overexpressing targeted receptors.[38, 56-57] Given the structural similarity between PEO-PMCL and VS-PEO-PMCL, by blending the reactive polymer as the minority component prior to self-assembly it should be possible to simultaneously take advantage of both the shielding capacity of the PEO corona and the enhanced targeting due to bound ligands on the exterior of the vesicles. This system should serve as a versatile platform for specific delivery of a variety of therapeutic payloads and capable of utilizing a wide range of targeting moieties. These applications as well as polymer degradation behavior will be further explored in the following chapter.

3 Bioresorbable Polymersomes for Targeted Delivery of Cisplatin[†]

3.1 *Introduction*

The previous chapter addressed the synthesis and molecular characterization of the reactive amphiphilic diblock copolymer vinyl sulfone-poly(ethylene oxide)-*block*-poly(γ-methyl-ε-caprolactone) (VS-PEO-PMCL) as well as comparison to its nonreactive analog PEO-PMCL (Figure 3-1). This chapter describes efforts to apply these polymers to biological systems for targeted delivery of the anticancer drug cisplatin.
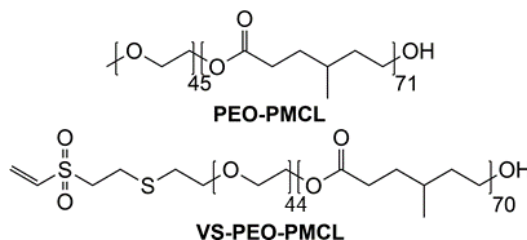
Figure 3-1: Molecular structure of the block copolymers PEO-PMCL and VS-PEO-PMCL used in this work. These polymers self-assemble in water, forming polymersomes capable of encapsulating both hydrophilic and hydrophobic payloads. The vinyl sulfone moiety allows selective conjugation, after self-assembly, to thiol-containing targeting ligands.

Many approaches to delivering cisplatin been investigated to diminish the side effects associated with nonspecific delivery of cisplatin.[262,263] One of the most promising, cisplatin encapsulated in liposomes, increased the amount of the drug that could be administered without major side effects and significantly increased platinum concentration

---

[†] Reproduced in part from Petersen, M.A., Hillmyer, M.A., Kokkoli, E., *Bioconjugate Chemistry*, ASAP (2013). Copyright 2013 American Chemical Society.

in the tumor.[264–267] Despite these promising inroads, therapy using the liposomal system proved to be ineffective due to the lack of a route for drug to reach the interior of target cells. Though liposomes and encapsulated drug had accumulated in the vicinity of cancer cells, there was no way for the drug to be delivered to the interior of cells, a crucial final step for administered drug to be effective.[268–272]

In this chapter the role of the targeting ligand was investigated, comparing binding and specificity between the cysteine-functionalized forms of the simple RGD and the PR_b peptide. The latter peptide enhanced binding to $\alpha_5\beta_1$-overexpressing cancer cells, such as DLD-1, with little or no binding to CACO-2, an intestinal epithelial cell line that expresses low levels of the $\alpha_5\beta_1$ integrin.[139,273–278] Release of a model drug from these peptide-functionalized polymersomes was tracked and release profiles were compared between simple buffered solutions and after binding and internalization into cells, exploring the effects of hydrolases on intracellular release. Intracellular trafficking and release of a model drug from polymersomes in live cells was observed *via* confocal microscopy to quantitatively and qualitatively study payload colocalization with intracellular organelles.[279] Finally, treatment efficacy of the chemotherapy drug cisplatin was compared between when it is free in solution and when it is encapsulated in polymersomes to determine the effect of targeting. The results indicated that targeted delivery using PR_b dramatically enhanced specific delivery of cisplatin to $\alpha_5\beta_1$-overexpressing DLD-1 human colon cancer cells but not to nontargeted CACO-2 cells relative to nontargeted formulations.

3.2   Experimental

Materials

All chemicals were obtained from Sigma-Aldrich (St. Louis, MO) and used as received unless otherwise noted. Polymers were synthesized according to previously described procedures and were composed of a PEO block with a number average molar mass of 2 kg mol^{-1} and a PMCL block with a number average molar mass of 9 kg mol^{-1} for both the nonreactive polymer PEO-PMCL and the vinyl-sulfone modified reactive polymer VS-PEO-PMCL.[194,252,280] Water was obtained from a Milli-Q water system purified to a resistivity of 18.2 MΩ cm. Unless otherwise specified, all phosphate buffered saline (PBS) was 100 mM and pH 7.4. Phosphate-citrate buffers were prepared using appropriate combinations of dibasic sodium phosphate and citric acid for the desired pH and ionic strength was adjusted to match the polymersome interior using sodium chloride. Peptides cPR_b (CKSSPHSRNSGSGSGSGSGRGDSP) and cGRGDSP (CGRGDSP) were synthesized by the Oligonucleotide and Peptide Synthesis Facility at the University of Minnesota. Antibodies were purchased from Millipore (Billerica, MA). Fluorescence readings were acquired using a Beckman Coulter DTX 880 spectrophotometer. Hoechst 33342 nucleic acid stain, CellLights Early Endosome-GFP (Rab5-GFP), and CellLights Lysosome-RFP (LAMP1-RFP) were obtained from Invitrogen (Carlsbad, CA). Fetal bovine serum (FBS) was purchased from Atlas Biologicals (Fort Collins, CO).

Polymersome Preparation

Polymersomes were prepared at 1 wt/vol% of polymer in water using thin-film hydration followed by peptide conjugation as described previously.[280] All targeting

polymersomes were formulated to incorporate 10 mol% VS-PEO-PMCL polymer and 90 mol% of PEO-PMCL, resulting in a final peptide concentration of 9 mol% on the vesicle exterior. The disparity between incorporated reactive polymer and final peptide concentration was attributed primarily to vinyl sulfone hydrolysis during polymer purification and vesicle formation as described in the previous chapter. Cisplatin, sulforhodamine B, and calcein blue were encapsulated by dissolution at the desired concentration in the suspension media prior to polymersome formation. After a minimum of 7 d of stirring, samples were subjected to 10 freeze-thaw cycles using liquid nitrogen and a water bath at ~65 °C and unincorporated drug and peptide removed *via* filtration through a Sepharose CL-4B column using an Amersham Acta Fast Protein Liquid Chromatograph at 0.85 mL s^{-1}. To ensure that the same amount of encapsulated payload was delivered in experiments testing binding, release, and toxicity, encapsulated dye was quantified by lysing a known volume of purified polymersomes and measuring fluorescence.
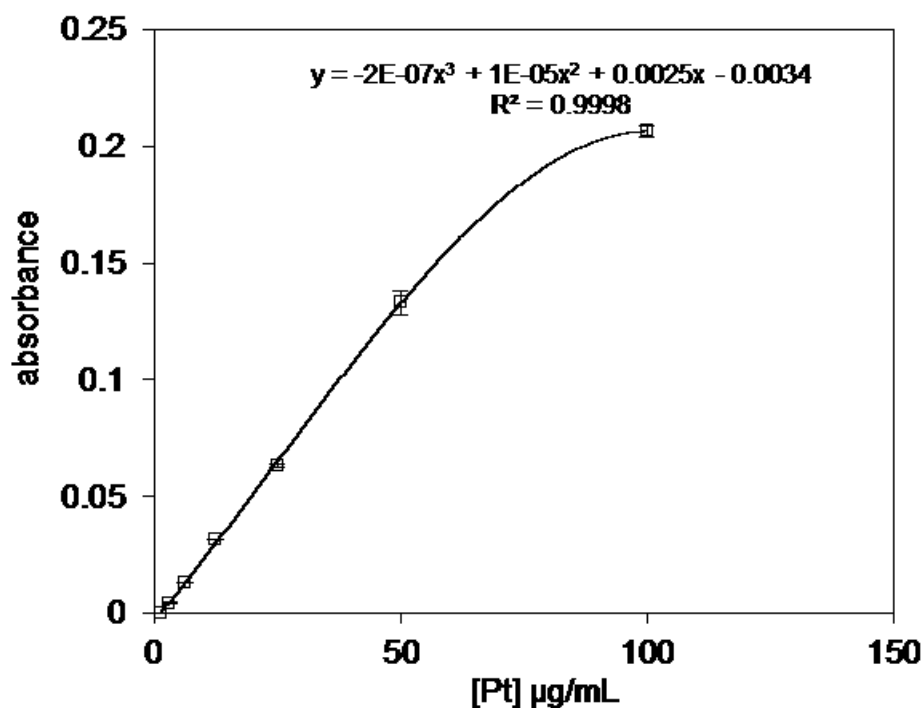
Figure 3-2: Example calibration curve used to determine concentrations of platinum concentration using the *o*-phenylenediamine assay. Similar curves were used for determining platinum concentrations in polymersomes and for cisplatin release experiments. Error bars are from three wells at identical nominal concentrations.

Polymersome Characterization

Cisplatin concentrations were determined using *o*-phenylenediamine, which chelates platinum to elicit a concentration-dependent change in absorbance at 703 nm. The magnitude of this color change was used to determine concentration by comparison to a calibration curve of known platinum concentrations (Figure 3-2).[281] Encapsulation efficiency for cisplatin ranged from 3-5%, which is on the lower side of the efficiencies reported for other polymersomal systems[222,282,283] and could likely be improved by increasing polymer concentration during hydration, though verification of the resulting morphology would be necessary upon altering this parameter.
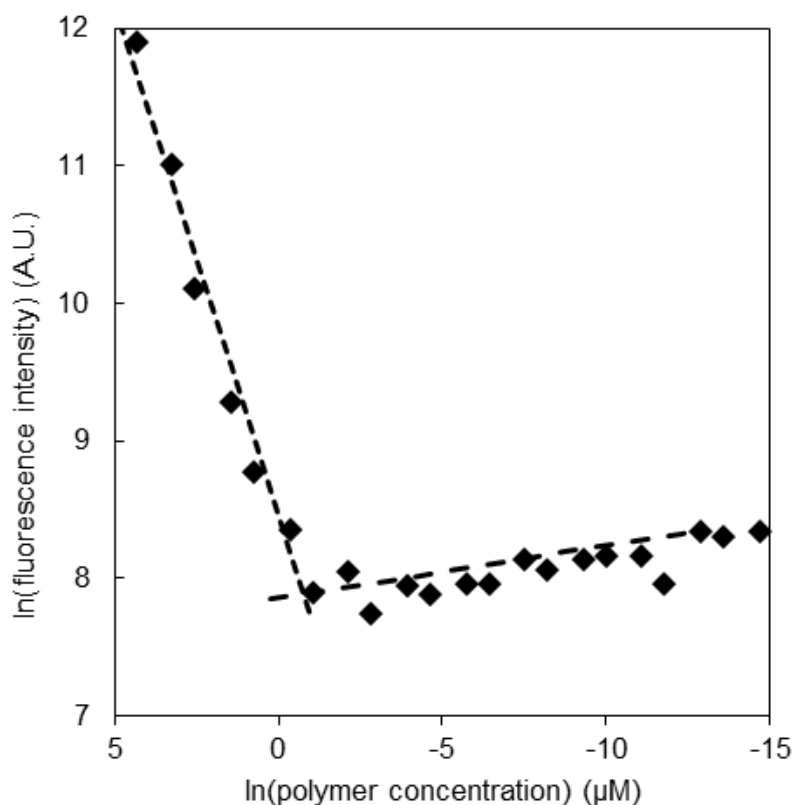
Figure 3-3: The critical aggregation concentration (CAC) of the PEO-PMCL amphiphilic block polymer was determined using the Nile Red assay.[284] To determine the CAC, data were linearized on a ln-ln plot and linear fits were made to the high- and low-slope data. The intersection of these lines was taken to be the CAC. Representative data from a single experiment are shown above. This experiment was repeated in quadruplicate 3 times (n=3) with an average CAC of 0.38 ± 0.06 µM.

Critical Aggregation Concentration

The critical aggregation concentration (CAC) was determined using a Nile Red assay and PEO-PMCL diblock copolymer. This dye has minimal fluorescence in aqueous environments, but in nonpolar environments (such as the interior of the polymersome shell layer) fluorescence increases dramatically.[284–286] As such, upon reaching the CAC, fluorescence will increase. To determine the CAC, serial dilutions of PEO-PMCL dissolved in tetrahydrofuran (THF) were made into known volumes of pH 7.4 PBS with at least a 50-fold excess of buffer versus THF in a 96-well plate. 1 µL of Nile Red dissolved

in methanol at approximately 1 mg mL^{-1} was then added to each well to a total volume of 150 μL per well. The plate was mixed on an orbital shaker for 0.5 h and fluorescence measured at $\lambda_{ex}/\lambda_{em}$ of 485/525 nm. As shown in Figure 3-3, by plotting the natural logarithm of fluorescence versus the natural logarithm of polymer concentration, it was possible to construct linear fits that met at 0.38 ± 0.06 μM. This concentration that was taken to be the CAC for PEO-PMCL.

Table 3-1: Hydrodynamic diameter of the polymersomes as determined using NTA. The experiment was performed five times and the standard deviations were calculated using these data. Histograms are shown in Figure 3-4.

Sample	Size ± SD (D$_h$, nm)
Nontargeted	217 ± 63
cGRGDSP	214 ± 62
cPR_b	234 ± 45
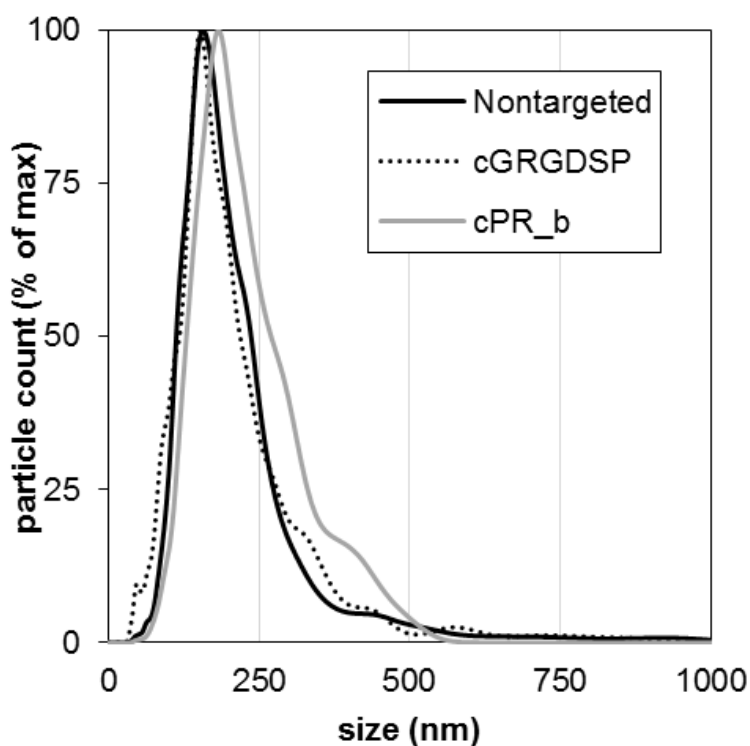
Figure 3-4: Pooled NTA experiments to measure particle size for each polymersome formulation. These histograms are the sum of the five individual histograms collected for each formulation and were analyzed to determine the mean particle size and standard deviation, which is reported in Table 3-1. To allow comparison of particle size distributions, peak heights have been normalized to the maximum peak height of each distribution.

Particle Size

The size of the nanoparticles was characterized by Nanoparticle Tracking Analysis (NTA) using a NanoSight LM10-HSBT14 Nanoparticle Characterization System with a 640 nm laser and a high resolution CCD camera. Each of the three polymersome formulations used for the measurements was diluted approximately 1000-fold into pH 7.4 phosphate buffered saline and injected using a clean 1 mL syringe into the sample flow cell maintained at 23.3 ºC using clean syringes. Measurements were performed for 60 seconds five times for each sample using a detection threshold of 5 and automatic shutter and gain adjustment. Size and standard deviation were determined from these pooled results

assuming that particles were spherical, performing the experiment five times per formulation. The results of this analysis are shown in Figure 3-4 and summarized in Table 3-1.
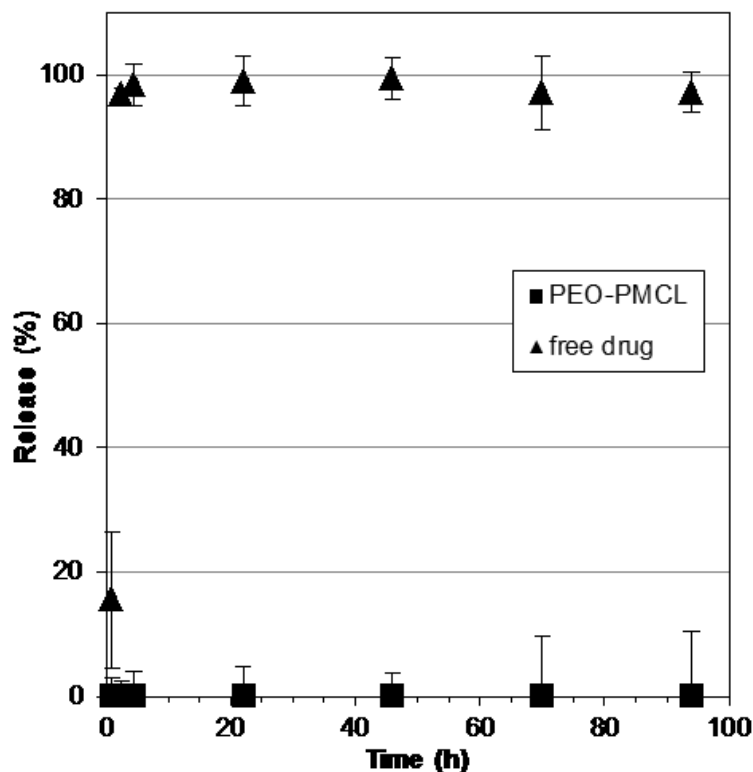
Figure 3-5: A dialysis technique was used to determine the release profile of cisplatin from polymersomes. Escape from a dialysis bag was compared between cisplatin encapsulated in polymersomes and the free drug. Free drug, which is much smaller than the dialysis bag pore size (50 kDa), rapidly equilibrated across the membrane, while drug encapsulated in polymersomes had minimal escape. Data are the mean ± standard error of 2 separate experiments (n=2).

Cisplatin Release

To verify that cisplatin was not leaking from polymersomes prior to delivery, a dialysis experiment was used to measure release rates. Cisplatin was encapsulated into polymersomes and unencapsulated drug removed as described above. The purified polymersomes were then placed into a dialysis bag (regenerated cellulose, MWCO 50 kDa)

that was in turn placed into a tenfold excess of pH 7.4 PBS. In parallel, free drug (200 μg mL^{-1} in PBS) was placed into another dialysis bag and placed into another identical but separate volume of PBS. Both dialysis systems were then subjected to gentle magnetic stirring. An aliquot of the liquid from outside the dialysis bag was periodically removed and frozen at -20°C. At the end of the experiment, all samples were thawed, vortexed thoroughly, and the platinum concentrations determined with the *o*-phenylenediamine assay described above. The results of this release study are shown in Figure 3-5 and suggest that leakage of the drug from polymersomes was minimal over the time scale of the toxicity experiments.

Cell Culture

DLD-1 human colon cancer cells were grown in growth media (GM: RPMI 1640 supplemented with 10% FBS and 1% penicillin/streptomycin) in an incubator maintained at 37 °C and 5% CO_2. Cells were kept in T-75 flasks and fed every 2 d. When cells reached approximately 90% confluence, they were washed twice with PBS, trypsinized (1 mL of 0.25% trypsin with 0.1% ethylenediaminetetraacetic acid), resuspended in GM and seeded at 10^6 cells per flask. For CACO-2 cells, the same procedure was used but with GM containing 20% FBS.

Flow Cytometry

DLD-1 cells were grown to 90% confluence, trypsinized, and 10^6 cells suspended in three microcentrifuge tubes each containing 1 mL of fluorescence buffer (FB: PBS with 0.02% sodium azide and 2.5% FBS) at 0 °C. Mouse IgG was added to one tube for isotype control and mouse anti-human integrin $\alpha_5\beta_1$was added to a second tube. All three tubes were placed on a rotary shaker for 35 minutes at 4 °C. All three were pelleted, washed

twice with FB and resuspended in 1 mL of FB. Secondary antibody (5 μL donkey anti-mouse IgG-FITC) was added to the isotype control and $\alpha_5\beta_1$ tubes and mixed by rotary shaker at 4 °C for an additional 40 minutes. All tubes were again washed twice in FB and resuspended in 1 mL of FB. Flow cytometry was performed using a FACSCalibur flow cytometer at the Flow Cytometry Core facility in the Cancer Research Center at the University of Minnesota. 1.5×10^4 cells were counted for each curve.
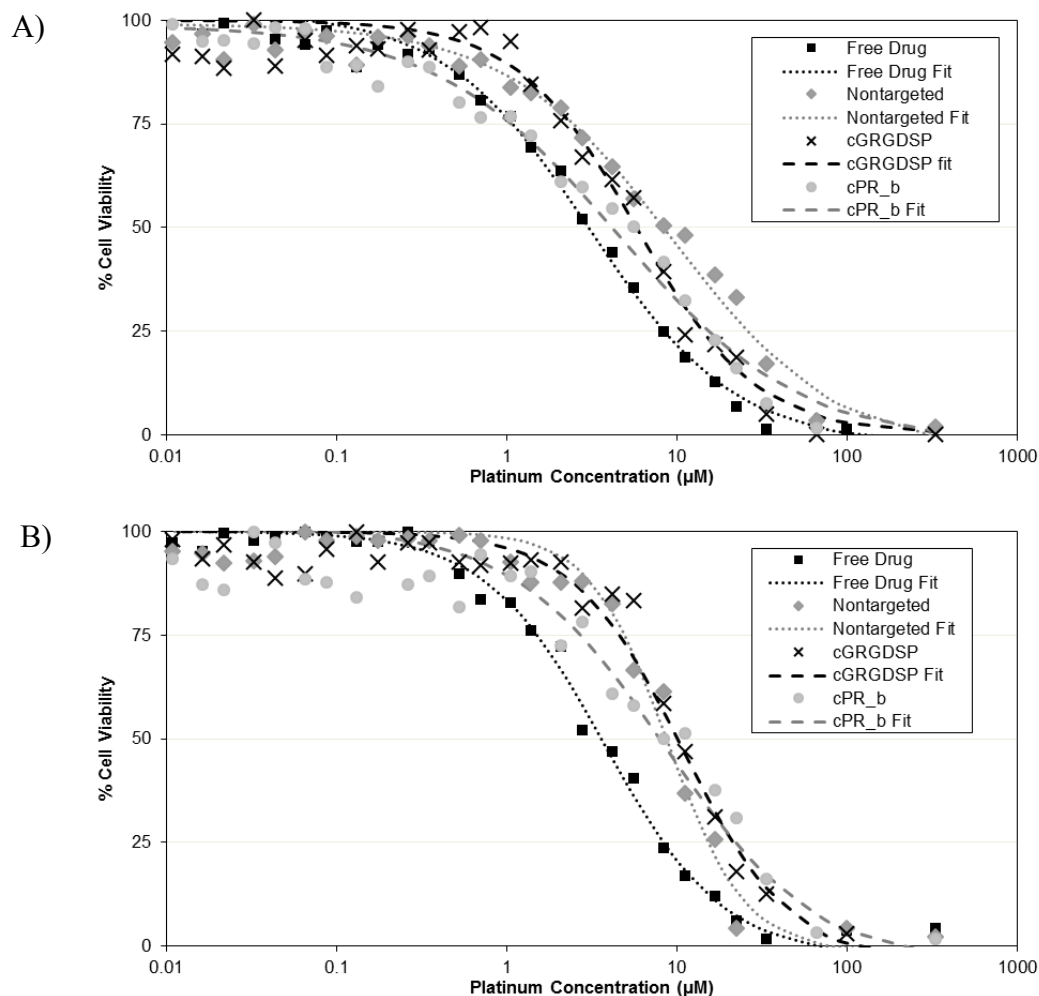
Figure 3-6: Representative curves used to determine IC_{50} values for A) DLD-1 and B) CACO-2 cells. Data points are experimental measurements while dotted lines indicate fitting curves. To determine IC_{50} values, measurements were conducted using a range of platinum concentrations either as the free drug or encapsulated in polymersomes. Viability was assessed using the MTT viability assay and values were normalized to untreated cells. Curves were fit to the data and IC_{50} for a given experimental formulation was determined as the intersection of the fit curve with 50% cell viability.

Viability Assays

Cells were seeded onto polystyrene plates at 2×10^5 cells per well and allowed to attach overnight in GM. The media was then removed, fresh GM added and polymersomes containing either PBS or cisplatin were added at the desired concentrations. Plates were returned to the incubator for 24 h. Following this incubation, the GM and polymersomes were removed, the plates were washed twice with warm PBS, fresh GM was added and the plates were returned to the incubator for 2 d. After 2 d, the MTT assay was performed according to the recommendations of the manufacturer (Sigma-Aldrich), with measurements of optical density taken using a Molecular Devices Spectramax Plus 384 spectrophotometer. Viability curves were fit to a sigmoidal curve to determine 50% inhibition concentrations (IC_{50}) using untreated cells to establish 0% inhibition. Representative curves can be found in Figure 3-6.

Binding Assays

Cells were plated at 10^6 cells per well in a white-bottomed 96-well plate and allowed to adhere for 18 h. The media was then exchanged for 100 μL of fresh GM. Free peptide was added at various concentrations and sufficient GM was added so all wells contained a total volume of 125 μL. 15 μL of polymersomes containing 2 mM sulforhodamine B was added and plates were returned to the incubator for 1 h. The polymersome solutions were diluted as necessary using isotonic PBS to ensure equal dye concentrations were delivered to all wells. Plates were washed 3 times with PBS to remove unbound polymersomes and 100 μL of fresh GM was added to each well. Fluorescence measurements were taken at 37 °C using an excitation wavelength of 535 nm and an

emission wavelength of 595 nm. Wells that contained approximately the same number of cells but to which no dye had been added were used to account for autofluorescence.

Polymer Degradation

To evaluate degradation of PEO-PMCL polymersomes, both molecular and morphological changes were tracked as a function of time. Phosphate-citrate buffers of 100 mM were formulated at pH 7.4, 6.5, 5.5 and 4.5 with 0.02% NaN_3 added to prevent bacterial growth. Polymersomes of PEO-PMCL with no targeting functionality were prepared in each of these buffers *via* thin film hydration at 1 wt/vol% and maintained at 37 °C in an incubator. Samples of approximately 500 μL were occasionally withdrawn, frozen, lyophilized, dissolved in deuterated chloroform, filtered through a 0.2 μm PTFE membrane to remove insoluble salts, and subjected to ^1H NMR and GPC. For ^1H NMR, tetramethylsilane was used as a reference to establish a chemical shift of 0 ppm and molar masses were determined by comparison of the integration values of PMCL protons at 4.10 ppm to the integration values of the PEO chain at 3.65 ppm. For GPC, apparent molar mass was determined versus a set of polystyrene standards. In parallel, aliquots of pH 7.4 and pH 4.5 samples were periodically withdrawn and cryo-TEM was performed by Ligeng Yin using techniques described in the prior chapter and elsewhere.[280]

Solution Release

To evaluate release as a function of pH, polymersomes containing 100 mM sulforhodamine B were formed and purified as described above. Phosphate-citrate buffer was formulated to pH 7.4, 6.5, 5.5 and 4.5 and 150 μL of these four buffers were added to separate wells in a 96 well plate. To these buffers, 1 μL of purified polymersome solution was added. Then fluorescence was measured over time. After 24 h, wells were frozen at -

80 °C for 2 h, thawed at 37 °C for 2 h and final fluorescence was measured. Wells to which

no polymersomes had been added gave background fluorescence measurements.
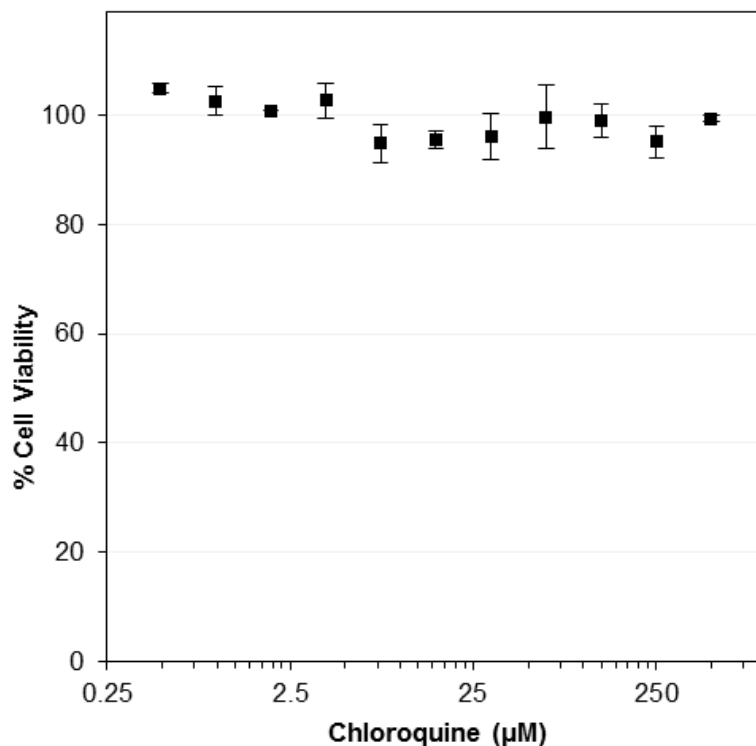
Figure 3-7: An MTT viability assay was used to verify the concentrations of chloroquine used in experiments were not toxic to DLD-1 human colon cancer cells. Viability was determined using the same procedure described in the main text. Data are the mean ± standard error of 2 separate experiments (n=2), with each experiment performed in triplicate.

Intracellular Release

DLD-1 cells were plated at 10^6 per well in a 96-well plate and allowed to adhere

for 18 h in GM. The media was then exchanged for 100 μL of fresh GM with or without

500 μM of chloroquine. Polymersomes were immediately added, diluting as necessary to

ensure equal dye concentrations, and after gentle shaking, plates were returned to the

incubator for 30 minutes. Wells were then washed twice with warm GM and 150 μL of

fresh GM was added to each well, with those wells previously containing chloroquine again

supplemented with the drug to 500 μM. Fluorescence was measured immediately and again at 2 h, 8 h, and 24 h, as described above. Plates were then placed in a -80 °C freezer for 2 h, thawed for 2 h at 37 °C, and final fluorescence was measured. To control for autofluorescence, wells containing polymersomes without fluorescent dye were included. Nonspecific adhesion of polymersomes to the plate was not found to result in significant fluorescence. Chloroquine was verified to not affect cell viability in the concentration ranges used in this experiment (Figure 3-7).
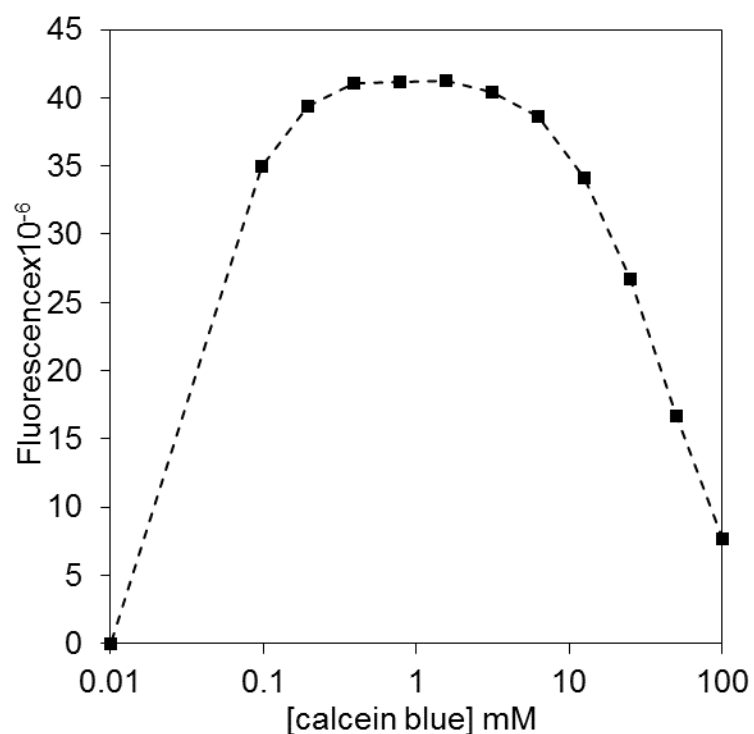
Figure 3-8: Fluorescence versus concentration for calcein blue dye. Calcein blue was diluted into PBS, pH 7.4, to verify quenching. Serial dilutions were made in a 96-well plate and fluorescence was measured at $\lambda_{ex}/\lambda_{em}$ of 340/430 nm. Error bars from five separate wells were smaller than the points on the graph.

Calcein Blue Fluorescence

To determine the optimal concentration of calcein blue to use for microscopy, a solution of the dye was made at 100 mM in pH 7.4 PBS. Using a multipipettor and a 96-well black polystyrene plate, serial dilutions were made into pH 7.4 PBS from 100 mM to 0.01 mM. Fluorescence was then measured on a Beckman Coulter DTX 880 spetrophotometer using λex/λem of 340/430 nm as shown in Figure 3-8. On the basis of this result, 5 mM and 100 mM calcein blue were selected for encapsulation into polymersomes for nonquenching and quenching concentrations, respectively.

Confocal Microscopy

DLD-1 cells were seeded onto a glass-bottomed 24-well plate at $5x10^4$ cells per well in 200 μL of GM per well and allowed to attach overnight in an incubator. Media was then exchanged for 200 μL of fresh GM in each well. Wells to be used for imaging received 2.5 μL of CellLights early endosomes-GFP and 7.5 μL of CellLights lysosome-RFP, the media was mixed and the cells returned to the incubator for 18 h. Following incubation, 25 μL of purified cPR_b-functionalized polymersomes containing either nonquenching (5 mM) or quenching (100 mM) concentrations of calcein blue were added. After 2 h of incubation at 37 ° C, media was removed and each well washed twice with warm GM. 2 h wells were immediately nuclear stained using Hoechst 33342 (see below) while 150 μL of GM was added to 24 h wells. Immediately prior to imaging, media was replaced with 100 μL of warm GM containing diluted Hoechst 33342 at 1 μM, which was allowed to stain the nuclei for 5 minutes at 37 °C. These wells were washed twice with warm GM and finally filled with 150 μL of GM prior to imaging.

Imaging was performed on a Zeiss Cell Observer SD spinning disk confocal microscope at 37 °C and 5% CO_2 at the University of Minnesota Biomedical Image Processing Lab. A 100x objective was used, and the green channel used for GFP-tagged early endosomes, the red channel used for RFP-tagged lysosomes and the blue channel used for both nuclei and calcein blue. Slices were taken every 0.25 μm from the bottom to the top of cells, collecting each channel in series for each slice. A slice at the center of the central cell was used for analysis. The Manders coefficients between the blue channel and the green channel as well as the blue channel and the red channel were determined, accounting for background fluorescence according to the Costes technique in NIH ImageJ and gating out nuclei so as to consider only polymersomes.[287,288]

3.3   Results and Discussion

Introduction

Particle size and prolonged circulation are vital for enhancing the carrier concentration in tumors; however, the EPR effect is only effective for localizing the delivery vehicle to the tumor interstitium, not for achieving internalization into cells. This last step has proven to be a major stumbling block for past attempts to deliver cisplatin.[268–272] In these cases, cisplatin loaded into liposomes was delivered systemically and, as desired, platinum concentrations in the tumor were enhanced and the tolerated dose increased significantly due to decreased side effects, presumably *via* the EPR effect and the drug being sequestered inside of the liposomes. However, treatment outcomes were not improved due to the limited uptake of cisplatin into the cancer cells. To achieve internalization, active targeting groups show great promise. Using ligands tethered to the delivery vehicle, the cell's

existing uptake pathways and overexpression of certain cell-surface receptors can be used, affording a route for selective internalization. Such an approach may also allow some modes of resistance to cisplatin or other encapsulated drugs to be circumvented, as has been shown in studies demonstrating selective binding and uptake of nanoparticle-based cisplatin carriers.[12,76–84]

Active targeting capability was incorporated into PEO-PMCL polymersomes using a vinyl sulfone moiety capable of site-specifically tethering a targeting peptide following self-assembly as discussed in the previous chapter. Due to compatibility between PEO-PMCL and VS-PEO-PMCL and the high reactivity between vinyl sulfone and thiol-containing peptides, the amount of targeting peptide incorporated into the corona could be easily controlled, here using either 0 or 9 mol% peptide by mixing appropriate ratios of the two polymers prior to self-assembly.
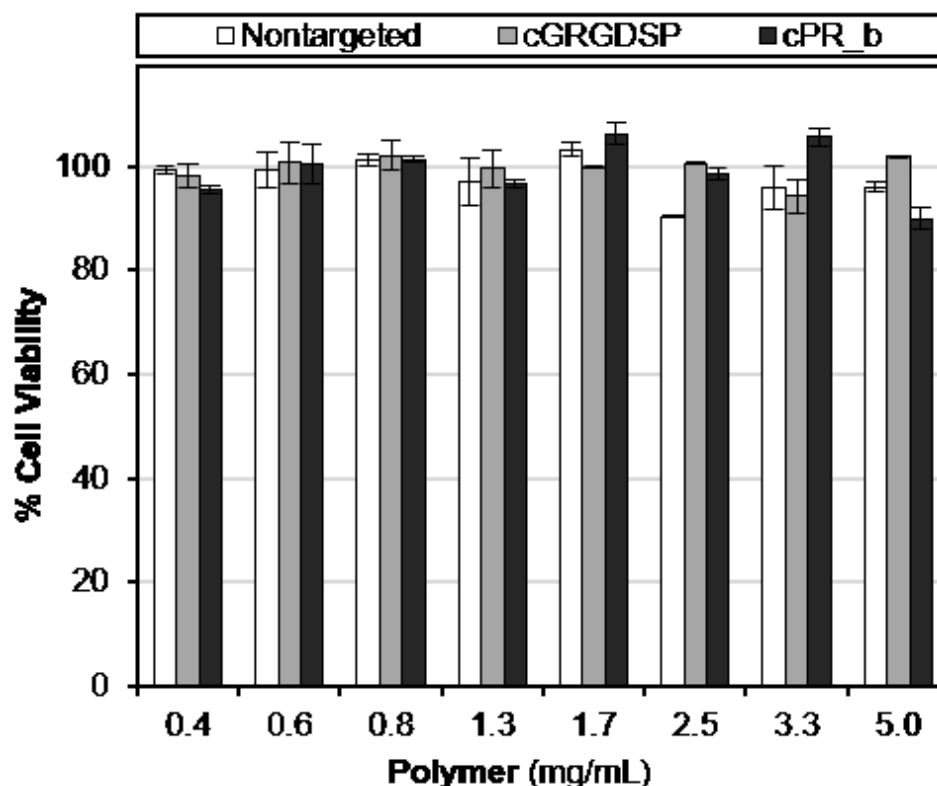
Figure 3-9: Toxicity of unloaded polymersomes to the DLD-1 human colon cancer cells. Toxicity was evaluated with an MTT viability assay after 24 h of incubation at 37 °C. While in the rest of this work polymer concentrations never exceeded 0.8 mg mL^{-1}, no significant decrease in viability was observed even at much higher concentrations. Data is the mean ± standard error of 4 separate experiments (n=4), with each experiment performed in triplicate.

Biocompatibility and Binding

While the chemical similarity of PEO-PMCL to the more commonly studied and biocompatible PEO-poly(ε-caprolactone)[289,290] suggested PEO-PMCL would also be nontoxic, the biocompatibility of this polymer had not yet been examined directly. The effect of both nontargeted and targeted PEO-PMCL polymersomes on the viability of DLD-1 human colon cancer cells was investigated. As shown in Figure 3-9, neither targeted nor nontargeted PEO-PMCL polymersomes impacted cell viability following a 24 h incubation period of cells with unloaded polymersomes. High cell viability was observed

even at concentrations much greater than 0.8 mg mL^{-1}, the maximum concentration of polymersomes used in this work, indicating the polymer should have no impact on cellular viability.
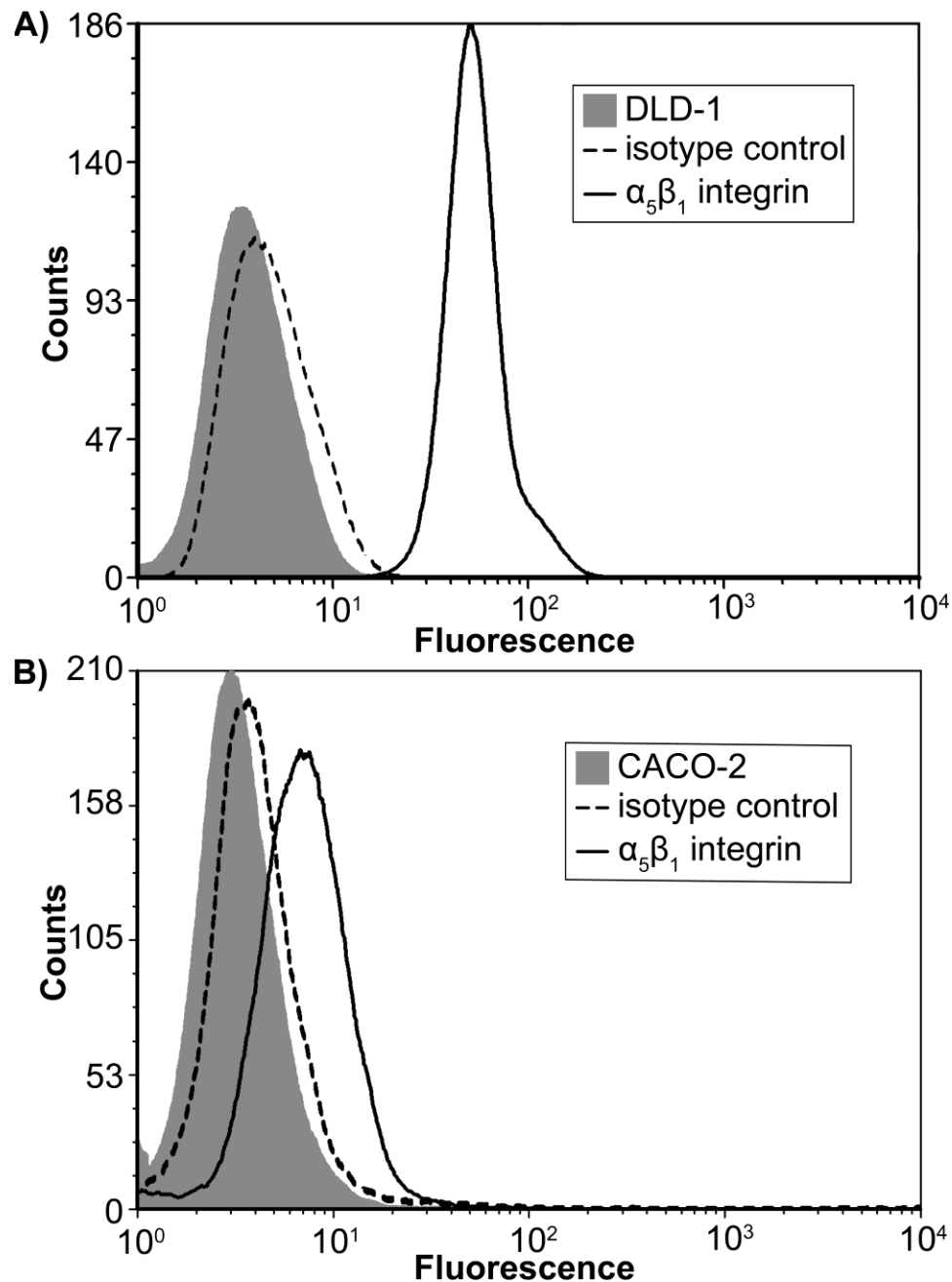
Figure 3-10: Histograms from flow cytometry experiments used to determine the expression of $\alpha_5\beta_1$ integrin, the target of cPR_b peptides. Experiments were performed using (A) DLD-1 and (B) CACO-2 cell lines. Untreated cells were used to measure cell autofluorescence and an isotype control was included to verify the binding was specific. The pronounced shift to higher fluorescence values in DLD-1 cells – but not in CACO-2 – following incubation with an antibody specific to $\alpha_5\beta_1$ integrin is indicative of much higher expression of the integrin on DLD-1 cells. These data are from a single experiment but are representative of n = 2.

To evaluate binding specificity, it was necessary to first determine the expression levels of the target $\alpha_5\beta_1$ integrin on DLD-1 and CACO-2 human colon cancer cells. To do this, both cells lines were evaluated *via* flow cytometry with an anti-human $\alpha_5\beta_1$ antibody. While some expression was observed in CACO-2 (Figure 3-10B), the pronounced shift towards higher fluorescence in DLD-1 (Figure 3-10A) indicated $\alpha_5\beta_1$ expression was much greater in this cell line. On the basis of these results, CACO-2 was adopted as a model for 'bystander' tissue in the body, nontargeted cells that express low levels of integrin $\alpha_5\beta_1$, which is the target of the cPR_b peptide, to which drug delivery is not desired due to the potential for deleterious side effects.
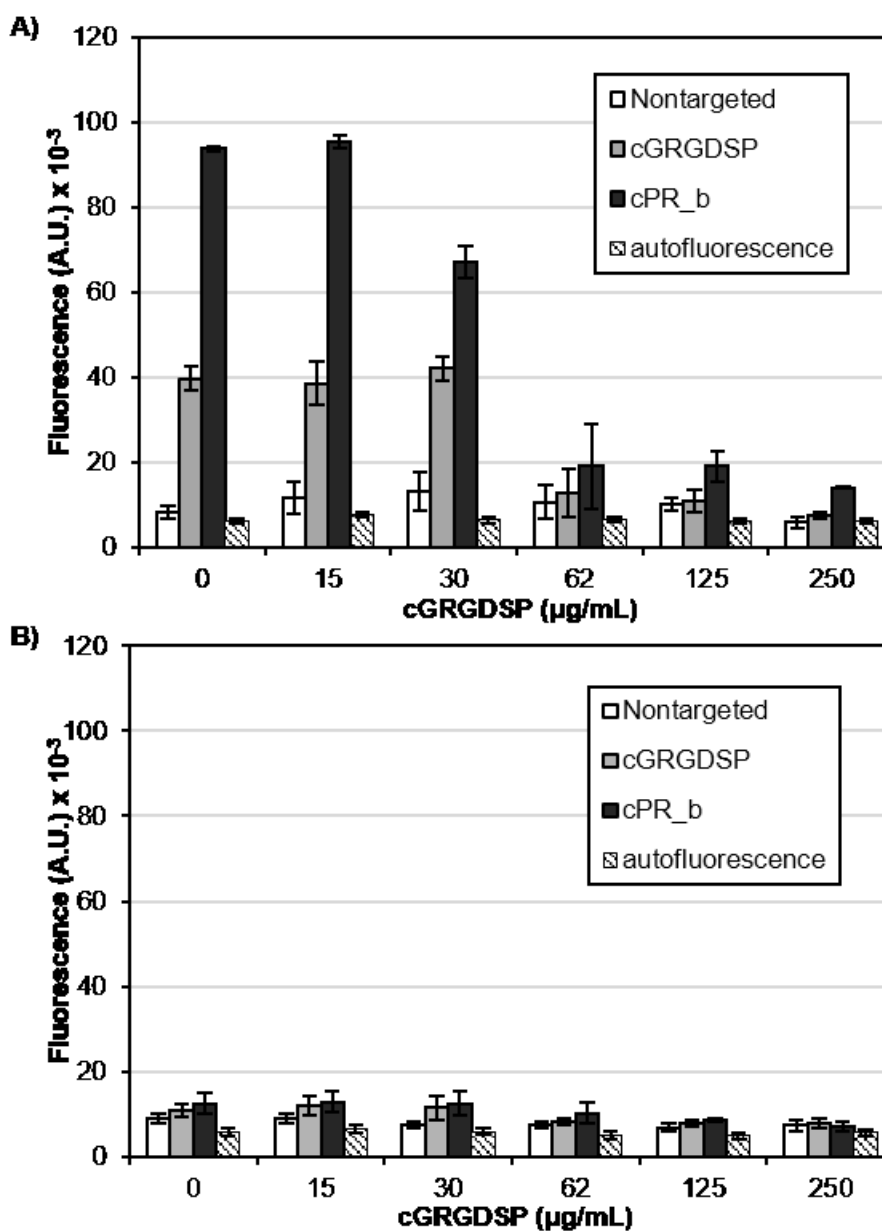
Figure 3-11. Specificity of targeting to the $\alpha_5\beta_1$ integrin using several formulations of polymersomes was evaluated. Polymersomes were formulated to encapsulate 2 mM sulforhodamine B without a targeting group, with 9 mol% cGRGDSP, or with 9 mol% cPR_b incubated with either (A) high $\alpha_5\beta_1$-expressing DLD-1 cells or (B) low $\alpha_5\beta_1$-expressing CACO-2 cells. Increasing concentrations of free cGRGDSP peptide were added prior to incubation to determine if binding between integrins and fluorescent polymersomes could be blocked. Following 1 h incubation at 37 °C, unbound polymersomes were washed away and the fluorescence of bound polymersomes was measured. Autofluorescence of cells was measured using untreated cells. Data are the mean ± standard error of 3 separate experiments (n=3), with each experiment performed in quadruplicate.

To minimize the negative side effects of chemotherapy it is essential that binding of the delivery vehicle occurs with high specificity for the target cells. To determine if employing a high-affinity targeting peptide such as cPR_b would yield improved binding to $\alpha_5\beta_1$-overexpressing cancer cells, the effect of the targeting ligand on the binding of polymersomes to DLD-1 cells was evaluated (Figure 3-11A). Here minimal binding occurred in the absence of a targeting peptide, a pronounced increase when the cGRGDSP peptide was used, and a maximum effect using the cPR_b peptide. Further, this binding could be inhibited by including free cGRGDSP peptide in media, which hindered the interaction between the peptides and integrins. Across all experiments using nontargeted polymersomes, the peptide concentration of the free cGRGDSP in the media was not found to have a statistically significant effect on fluorescence.

To determine if binding to cells with lower expression of $\alpha_5\beta_1$ integrin would be significant, potentially resulting in nonspecific delivery, the same experiment was performed using low-$\alpha_5\beta_1$-expressing CACO-2 cells, a cell line often used as a model of intestinal epithelia.[139,273–278] Little or no binding enhancement was observed (Figure 3-11B) using targeted polymersomes compared to nontargeted polymersomes regardless of the concentration of the blocking peptide. These results suggested that polymersomes functionalized with the cPR_b sequence could promote delivery to the cancer cells of interest that overexpress the $\alpha_5\beta_1$ integrin with minimal delivery to bystander cells even if they express low levels of the integrin.
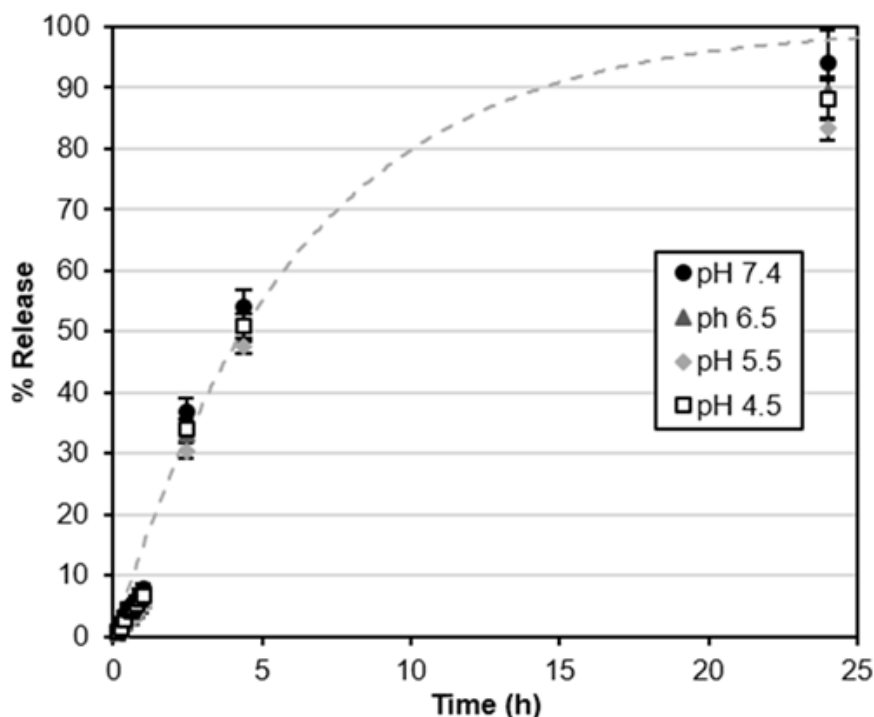
Figure 3-12. Release rates of PEO-PMCL polymersomes were first measured in simple buffered solution. To measure release, polymersomes were loaded with self-quenching (100 mM) concentrations of sulforhodamine B. Release was first evaluated in isotonic phosphate-citrate buffer at 37 °C with pH 7.4, typical of circulating blood, to 4.5, typical of lysosomes. No significant difference was observed in release rate at different pHs. Data is the mean ± standard error of 3 separate experiments (n=3), with each experiment performed in quadruplicate.

Degradation and Release

To evaluate the release properties of PEO-PMCL polymersomes and degradation of the polymer, studies were first conducted in simple buffered solution at pH values from 7.4 to 4.5 (Figure 3-12), levels commonly used to simulate the decreasing pH level encountered by a drug delivery vehicle as it is trafficked from outside the cell to different organelles following endocytosis.[291–294] Fluorescent sulforhodamine B was loaded into polymersomes at self-quenching (100 mM) concentrations, unencapsulated dye was removed, and fluorescence was tracked for 24 h by monitoring increasing fluorescence as dye escaped polymersomes. The remainder of the dye was then released to determine the

fluorescence corresponding to 100% escape. After 24 h, release was nearly complete in all cases, with no apparent effect of pH on release kinetics. The release profile was well-described by first-order release kinetics over the entirety of the experiment.
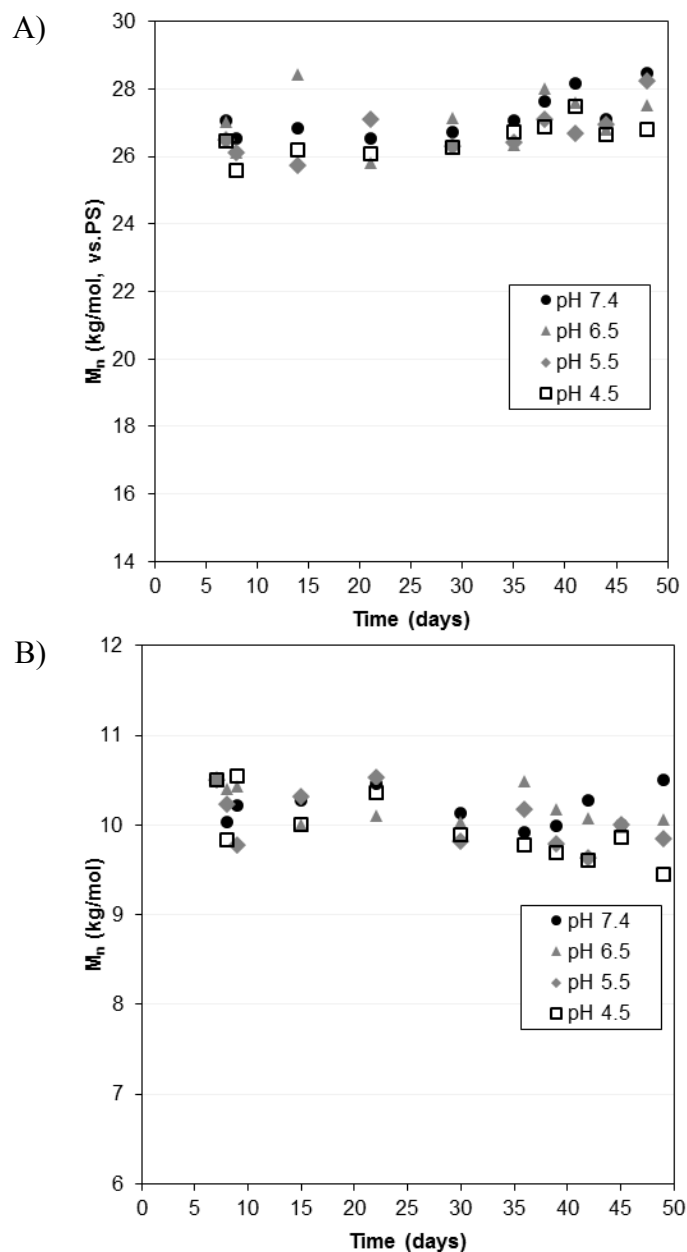
Figure 3-13: To determine if degradation of PEO-PMCL polymer was occurring in buffered solution, polymer molar mass was tracked by (A) GPC and (B) ^{1}H NMR. In both cases degradation appeared to be minimal over the time period of the experiment.

Consistent with previous reports[295,296] little polymer degradation was observed spectroscopically or chromatographically over 50 days at pH 7.4, 6.5, 5.5, or 4.5 (Figure 3-13), suggesting the release mechanism in this pH range is not polymer degradation and that dye release is likely due to diffusion of the dye through the polymersome membrane. In addition, cryo-TEM studies at pH 7.4 and 4.5 showed no major changes to polymersome morphology at either pH over 31 days at 37 °C (Figure 3-14 through Figure 3-21).
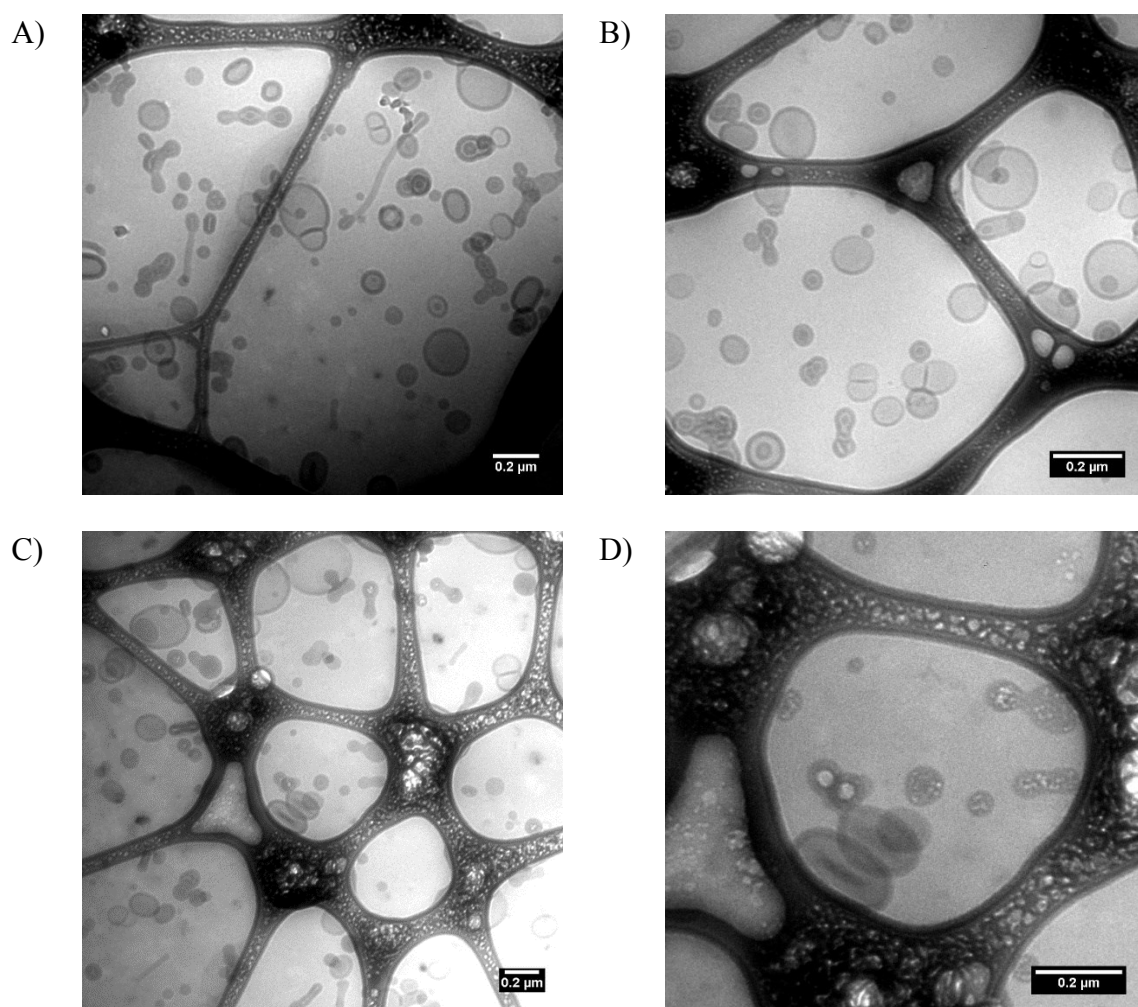
Figure 3-14: Cryo-TEM of PEO-PMCL, Day 0, pH 7.4. Some coexisting phases, mainly wormlike micelles, are present, but the predominant morphology is vesicles. Here D) is a portion of C) collected at higher magnification. Cryo-TEM by Ligeng Yin.
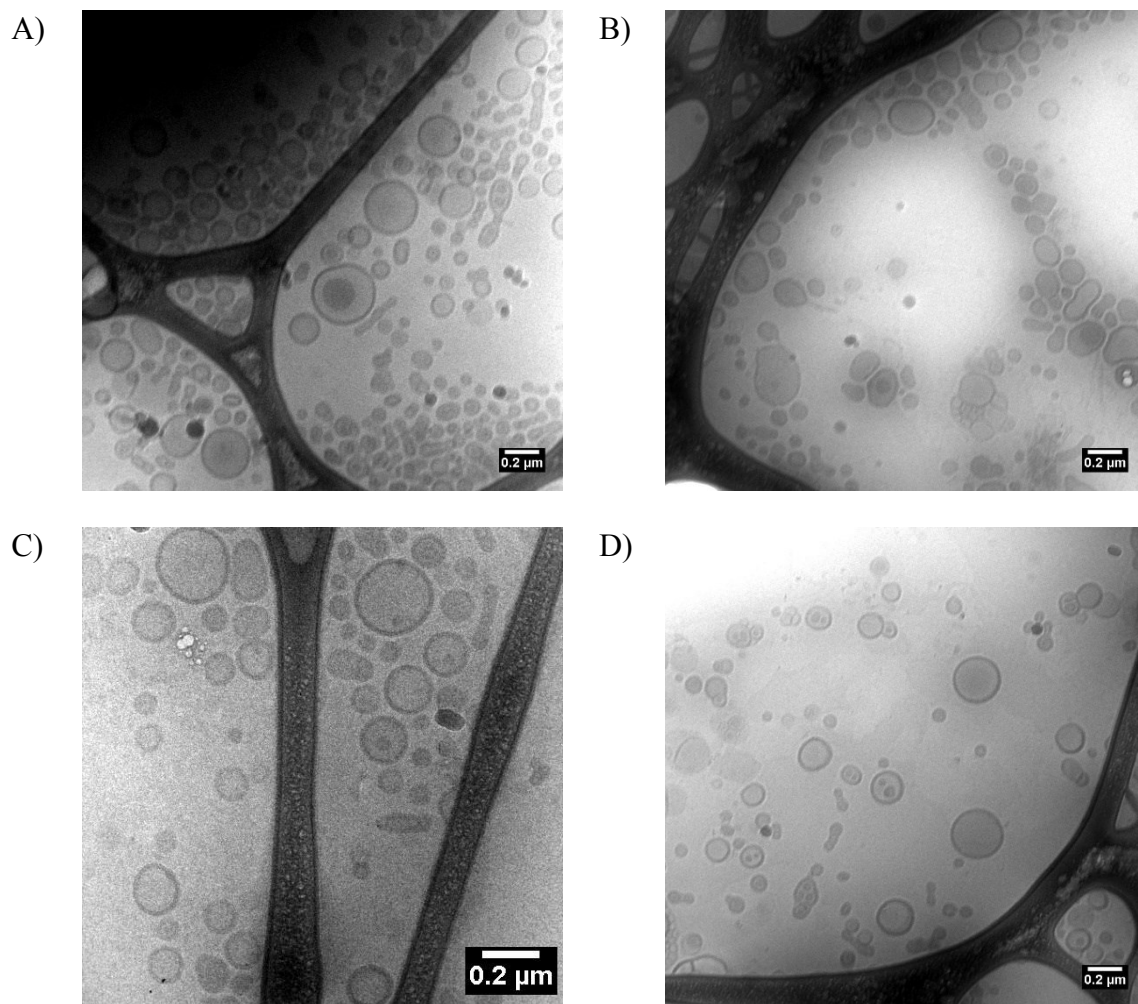
Figure 3-15: Cryo-TEM of PEO-PMCL, Day 0. pH 4.5. The predominant morphology appears to be polymersomes. Cryo-TEM by Ligeng Yin.

A)

B)

C)

D)
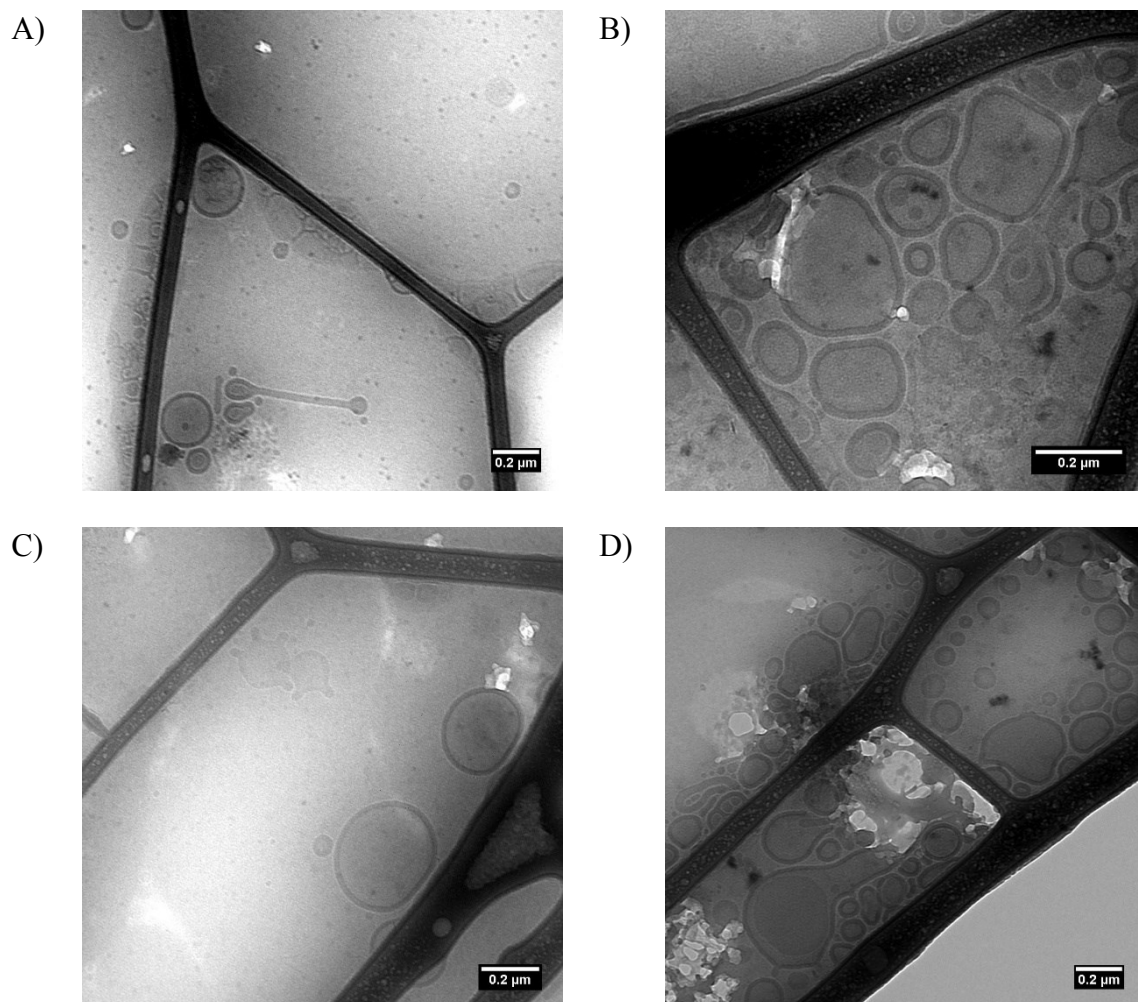
Figure 3-16: Cryo-TEM of PEO-PMCL, Day 10, pH 7.4. As at earlier time points, polymersomes are the predominant morphology with minor coexistence of wormlike micelles and some complicated structures, particularly immediately adjacent to the lacey carbon. Cryo-TEM by Ligeng Yin.
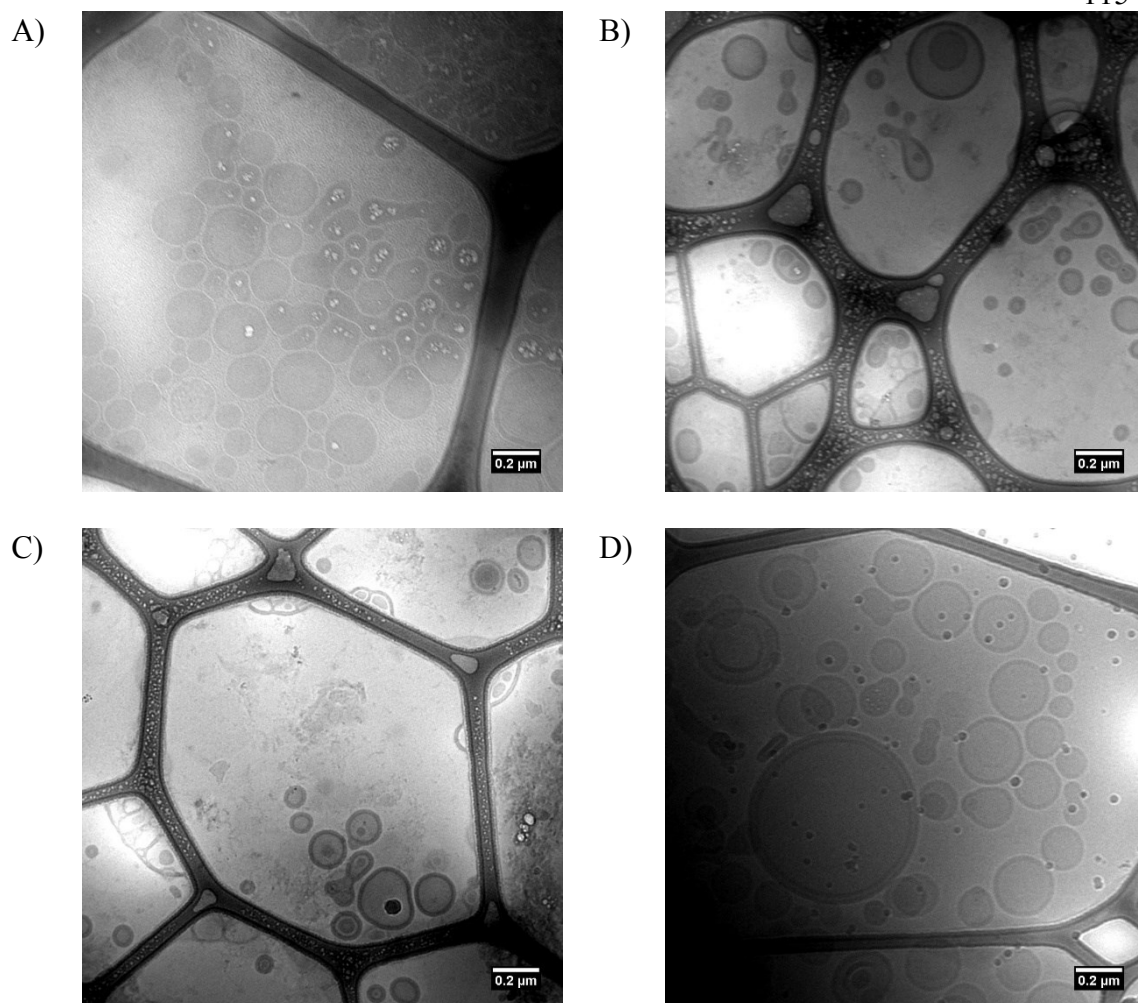
Figure 3-17: Cryo-TEM, Day 10, pH 4.5 of PEO-PMCL. Vesicles are again the predominant morphology, including some multilamellar structures as well as the complicated aggregates near the lacey carbon 'struts' observed at pH 4.5. White disruptions in A) are beam damage. Cryo-TEM by Ligeng Yin.

A)

B)

C)

D)
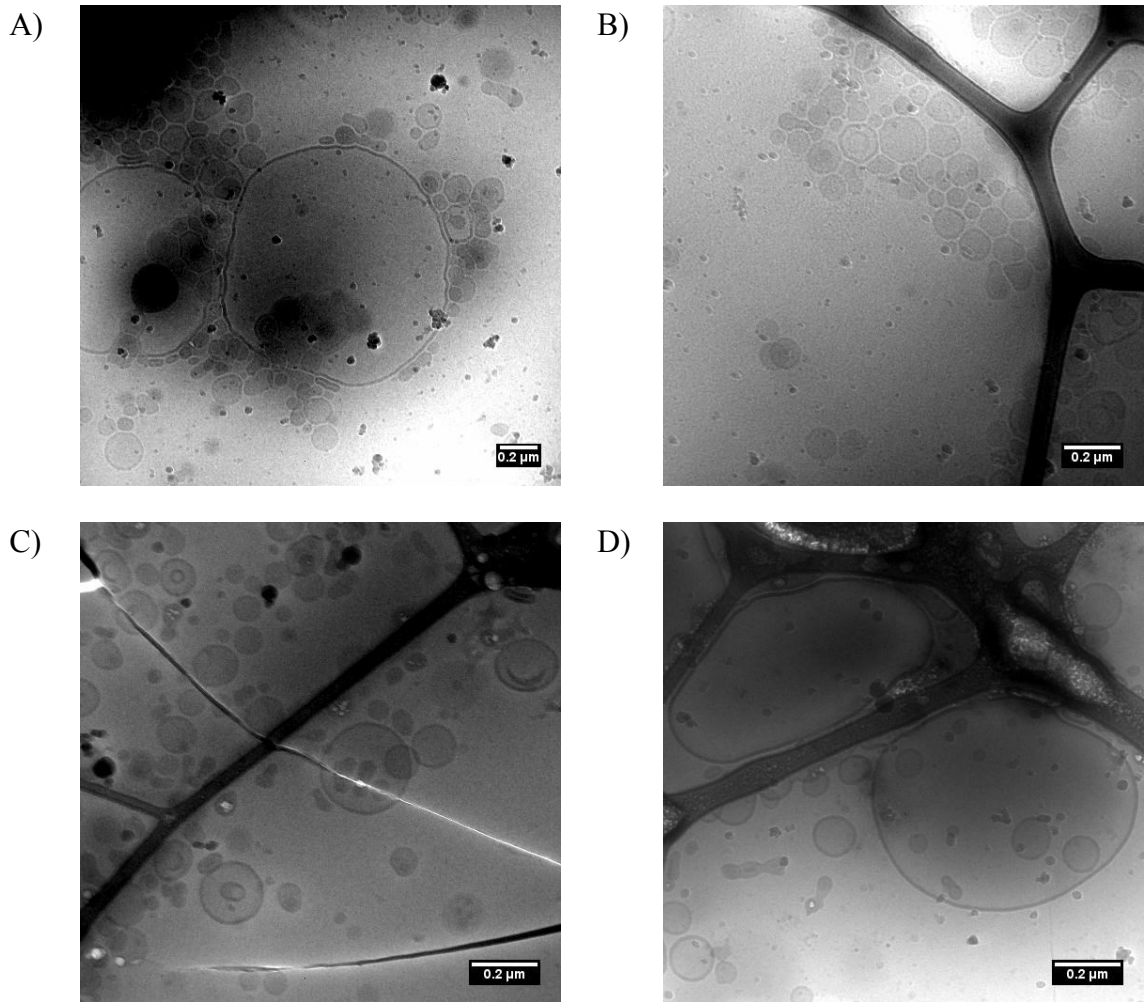
Figure 3-18: Cryo-TEM of PEO-PMCL, Day 20. pH 7.4. As at earlier time points vesicles remain the predominant morphology observed, including some quite large vesicles of several µm diameter. Cryo-TEM by Ligeng Yin.

A)

B)

C)

D)
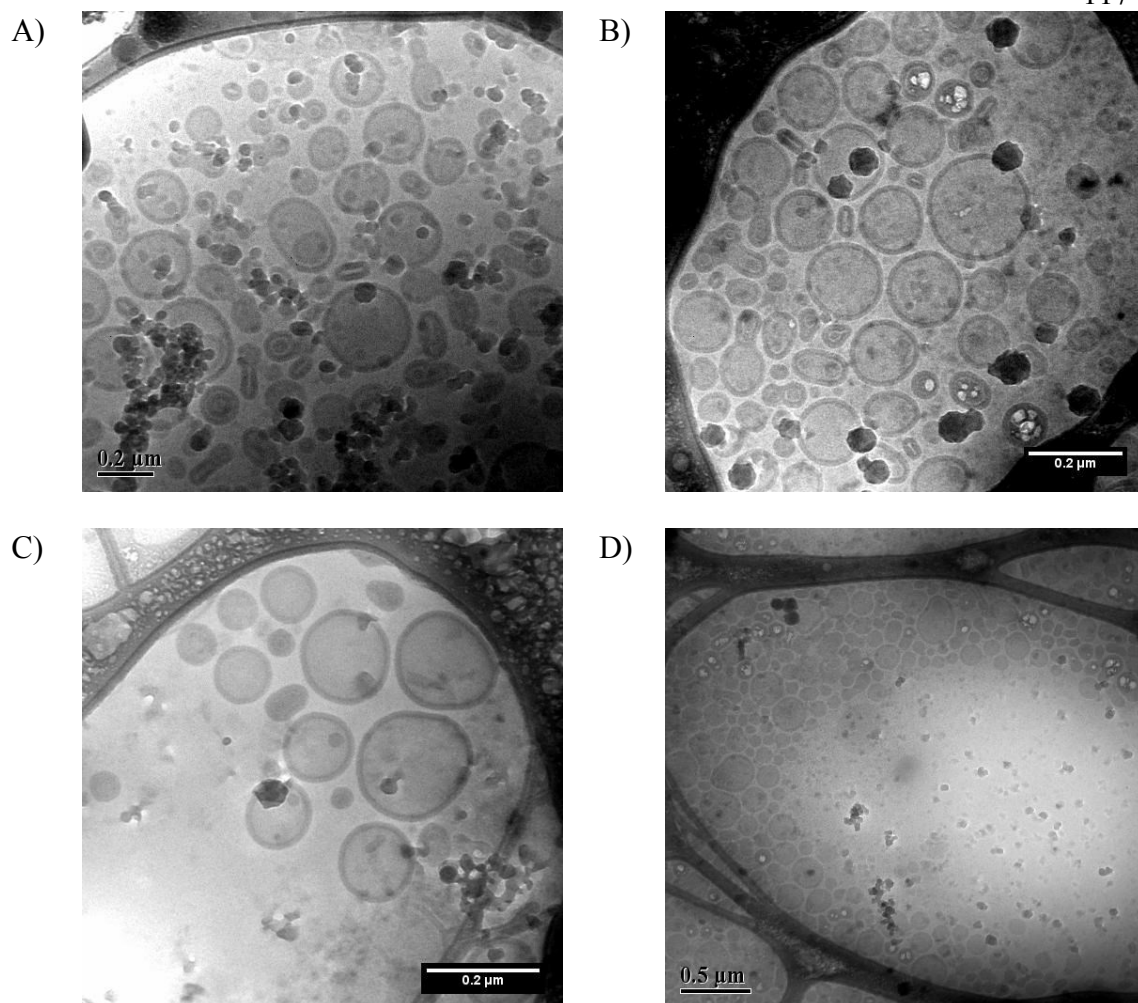
Figure 3-19: Cryo-TEM of PEO-PMCL, Day 20, pH 4.5. As with pH 7.4, the predominant morphology observed here are vesicles, including multilamellar vesicular structures. The large vesicles observed at pH 7.4 are not seen here, but this may be due to the limited 'window' afforded by the technique. Dark regions are likely ice crystals and white spots are beam damage. Cryo-TEM by Ligeng Yin.

A)

B)

C)

D)
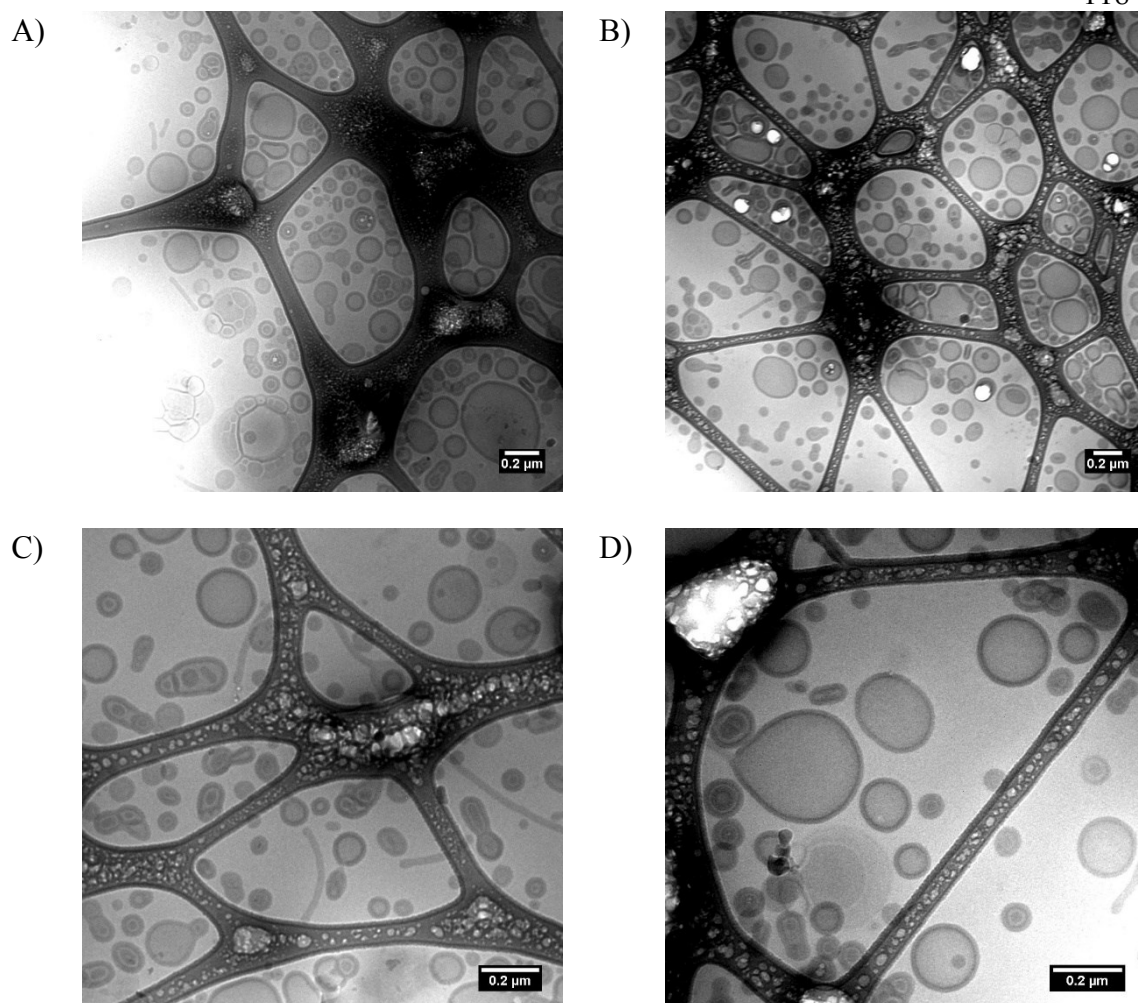
Figure 3-20: Cryo-TEM, Day 31 of PEO-PMCL, pH 7.4. After 31 days, vesicles remain the primary structure, albeit accompanied somewhat more by coexisting articulated and wormlike structures. Cryo-TEM by Ligeng Yin.

A)

B)

C)

D)
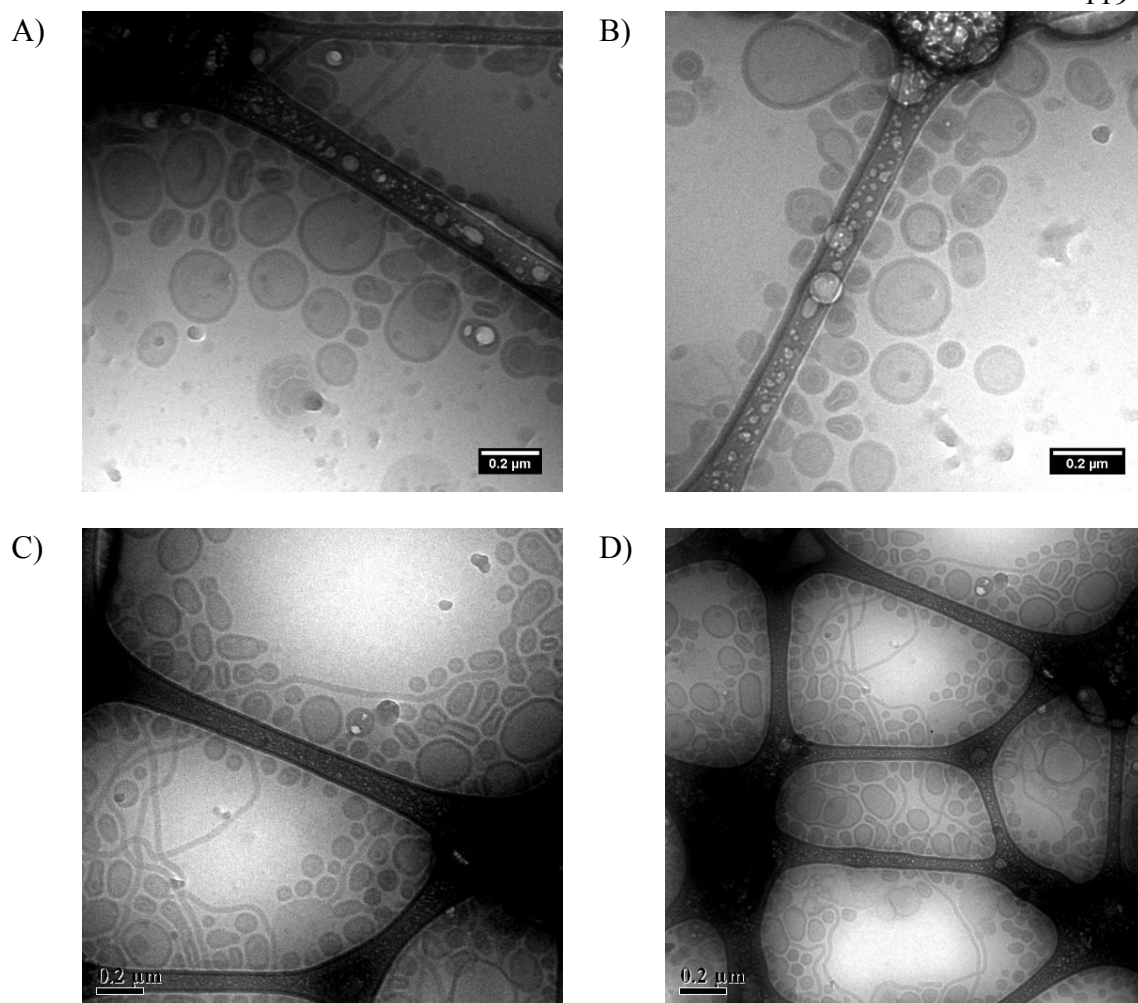
Figure 3-21: Cryo-TEM of PEO-PMCL, Day 31, pH 4.5. As with the pH 7.4 sample above, here vesicles seem to be accompanied by somewhat more coexisting articulated structures and wormlike micelles. Despite this, vesicles remain the predominant morphology. Cryo-TEM by Ligeng Yin.
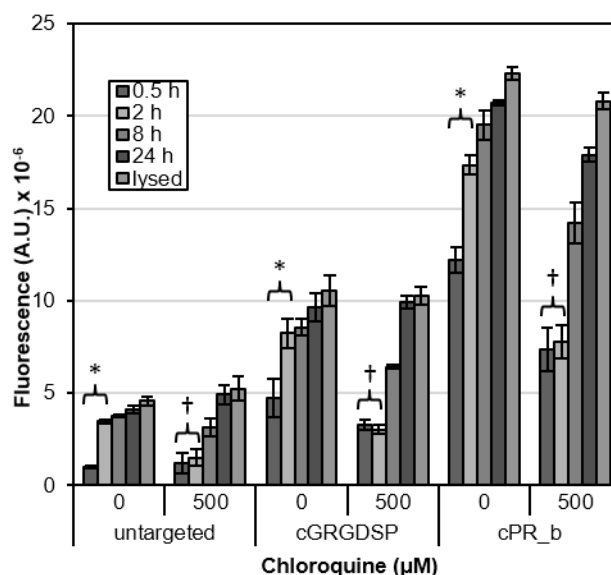
Figure 3-22. Release rates of targeted PEO-PMCL polymersomes were measured in in the presence of DLD-1 cells. To determine if release rates changed following cell binding and uptake, polymersomes containing 100 mM sulforhodamine B were incubated for 1 h at 37 °C with DLD-1 cells with or without chloroquine. Cells were washed with 37 °C PBS and sulforhodamine B release was monitored for up to 24 h. Release in the first 2 h was much faster than observed in solution release experiments (Figure 3-12) but could be inhibited by chloroquine. After 24 h nearly complete release of dye had occurred with or without chloroquine, consistent with results observed in simple buffered solutions (A). Total dye delivery was enhanced by the presence of targeting peptides, particularly cPR_b, and chloroquine had no significant effect on total dye delivered, as total fluorescence following lysis were not significantly different between untreated samples and those treated with chloroquine. Data is the mean ± standard error of 3 separate experiments (n=3), with each experiment performed in quadruplicate. *=statistically significant difference (p<0.02), †=no statistical significant difference (p>0.10) *via* paired t-test.

Intracellular Release. While simple buffered solutions can simulate the pH encountered following uptake, the absence of digestive enzymes limits the conclusions that can be drawn.[297–299] To address this limitation, release was monitored for 24 h from PEO-PMCL polymersomes following binding to DLD-1 human colon cancer cells (Figure 3-22). As in binding studies (Figure 3-11), the total amount of delivered dye was enhanced with targeted polymersomes and cPR_b peptide outperformed cGRGDSP. After 24 h, most of the dye had been released, consistent with the solution release study (Figure 3-12).

However, in the absence of chloroquine, release in cells was much more rapid, with >75% of the dye released within 2 h.

Dye release was also tracked in the presence of 500 μM chloroquine, a concentration verified to be nontoxic to DLD-1 cells (Figure 3-7). This small-molecule drug is membrane-permeable at neutral pH, yet upon entering an acidic cellular compartment is protonated, rendering it membrane-impermeable and resulting in rapid accumulation of drug. This protonation raises compartment pH, decreasing the activity of hydrolases in acidic organelles such as the late endosome and lysosome.[300–303] As shown in Figure 3-22, if enzymes are not inhibited, release rates in the presence of cells were substantially faster than release rates observed in solution (Figure 3-12). For example, in the case of cPR_b-targeted polymersomes, after 2 h approximately 80% release had occurred in the presence of uninhibited (0 μm chloroquine) DLD-1 cells while approximately 30% release had occurred in simple buffered solution. However, when digestive enzymes were inhibited (500 μm chloroquine) during delivery of the same polymersome formulation to DLD-1 cells approximately 35% of dye had been released after 2 h, nearly recovering solution release rates. Similar trends in relative release rates between inhibited and uninhibited cells could also be observed for nontargeted and cGRGDSP-targeted polymersomes.

The rapid dye release seen in uninhibited cells was dramatically slower upon inhibition, suggesting that acidic conditions are necessary but not sufficient for rapid release and that enzymatic hydrolases play a major role in compromising polymersomes to rapidly release the encapsulated dye. By hydrolyzing the labile ester linkages in the PMCL

block curvature is induced in the polymersome membrane resulting in pore formation and payload release. This is a phenomenon active in triggering payload release in other degradable polymersomal delivery systems subject to hydrolysis[240,241,304] and potentially affords a route to release of drug from the endosomal-lysosomal pathway into the cytosol.

Confocal Microscopy

To better understand the trafficking and release of dye from polymersomes live-cell confocal microscopy was used to directly visualize trafficking and release in DLD-1 cells transfected to express both Rab5-GFP and LAMP1-RFP, markers of early endosomes and lysosomes respectively. Labeling of organelles using these fusion proteins allowed more selective labeling of organelles than is possible using more conventional dyes that rely upon accumulation in acidic organelles. Polymersomes encapsulating 5 mM calcein blue were administered in growth media for 2 h, unbound polymersomes washed away with warm growth media and cells imaged either immediately or 22 h later. The rapid image collection allowed by spinning disc confocal microscopy allowed visualization of trafficking in live cells in real time, but for analysis of colocalization still frames were used.

red channel
(lysosome)

blue channel
(nucleus + calcein blue)

green channel
(endosome)

red-blue colocalization

green-blue colocalization

Figure 3-23: Confocal microscopy was used to visualize trafficking of nonquenching targeted polymersomes (9 mol% cPR_b) in live DLD-1 cells. Results shown here are for 2 h at 37 °C. Cells were transfected to express LAMP1-RFP (lysosome, red channel) and Rab5-GFP (early endosome, green channel). Polymersomes encapsulated 5 mM calcein blue and nuclei stained with Hoechst 33342 (both blue channel). Scale bars indicate 10 μm.

red channel
(lysosome)

blue channel
(nucleus + calcein blue)

green channel
(endosome)

red-blue colocalization

green-blue colocalization

Figure 3-24: Confocal microscopy was used to visualize trafficking of nonquenching targeted polymersomes (9 mol% cPR_b) in live DLD-1 cells. Results shown here are for 2 h at 37 °C. Cells were transfected to express LAMP1-RFP (lysosome, red channel) and Rab5-GFP (early endosome, green channel). Polymersomes encapsulated 5 mM calcein blue and nuclei stained with Hoechst 33342 (both blue channel). Scale bars indicate 10 μm.

red channel
(lysosome)

blue channel
(calcein blue)

green channel
(endosome)

red-blue colocalization

green-blue colocalization

Figure 3-25: Confocal microscopy was used to visualize trafficking of nonquenching targeted polymersomes (9 mol% cPR_b) in live DLD-1 cells without nuclear stain. Results shown here are for 2 h at 37 °C. Cells were transfected to express LAMP1-RFP (lysosome, red channel) and Rab5-GFP (early endosome, green channel). Polymersomes encapsulated 5 mM calcein blue (blue channel). Scale bars indicate 10 μm.

red channel
(lysosome)

blue channel
(nucleus + calcein blue)

green channel
(endosome)

red-blue colocalization

green-blue colocalization
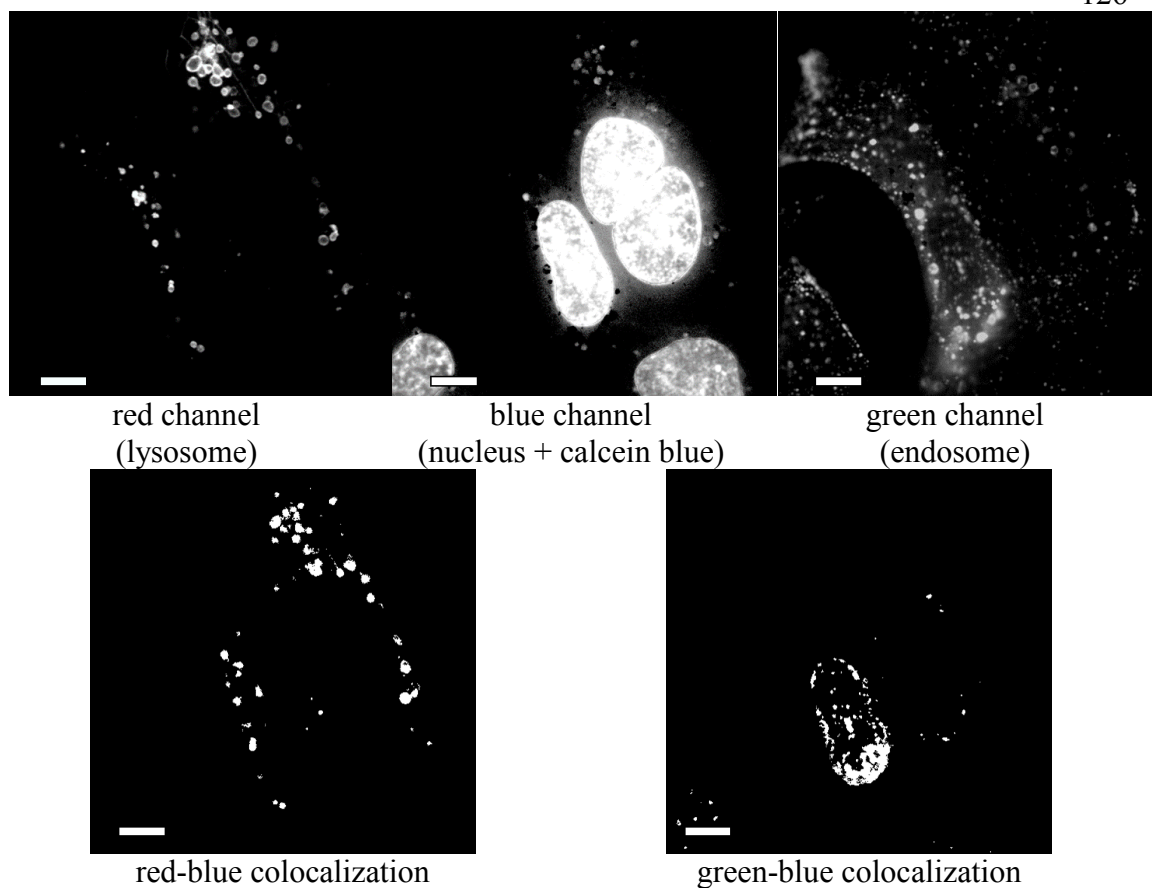
Figure 3-26: Confocal microscopy was used to visualize trafficking of quenching targeted polymersomes (9 mol% cPR_b) in live DLD-1 cells. Results shown here are for 2 h at 37 °C. Cells were transfected to express LAMP1-RFP (lysosome, red channel) and Rab5-GFP (early endosome, green channel). Polymersomes encapsulated 100 mM calcein blue and nuclei stained with Hoechst 33342 (both blue channel). Scale bars indicate 10 μm.

red channel
(lysosome)

blue channel
(nucleus + calcein blue)

green channel
(endosome)

red-blue colocalization

green-blue colocalization
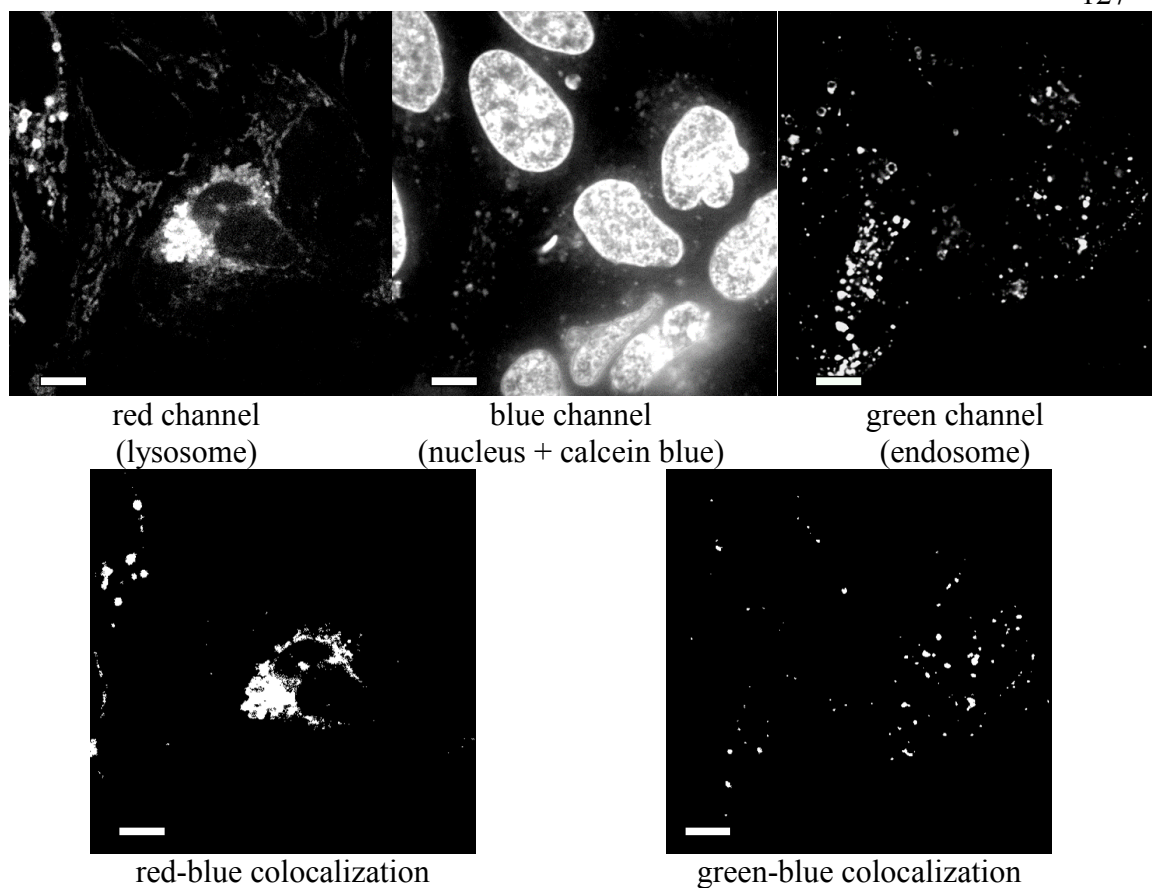
Figure 3-27: Confocal microscopy was used to visualize trafficking of quenching targeted polymersomes (9 mol% cPR_b) in live DLD-1 cells. Results shown here are for 2 h at 37 °C. Cells were transfected to express LAMP1-RFP (lysosome, red channel) and Rab5-GFP (early endosome, green channel). Polymersomes encapsulated 100 mM calcein blue and nuclei stained with Hoechst 33342 (both blue channel). Scale bars indicate 10 μm.

red channel
(lysosome)

blue channel
(nucleus + calcein blue)

green channel
(endosome)

red-blue colocalization

green-blue colocalization
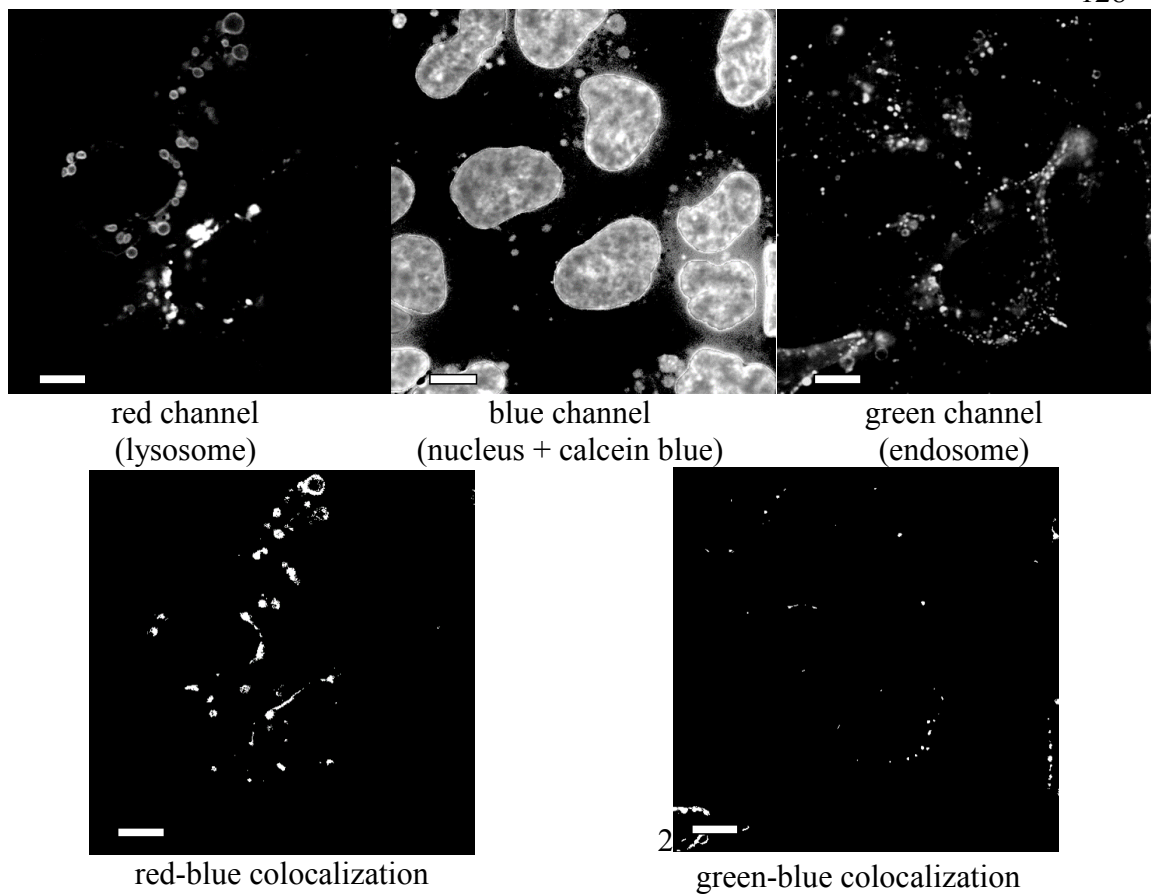
Figure 3-28: Confocal microscopy was used to visualize trafficking of quenching targeted polymersomes (9 mol% cPR_b) in live DLD-1 cells. Results shown here are for 22 h at 37 °C. Cells were transfected to express LAMP1-RFP (lysosome, red channel) and Rab5-GFP (early endosome, green channel). Polymersomes encapsulated 5 mM calcein blue and nuclei stained with Hoechst 33342 (both blue channel). Scale bars indicate 10 μm.

red channel
(lysosome)

blue channel
(nucleus + calcein blue)

green channel
(endosome)

red-blue colocalization

green-blue colocalization
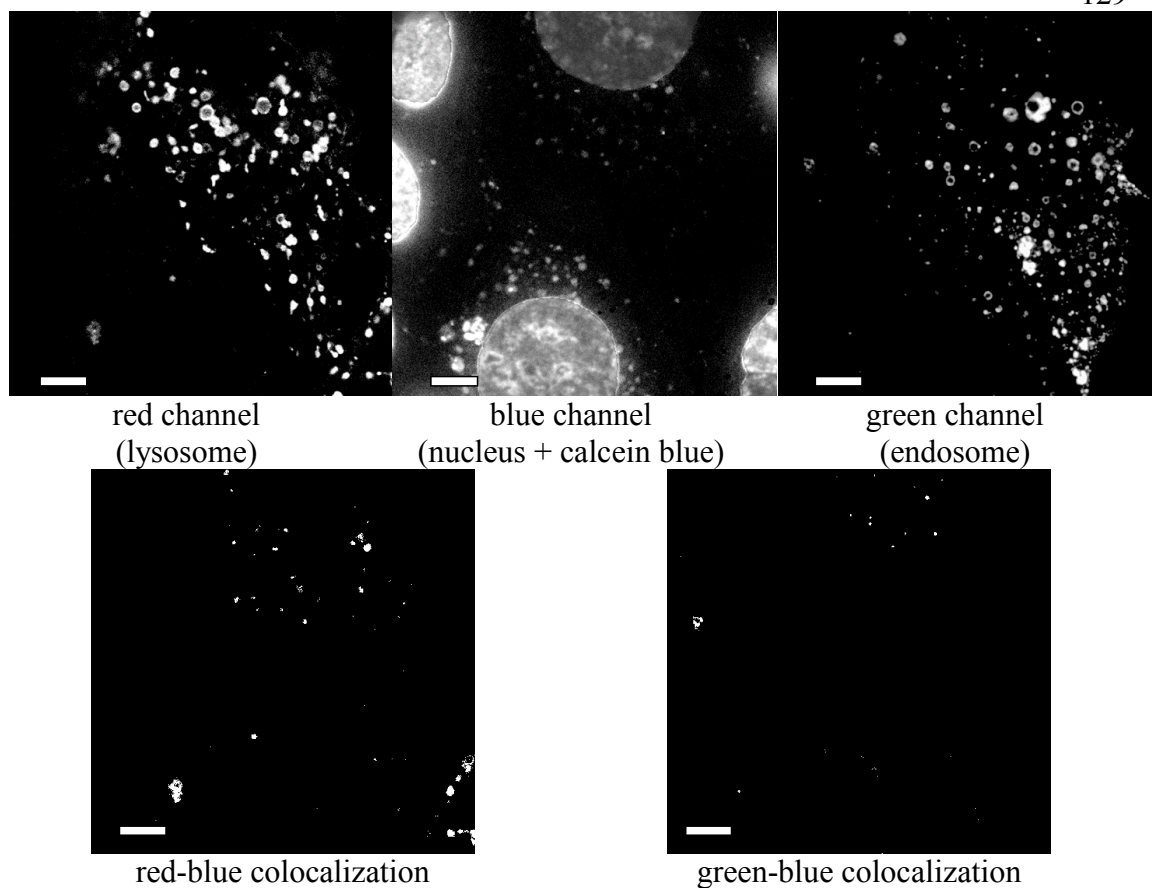
Figure 3-29: Confocal microscopy was used to visualize trafficking of quenching targeted polymersomes (9 mol% cPR_b) in live DLD-1 cells. Results shown here are for 22 h at 37 °C. Cells were transfected to express LAMP1-RFP (lysosome, red channel) and Rab5-GFP (early endosome, green channel). Polymersomes encapsulated 5 mM calcein blue and nuclei stained with Hoechst 33342 (both blue channel). Scale bars indicate 10 μm.

red channel
(lysosome)

blue channel
(nucleus + calcein blue)

green channel
(endosome)

red-blue colocalization

green-blue colocalization
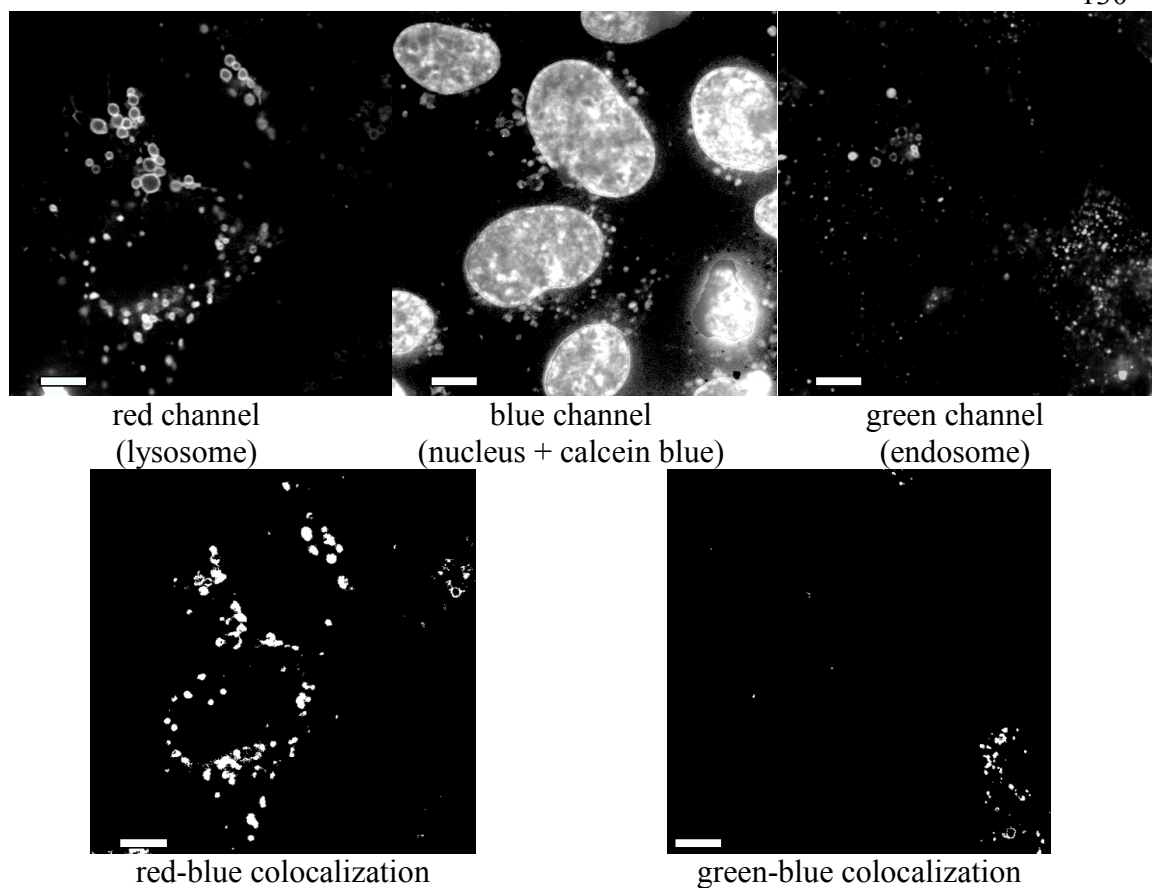
Figure 3-30: Confocal microscopy was used to visualize trafficking of quenching targeted polymersomes (9 mol% cPR_b) in live DLD-1 cells. Results shown here are for 22 h at 37 °C. Cells were transfected to express LAMP1-RFP (lysosome, red channel) and Rab5-GFP (early endosome, green channel). Polymersomes encapsulated 100 mM calcein blue and nuclei stained with Hoechst 33342 (both blue channel. Scale bars indicate 10 μm.

red channel
(lysosome)

blue channel
(nucleus + calcein blue)

green channel
(endosome)

red-blue colocalization

green-blue colocalization
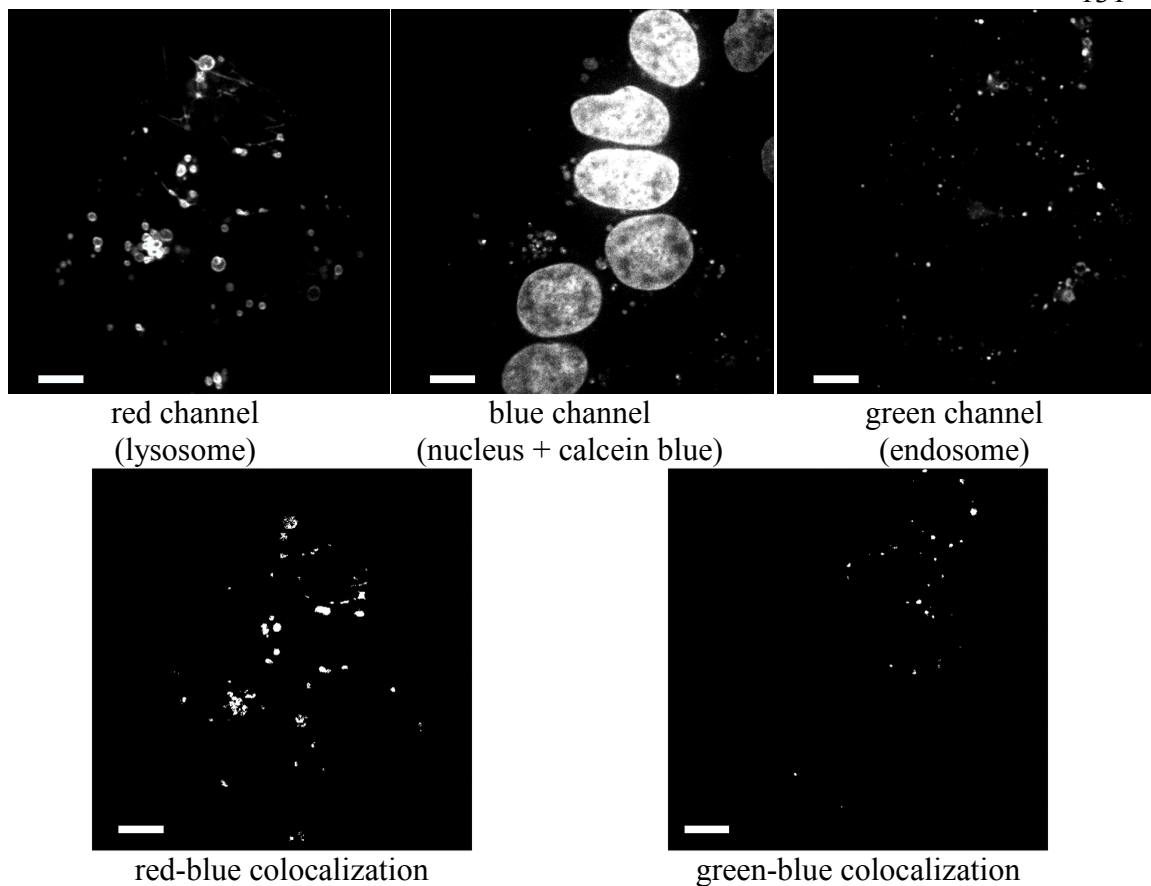
Figure 3-31: Confocal microscopy was used to visualize trafficking of quenching targeted polymersomes (9 mol% cPR_b) in live DLD-1 cells. Results shown here are for 22 h at 37 °C. Cells were transfected to express LAMP1-RFP (lysosome, red channel) and Rab5-GFP (early endosome, green channel). Polymersomes encapsulated 100 mM calcein blue and nuclei stained with Hoechst 33342 (both blue channel). Scale bars indicate 10 μm.

red channel
(lysosome)

blue channel
(calcein blue)

green channel
(endosome)

red-blue colocalization

green-blue colocalization
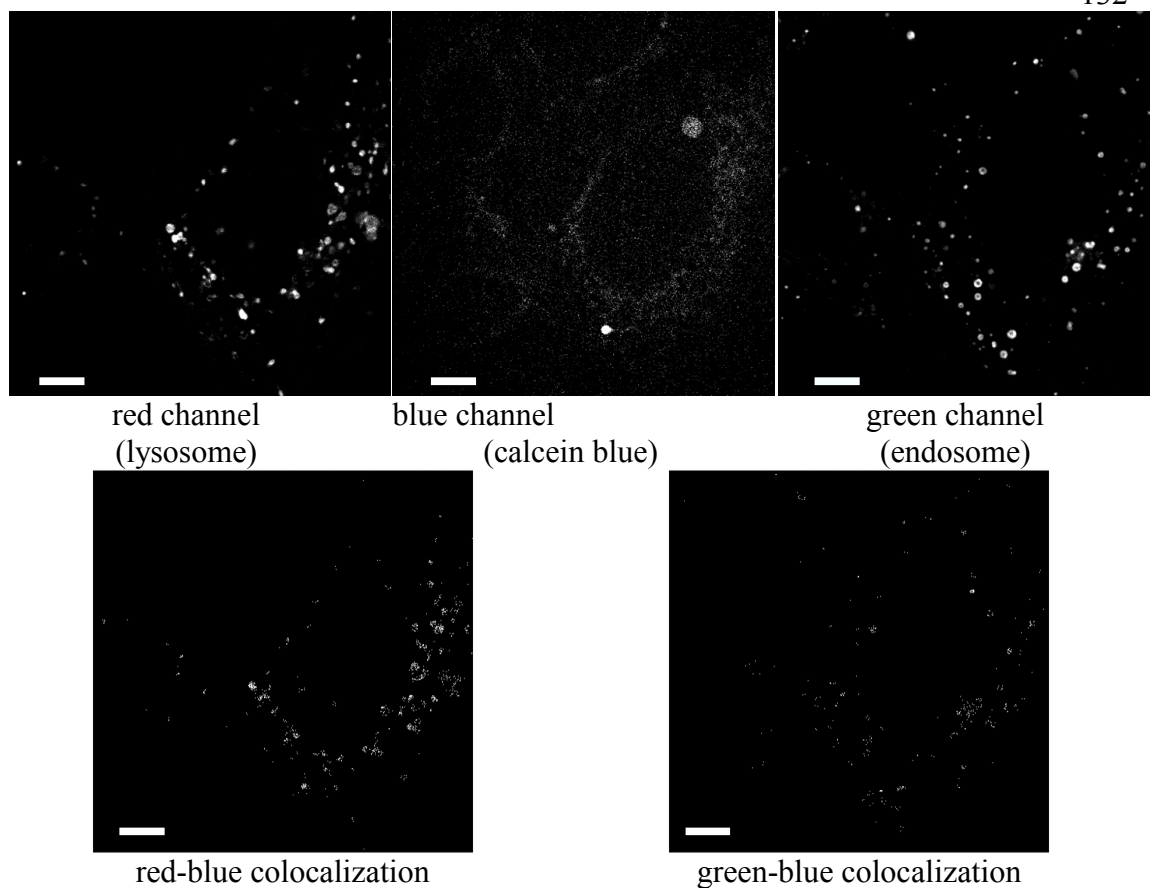
Figure 3-32: Confocal microscopy was used to visualize trafficking of quenching targeted polymersomes (9 mol% cPR_b) in live DLD-1 cells without nuclear stain. Results shown here are for 22 h at 37 °C. Cells were transfected to express LAMP1-RFP (lysosome, red channel) and Rab5-GFP (early endosome, green channel). Polymersomes encapsulated 100 mM calcein blue (blue channel). Scale bars indicate 10 μm.

red channel
(lysosome)

blue channel
(calcein blue)

green channel
(endosome)

red-blue colocalization

green-blue colocalization

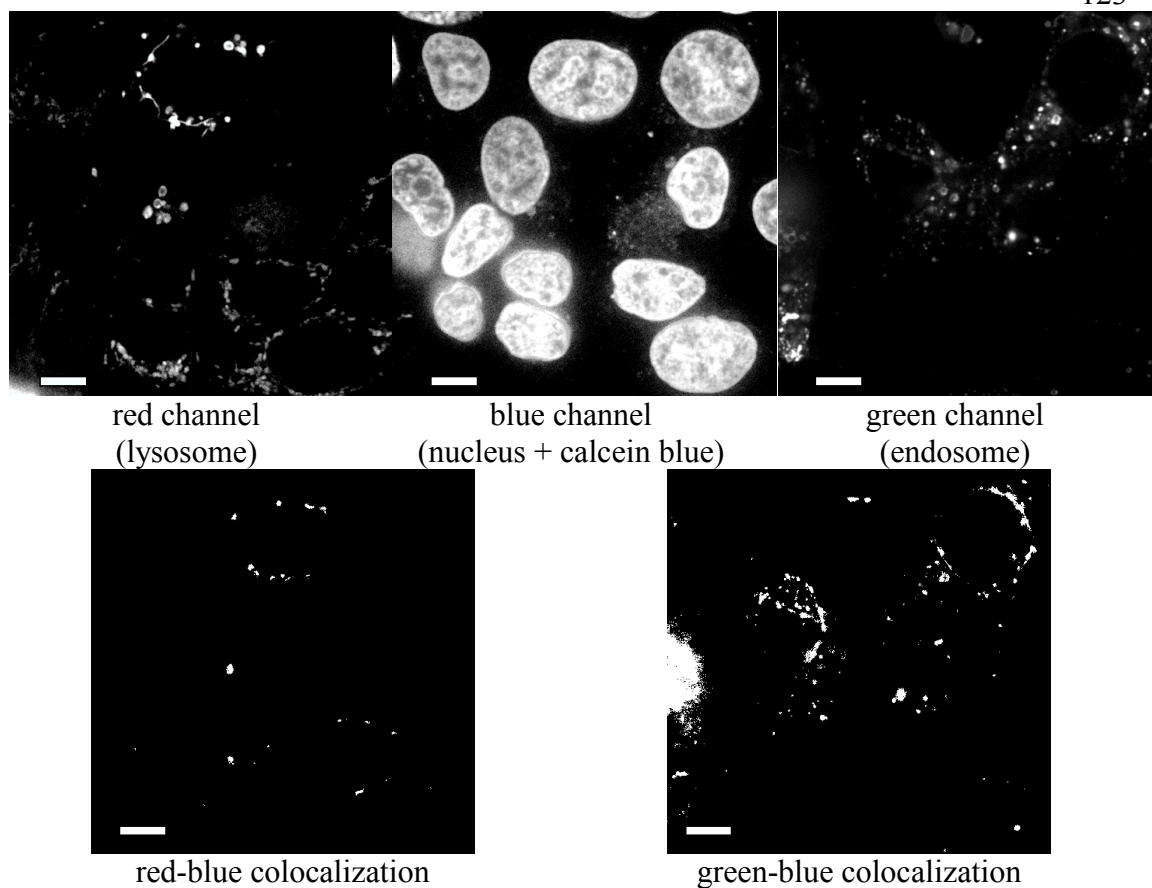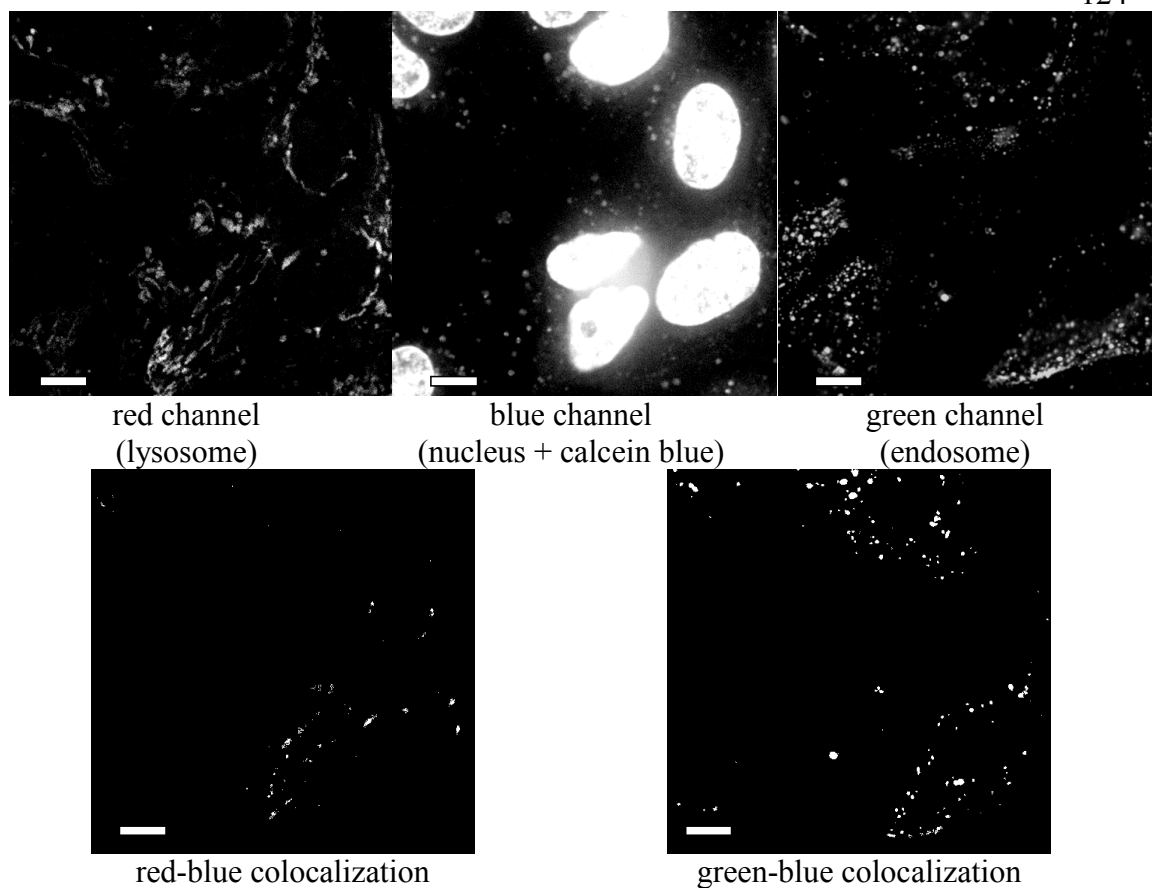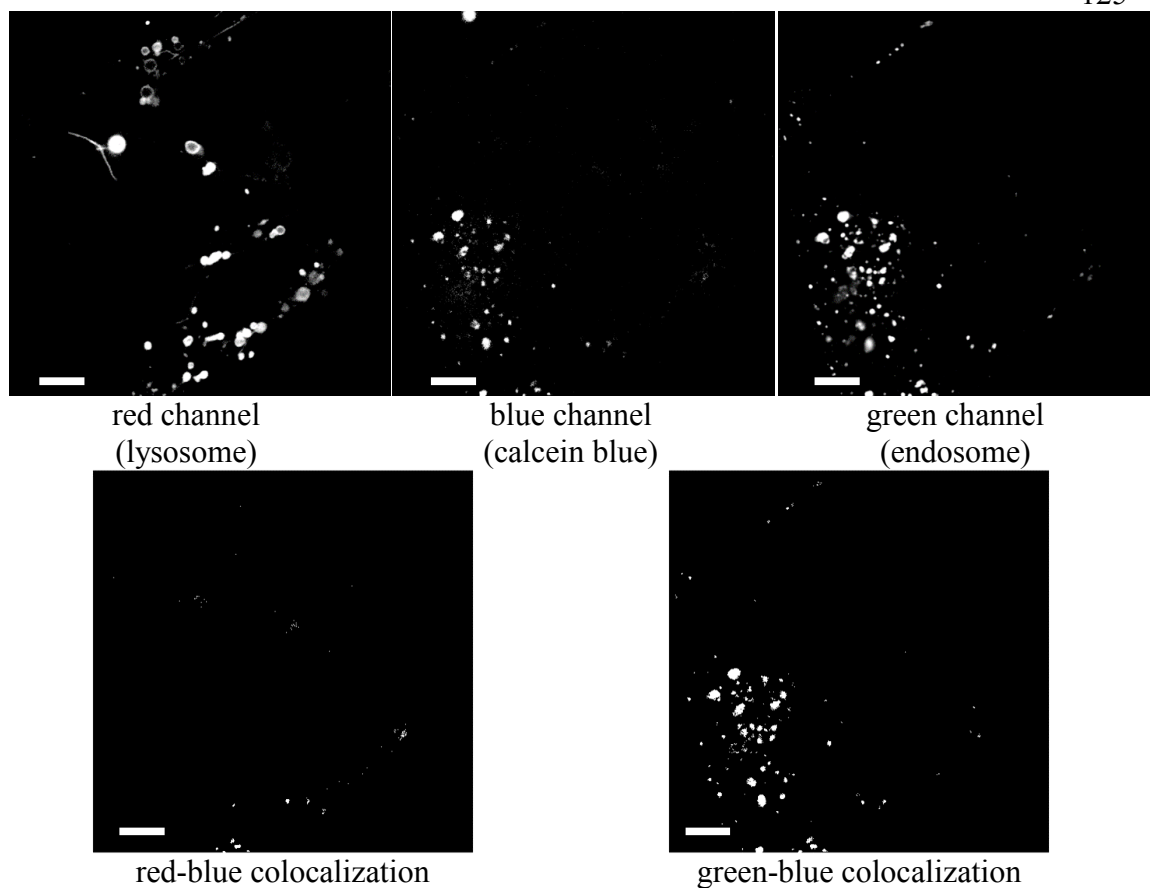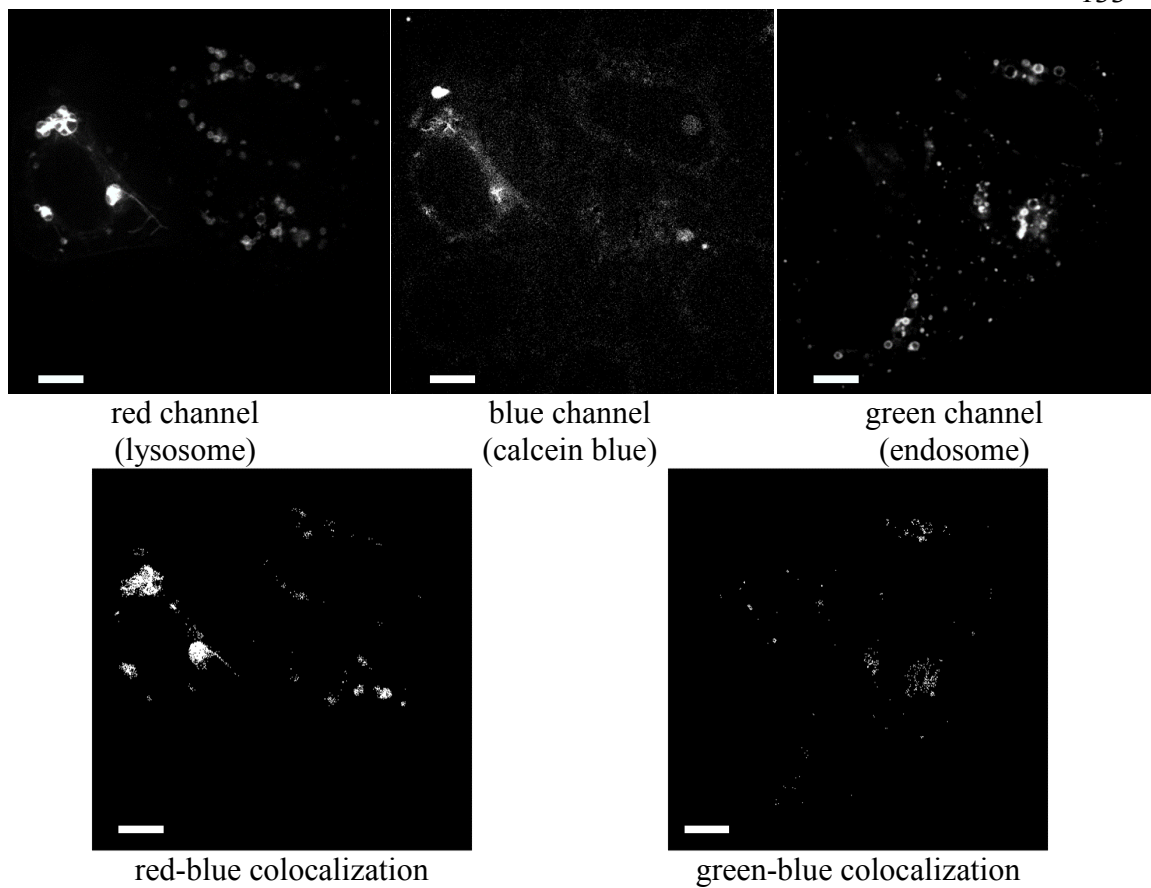Figure 3-33: Confocal microscopy was used to visualize trafficking of quenching targeted polymersomes (9 mol% cPR_b) in live DLD-1 cells without nuclear stain. Results shown here are for 22 h at 37 °C. Cells were transfected to express LAMP1-RFP (lysosome, red channel) and Rab5-GFP (early endosome, green channel) while polymersomes encapsulated 100 mM calcein blue (blue channel). Scale bars indicate 10 μm.

Table 3-2: Manders coefficients were determined for cPR_b-functionalized polymersomes delivered to DLD-1 cells. These data were used to quantitatively describe colocalization between the blue channel (polymersomes) and either the green (early endosomes) or red (lysosomes) channels after 2 h and 24 h.[287,288] M_1 describes the portion of the blue channel that overlaps with either the red or the green channel while M_2 describes the portion of the red or green channel that overlaps with the blue channel. Nonquenching dye concentrations (5 mM) were used to study trafficking while quenching concentrations (100 mM) were used to determine the location of intracellular dye release. In all calculations nuclei were omitted. Nonquenching analysis used Figure 3-24 and Figure 3-28 for 2 h and 24 h, respectively. For analysis of quenching formulations Figure 3-26 and Figure 3-31 were used for 2 h and 24 h, respectively.

Time	Channel	M_1	M_2	Dye
2 h	green	0.3792	0.0402	5 mM
2 h	red	0.6405	0.0719	5 mM
24 h	green	0.0455	0.0211	5 mM
24 h	red	0.8452	0.1948	5 mM
2 h	green	0.0824	0.0337	100 mM
2 h	red	0.8694	0.4686	100 mM
24 h	green	0.0186	0.0902	100 mM
24 h	red	0.9290	0.1886	100 mM

To study trafficking, calcein blue was encapsulated at a nonquenching concentration (5 mM), allowing visualization of concentrated dye regardless of release. The Manders coefficients were calculated after 2 and 24 h (Table 3-2), allowing a quantitative evaluation of colocalization.[287,288] Here M_1 describes the portion of blue from dye delivered in polymersomes that overlaps with endosomes (green) or lysosomes (red) while M_2 describes the portion of the green or red channels that overlaps with blue. The values shown in Table 3-2 indicate that at early time points polymersomes had been trafficked to both the endosomes and the lysosomes. However, after 24 h the dye was predominantly colocalized with lysosomes. This result is consistent with previous reports of intracellular trafficking following binding to the $\alpha_5\beta_1$ integrin.[139,293,294]. To verify that blue fluorescence was not entirely due to the nuclear stain, images were collected with

nonquenching concentrations of calcein blue but without the nuclear stain. In this case, similar colocalization patterns emerged as when Hoechst was present, an example of which can be seen in Figure 3-25.

By encapsulating a self-quenching concentration of calcein blue into polymersomes (100 mM) it was possible to track where the payload was released as the dye would only be visible when diluted by release from the polymersomes. As in trafficking studies, colocalization was quantitatively determined using the Manders coefficients at 2 and 24 h (Table 3-2). In contrast to the nonquenching experiment, where some colocalization was observed between the early endosomes and the dye at early time points, for the quenching concentrations most colocalization of the dye was observed in the lysosomes even at 2 h. This trend is especially pronounced after 24 h, with very little colocalization between the early endosomes and calcein blue and more pronounced accumulations of blue dye within lysosomes. This release in the lysosomes (and to a lesser extent in the early endosomes) after 2 h is in keeping with the release rates shown Figure 3-12 and further emphasize the key role that digestive enzymes play in release of encapsulated payloads from delivery vehicles. As with nonquenching concentrations, images collected in the absence of nuclear stain had similar colocalization patterns as when the Hoechst was present, examples of which can be seen in Figure 3-32 and Figure 3-33.

The observed rapid release is in stark contrast to the much slower release rate observed at even low pH in simple buffered solution, underscoring the role of enzymatic activity on intracellular payload release. Further, the fact that not all blue fluorescence from polymersomes overlaps with endosomes or lysosomes, particularly at later time points,

suggests that the entire payload is not ultimately sequestered in these organelles. Nonetheless, given the low expected fluorescence of dye dispersed in the cytosol, definitively establishing escape from the endosomal-lysosomal degradation pathway on the basis of this analysis alone is challenging. This question was instead addressed by determining if a drug delivered in the polymersomes that requires delivery to the cytosol or nucleus inhibits cell growth, as only drug that is released from these organelles would inhibit growth and drug sequestered in the endosomes or lysosomes would not be expected to affect viability.
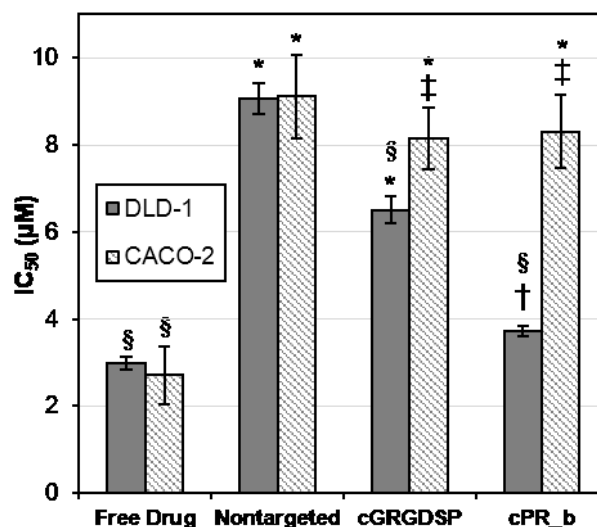
Figure 3-34: The IC_{50} value for free cisplatin, nontargeted polymersomes, cGRGDSP-functionalized polymersomes (9 mol% cGRGDSP), and cPR_b-functionalized polymersomes (9 mol% cPR_b) was determined for DLD-1 cells following incubation for 24 h at 37 °C. Free cisplatin had the lowest IC_{50}, followed closely by cisplatin encapsulated in targeted polymersomes using the cPR_b peptide. Significantly more drug was necessary to inhibit cell growth when encapsulated in cGRGDSP-functionalized polymersomes, while approximately three times more cisplatin was required to inhibit cell growth when encapsulated in nontargeted polymersomes compared to free drug. In contrast, delivery to the CACO-2 cell line showed no significant difference from the nontargeted polymersomes regardless of the targeting peptide. Results (mean ± standard error) for the DLD-1 are from four separate experiments (n=4) each conducted in triplicate and results for the CACO-2 are from three separate experiments (n=3) each conducted in triplicate. * Statistically significant difference from free drug (p<0.05), † no statistical difference from free drug (p>0.10), § statistically significant difference from nontargeted polymersomes (p<0.05), ‡ no statistical difference from nontargeted polymersomes (p>0.10) *via* paired t-test.

Cisplatin Delivery

Cisplatin was encapsulated into polymersomes and delivered to DLD-1 cells to determine if the enhanced binding of targeted polymersomes observed in Figure 3-11 and Figure 3-22 would yield commensurate gains in treatment efficacy. Cisplatin interacts with nucleic acids of rapidly-dividing cancer cells to hinder their growth and is not expected to inhibit growth if wholly sequestered in lysosomes.[305,306] The well-established MTT viability assay, which relies on cellular metabolism to convert yellow (3-(4,5-

dimethylthiazol-2-yl)-2,5-diphenyltetrazolium bromide (MTT) to its purple formazan derivative, was used to determine the IC_{50} of DLD-1 and CACO-2 cultures following treatment with free cisplatin or the drug encapsulated in non-, cGRGDSP-, or cPR_b-targeted polymersomes (Figure 3-34). Prior to cell studies, polymersomes were verified to encapsulate cisplatin, with encapsulation efficiencies (3-5%) on the lower side of previous reports using polymersomes to encapsulate drugs not amenable to 'active' loading.[222,282,283] Following encapsulation, polymersomes were verified to release the drug quite slowly in simple buffered media (Figure 3-5).

Free drug required the lowest dose to inhibit growth using both $\alpha_5\beta_1$-overexpressing DLD-1 cells and low $\alpha_5\beta_1$-expressing CACO-2 cells, which was attributed to the drug being free to interact with the cell without first releasing from a polymersome. In contrast, when encapsulated in nontargeted polymersomes significantly more drug was necessary to inhibit growth. Given the results of polymer toxicity studies (Figure 3-9) this low toxicity from the cisplatin encapsulated in the nontargeted formulations is probably the result of drug release following limited delivery *via* the same nonspecific uptake pathway that was responsible for fluorescence in nontargeted formulations in Figure 3-11A and Figure 3-22. When a targeting peptide was used, the enhancements to binding and payload delivery compared to the nontargeted formulations, also as observed in these experiments, resulted in decreased viability for $\alpha_5\beta_1$-overexpressing DLD-1 cells while IC_{50} values were not significantly affected for CACO-2 cells. For DLD-1 cells, the cGRGDSP peptide was effective relative to nontargeted polymersomes while cPR_b reduced the amount of cisplatin required by more than 50% relative to the nontargeted formulation. Statistical

comparison indicated no significant difference between the amounts of drug needed using cPR_b-functionalized polymersomes and free drug in DLD-1 cells. Taken together with the binding experiments shown in Figure 3-11 it can be seen that targeting with the cPR_b peptide not only enhanced binding to $\alpha_5\beta_1$-overexpressing cells and delivery of the encapsulated drug but it also left almost unaffected cells with low levels of the targeted $\alpha_5\beta_1$ integrin receptor.

A substantial difference is apparent between relative binding (Figure 3-11), and relative growth inhibition, as observed in the IC_{50} (Figure 3-34). This difference is consistent with microscopy, which indicated that a substantial fraction of the polymersomes' payload was delivered to the lysosomes, where it is physically sequestered away from nuclear DNA to which it would otherwise bind to inhibit cellular function and growth.[12,307–310] Nonetheless, the effectiveness of cisplatin delivery using targeted polymersomes suggests the lysosome is not the only site of their delivery and release, as sufficient quantities of the cisplatin drug must be escaping from polymersomes and lysosomes following their uptake in order to see the observed growth inhibition.

3.4   Conclusions

Cisplatin therapy is often limited by major side effects and resistance. By tethering the cPR_b targeting peptide to the outside of PEO-PMCL polymersomes it was possible to obtain specific binding and uptake into $\alpha_5\beta_1$-overexpressing human colon cancer cells, greatly exceeding the amount of binding seen with a cGRGDSP ligand while maintaining minimal binding to cells with low levels of $\alpha_5\beta_1$ expression. Intracellular release was tracked and imaged by a combination of fluorescent plate assays and live-cell confocal

microscopy. The effect of pH alone on polymer degradation and payload release rates was found to be minimal from pH 7.4 to 4.5. Release occurred much more rapidly following endocytosis and the slower solution release rates could be recovered by inhibiting enzymes in acidic organelles, implicating enzymatic hydrolysis as a key mode of release for PEO-PMCL polymersomes. When cPR_b-functionalized polymersomes were used to encapsulate cisplatin, toxicity to $\alpha_5\beta_1$-overexpressing cells outperformed nontargeted and cGRGDSP-functionalized polymersomes, with IC_{50} values on par with those of the free drug, while maintaining low levels of toxicity to cells expressing low levels of the integrin. PEO-PMCL polymersomes with cPR_b targeting appear to be promising carriers for minimizing side effects due to nonspecific delivery into $\alpha_5\beta_1$-overexpressing cancer cells.

Despite these encouraging results, the lack of degradability in simple buffered solutions, even those with quite acidic conditions, may hamper efforts towards the kind of responsive, triggered release of payload that remains a major goal in the drug delivery literature. The next chapter addresses efforts to develop new means to introduce acid-sensitive functionality in the polymer chain make it more prone acidic degradation and enhance the triggered release capability of future drug delivery systems.

4   Controlled Polymerization of an Acetal-Containing Polyester for Hydrolysis in Acidic Conditions

4.1   Introduction

The previous chapters addressed the synthesis (Chapter 2) and application (Chapter 3) of the amphiphilic diblock copolymer PEO-PMCL and its reactive analog VS-PEO-PMCL. However, this polyester-based system proved slow to degrade in the acidic conditions experienced following endocytosis into target cells, hindering payload release. This chapter describes efforts to address these shortcomings by developing a polymer that integrates a more pH-sensitive functional group to enhance treatment efficacy by triggering polymer degradation and payload release under mildly acidic conditions.

Environmentally-responsive polymers have proven to be an extremely rich area of research, opening new avenues to address longstanding needs unmet by conventional macromolecules. Contributions have been made to the fields of biomedicine, sensing, electronics, textiles, and filtration, among others.[311–317] A major focus of interest has been on polymers that are sensitive to changes in pH for drug delivery vehicles which are capable of payload release near or inside of targeted cancer cells.[85,149,318,319] This approach to delivery takes advantage of the fact that in comparison to physiological conditions in the bloodstream (pH 7.4), the environments in the vicinity of a tumor (pH 5.5-6.5) and in the endosome following uptake (pH 5.0–5.5) tend to be more acidic.[320,321]

Polymers sensitive to changes in pH are generally of two main classes. The first class is composed of macromolecules that incorporate a protonatable moiety capable of a

reversible ionization state, generally resulting in a change to either solubility or conformation.[322,323] The second class is comprised of polymers that undergo irreversible degradation.[324] Simple polyesters, including those described in the previous chapters, are an example of this second class, and have been used extensively.[280,325–328] However, to induce rapid degradation and payload release in physiologically-relevant pH ranges, more acid-labile degradable groups are required due to the slow hydrolysis rates of many polyesters at mildly-acidic pH values.
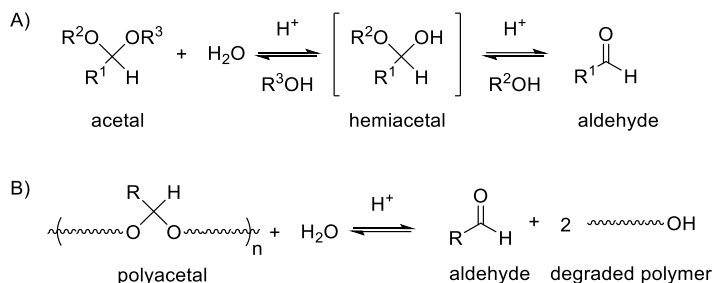
Figure 4-1: Structure of acetals, the group used to enhance pH-responsive degradation. A) General structure of acetals and equilibria with acid-catalyzed hydrolysis to the aldehyde *via* the hemiacetal. B) Structure of a polymer with acetals in the backbone and structure after acid-catalyzed hydrolysis. In the case of ketals, the hydrogen in the aldehyde and derivatives is replaced by an arbitrary substituent.

Acetals and ketals (Figure 4-1) are classes of functional group that have been investigated extensively for triggered degradation in acidic conditions. Interest has been particularly focused on drug delivery applications due to the groups' relative resistance to hydrolysis at physiological pH (7.4) but rapid degradation in acidic conditions analogous to those of the endosomal compartment (pH 5.0-5.5) after endocytosis.[24,320,329] The precise rate of degradation is affected by both the substituents present[330,331] and the hydrophilicity of the polymer.[332,333]
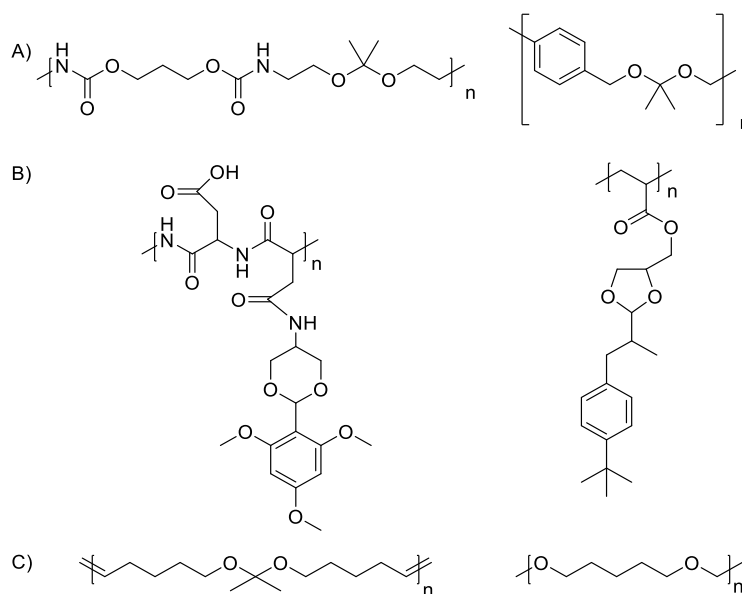
Figure 4-2: Examples of approaches used to incorporate acid-labile acetal or ketal functionality into polymers, including A) in the polymer backbone following step-growth polymerizations,[334,335] B) as pendant groups following step-growth[336] or conventional radical[333] polymerizations, and C) as part of the backbone following Ru-catalyzed methathesis[337] or an analogous acid-catalyzed acetal exchange polymerization.[338] Many

polymers incorporating acetal or ketal functional groups have been synthesized (some

sample structures are shown in Figure 4-2), but often by means that complicate their use in

drug delivery applications. Synthesis has generally been either by uncontrolled cationic[339–341] or step-growth[334,335,342–346] polymerizations, which result in polydisperse systems that

complicate achieving specific self-assembled morphologies, or as nondegradable polymers

which incorporate acetal functionality only as pendant groups,[336,347–349] potentially limiting

post-delivery clearance of the polymer from the body. Interesting new approaches have

also been investigated, including Ru-catalyzed metathesis[337,350] and a metathesis analog

using acid-catalyzed acetal exchange reactions.[338] Such approaches may mitigate some of

the disadvantages of existing synthetic methods while still incorporating a diverse range of

acetals in the polymer backbone, but cannot be easily integrated into existing approaches

to synthesizing amphiphiles to target promising self-assembled nanocarrier morphologies such as polymersomes or wormlike micelles.[207,219,234]

This chapter reports on efforts to develop 2-methyl-1,3-dioxan-4-one (MDO) as a cyclic ester monomer for ring-opening transesterification polymerization (ROTEP) to a polyester which contains acetals in the backbone for triggered degradation in low-pH conditions. The chapter includes structural and kinetic characterization of the polymerization of MDO into two distinct polymers, the nearly acetal-free poly(3-hydroxypropionic acid) (P-3(HPA)) and the acetal-retaining poly(2-methyl-1,3-dioxan-4-one) (PMDO). Thermodynamic parameters for polymerization of MDO to PMDO were measured from equilibrium monomer concentrations, and the degradation behavior of these polymers when exposed to physiologically-relevant pH conditions was investigated and compared.

4.2   Results and Discussion
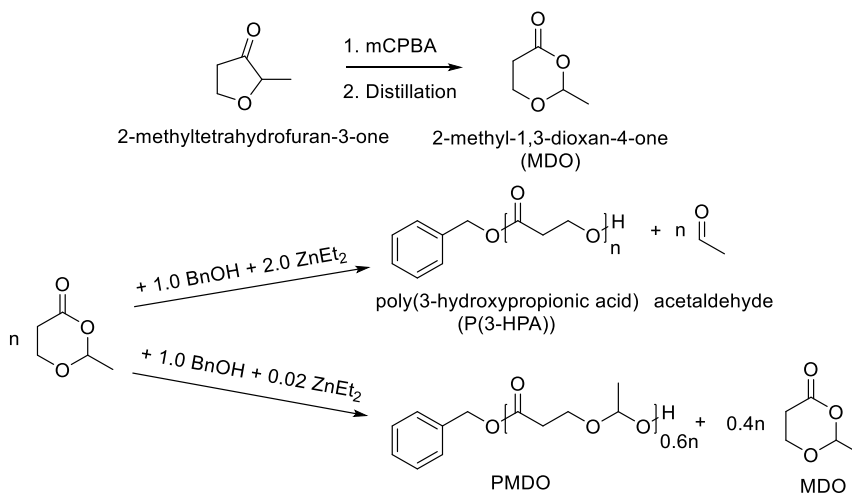
Figure 4-3: Scheme depicting the synthesis of MDO monomer and bulk polymerizations using diethylzinc to P(3-HPA) at higher catalyst loadings (with loss of acetal functionality) or to high-acetal PMDO at lower loadings of the catalyst.
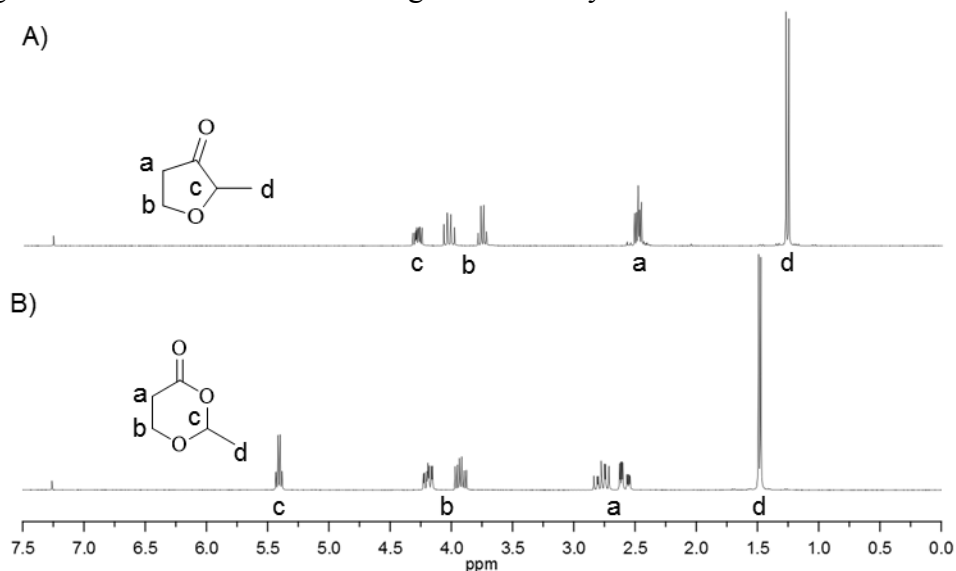
Figure 4-4: ^{1}H NMR spectra and proton assignments for A) 2-methyltetrahydrofuran-3-precursor and B) 2-methyl-1,3-dioxan-4-one (MDO) after Baeyer-Villiger oxidation and purification.
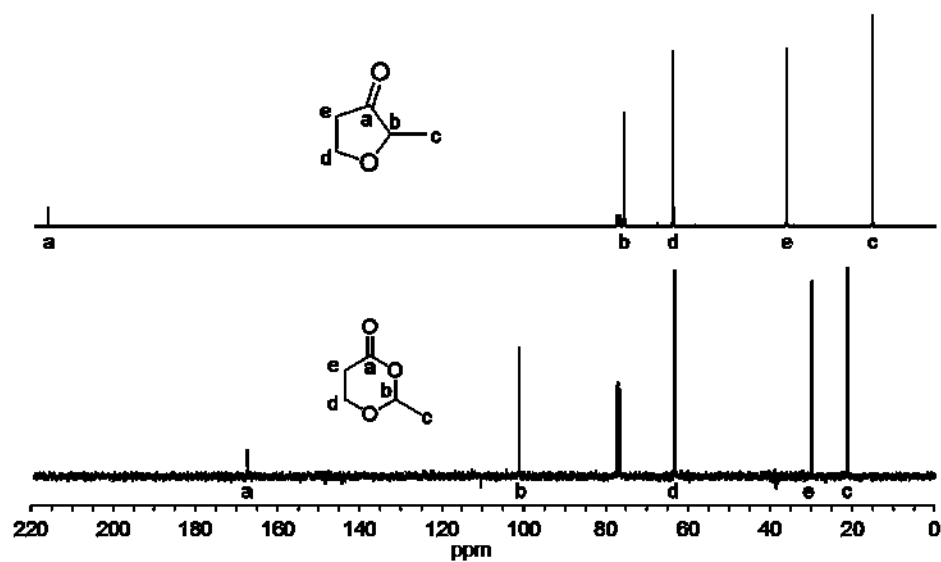
Figure 4-5: ^{13}C NMR spectra and structural assignments for A) 2-methyltetrahydrofuran-3-one starting material and B) MDO monomer after purification from Baeyer-Villiger oxidation of the furanone precursor.
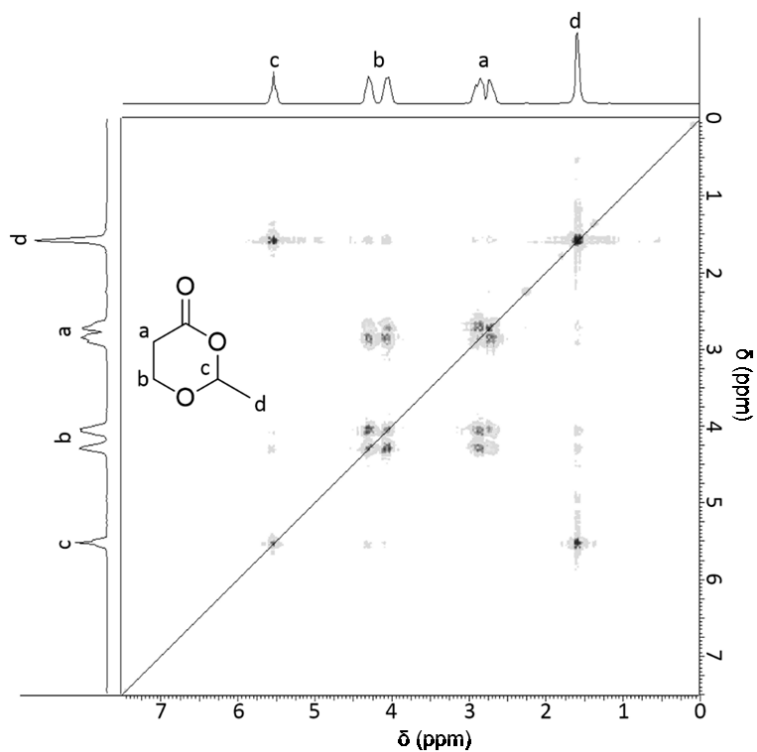
Figure 4-6: COSY spectrum of MDO monomer with proton assignments.

Synthesis of 2-methyl-1,3-dioxan-4-one (MDO)

MDO is a cyclic ester that incorporates acetal functionality and would be expected to decompose to 3-hydroxypropionic acid and acetaldehyde upon hydrolysis. To synthesize this monomer, racemic 2-methyltetrahydrofuran-3-one was treated with *meta*-chloroperoxybenzoic acid (mCPBA), resulting in Baeyer-Villiger oxidation to obtain MDO following workup and distillation. The reaction is shown in Figure 4-5 and the monomer was characterized by several techniques, including ^{1}H NMR spectroscopy (Figure 4-4), ^{13}C NMR spectroscopy (Figure 4-5), and 2-D homonuclear correlation spectroscopy (COSY, Figure 4-6). To the best of our knowledge, this is a novel route to this molecule, which previously has been reported in the French and Japanese patent literature, but only as the product of a ring-closing reaction between 3-hydoxypropionic acid and acetaldehyde.[351,352]
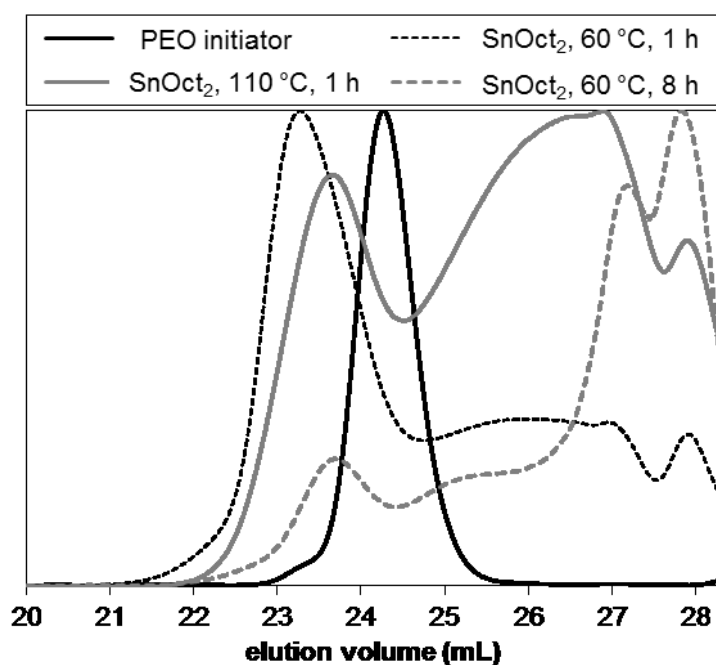
Figure 4-7: Bulk polymerization of MDO in the presence of PEO methyl ether (2 kg mol^{-1}) macroinitiator using tin octoate catalyst at 60 °C and 110 °C ([MDO]$_o$/[PEO]$_o$ = 200, [SnOct$_2$]$_o$ ≈ 10 mM). Some shift of the initiator peak occurred towards lower elution volumes, suggesting polymerization from PEO, but formation of oligomers was significant and molar mass distributions were very broad for all temperatures and polymerization times.
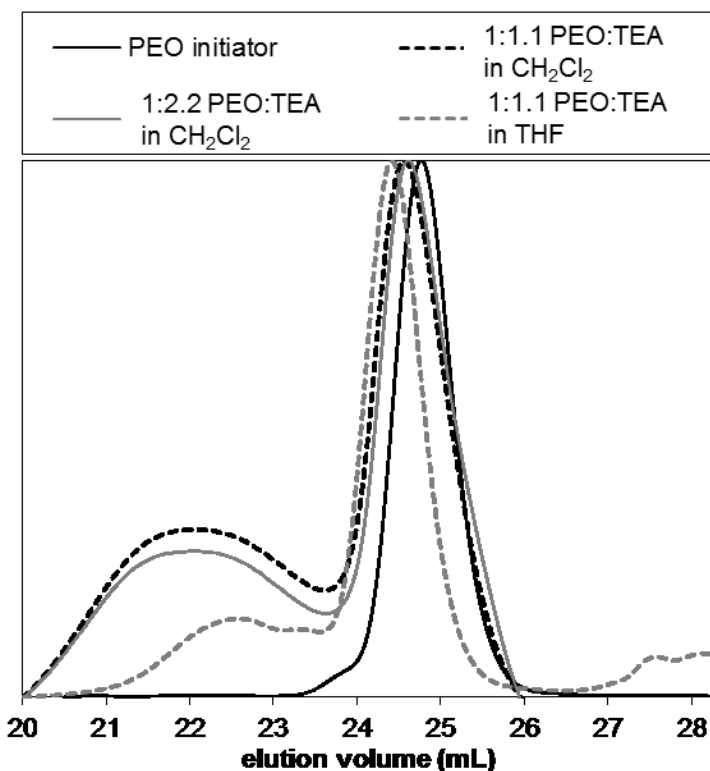
Figure 4-8: Solution polymerizations of MDO in the presence of PEO methyl ether (2 kg mol^{-1}) macroinitiator using TEA catalyst ($[MDO]_o$ = 1.5 M, $[PEO]_o$ = 7.5 mM, T_{polym} = 60 °C, t_{polym} = 1 h) at two concentrations in CH_2Cl_2 ($[TEA]_o/[PEO]_o$ = 1.1 and $[TEA]_o/[PEO]_o$ = 2.2) as well as a reaction in THF ($[TEA]_o/[PEO]_o$ = 1.1). Some shift of the initiator peak to lower elution volumes was accompanied by the formation of high molar mass molecules with very broad molar mass distributions.
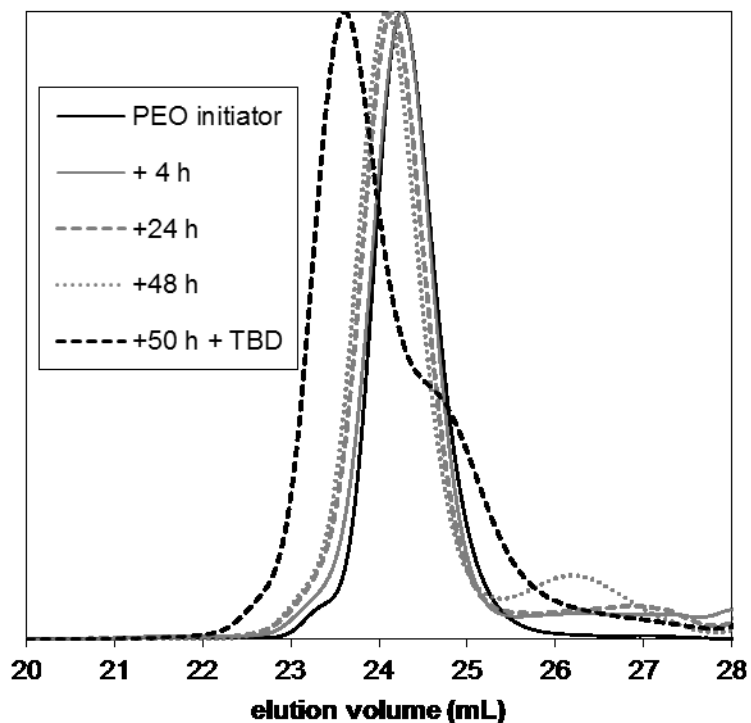
Figure 4-9: Bulk polymerization of MDO using TBD catalyst at room temperature and PEO methyl ether as a macroinitiator ($[TBD]_o = 30$ mM, $[MDO]_o/[PEO]_o = 200$). After an initial monomodal increase in molar mass, no further conversion occurred over multiple days until more TBD was added, which resulted in a rapid shift to lower elution volumes with some broadening of the molar mass distribution.

Early Polymerization Efforts

Polymerization of MDO was first attempted using PEO methyl ether (2 kg mol^{-1}) as an initiator and several common catalyst systems: stannous octoate (SnOct$_2$), triethyl aluminum (TEA) and triazabicyclodecene (TBD). These reactions were attempted either in the bulk (SnOct$_2$, TBD), or in solution (TEA). In trial reactions using stannous octoate ($[SnOct_2]_o \approx 10$ mM, $T_{polym} = 110$ °C and 60 °C), and triethyl aluminum ($[MDO]_o \approx 1.5$ M, $[TEA]_o = 8.25$ mM or 16.5 mM, $T_{polym} = 60$ °C in both THF and CH$_2$Cl$_2$), some higher molar mass species were observed in SEC elugrams, but monomer conversions were low

and molar mass distributions were extremely broad (Đ > 3.0, Figure 4-7 and Figure 4-8).

Due to the poor control over these polymerizations, both tin octoate and TEA were not

pursued further for polymerization of MDO. In the case of the TBD-catalyzed bulk

polymerization of MDO at room temperature ($[TBD]_o = 30$ mM), only minimal monomer

conversion occurred unless large amounts of catalyst were added (Figure 4-9). Due to the

inefficiency of this approach, this route to MDO polymerization was also abandoned. More

detailed information regarding these early efforts can be found in the Experimental section.

Table 4-1: Several polymers were synthesized by diethylzinc-catalyzed bulk polymerization of 2-methyl-1,3-dioxan-4-one (MDO) monomer using benzyl alcohol as the initiator. At higher catalyst loadings, nearly all acetal groups were eliminated as acetaldehyde, resulting in P(3-HPA). The number average degree of polymerization (by ^{1}H NMR spectroscopy) for each polymer is indicated by the number in the sample name.

Sample	$[C]_o$ (mM)	M_n, NMR (kg/mol)	M_n, SEC (kg/mol)	Đ	Repeat (ESI-MS)	% acetal (NMR)	T_g (°C)	T_m (°C)
HPA110	140	7.92	7.7[*]	1.14[*]	72.02	<1	-33.2	58.4
HPA131	120	9.46	8.9[*]	1.22[*]	72.02	<1	-31.3	73.1
HPA594	31	42.8	35.2[*]	1.23[*]	72.02	<1	-27.0	78.5

[*]Using CHCl$_3$ SEC calibrated with polystyrene standards.
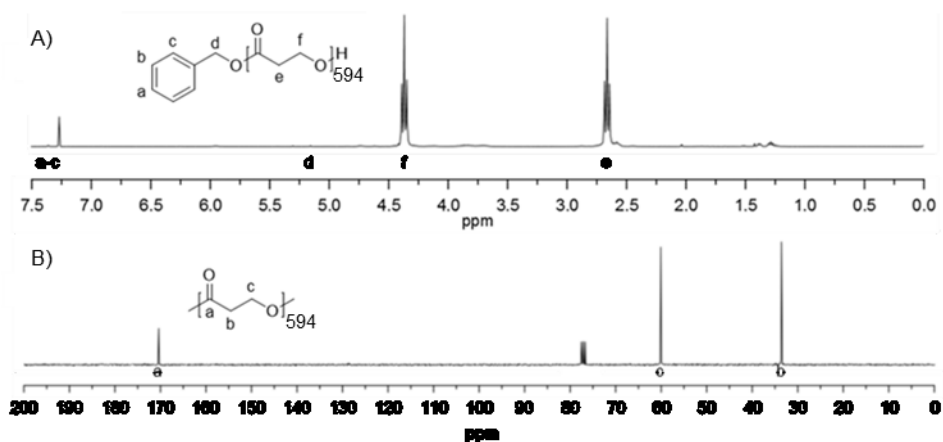
Figure 4-10: Representative A) ^{1}H and B) ^{13}C NMR spectra and structural assignments of P(3-HPA) samples synthesized by diethylzinc-catalyzed polymerization of MDO at higher (20 mM - 150 mM) catalyst concentrations. Spectra here are from sample HPA594 (42.8 kg mol^{-1}), where polymerization was conducted in the bulk at room temperature with $[ZnEt_2]_o = 31$ mM, $[BnOH]_o = 15.2$ mM, and $t_{polym} = 8$ h. Characterization data for these polymers are summarized in Table 4-1 and NMR spectra for other molar masses of P(3-HPA) can be found in Figure 4-24.

Synthesis of Poly(3-hydroxypropionic acid) (P(3-HPA))

Diethylzinc (ZnEt$_2$), a catalyst used in the past for polymerization of cyclic esters,[353–355] was investigated for bulk polymerization of MDO using benzyl alcohol as the initiator. Under these conditions ($[MDO]_o = 10.1$ M, $[BnOH]_o = 100.7$ mM, $[ZnEt_2]_o = 2.0$ mM, $t_{polym} = 8$ h, room temperature), combining MDO with a twofold excess of diethylzinc with respect to benzyl alcohol resulted in rapid polymerization to high fractional monomer conversions (>95%) with relatively narrow molar mass distributions (Đ < 1.3). Several polymers were synthesized in this manner, using varying ratios of $[MDO]_o/[BnOH]_o$ to generate polymers with molar masses from 7.92 kg mol^{-1} to 42.8 kg mol^{-1} (Table 4-1). These polymers could be isolated from the residual monomer by precipitation, forming white solids. In all cases, NMR spectra of these polymers contained only a small fraction (< 1%) of the characteristic acetal methyl and methine resonances present in the monomer, while methylene resonances persisted after polymerization ($\delta = 4.35$ and 2.65 ppm in the

^{1}H NMR spectrum; 60.25 and 33.76 ppm in the ^{13}C NMR spectrum, Figure 4-10). This, along with the loss of methylene proton splitting due to the acetal stereocenter, suggested that acetal functionality was no longer present following polymerization. Efforts to synthesize P(3-HPA) polymers with molar masses beyond approximately 50 kg mol^{-1} were met inconsistent final molecular weights and may have been limited by initiation due to residual monomer hydrolysis products with similar boiling points to MDO that were incompletely removed by distillation.
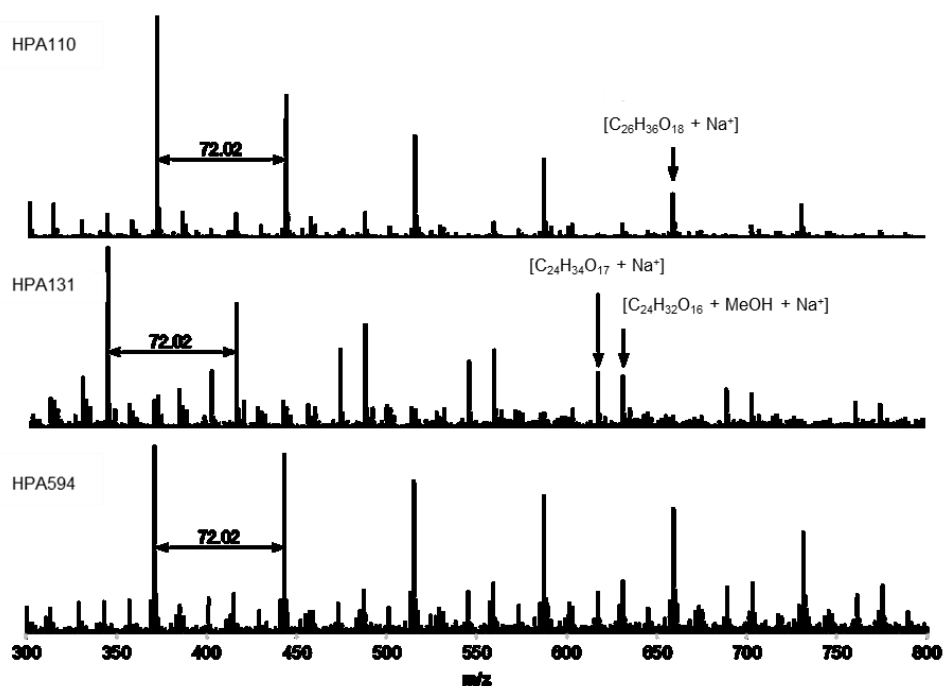
Figure 4-11: Electrospray ionization (ESI-MS) mass spectra of P(3-HPA) for several molar masses using 9:1 MeOH:CH$_2$Cl$_2$, where the numbers in sample names indicate the number-average degree of polymerization. The repeat unit of m/z = 72.02 found in all polymers is consistent with a molecule lacking MDO's acetal functionality, resulting in a 3-HPA repeat unit. High molar mass peaks were not observed, potentially as a result of polymer fragmentation during ionization. Exact m/z values for all polymers were consistent with retention of a single acetal, possibly as an uneliminated end group. For HPA131 and HPA594, a peak consistent with a methanol adduct could also be observed. Characterization data for these polymers is summarized in Table 4-1.
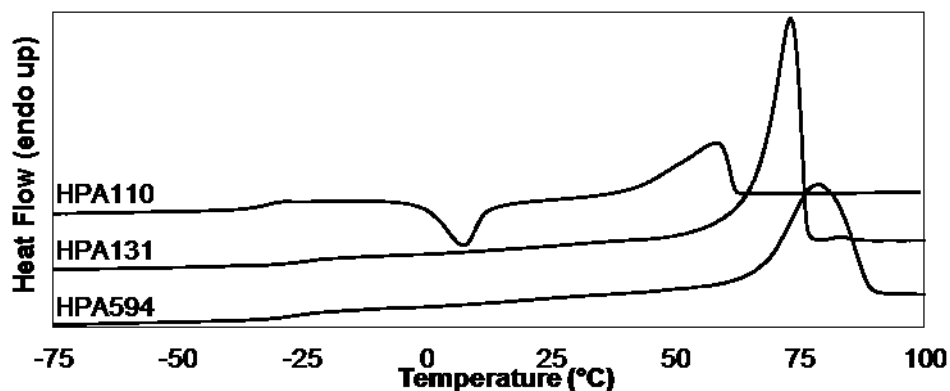
Figure 4-12: DSC thermograms for P(3-HPA) samples, with the numbers in sample names indicating the number-average degree of polymerization. Clear melting transitions were apparent for these polymers, ranging from 58.4 °C to 78.5 °C, indicating crystallinity. The glass transition temperature was quite low, ranging from -27.0 °C to -33.2 °C. Traces have been shifted vertically to aid visual comparison but relative peak heights and slopes have not been adjusted. Characterization data for these samples are summarized in Table 4-1.

To verify the structural assignment of P(3-HPA) to these polymers, electrospray ionization mass spectrometry (ESI-MS) was used to verify the repeat unit and differential scanning calorimetry (DSC) was used to measure thermal properties for comparison with previous work. While high molar mass ions were not observed in mass spectra (Figure 4-11), fragments could be clearly distinguished with a repeat of m/z = 72.02, consistent with the expected repeat unit for P(3-HPA). The exact m/z values of fragments were consistent with the presence of a single acetal-containing repeat unit (discussed in more detail below when considering a possible polymerization mechanism in Figure 4-14), as well as the expected m/z values for acetal-free P(3-HPA). DSC thermograms (Figure 4-12) of each polymer contained a clear glass transition temperature (T_g) ranging from -27.0 °C to -33.2 °C, and a melting endotherm at a temperature (T_m) ranging from 58.4 °C to 78.5 °C. Values of both T_g and T_m were consistent with those reported previously for P(3-HPA) synthesized by a macrocyclic route, [356] and further supported the structural assignments made for this polymer using NMR spectroscopy and mass spectroscopy.
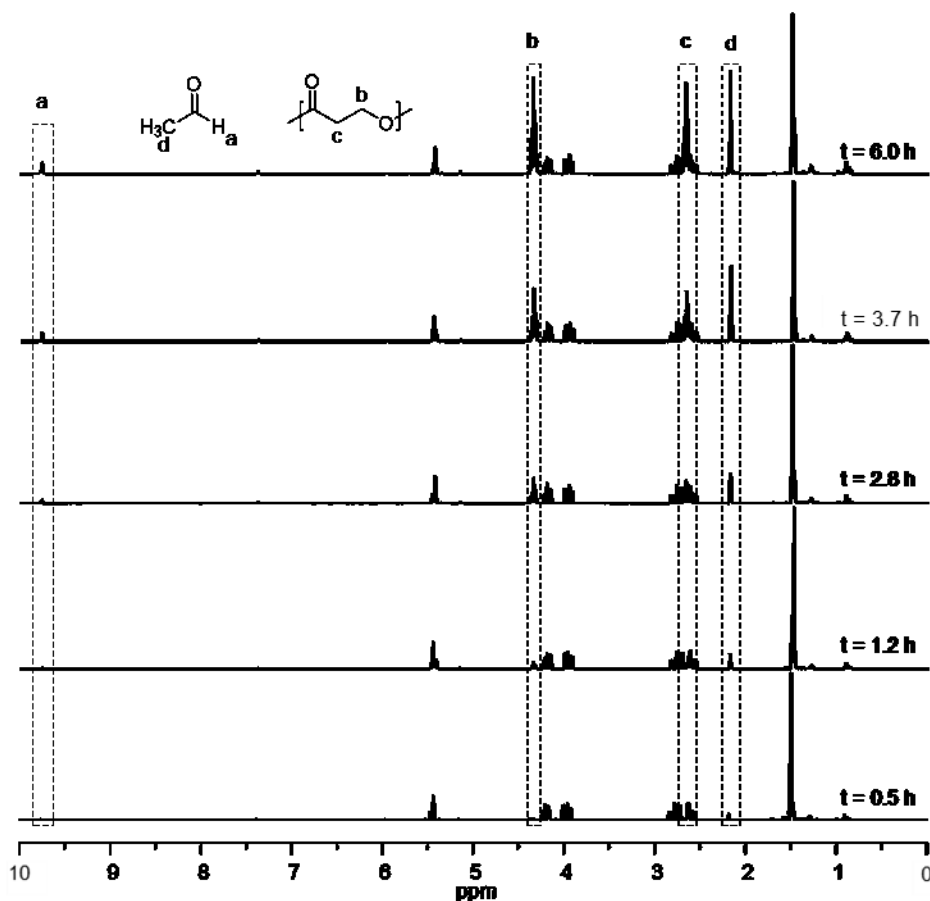
Figure 4-13: To investigate the loss of the MDO acetal functionality, the polymerization of MDO to P(3-HPA) was performed in CD_2Cl_2 to allow *in situ* tracking of byproducts using ^{1}H NMR spectroscopy. As the polymerization proceeded, the increase in resonances from P(3-HPA) methylene protons at 4.35 (b) and 2.65 ppm (c) was accompanied by a commensurate increase in resonances at $\delta = 9.77$ (a) and 2.18 (d) ppm consistent with acetaldehyde. Polymerizations were conducted using $[MDO]_o = 1$ M, $[BnOH]_o = 10$ mM, and $[ZnEt_2]_o = 20$ mM at room temperature.

In an effort to determine the source of acetal loss, a solution polymerization of MDO was set up at room temperature in CD_2Cl_2 ($[MDO]_o = 1$ M, $[BnOH]_o = 10$ mM, and $[ZnEt_2]_o = 20$ mM) to allow tracking of both polymerization and evolution of byproducts *in situ* (Figure 4-13). As MDO was converted to P(3-HPA), apparent as an increase in MDO methylene resonances at 4.35 and 2.65 ppm, a proportional increase was also

observed in resonances at 9.77 and 2.18 ppm consistent with acetaldehyde, the expected

aldehyde form of the acetal group present in MDO.

Combined with the NMR and mass spectroscopic characterization data above, these

results suggested that the loss of acetal functionality that occurred during polymerization

of MDO to P(3-HPA) was the result of elimination of acetaldehyde, which is a gas at room

temperature. This ROTEP-elimination reaction is analogous to ring opening-elimination

reactions used to form synthetic polypeptides, in which CO_2 is eliminated as a volatile

byproduct.[357,358]
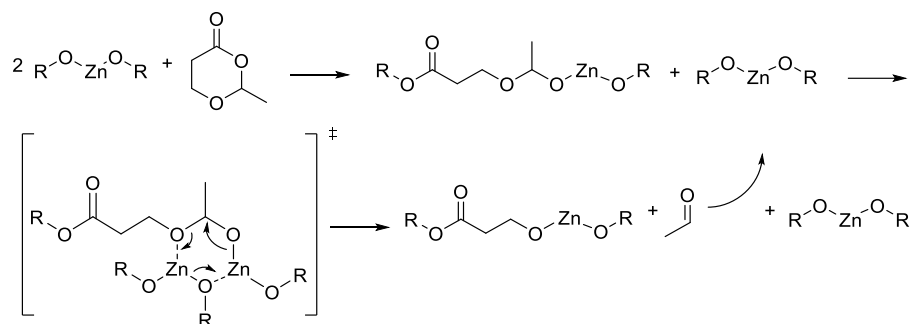
Figure 4-14: Proposed mechanism for elimination of acetaldehyde from MDO to form P(3-HPA). At higher $ZnEt_2$ catalyst concentrations, following the coordination-insertion ring-opening of MDO,[359,360] two zinc sites can complex with the acetal-containing chain end and undergo chain transfer, eliminating acetaldehyde and leaving a 3-HPA repeat unit. At lower catalyst concentrations, the incidence of two such sites forming the required transition state shown in this mechanism is quite low, minimizing elimination and leading to retention of the acetal in PMDO.

A possible mechanistic route explaining why acetaldehyde was lost at high catalyst

concentrations, while the acetal group is retained at lower catalyst concentrations, is shown

in Figure 4-14. Here, following the coordination-insertion ring-opening of MDO by zinc

by the standard mechanism,[359,360] a second catalytic site coordinates with the acetal end

group. At this point, chain transfer to the second catalytic site occurs, leading to elimination

of the acetal as acetaldehyde and leaving a 3-HPA repeat unit. Due to the increased entropy

associated with loss of this volatile byproduct, this process would be expected to be quite

thermodynamically favorable. At lower catalyst concentrations, the decreased likelihood

of two such sites forming the required complex results in retention of the acetal to form an

MDO repeat unit. This mechanism explains the results of P(3-HPA) ESI-MS (Figure 4-11),

where exact masses were observed consistent with a single acetal unit being present. In a

polymerization where the catalyst concentration is sufficiently high, prior to coordination

with the second catalytic site the chain would be expected to contain a single acetal as an

end group. While increasing [ZnEt$_2$] was found anecdotally to increase the polymerization

rate in reactions forming both P(3-HPA) and PMDO, in the absence of direct measurement

of the order of the reaction in catalyst, kinetic data were fit to the pseudo-first order rate

law shown in Figure 4-15 and catalyst concentration was incorporated into k_{app} for a given

reaction.

$$ln\left(\frac{[M]_o - [M]_{eq}}{[M] - [M]_{eq}}\right) = k_{app} \cdot t$$

Figure 4-15: Pseudo-first order rate law used to fit kinetics data for polymerization of MDO
to form P(3-HPA) and PMDO.
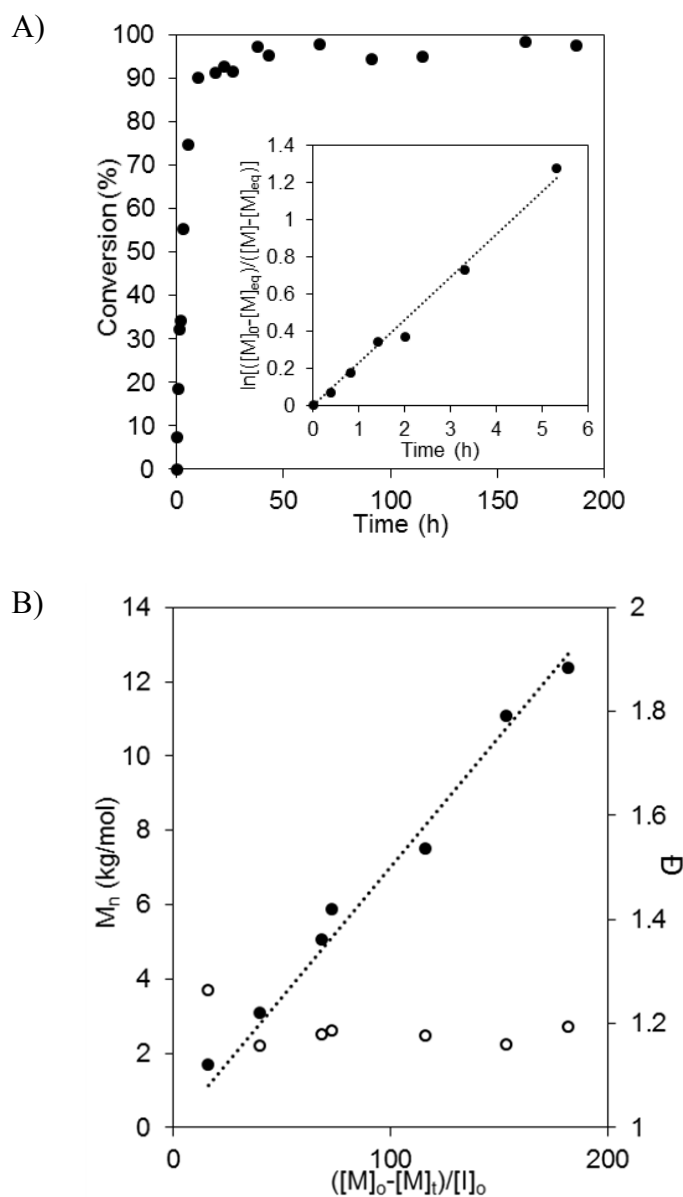
Figure 4-16: Diethylzinc-catalyzed bulk polymerization of MDO to low-acetal P(3-HPA) was tracked by ^{1}H NMR spectroscopy and SEC of aliquots taken during polymerization. A) When monomer conversion was tracked by ^{1}H NMR spectroscopy, conversion data indicated that within several hours the polymerization was essentially complete. The first several hours of polymerization (up to 90% monomer conversion) were linearized (inset) using Figure 4-15 to determine the apparent first order rate constant k_{app} = 0.24 h^{-1} at 23 °C, [MDO]$_o$ = 9.26 M, [BnOH]$_o$ = 46.3 mM, and [ZnEt$_2$]$_o$ = 87 mM. B) Molar mass (●, apparent M_n versus polystyrene standards) and the molar mass distribution (○, Đ) were also tracked by SEC during this reaction. Molar mass increased linearly with conversion of monomer, consistent with a controlled polymerization, and the molar mass distributions were relatively narrow (Đ < 1.3) throughout the polymerization.

In order to more fully characterize the behavior of diethylzinc-catalyzed bulk polymerizations of MDO to P(3-HPA), the reaction was tracked by both ^{1}H NMR spectroscopy and SEC of aliquots removed during the reaction. As shown in Figure 4-16A, within 5 h nearly 90% of MDO had been converted to P(3-HPA). To extract kinetic parameters for the polymerization, conversion data from this 5 h portion were used. Using Figure 4-15 and the experimentally determined ρ_{MDO} = 1.183 g mL^{-1} and the literature value[361] of $\rho_{P(3\text{-}HPA)}$ = 1.38 g mL^{-1}, it was possible to extract the pseudo-first order rate constant k_{app} = 0.24 h^{-1} at 23 °C when [MDO]$_o$ = 9.26 M, [BnOH]$_o$ = 46.3 mM, and [ZnEt$_2$]$_o$ = 87 mM (inset, Figure 4-16A). The apparent molar mass of the aliquots was also determined using SEC, and was plotted as a function of monomer conversion (Figure 4-16B). The correlation between these values was linear, consistent with a controlled polymerization, and the breadth of the molar mass distribution remained relatively low (Đ < 1.3) throughout the polymerization.

The polymerization of MDO using relatively high catalyst loadings ([ZnEt$_2$]$_o$ = 20 mM - 150 mM) provides a route to P(3-HPA) with only trace incorporation of the acetal functionality, with the vast majority of the hydrolytically labile linkage eliminated during polymerization as volatile acetaldehyde. This represents a new route to controlled polymerization yielding P(3-HPA) in the bulk over practically convenient time periods with molar mass distributions narrower than existing condensation,[362] microbial,[363,364] ring-opening,[365–368] and macrocyclic[356] syntheses.

Table 4-2: Several polymers were synthesized by diethylzinc-catalyzed bulk polymerization of 2-methyl-1,3-dioxan-4-one (MDO) monomer using benzyl alcohol as the initiator. At low catalyst loadings, the acetal group was retained, resulting in PMDO. The number average degree of polymerization (by ^{1}H NMR spectroscopy) for each polymer is indicated by the number in the sample name.

Sample	$[C]_o$ (mM)	M_n, NMR (kg/mol)	M_n, SEC (kg/mol)	Đ	Repeat (ESI-MS)	% acetal (NMR)	T_g (°C)	T_m (°C)
MDO66	1.7	7.64	8.1*	1.62*	116.05	>98	-32.3	-
MDO77	1.3	8.96	11.1*	1.62*	116.05	>98	-25.7	-
MDO259	0.41	30.1	33.8*	1.61*	116.05	>98	-31.1	-

*Using THF SEC calibrated with polystyrene standards
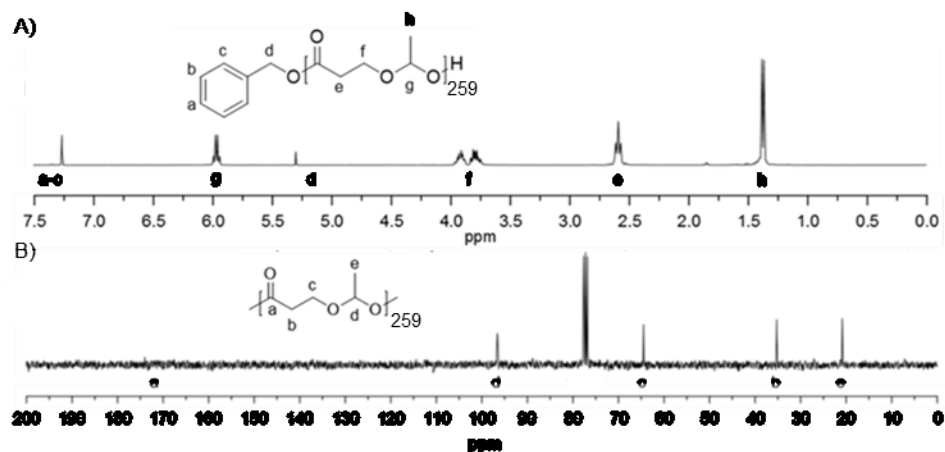
Figure 4-17: Representative A) ^{1}H and B) ^{13}C NMR spectra and structural assignments of PMDO synthesized by diethylzinc-catalyzed polymerization of MDO at lower (0.41 mM – 1.7 mM) catalyst concentrations. Spectra here are from sample MDO259 (30.1 kg mol^{-1}), where the polymerization was conducted in the bulk at room temperature using $[ZnEt_2]_o$ = 0.41 mM, $[BnOH]_o$ = 20.3 mM, and t_{polym} = 120 h. Characterization data for these polymers are summarized in Table 4-2, and NMR spectra for other molar masses of PMDO are in Figure 4-25.

Synthesis of Poly(2-methyl-1,3-dioxan-4-one)

To explore the effect of catalyst loading on polymer structure, bulk polymerization of MDO was also undertaken using $ZnEt_2$ at much lower concentrations ($[ZnEt_2]_o = 0.41$ mM − 1.7 mM). Several molar masses were targeted by varying the initial ratio of MDO monomer to benzyl alcohol initiator at room temperature. Under these conditions, as the polymerizations proceeded, the viscosity of the mixture slowly increased over several days, but the reaction remained a clear liquid rather than the white solid that developed during higher-catalyst polymerizations forming P(3-HPA). The polymer could be isolated from remaining monomer by opening the vessel to air to quench polymerization, dissolution of the reaction mixture in CH_2Cl_2, and precipitation into 9:1 hexanes:tetrahydrofuran to isolate a clear, viscous liquid. NMR spectra contained clear resonances from acetal methane and methine groups with integrations of ^1H NMR spectra consistent with nearly complete retention of this functional group ($\delta = 5.92$ and 1.33 ppm in ^1H NMR spectrum; 96.59 and 32.23 ppm in ^{13}C NMR spectrum, Figure 4-17). Also, the distinct splitting pattern of methylene protons due to the acetal stereocenter in the monomer (multiplets at $\delta = 4.22$ and 3.94 ppm), lost in P(3-HPA), was preserved under these conditions ($\delta = 3.88$ and 3.76 ppm). However, SEC of polymers prepared under these conditions indicated that molar mass distributions were broader than those observed for P(3-HPA) (Đ $\approx$ 1.6), an aspect of these polymerizations that will be discussed below. Additionally, synthesis of high PMDO with molar mass beyond approximately 50 kg mol^{-1} was, as with P(3-HPA), inconsistent, potentially due to initiation from residual monomer hydrolysis products.
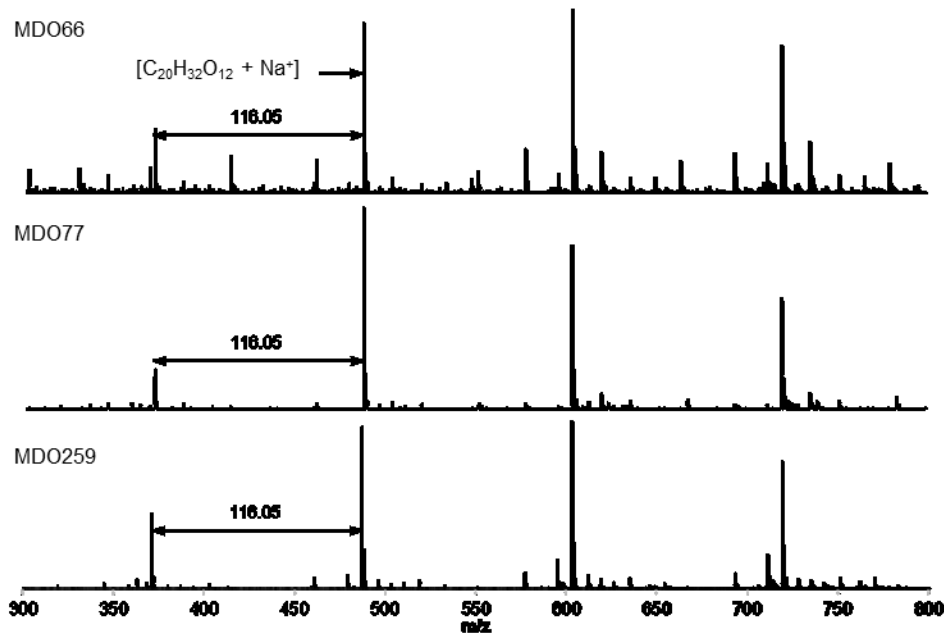
Figure 4-18: ESI-MS in 9:1 MeOH:CH$_2$Cl$_2$ for several molar masses of PMDO, with numbers in the sample names indicating the number-average degree of polymerization. As with P(3-HPA) samples, high molar mass ions were not observed, but the repeat unit is consistent with that expected for retention of the MDO monomer's acetal functionality to form PMDO. Characterization data for these polymers are summarized in Table 4-2.
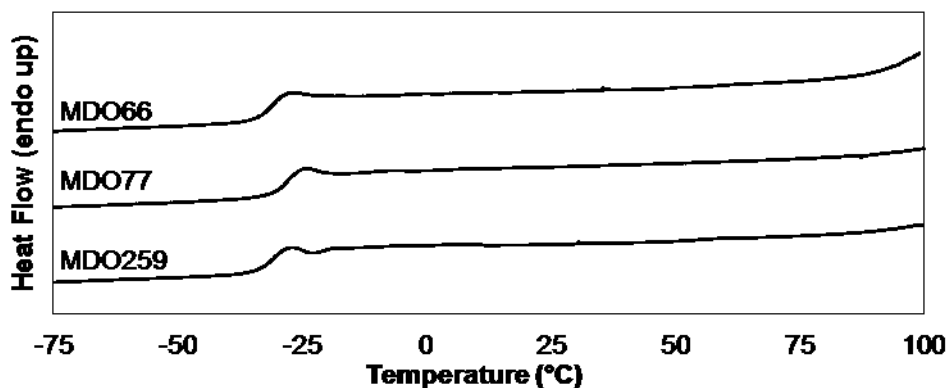
Figure 4-19: DSC thermograms for PMDO samples, with the numbers in sample names indicating the number-average degree of polymerization. Unlike P(3-HPA), no significant crystallinity was observed in PMDO samples, as evidenced by the lack of a melting endotherm. The glass transition temperature (T$_g$) for PMDO, like that of P(3-HPA) polymers, was quite low, ranging from -25.7 °C to -32.3 °C. Traces have been shifted vertically to aid visual comparison but relative peak heights and slopes have not been adjusted. Characterization data for these samples are summarized in Table 4-2.

To verify that the polymer produced at low catalyst loadings was structurally distinct from P(3-HPA), ESI-MS and DSC were again used. ESI-MS was used to determine the polymers' repeat unit (Figure 4-18), allowing identification of a repeating unit of m/z = 116.05, the expected value for a polymer retaining MDO's acetal functionality in each repeat unit. Thermal properties also departed from those observed for P(3-HPA). While glass transition temperatures remained low (T_g = -25.7 °C to -32.3 °C), no melting endotherms were observed (Figure 4-19).

The combination of diverse characterization data for this polymer (summarized in Table 4-2) indicate that by decreasing the catalyst concentration in the polymerization medium acetal functionality could be retained with minimal elimination as acetaldehyde, leading to PMDO, a chemically distinct polymer from P(3-HPA), as summarized in Figure 4-5. These characterization data are summarized for several molar masses of PMDO in Table 4-2.
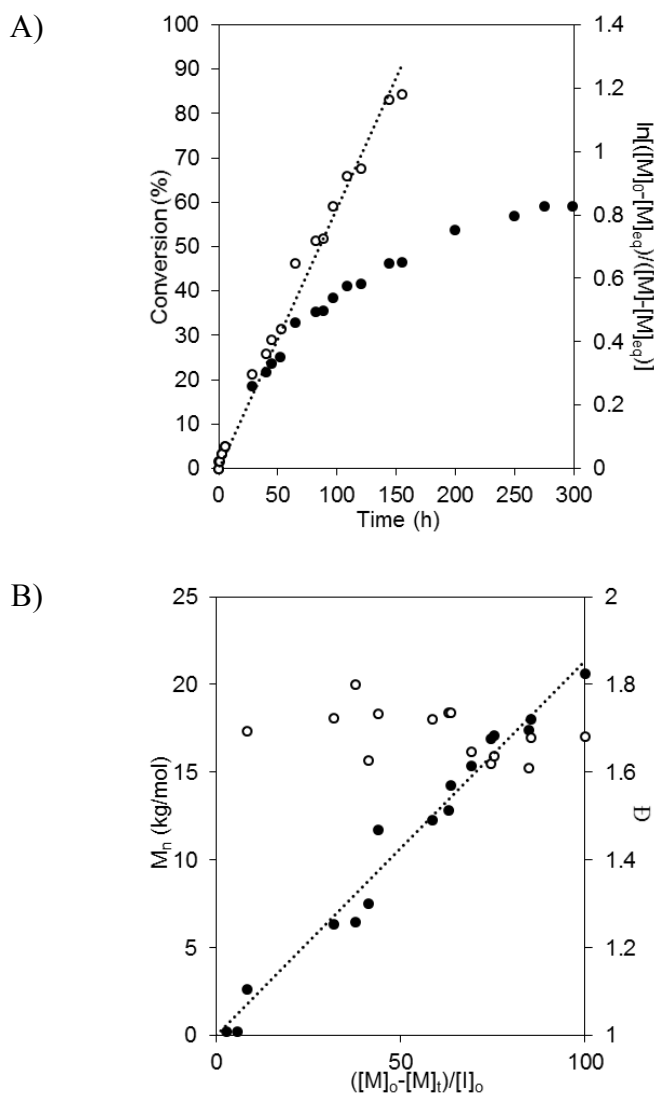
Figure 4-20: Bulk polymerization of MDO to high-acetal PMDO at low diethylzinc concentrations was monitored by analyzing ^{1}H NMR spectra and SEC elugrams of aliquots removed during the polymerization. A) Monomer conversion (●) was tracked by ^{1}H NMR spectroscopy. Results showed that MDO monomer was not fully consumed even at longer reaction times and that the reaction ceased to consume monomer beyond $[M]_t/[M]_o \approx 0.6$. The first 150 h (○, to approximately 50% monomer consumption) of the polymerization were linearized using Figure 4-15 to determine the apparent first order rate constant $k_{app} = 0.0079$ h^{-1} where $[MDO]_o = 10.1$ M, $[BnOH]_o = 49.4$ mM, and $[ZnEt_2]_o = 1.0$ mM using $[M]_{eq} = 4.53$ M at room temperature. B) Apparent molar mass (M_n, ●) and molar mass distribution (Đ, ○) were tracked by SEC. Consistent with a controlled polymerization, the relationship between monomer consumption and molar mass was linear. Polydispersity was relatively high, which may have been the result of significant depolymerization throughout the reaction due to the relatively high value of $[M]_{eq}$. No values of Đ are reported for early time points due the inherent inaccuracy of measuring this value at very low molar mass.

Kinetics of Polymerization of MDO to PMDO

Bulk polymerization of MDO at low catalyst loadings ($[BnOH]_o$ = 49.4 mM and

$[ZnEt_2]_o$ = 1.0 mM at room temperature) was tracked by removing aliquots from the

reaction and analyzing them by ^1H NMR spectroscopy and SEC. Tracking monomer

consumption by ^1H NMR spectroscopy (Figure 4-20A) revealed that in contrast to

polymerizations at higher catalyst loadings yielding P(3-HPA), polymerizations yielding

PMDO reached much lower monomer conversions (under 60%), and were much slower

(approximately 200 h to reach $[M]_t/[M]_o$ = 0.5). Using measured values of ρ_{MDO} = 1.183 g

mL^{-1} and ρ_{PMDO} = 1.421 g mL^{-1}, it was determined that at room temperature $[M]_{eq}$ = 4.53

M. Using this value of $[M]_{eq}$, the conversion data were again linearized using Figure 4-15

to determine the room temperature pseudo-first order rate constant k_{app} = 0.0079 h^{-1} under

these reaction conditions. This indicates reaction times on the order of several days are

necessary in order to attain sufficiently high conversions for most practical applications.

SEC was used to track the evolution of molar mass and polydispersity during the

polymerization (Figure 4-20B). Plotting of molar mass versus consumption of monomer

indicated the relationship was linear (R^2 = 0.968), suggesting a controlled polymerization.

However, the breadth of the molar mass distribution ($Đ$ > 1.5) exceeded the low values

observed for the polymerization of P(3-HPA) and many other controlled polymerizations.

This behavior may be the result of the relatively high value of $[M]_{eq}$ (4.53 M under these

conditions). As the concentration of monomer at any point of polymerization is not far

from the equilibrium monomer concentration (i.e. $[M]_t \gg [M]_{eq}$ is not satisfied), it is likely

that depolymerization is significant even at low monomer conversions. This may lead to

broader molar mass distributions than when polymerization is nearly irreversible, and is a

phenomenon that has been explored in previous theoretical and experimental studies.[369–373]
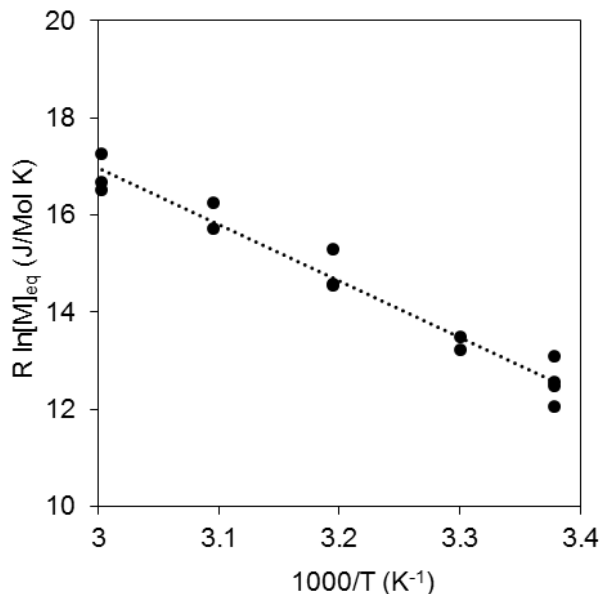
Figure 4-21: Polymerization thermodynamics for polymerization of MDO to PMDO. Parallel polymerizations were performed in the bulk using $[BnOH]_o$ = 223 mM and $[ZnEt_2]_o$ = 4.33 mM at a range of temperatures, with polymerizations allowed to proceed for at least two weeks to ensure that equilibrium had been reached before quenching at the reaction temperature. Final monomer conversions were used to calculate values of $[M]_{eq}$ at each temperature using ρ_{MDO} = 1.183 g mL^{-1} and ρ_{PMDO} = 1.421 g mL^{-1}. Using these data and Figure 4-22 (taking $[M]_s$ = 1 M) it was possible to calculate ΔH_p = -11.6 kJ mol^{-1} and ΔS_p = -51.8 J mol^{-1} K^{-1}.

$$R \ln \left(\frac{[M]_{eq}}{[M]_s} \right) = \Delta H_p \left(\frac{1}{T} \right) - \Delta S_p$$

Figure 4-22: Equation used to determine thermodynamic parameters ΔH_p and ΔS_p from equilibrium monomer concentration measurements (Figure 4-21), where $[M]_s$ was taken to be 1M.

Thermodynamics of MDO Polymerization to PMDO

To further characterize and explore the source of the limited polymerization observed in low-catalyst reactions producing PMDO, a number of polymerizations with identical starting conditions ($[MDO]_o$ = 10.1 M, $[BnOH]_o$ = 223 mM and $[ZnEt_2]_o$ = 4.33 mM) were allowed to reach equilibrium over at least two weeks at a variety of temperatures and quenched at the polymerization temperature. By using ^1H NMR spectroscopy to measure the amount of remaining monomer at each of these temperatures and using measured values of ρ_{MDO} = 1.183 g mL^{-1} and ρ_{PMDO} = 1.421 g mL^{-1}, a linear fit to Figure 4-22 was used to determine that the thermodynamic parameters for this polymerization were ΔH_p = -11.6 kJ mol^{-1} and ΔS_p = -51.8 J mol^{-1} K^{-1} (Figure 4-21). Using these thermodynamic parameters and the density of MDO, the theoretical ceiling temperature for neat monomer was calculated to be 90.6 °C.[341] The enthalpic component was consistent with similar measurements of other six-membered lactones with similar chemical structure, such as δ-valerolactone (-8.4 to -10.5 kJ mol^{-1}), and δ-caprolactone (-13.8 kJ mol^{-1}),[374] though less than that observed for δ-decalactone (-17.1 kJ mol^{-1}).[375] In contrast, the entropic component, while unfavorable as expected, was more significant than most of these similar molecules. At -51.8 J mol^{-1} K^{-1} it was more unfavorable than δ-valerolactone (-14.7 to -15.0 J mol^{-1} K^{-1}), and δ-caprolactone (-41.2 J mol^{-1} K^{-1}),[374] and was closer to that observed for δ-decalactone (-54 J mol^{-1} K^{-1}).
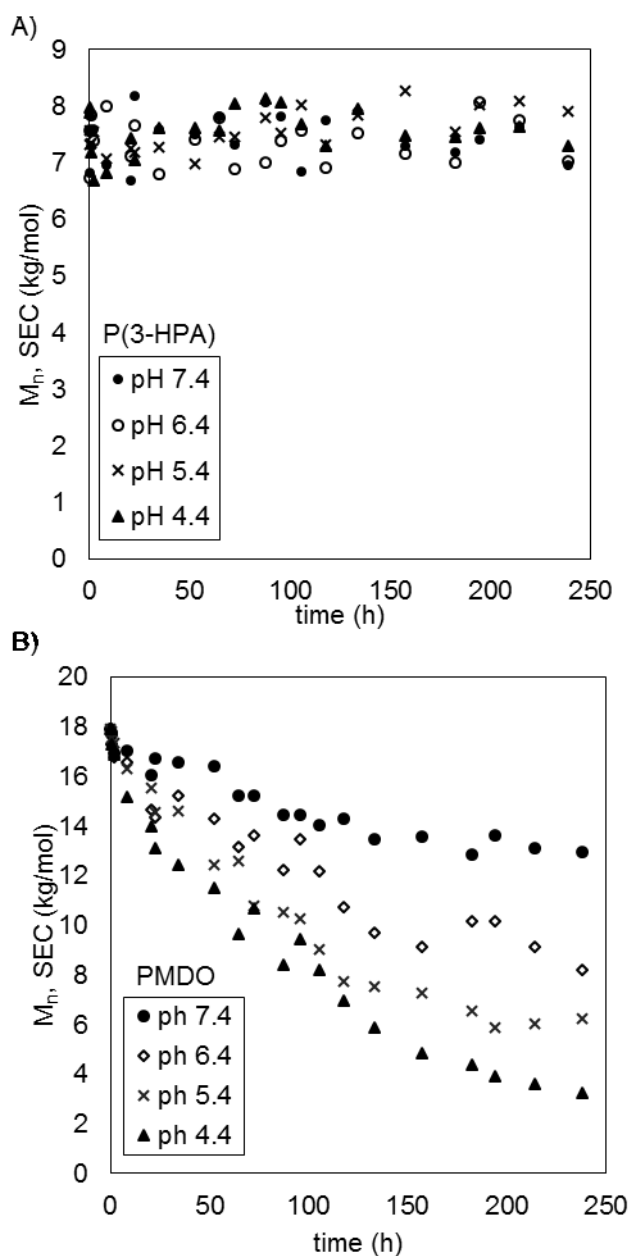
Figure 4-23: Degradation of polymers as a function of pH. Both A) P(3-HPA) and B) PMDO were subjected to degradation at room temperature in a 100 mM phosphate-citrate buffer at pH 7.4, 6.4, 5.4 and 4.4. Samples were periodically lyophilized and analyzed by SEC to determine changes in molar mass. In P(3-HPA), which lacks the acetal linkage, little degradation occurred even at low pH. In PMDO, where acetal linkages were preserved during polymerization, degradation was observed at all pH values, with an increase in degradation rates as the pH decreased.

Degradation

Having characterized the syntheses of P(3-HPA) and PMDO, it was essential to determine the degradation characteristics of these polymers to assess their susceptibility to degradation under conditions relevant for drug delivery applications. Samples of PMDO, with initial SEC apparent molar mass of 17.9 kg mol^{-1}, and P(3-HPA), with initial SEC apparent molar mass of 8.1 kg mol^{-1}, were subjected to treatment with a 100 mM phosphate-citrate buffer at pH 7.4, 6.4, 5.4, and 4.4. Degradation was tracked using the apparent molar mass from SEC elugrams of samples taken during the experiment (Figure 4-23). In the P(3-HPA) system, little degradation was observed at any pH. This lack of degradation may be due to a combination of the crystallinity present in the polymer and its relative hydrophobicity. These results are consistent with previous work using PMCL,[328] which under comparable conditions did not degrade appreciably over several weeks. They are also consistent with experiments performed using homopolymers and block copolymers of polylactide and polymenthide,[376] which degraded substantially over a time scale of weeks to months, but showed little hydrolysis over the much shorter 10 day time span monitored here. In contrast, PMDO experienced significant degradation at all pH levels. PMDO degradation was considerably faster at lower pH, with apparent molar mass decreasing six fold over 240 h at pH 4. This result is faster than that observed for the polyesters mentioned above, and broadly consistent with the relative rates of degradation observed in the past for other systems incorporating acetal linkages.[343] Degradation was, as expected, slower than that observed for the more hydrolytically-sensitive ketals.[335,345]

4.3   Conclusions

A key attribute for effective targeted drug delivery is triggered release of the payload from the carrier upon reaching the target site. In targeted cancer therapy, low pH is a particularly appealing trigger for release due to the combination of subphysiological pH within tumors and a further, pronounced increase in acidity experienced by the carrier following cellular uptake into the endosome. Our previous efforts to induce pH-triggered release from polymeric carriers with simple polyester backbones were limited by negligible degradation at physiologically-relevant low pH conditions. This prompted the current investigation of integrating the more acid-labile acetal linkage into the polyester backbone.

To make a polymer containing an acetal group, the MDO monomer was used, and a new synthetic route to this acetal-containing cyclic ester was developed and characterized. Several approaches to polymerize this monomer were investigated, leading to reproducible and controlled bulk polymerizations using diethylzinc as a catalyst. By varying the amount of this catalyst present in the system, it was possible to generate two distinct polymers. At high catalyst concentrations, nearly all acetal functionality was expelled as volatile acetaldehyde to form slow-degrading P(3-HPA) by a novel route. At low catalyst concentrations, nearly all of the acetal linkages were retained to form the new acid-sensitive polymer PMDO.

Development of PMDO represents a step towards new, more pH responsive drug delivery vehicles. While this particular system is limited by unfavorable thermodynamics and slow polymerization kinetics, the synthetic approaches employed to synthesize PMDO are amenable to synthesis of analogous monomers and polymers that could address some

of the practical shortcomings of this system while maintaining the advantages of this new acid-sensitive polymer.

4.4 Experimental

Materials and Analysis

All chemicals were obtained from Sigma-Aldrich (St. Louis, MO) and used as received unless otherwise noted. ^{1}H, ^{13}C, and COSY NMR spectra were obtained at room temperature on a Varian VAC-300 spectrometer in CDCl$_3$ at 300 MHz for ^{1}H and COSY NMR spectra and 75 MHz for ^{13}C NMR spectra. Reported chemical shifts were referenced to CHCl$_3$ at 7.26 ppm for ^{1}H NMR spectra and 77.23 ppm for ^{13}C NMR spectra. Integrations of ^{1}H NMR data are referenced to initiator BnOH methylene protons at 5.10 ppm. Elemental Analysis of MDO was performed by Atlantic Microlab (Norcross, GA). DSC was performed using a TA Instruments Q2000 at a scanning rate of 5 °C min^{-1}. DSC data analysis was performed using TA Instruments TRIOS software and utilizing the second heating curve. ESI-MS data were acquired using a Bruker BioTOF instrument with samples dissolved at approximately 0.05 mg mL^{-1} in 9:1 MeOH:CH$_2$Cl$_2$ and data were analyzed using Bruker DataAnalysis software with masses calibrated using poly(propylene glycol) standards. PMDO samples were analyzed by SEC using an Agilent 1260 series chromatograph (THF, 35 °C, 1 mL min^{-1}) with three Styragel columns and equipped with a Wyatt Dawn Heleos-II LS light scattering detector and Optilab T-rEX RI detector, the latter of which was used for analysis. SEC for P(3-HPA) samples was performed using a Hewlett-Packard series 1100 liquid chromatography system (CHCl$_3$, 35 °C, 1 mL min^{-1}), equipped with a Hewlett-Packard 1047A RI detector and three PLgel 5 μm MIXED-C

columns. Significant peak broadening occurred during SEC for PMDO in CHCl$_3$ and for

P(3-HPA) in THF, even at high dilutions. As a result, SEC of PMDO used THF and SEC

of P(3-HPA) used CHCl$_3$. In both cases, apparent molar masses were reported versus

polystyrene standards (Polymer Laboratories).

Synthesis of 2-methyl-1,3-dioxan-4-one (MDO)

MDO was prepared by Baeyer-Villiger oxidation of racemic 2-methyltetrahydrofuran-

3-one (Sigma FG ≥ 97%) using mCPBA in CH$_2$Cl$_2$ following analogous procedures to

those used previously to introduce ester functionality to a range of

monomers.[194,252,353,377,378] Reactions were performed with a 1.3-fold molar excess of

mCPBA relative to 2-methyltetrahydrofuran-3-one at approximately 10 w/v % in CH$_2$Cl$_2$.

To minimize MDO hydrolysis by water present in mCPBA, after dissolution into CH$_2$Cl$_2$

the mCPBA solution was dried over MgSO$_4$, which was then removed by filtration. The

solvent-mCPBA mixture was cooled to 0 °C in an ice bath and 2-methyltetrahydrofuran-

3-one was added dropwise over 45 min while vigorously stirring. The solution was allowed

to warm to room temperature over 3–4 h. The precipitated *meta*-chlorobenzoic acid

(mCBA) byproduct was removed by filtration, the volume of solvent was reduced using

rotary evaporation and mCBA again removed by filtration. The mixture was then cooled

in a dry ice/acetone bath and mCBA filtered again. Cooling and filtration was repeated

until no further precipitate formed during cooling. The solution was then washed twice

with saturated sodium bicarbonate, once with brine, and stirred over MgSO$_4$. It should be

noted that complete neutralization of reaction mixture with sodium bicarbonate solution

was essential to avoid excessive hydrolysis of the monomer with commensurate losses to

reaction yield. CH$_2$Cl$_2$ was removed using a rotary evaporator and the resulting crude oil

was dried with calcium hydride and distilled (44 °C at 400 mTorr) to give racemic MDO

in 40–60% overall yield. The monomer was stored under nitrogen in the glove box at –23

°C, where it solidified. ^{1}H NMR (CDCl$_3$): δ 5.43 (q, 1H, -O-C*H*(CH$_3$)-O-), 4.22 (ddd, 1H,

–C(O)-CH$_2$- C*H*$_2$-O-), 3.94 (ddd, 1H, –C(O)-CH$_2$-C*H*$_2$-O-), 2.81 (ddd, 1H, –C(O)-C*H*$_2$-

CH$_2$-O-), 2.61 (ddd, 1H, –C(O)-C*H*$_2$-CH$_2$-O-), 1.52 (d, 3H, -O-CH(C*H*$_3$)-O-). ^{13}C NMR

(CDCl$_3$): δ 167.35, 101.08, 63.23, 29.84, 21.02. Elemental Analysis: calculated: C:

51.72%, H 6.94%. Experimental: C: 51.92%, H 7.07%. T_m = 10.8 °C by DSC.

Initial MDO Polymerization Efforts

Polymerization of MDO was first attempted using poly(ethylene oxide) (PEO)

methyl ether (M_n = 2 kg mol^{-1}) as a macroinitiator and employing several common catalyst

systems. Polymerizations were conducted under nitrogen in a dry box using flame-dried

pressure vessels with Teflon stir bars and were sealed prior to removal from the box. In all

cases, PEO was dried by heating the polymer to 80 °C under vacuum for at least 18 h prior

to polymerizations. Polymerizations included MDO at a molar excess of 200:1 with respect

to macroinitiator hydroxyl end groups ([PEO]$_o$ = 85 mg per 1 g MDO).

For reactions using tin octoate as the catalyst, conditions for bulk polymerization

mimicked those used for polymerization of PEO-PMCL and VS-PEO-PMCL, though two

reaction temperatures were investigated ([SnOct$_2$]$_o$ ≈ 10 mM, T_{polym} = 110 °C and 60 °C,

t_{polym} = 1 h or 8 h). SEC elugrams for these polymerizations can be seen in Figure 4-7.

For polymerizations with TEA as the catalyst, solution polymerization conditions

similar to those used by others for PEO-PMCL[194] were used ([M]$_o$ ≈ 1.5 M, T_{polym} = 60 °C

in both THF and CH$_2$Cl$_2$, t_{polym} = 1 h) and two concentrations of TEA (added from 1 M

stock in hexanes) with respect to PEO macroinitiator were used ($[TEA]_0/[PEO]_0 = 1.1$ and

$[TEA]_0/[PEO]_0 = 2.2$). SEC elugrams for these polymerizations can be seen in Figure 4-8.

Polymerization in the bulk using the organocatalyst triazabicyclodecene (TBD) was

also investigated. Conditions were analogous to those used for bulk polymerization of δ-

decalactone ($[TBD]_0 = 30$ mM),[375] but performed at room temperature. The SEC traces of

these polymerizations can be seen in Figure 4-9.
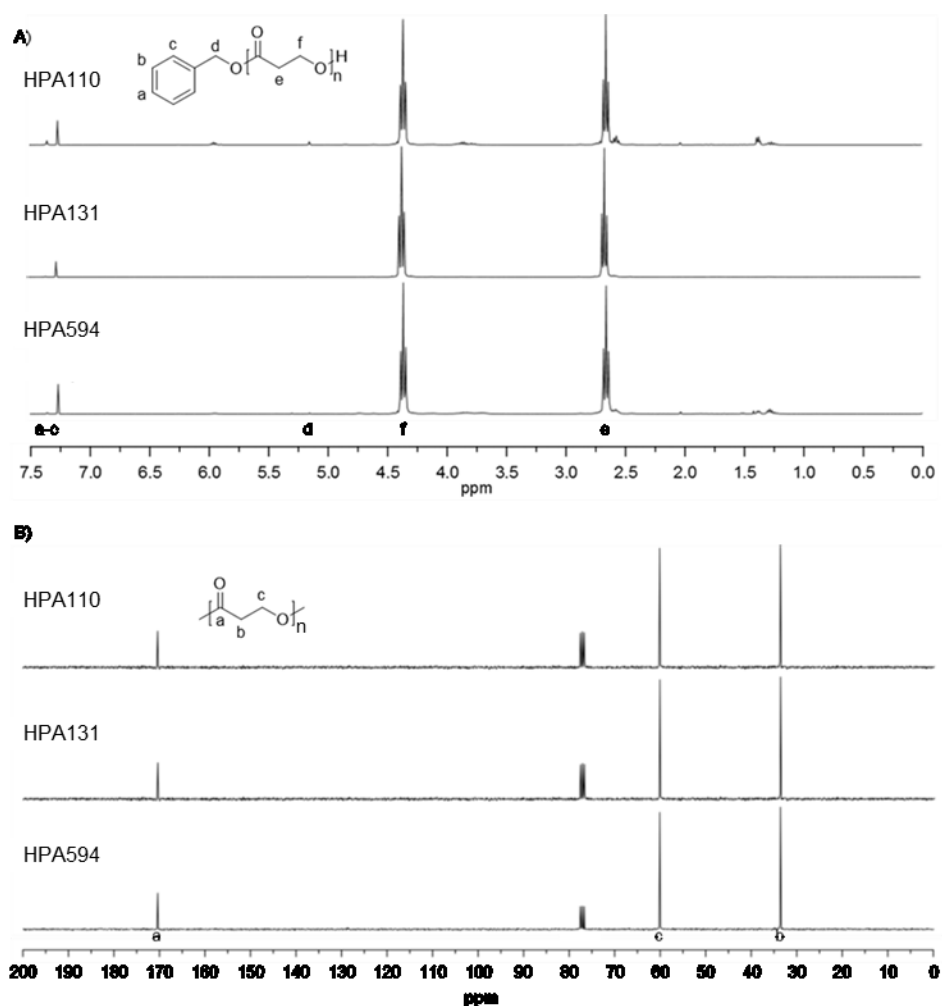
Figure 4-24: NMR spectra and structural assignments for several molar masses of P(3-HPA) synthesized by diethylzinc-catalyzed polymerization of MDO from benzyl alcohol with peak assignments for A) ^{1}H and B) ^{13}C spectra. Numbers in the sample names indicate the number-average degree of polymerization and characterization data for these polymers are summarized in Table 4-1.
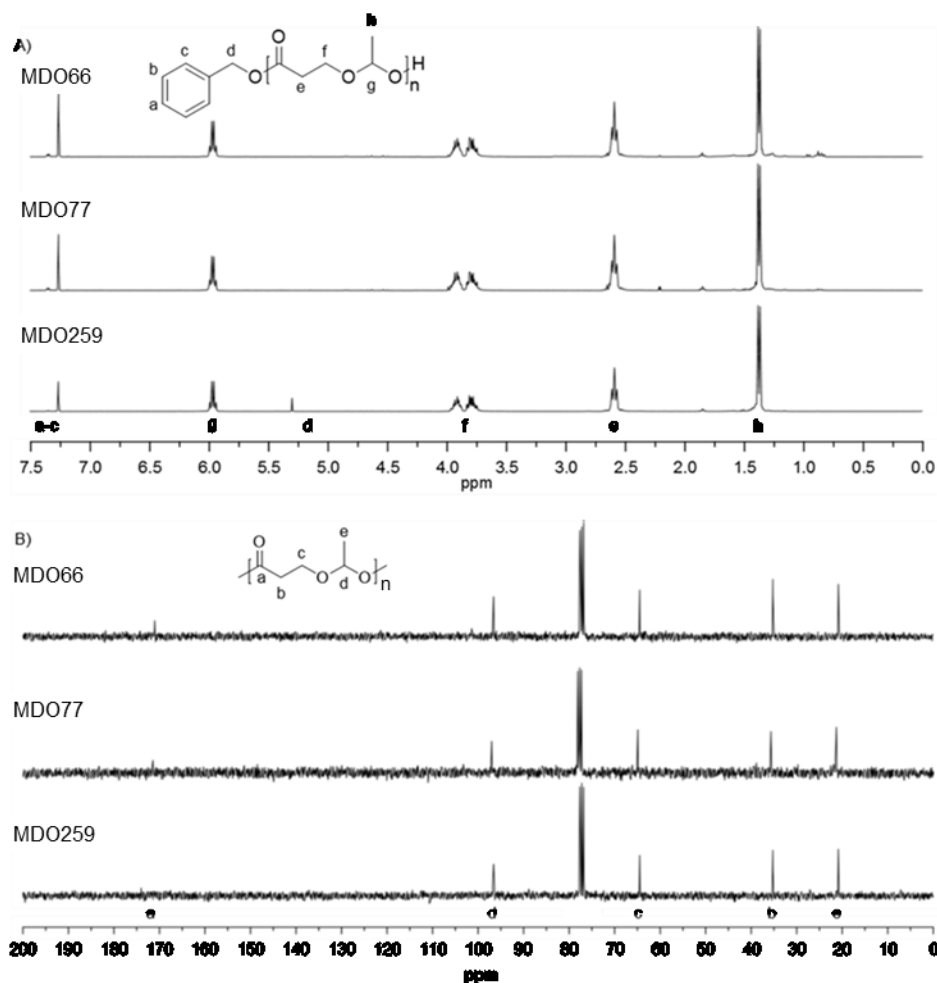
Figure 4-25: Spectroscopic characterization of PMDO samples and peak assignments for A) ^{1}H and B) ^{13}C spectra. The number in sample names refers to the number-average degree of polymerization. Characterization data for these polymers are summarized in Table 4-2.

Synthesis of Polymers Using Diethylzinc

Polymerizations using diethylzinc catalyst for ROTEP of MDO were set up in a dry box using flame-dried glassware with a Teflon stir bar and were sealed prior to removal from the box. For a typical polymerization, the appropriate amount of racemic MDO monomer (generally 1.5 g) was added to the reaction vessel. An appropriate amount of benzyl alcohol initiator was added to target the desired molar mass, using an ultimate conversion of 55% for PMDO and 80% for P(3-HPA) for calculations. Diethylzinc catalyst

(1.0 M in hexanes), typically using $[C]_o:[I]_o = 0.02:1$ for high-acetal PMDO and $[C]_o:[I]_o$ = 2:1 for low-acetal P(3-HPA), was then added to the reaction mixture by microsyringe and allowed to mix thoroughly. The reaction vessels were sealed and allowed to react while stirring at room temperature. While still in the glove box, periodic samples were taken for analysis by SEC and ^{1}H NMR spectroscopy. To isolate polymers, reaction vessels were opened to air, halting the reaction, and the reaction mixture was dissolved completely in CH_2Cl_2. Polymers were then precipitated by dropwise addition of the dissolved reaction mixture into 9:1 hexanes:THF, and dried under vacuum. For P(3-HPA) (given degree of polymerization = 100): ^{1}H NMR ($CDCl_3$): δ 7.31 (m, 0.05H, Ph-CH$_2$-O-), 5.10 (s, 0.02H, Ph-CH_2-O-), 4.35 (t, 2H, –C(O)-CH_2-CH$_2$-O-), 2.65 (t, 2H, –C(O)-CH$_2$-CH_2-O-). ^{13}C NMR ($CDCl_3$): δ 170.45, 60.25, 33.76. For PMDO (given degree of polymerization = 100): ^{1}H NMR ($CDCl_3$): δ 7.31 (m, 0.05H, Ph-CH$_2$-O-), 5.92 (q, 1H, -O-CH(CH$_3$)-O-), 5.10 (s, 0.02H, Ph-CH_2-O-), 3.88 (m, 1H, –C(O)-CH$_2$-CH_2-O-), 3.76 (m, 1H, –C(O)-CH$_2$-CH_2-O-), 2.57 (m, 2H, –C(O)-CH_2-CH$_2$-O-), 1.33 (d, 3H, -O-CH(CH_3)-O-). ^{13}C NMR ($CDCl_3$): δ 171.04, 96.59, 64.50, 32.23, 20.84.

To monitor byproduct formation, a polymerization was performed in solution using CD_2Cl_2 which had been dried for 18 h by stirring over 3 Å molecular sieves and degrassed by three freeze-pump-thaw cycles before being brought into the glove box. The solvent (750 μL) was added to a flame-dried round-bottom flask containing a Teflon-coated stir bar. MDO was then added (to [MDO] = 1 M) followed by benzyl alcohol (to [BnOH] = 10 mM). After stirring for 10 min, diethylzinc was added (1 M in hexanes, to [ZnEt$_2$] = 20 mM). This solution was allowed to mix for 5 minutes, then loaded into a throughly dried

NMR tube and sealed while still in the glove box. Over the next several hours, ^{1}H spectra of the reaction were periodically collected and used to monitor polymerization and byproducts as described in the main text.

Density Measurements

The density of MDO was measured by determining the mass of known volumes of the monomer dispensed by a calibrated micropipette. Nine separate measurements were taken to determine $\rho_{MDO} = 1.183 \pm 0.018$ g mL^{-1}. To measure the density of PMDO, a volumetric flask with a fritted glass cap was filled with cyclohexane, a poor solvent for PMDO. The flask was capped, any bubbles excluded, and excess cyclohexane allowed to evaporate until mass measurements stabilized for 30 s, then the mass of cyclohexane and flask was recorded. A known mass of PMDO was then added to the flask and the vessel was again capped, which displaced a volume of cyclohexane. This cyclohexane was wiped off, and the solvent residue was allowed to evaporate until the mass had again stabilized for 30 s. The mass of the flask, the remaining cyclohexane and the added polymer was then measured. The volume of the excluded cyclohexane and the density of the polymer were calculated using $\rho_{CHX} = 0.7781$ g mL^{-1} and the known mass of the added polymer. This measurement was performed four independent times (n=4) to determine that the density of PMDO at room temperature was 1.421 ± 0.072 g mL^{-1}. For calculations involving the density of P(3-HPA), the room temperature density of the polymer was taken to be 1.38 g mL^{-1} based on literature values.[361]

Thermodynamic Characterization

To explore the source of the limited conversion observed for PMDO, a series of experiments were conducted to measure equilibrium monomer conversions of identical reaction mixtures at a variety of temperatures. In a sample reaction, in a glove box under nitrogen, 1 g (8.62 mmol) of MDO was combined with 8.9 μL of (89 μmol) benzyl alcohol and allowed to mix thoroughly for approximately 10 minutes. 1.7 μL of ZnEt$_2$ (1 M in hexanes, 1.7 μmol) was then added and allowed to mix for an additional 10 minutes. The reaction was then split into four separate reaction vessels, each of which was sealed. These were brought to temperatures ranging from 23 °C to 60 °C and stirred by magnetic stir bar for 14 days. The vessels were opened to air, the reaction mixture dissolved in CDCl$_3$, and the fraction of remaining monomer determined using ^{1}H NMR spectroscopy. From these experiments, [M]$_{eq}$ values for a given temperature were calculated using ρ_{MDO} = 1.183 g mL^{-1} and ρ_{PMDO} = 1.421 g mL^{-1}. Values of [M]$_{eq}$ for each temperature were measured in at least three separate experiments. Integrations used to determine monomer conversion in ^{1}H NMR spectra (methylene protons from MDO at δ = 4.22 ppm and PMDO at δ = 3.76 ppm as well as methyl protons from MDO at 1.52 ppm, and PMDO at 1.33 ppm) did not change appreciably over several days, suggesting depolymerization was not a significant factor after opening to air and dilution.

As a control experiment to determine if the value of [M]$_{eq}$ would shift reversibly with temperature, a polymerization was set up as described for the above equilibrium experiments but not initially split into separate reaction vessels. This reaction was allowed to react at 40 °C for 7 days. An aliquot taken from the reaction at this point showed that 43% of MDO had been converted to PMDO over 7 days ([M] = 6.3 M). In a glove box, the

viscous liquid was split into two vessels which were each sealed and allowed to react for an additional 14 days, one at room temperature and one at 60 °C. The vessels were then opened, the reaction mixture dissolved in CDCl$_3$, and conversion measured by ^{1}H NMR spectroscopy, from which values of [M] were determined using experimentally measured densities of MDO and PMDO. The conversion of the room temperature reaction reached 58% ([M] = 4.7 M) while the polymerization at 60 °C reached 33% ([M] = 7.2 M). These values were consistent with [M]$_{eq}$ values measured in samples heated directly to these temperatures (Figure 4-21), and indicated that equilibrium monomer concentration could, as expected for an equilibrium process, be reversibly shifted by a change in temperature.

Catalyst Activity

To verify the diethylzinc catalyst was not deactivated after extended time periods, a bulk polymerization was set up using 1 g of MDO under conditions previously observed to result in high-acetal PMDO ([ZnEt$_2$]$_o$ = 2.3 mM, [BnOH]$_o$ = 100.5 mM). The reaction was sealed and allowed to proceed for 21 days at room temperature. An aliquot of the viscous liquid was taken and found to have conversion (by ^{1}H NMR spectroscopy) of approximately 58% (degree of polymerization 58, apparent molar mass 4.5 kg mol^{-1} by SEC), near the result observed in similar kinetics studies (Figure 4-20). The liquid was then divided in two under nitrogen and monomer (approximately 0.5 g) added to one portion. Both portions were sealed and allowed to react while mixing for an additional 5 days at room temperature before being opened to air. The sample with no additional monomer maintained the same conversion of MDO at 21 days and had an apparent molar mass of 4.6 kg mol^{-1} by SEC. The sample with additional monomer had an increased degree of polymerization (74 by ^{1}H NMR spectroscopy) and its apparent molar mass by SEC had

increased to 11.0 kg mol^{-1}. This increase in molar mass showed that the catalyst remained active for polymerization even after weeks in the reaction medium.

5 Bibliography

(1)   Ehrlich, P. *Münch. Med. Wschr.* **1901**, *18*, 2123.

(2)   Winau, F.; Westphal, O.; Winau, R. *Microbes and Infection* **2004**, *6*, 786–789.

(3)   Majer, M.; Akerley, W.; Kuwada, S. K. *Anti-Cancer Agents in Medicinal Chemistry* **2007**, *7*, 492–503.

(4)   Greene, F. L.; Page, D. L.; Fleming, G. F. AJCC Cancer Staging Manual **2002**.

(5)   Sabin, L. H.; Wittekind, C. *UICC: TNM Classification of Malignant Tumours*; 6th ed.; Jogn Wiley and Sons: London, 2002.

(6)   Greene, F. L. M. D.; Stewart, A. K. M. A.; Norton, H. J. P. *Annals of Surgery* **2002**, *236*, 416–421.

(7)   Andre, N.; Schmiegel, W. *Gut* **2005**, *54*, 1194–1202.

(8)   Gill, S.; Loprinzi, C. L.; Sargent, D. J.; Thome, S. D.; Alberts, S. R.; Haller, D. G.; Benedetti, J.; Francini, G.; Shepherd, L. E.; Francois Seitz, J.; Labianca, R.; Chen, W.; Cha, S. S.; Heldebrant, M. P.; Goldberg, R. M. *J Clin Oncol* **2004**, *22*, 1797–1806.

(9)   Graham, J.; Muhsin, M.; Kirkpatrick, P. *Nat Rev Drug Discov* **2004**, *3*, 11–12.

(10)   Barabas, K.; Milner, R.; Lurie, D.; Adin, C. *Veterinary and Comparative Oncology* **2008**, *6*, 1–18.

(11)   Stewart, D. J.; Benjamin, R. S.; Luna, M.; Feun, L.; Caprioli, R.; Seifert, W.; Loo, T. L. *Cancer Chemotherapy and Pharmacology* **1982**, *10*, 51–54.

(12)   Siddik, Z. H. *Oncogene* **2003**, *22*, 7265–7279.

(13)   Iyer, L.; Ratain, M. J. *Cancer Chemotherapy and Pharmacology* **1998**, *42*, S31–S43.

(14)   Baselga, J. *Oncologist* **2002**, *7*, 2–8.

(15)   Kabbinavar, F.; Hurwitz, H. I.; Fehrenbacher, L.; Meropol, N. J.; Novotny, W. F.; Lieberman, G.; Griffing, S.; Bergsland, E. *J Clin Oncol* **2003**, *21*, 60–65.

(16) Adam, R.; Avisar, E.; Ariche, A.; Giachetti, S.; Azoulay, D.; Castaing, D.; Kunstlinger, F.; Levi, F.; Bismuth, F. *Annals of Surgical Oncology* **2001**, *8*, 347–353.

(17) Ki Young, C.; Saltz, L. B. *Cancer Journal* **2007**, *13*, 192–197.

(18) Saltz, L. B.; Douillard, J.-Y.; Pirotta, N.; Alakl, M.; Gruia, G.; Awad, L.; Elfring, G. L.; Locker, P. K.; Miller, L. L. *Oncologist* **2001**, *6*, 81–91.

(19) Levis, M.; Pham, R.; Smith, B. D.; Small, D. *Blood* **2004**, *104* , 1145–1150.

(20) Soriano, A. F.; Helfrich, B.; Chan, D. C.; Heasley, L. E.; Bunn, P. A.; Chou, T.-C. *Cancer Research* **1999**, *59* , 6178–6184.

(21) Partridge, A. H.; Winer, E. P. *Breast Disease* **2004**, *21*, 55–64.

(22) Matsumura, Y.; Maeda, H. *Cancer Res* **1986**, *46*, 6387–6392.

(23) Meng, F.; Zhong, Z.; Feijen, J. *Biomacromolecules* **2009**, *10*, 197–209.

(24) Ganta, S.; Devalapally, H.; Shahiwala, A.; Amiji, M. *Journal of Controlled Release* **2008**, *126*, 187–204.

(25) Noguchi, Y.; Wu, J.; Duncan, R.; Strohalm, J.; Ulbrich, K.; Akaike, T.; Maeda, H. *Cancer Science* **1998**, *89*, 307–314.

(26) Van Vlerken, L. E.; Duan, Z.; Seiden, M. V; Amiji, M. M. *Cancer Res* **2007**, *67*, 4843–4850.

(27) Hobbs, S. K.; Monsky, W. L.; Yuan, F.; Roberts, W. G.; Griffith, L.; Torchilin, V. P.; Jain, R. K. *Proceedings of the National Academy of Sciences of the United States of America* **1998**, *95*, 4607–4612.

(28) Yuan, F.; Dellian, M.; Fukumura, D.; Leunig, M.; Berk, D. A.; Torchilin, V. P.; Jain, R. K. *Cancer Res* **1995**, *55*, 3752–3756.

(29) Unezaki, S.; Maruyama, K.; Hosoda, J.-I.; Nagae, I.; Koyanagi, Y.; Nakata, M.; Ishida, O.; Iwatsuru, M.; Tsuchiya, S. *International Journal of Pharmaceutics* **1996**, *144*, 11–17.

(30) Skinner, S. A.; Tutton, P. J. M.; O'Brien, P. E. *Cancer Res* **1990**, *50*, 2411–2417.

(31) Iyer, A. K.; Khaled, G.; Fang, J.; Maeda, H. *Drug Discovery Today* **2006**, *11*, 812–818.

(32)   Moghimi, S. M.; Hunter, A. C.; Murray, J. C. *Pharmacol Rev* **2001**, *53*, 283–318.

(33)   Wisse, E.; Braet, F.; Dianzhong Luo; De Zanger, R.; Jans, D.; Crabbe, E.; Vermoesen, A. N. *Toxicologic Pathology* **1996**, *24* , 100–111.

(34)   Takakura, Y.; Mahato, R. I.; Hashida, M. *Advanced Drug Delivery Reviews* **1998**, *34*, 93–108.

(35)   Sonavane, G.; Tomoda, K.; Makino, K. *Colloids and Surfaces B: Biointerfaces* **2008**, *66*, 274–280.

(36)   Cho, K.; Wang, X.; Nie, S.; Chen, Z.; Shin, D. M. *Clinical Cancer Research* **2008**, *14*, 1310–1316.

(37)   Seymour, L. W. *Critical Reviews in Therapeutic Drug Carrier Systems* **1992**, *9*, 135–187.

(38)   Torzilli, P. A.; Arduino, J. M.; Gregory, J. D.; Bansal, M. *Journal of Biomechanics* **1997**, *30*, 895–902.

(39)   Conhaim, R. L.; Eaton, A.; Staub, N. C.; Heath, T. D. *Journal of Applied Physiology* **1988**, *64* , 1134–1142.

(40)   Nakaoka, R.; Tabata, Y.; Yamaoka, T.; Ikada, Y. *Journal of Controlled Release* **1997**, *46*, 253–261.

(41)   Moghimi, S. M. *Advanced Drug Delivery Reviews* **1995**, *17*, 103–115.

(42)   Moghimi, S. M. *Advanced Drug Delivery Reviews* **1995**, *17*, 61–73.

(43)   Caliceti, P.; Veronese, F. M. *Advanced Drug Delivery Reviews* **2003**, *55*, 1261–1277.

(44)   Rothenfluh, D. A.; Bermudez, H.; O/'Neil, C. P.; Hubbell, J. A. *Nat Mater* **2008**, *7*, 248–254.

(45)   Liu, D.; Mori, A.; Huang, L. *Biochimica et Biophysica Acta - Biomembranes* **1992**, *1104*, 95–101.

(46)   Arfors, K. E.; Rutili, G.; Svensjo, E. *Acta Physiologica Scandanavica* **1979**, *463*, 93–103.

(47)   Gaumet, M.; Vargas, A.; Gurny, R.; Delie, F. *European Journal of Pharmaceutics and Biopharmaceutics* **2008**, *69*, 1–9.

(48) Storm, G.; Belliot, S. O.; Daemen, T.; Lasic, D. D. *Advanced Drug Delivery Reviews* **1995**, *17*, 31–48.

(49) Göppert, T. M.; Müller, R. H. *European Journal of Pharmaceutics and Biopharmaceutics* **2005**, *60*, 361–372.

(50) Vonarbourg, A.; Passirani, C.; Saulnier, P.; Benoit, J.-P. *Biomaterials* **2006**, *27*, 4356–4373.

(51) Moghimi, S. M.; Hedeman, H.; Muir, I. S.; Illum, L.; Davis, S. S. *Biochimica et Biophysica Acta (BBA) - General Subjects* **1993**, *1157*, 233–240.

(52) Owens III, D. E.; Peppas, N. A. *International Journal of Pharmaceutics* **2006**, *307*, 93–102.

(53) Li, S.-D.; Huang, L. *Molecular Pharmaceutics* **2008**, *5*, 496–504.

(54) Chanan-Khan, A.; Szebeni, J.; Savay, S.; Liebes, L.; Rafique, N. M.; Alving, C. R.; Muggia, F. M. *Ann Oncol* **2003**, *14*, 1430–1437.

(55) Dobrovolskaia, M. A.; Aggarwal, P.; Hall, J. B.; McNeil, S. E. *Molecular Pharmaceutics* **2008**, *5*, 487–495.

(56) Reddy, S. T.; Van der Vlies, A. J.; Simeoni, E.; Angeli, V.; Randolph, G. J.; O'Neil, C. P.; Lee, L. K.; Swartz, M. A.; Hubbell, J. A. *Nat Biotech* **2007**, *25*, 1159–1164.

(57) Nagayama, S.; Ogawara, K.; Fukuoka, Y.; Higaki, K.; Kimura, T. *International Journal of Pharmaceutics* **2007**, *342*, 215–221.

(58) Bartlett, D. W.; Davis, M. E. *Bioconjugate Chem.* **2007**, *18*, 456–468.

(59) Stolnik, S.; Illum, L.; Davis, S. S. *Advanced Drug Delivery Reviews* **1995**, *16*, 195–214.

(60) Claesson, P. M.; Blomberg, E.; Fröberg, J. C.; Nylander, T.; Arnebrant, T. *Advances in Colloid and Interface Science* **1995**, *57*, 161–227.

(61) Leckband, D.; Israelachvili, J. *Quarterly Reviews of Biophysics* **2001**, *34*, 105–267.

(62) Chonn, A.; Semple, S. C.; Cullis, P. R. *Journal of Biological Chemistry* **1992**, *267*, 18759–18765.

(63)   Juliano, R. L.; Stamp, D. *Biochemical and Biophysical Research Communications* **1975**, *63*, 651–658.

(64)   Devine, D. V; Wong, K.; Serrano, K.; Chonn, A.; Cullis, P. R. *Biochimica et Biophysica Acta (BBA) - Biomembranes* **1994**, *1191*, 43–51.

(65)   Macritchie, F. *Journal of Colloid and Interface Science* **1972**, *38*, 484–488.

(66)   Jeon, S. I.; Lee, J. H.; Andrade, J. D.; De Gennes, P. G. *Journal of Colloid and Interface Science* **1991**, *142*, 149–158.

(67)   L., P. K.; M., W. G.; Prime, K. L.; Whitesides, G. M. *J. Am. Chem. Soc.* **1993**, *115*, 10714.

(68)   Van Vlerken, L.; Vyas, T.; Amiji, M. *Pharmaceutical Research* **2007**, *24*, 1405–1414.

(69)   Alexis, F.; Pridgen, E.; Molnar, L. K.; Farokhzad, O. C. *Molecular Pharmaceutics* **2008**, *5*, 505–515.

(70)   Gabizon, A.; Catane, R.; Uziely, B.; Kaufman, B.; Safra, T.; Cohen, R.; Martin, F.; Huang, A.; Barenholz, Y. *Cancer Research* **1994**, *54*, 987–992.

(71)   Gabizon, A.; Shmeeda, H.; Barenholz, Y. *Clinical Pharmacokinetics* **2003**, *42*.

(72)   Vonarbourg, A.; Passirani, C.; Saulnier, P.; Simard, P.; Leroux, J. C.; Benoit, J. P. *Journal of Biomedical Materials Research Part A* **2006**, *78A*, 620–628.

(73)   Al-Hanbali, O.; Rutt, K. J.; Sarker, D. K.; Hunter, A. C.; Moghimi, S. M. *Journal of Nanoscience and Nanotechnology* **2006**, *6*, 3126–3133.

(74)   Allen, T. M. *Advanced Drug Delivery Reviews* **1994**, *13*, 285–309.

(75)   Papisov, M. I. *Advanced Drug Delivery Reviews* **1998**, *32*, 119–138.

(76)   Kirpotin, D. B.; Drummond, D. C.; Shao, Y.; Shalaby, M. R.; Hong, K.; Nielsen, U. B.; Marks, J. D.; Benz, C. C.; Park, J. W. *Cancer Research* **2006**, *66*, 6732–6740.

(77)   Perez, R. P. *European Journal of Cancer* **1998**, *34*, 1535–1542.

(78)   Ohmichi, M.; Hayakawa, J.; Tasaka, K.; Kurachi, H.; Murata, Y. *Trends in Pharmacological Sciences* **2005**, *26*, 113–116.

(79) Iinuma, H.; Maruyama, K.; Okinaga, K.; Sasaki, K.; Sekine, T.; Ishida, O.; Ogiwara, N.; Johkura, K.; Yonemura, Y. *International Journal of Cancer* **2002**, *99*, 130–137.

(80) Krieger, M. L.; Eckstein, N.; Schneider, V.; Koch, M.; Royer, H.-D.; Jaehde, U.; Bendas, G. *International Journal of Pharmaceutics* **2010**, *389*, 10–17.

(81) Mai, J.; Song, S.; Rui, M.; Liu, D.; Ding, Q.; Peng, J.; Xu, Y. *Journal of Controlled Release* **2009**, *139*, 174–181.

(82) Dhar, S.; Gu, F. X.; Langer, R.; Farokhzad, O. C.; Lippard, S. J. *Proceedings of the National Academy of Sciences* **2008**, *105*, 17356–17361.

(83) Cao, Z.; Tong, R.; Mishra, A.; Xu, W.; Wong, G. C. L.; Cheng, J.; Lu, Y. *Angewandte Chemie International Edition* **2009**, *48*, 6494–6498.

(84) Mukhopadhyay, S.; Barnés, C. M.; Haskel, A.; Short, S. M.; Barnes, K. R.; Lippard, S. J. *Bioconjugate Chemistry* **2007**, *19*, 39–49.

(85) Levine, R. M.; Scott, C. M.; Kokkoli, E. *Soft Matter* **2013**, *9*, 985–1004.

(86) Conner, S. D.; Schmid, S. L. *Nature* **2003**, *422*, 37–44.

(87) Le Roy, C.; Wrana, J. L. *Nat Rev Mol Cell Biol* **2005**, *6*, 112–126.

(88) Rejman, J.; Bragonzi, A.; Conese, M. *Mol Ther* **2005**, *12*, 468–474.

(89) Marsh, M.; McMahon, H. T. *Science* **1999**, *285* , 215–220.

(90) Breunig, M.; Bauer, S.; Goepferich, A. *European Journal of Pharmaceutics and Biopharmaceutics* **2008**, *68*, 112–128.

(91) Nori, A.; Kopecek, J. *Advanced Drug Delivery Reviews* **2005**, *57*, 609–636.

(92) Minko, T.; Dharap, S. S.; Pakunlu, R. I.; Wang, Y. *Current Drug Targets* **2004**, *5*, 389–406.

(93) Byrne, J. D.; Betancourt, T.; Brannon-Peppas, L. *Advanced Drug Delivery Reviews* **2008**, *60*, 1615–1626.

(94) Brannon-Peppas, L.; Blanchette, J. O. *Advanced Drug Delivery Reviews* **2004**, *56*, 1649–1659.

(95)   Pendley, C.; Schantz, A.; Wagner, C. *Current opinion in molecular therapeutics* **2003**, *5*, 172–179.

(96)   Jain, R. K. *Cancer Research* **1990**, *50* , 814s–819s.

(97)   Chapman, A. P. *Advanced Drug Delivery Reviews* **2002**, *54*, 531–545.

(98)   Atobe, K.; Ishida, T.; Ishida, E.; Hashimoto, K.; Kobayashi, H.; Yasuda, J.; Aoki, T.; Obata, K.; Kikuchi, H.; Akita, H.; Asai, T.; Harashima, H.; Oku, N.; Kiwada, H. *Biological and Pharmaceutical Bulletin* **2007**, *30*, 972–978.

(99)   Maruyama, K.; Takahashi, N.; Tagawa, T.; Nagaike, K.; Iwatsuru, M. *FEBS Letters* **1997**, *413*, 177–180.

(100)   Backer, M. V; Gaynutdinov, T. I.; Patel, V.; Bandyopadhyaya, A. K.; Thirumamagal, B. T. S.; Tjarks, W.; Barth, R. F.; Claffey, K.; Backer, J. M. *Molecular Cancer Therapeutics* **2005**, *4* , 1423–1429.

(101)   Duda, D. G.; Batchelor, T. T.; Willett, C. G.; Jain, R. K. *Trends in Molecular Medicine* **2007**, *13*, 223–230.

(102)   Torchilin, V. P. *Nat Rev Drug Discov* **2005**, *4*, 145–160.

(103)   Thomas, T. P.; Shukla, R.; Kotlyar, A.; Liang, B.; Ye, J. Y.; Norris, T. B.; Baker, J. R. *Biomacromolecules* **2008**, *9*, 603–609.

(104)   Merrifield, R. B. *Journal of the American Chemical Society* **1963**, *85*, 2149–2154.

(105)   Berndt, P.; Fields, G. B.; Tirrell, M. *Journal of the American Chemical Society* **1995**, *117*, 9515–9522.

(106)   Aina, O. H.; Liu, R.; Sutcliffe, J. L.; Marik, J.; Pan, C.-X.; Lam, K. S. *Molecular Pharmaceutics* **2007**, *4*, 631–651.

(107)   Liu, R.; Enstrom, A. M.; Lam, K. S. *Experimental Hematology* **2003**, *31*, 11–30.

(108)   Myrberg, H.; Zhang, L.; xe; e, M.; Langel; xdc; lo *Bioconjugate Chem.* **2008**, *19*, 70–75.

(109)   Chen, Y.; Mant, C. T.; Farmer, S. W.; Hancock, R. E. W.; Vasil, M. L.; Hodges, R. S. *Journal of Biological Chemistry* **2005**, M413406200.

(110)   Pisabarro, M. T.; Serrano, L. *Biochemistry* **1996**, *35*, 10634–10640.

(111) Stachelhaus, T.; Schneider, A.; Marahiel, M. A. *Science* **1995**, *269* , 69–72.

(112) Varner, J. A.; Cheresh, D. A. *Current Opinion in Cell Biology* **1996**, *8*, 724–730.

(113) Hynes, R. O. *Cell* **2002**, *110*, 673–687.

(114) Wester, H.-J.; Kessler, H. *J Nucl Med* **2005**, *46*, 1940–1945.

(115) Hill, E.; Shukla, R.; Park, S. S.; Baker, J. R. *Bioconjugate Chem.* **2007**, *18*, 1756–1762.

(116) Mitra, A.; Coleman, T.; Borgman, M.; Nan, A.; Ghandehari, H.; Line, B. R. *Journal of Controlled Release* **2006**, *114*, 175–183.

(117) Pilkington-Miksa, M. A.; Sarkar, S.; Writer, M. J.; Barker, S. E.; Shamlou, P. A.; Hart, S. L.; Hailes, H. C.; Tabor, A. B. *European Journal of Organic Chemistry* **2008**, *2008*, 2900–2914.

(118) Xiong, X. B.; Mahmud, A.; Uludag, H.; Lavasanifar, A. *Biomacromolecules* **2007**, *8*, 874–884.

(119) Pierschbacher, M. D.; Ruoslahti, E. *Nature* **1984**, *309*, 30–33.

(120) Ruoslahti, E.; Pierschbacher, M. D. *Science* **1987**, *238*, 491.

(121) Ruoslahti, E.; Pierschbacher, M. D. *Cell* **1986**, *44*, 517–518.

(122) Kim, S.; Bell, K.; Mousa, S. A.; Varner, J. A. *The American Journal of Pathology* **2000**, *156*, 1345–1362.

(123) Muschler, J. L.; Horwitz, A. F. *Development* **1991**, *113*, 327–37.

(124) Van Golen, K. L.; Bao, L.; Brewer, G. J.; Pienta, K. J.; Kamradt, J. M.; Livant, D. L.; Merajver, S. D. *Neoplasia* **2002**, *4*, 373–379.

(125) Gong, J.; Wang, D. H.; Sun, L. Z.; Zborowska, E.; Wilson, J. K. V.; Brattain, M. G. *Cell Growth & Differentiation* **1997**, *8*, 83–90.

(126) Jayne, D. G.; Heath, R. M.; Dewhurst, O.; Scott, N.; Guillou, P. J. *European Journal of Surgical Oncology* **2002**, *28*, 30–36.

(127) Ellis, L. M. *American Surgery* **2003**, *69*, 3–10.

(128) Jia, Y.; Zeng, Z.-Z.; Markwart, S. M.; Rockwood, K. F.; Ignatoski, K. M. W.; Ethier, S. P.; Livant, D. L. *Cancer Research* **2004**, *64*, 8674–8681.

(129) Chen, J.; De, S.; Brainard, J.; Byzova, T. V. *Cell Communication and Adhesion* **2004**, *11*, 1–11.

(130) Maglott, A.; Bartik, P.; Cosgun, S.; Klotz, P.; Rondé, P.; Fuhrmann, G.; Takeda, K.; Martin, S.; Dontenwill, M. *Cancer Research* **2006**, *66*, 6002–6007.

(131) Mizejewski, G. J. *Proceedings of the Society for Experimental Biology and Medicine* **1999**, *222*, 124–138.

(132) Dingemans, A.-M. C.; Van den Boogaart, V.; Vosse, B. A.; Van Suylen, R.-J.; Griffioen, A. W.; Thijssen, V. L. *Molecular cancer* **2010**, *9*, 152.

(133) Aucoin, L.; Griffith, C. M.; Pleizier, G.; Deslandes, Y.; Sheardown, H. *Journal of Biomaterials Science, Polymer Edition* **2002**, *13*, 447–462.

(134) Kao, W. J. *Biomaterials* **1999**, *20*, 2213–2221.

(135) Kim, T.-I.; Jang, J.-H.; Lee, Y.-M.; Ryu, I.-C.; Chung, C.-P.; Han, S.-B.; Choi, S.-M.; Ku, Y. *Biotechnology Letters* **2002**, *24*, 2029–2033.

(136) Benoit, D. S. W.; Anseth, K. S. *Biomaterials* **2005**, *26*, 5209–5220.

(137) Petrie, T. A.; Capadona, J. R.; Reyes, C. D.; García, A. J. *Biomaterials* **2006**, *27*, 5459–5470.

(138) Mardilovich, A.; Craig, J. A.; McCammon, M. Q.; Garg, A.; Kokkoli, E. *Langmuir* **2006**, *22*, 3259–3264.

(139) Pangburn, T. O.; Bates, F. S.; Kokkoli, E. *Soft Matter* **2012**, *8*, 4449–4461.

(140) Shroff, K.; Pearce, T. R.; Kokkoli, E. *Langmuir* **2011**, *28*, 1858–1865.

(141) Demirgöz, D.; Pangburn, T. O.; Davis, K. P.; Lee, S.; Bates, F. S.; Kokkoli, E. *Soft Matter* **2009**, *5*, 2011–2019.

(142) Demirgöz, D.; Garg, A.; Kokkoli, E. *Langmuir* **2008**, *24*, 13518–13524.

(143) Garg, A.; Tisdale, A. W.; Haidari, E.; Kokkoli, E. *International Journal of Pharmaceutics* **2009**, *366*, 201–210.

(144) Garg, A.; Kokkoli, E. *Current Pharmaceutical Biotechnology* **2011**, *12*, 1135–1143.

(145) Atchison, N. A.; Fan, W.; Papas, K. K.; Hering, B. J.; Tsapatsis, M.; Kokkoli, E. *Langmuir* **2010**, *26*, 14081–14088.

(146) Shroff, K.; Kokkoli, E. *Langmuir* **2012**, *28*, 4729–4736.

(147) Pangburn, T. O.; Georgiou, K.; Bates, F. S.; Kokkoli, E. *Langmuir* **2012**, *28*, 12816–12830.

(148) Adil, M. M.; Belur, L.; Pearce, T. R.; Levine, R. M.; Tisdale, A. W.; Sorenson, B. S.; McIvor, R. C.; Kokkoli, E. *Biomaterials Science* **2013**, *In Press*.

(149) Pangburn, T. O.; Petersen, M. A.; Waybrant, B.; Adil, M. M.; Kokkoli, E. *Journal of Biomechanical Engineering* **2009**, *131*, 74005.

(150) Liechty, W. B.; Kryscio, D. R.; Slaughter, B. V.; Peppas, N. A. *Annual Review of Chemical and Biomolecular Engineering* **2010**, *1*, 149–173.

(151) Flenniken, M. L.; Liepold, L. O.; Crowley, B. E.; Willits, D. A.; Young, M. J.; Douglas, T. *Chemical Communications* **2005**, *4*, 447–449.

(152) Letchford, K.; Burt, H. *European Journal of Pharmaceutics and Biopharmaceutics* **2007**, *65*, 259–269.

(153) Agarwal, A.; Saraf, S.; Asthana, A.; Gupta, U.; Gajbhiye, V.; Jain, N. K. *International Journal of Pharmaceutics* **2008**, *350*, 3–13.

(154) Christian, N. A.; Milone, M. C.; Ranka, S. S.; Li, G.; Frail, P. R.; Davis, K. P.; Bates, F. S.; Therien, M. J.; Ghoroghchian, P. P.; June, C. H.; Hammer, D. A. *Bioconjugate Chem.* **2007**, *18*, 31–40.

(155) Bhadra, D.; Bhadra, S.; Jain, S.; Jain, N. K. *International Journal of Pharmaceutics* **2003**, *257*, 111–124.

(156) Khandare, J. J.; Jayant, S.; Singh, A.; Chandna, P.; Wang, Y.; Vorsa, N.; Minko, T. *Bioconjugate Chem.* **2006**, *17*, 1464–1472.

(157) Hiemenz, P. C.; Rajagopalan, R. *Principles of Colloid and Surface Chemistry*; CRC Press: Boca Raton, FL, 1997.

(158) Lindman, B. In *Surfactants*; Tadros, T. F., Ed.; Academic Press: London, 1984.

(159) McBain, J. W.; Salmon, C. S. *Proceedings of the Royal Society of London. Series A, Containing Papers of a Mathematical and Physical Character* **1920**, *97*, 44–65 CR – Copyright © 1920 The Royal Societ.

(160) Tanford, C. *The Hydrophobic Effect: Formation of Micelles and Biological Membranes*; John Wiley & Sons, Inc.: New York, 1973.

(161) Israelachvili, J. *Intermolecular and Surface Forces*; Academic Press: London, 1992.

(162) Pearce, T. R.; Shroff, K.; Kokkoli, E. *Advanced Materials* **2012**, *24*, 3803–3822.

(163) Yu, C.; Hu, Y.; Duan, J.; Yuan, W.; Wang, C.; Xu, H.; Yang, X.-D. *PLoS ONE* **2011**, *6*, e24077.

(164) Chu, T. C.; Marks, J. W.; Lavery, L. A.; Faulkner, S.; Rosenblum, M. G.; Ellington, A. D.; Levy, M. *Cancer Research* **2006**, *66*, 5989–5992.

(165) Nimjee, S. M.; Rusconi, C. P.; Sullenger, B. A. *Annual Review of Medicine* **2005**, *56*, 555–+.

(166) Bagalkot, V.; Farokhzad, O. C.; Langer, R.; Jon, S.; Vaishali Bagalkot, O. C. F. R. L. S. J. *Angewandte Chemie International Edition* **2006**, *45*, 8149–8152.

(167) Lasic, D. D.; Needham, D. *Chemical Reviews* **1995**, *95*, 2601–2628.

(168) Oku, N.; Anonymous *Advanced Drug Delivery Reviews* **1999**, *40*, 63–73.

(169) Safra, T.; Muggia, F.; Jeffers, S.; Tsao-Wei, D. D.; Groshen, S.; Lyass, O.; Henderson, R.; Berry, G.; Gabizon, A. *Ann Oncol* **2000**, *11*, 1029–1033.

(170) Jain, S.; Bates, F. S. *Macromolecules* **2004**, *37*, 1511–1523.

(171) Bywater, S. In *Physical Chemistry*; Springer Berlin / Heidelberg, 1979; Vol. 30, pp. 89–116.

(172) Matyjaszewski, K.; Miller, P. J.; Pyun, J.; Kickelbick, G.; Diamanti, S. *Macromolecules* **1999**, *32*, 6526–6535.

(173) Watzlawek, M.; Likos, C. N.; Löwen, H. *Physical Review Letters* **1999**, *82*, 5289–5292.

(174) Cui, H.; Chen, Z.; Zhong, S.; Wooley, K. L.; Pochan, D. J. *Science* **2007**, *317* , 647–650.

(175) Laschewsky, A. *Current Opinion in Colloid & Interface Science* **2003**, *8*, 274–281.

(176) Edmonds, W. F.; Li, Z.; Hillmyer, M. A.; Lodge, T. P. *Macromolecules* **2006**, *39*, 4526–4530.

(177) Li, Z.; Kesselman, E.; Talmon, Y.; Hillmyer, M. A.; Lodge, T. P. *Science* **2004**, *306* , 98–101.

(178) Bates, F. S.; Hillmyer, M. A.; Lodge, T. P.; Bates, C. M.; Delaney, K. T.; Fredrickson, G. H. *Science* **2012**, *336* , 434–440.

(179) Hajduk, D. A.; Kossuth, M. B.; Hillmyer, M. A.; Bates, F. S. *The Journal of Physical Chemistry B* **1998**, *102*, 4269–4276.

(180) Halperin, A.; Tirrell, M.; Lodge, T. *Macromolecules: Synthesis, Order and Advanced Properties* **1992**, 31–71.

(181) Zhang, L.; Eisenberg, A. *Polymers for Advanced Technologies* **1998**, *9*, 677–699.

(182) Stals, P. J. M.; Li, Y.; Burdyńska, J.; Nicolaÿ, R.; Nese, A.; Palmans, A. R. A.; Meijer, E. W.; Matyjaszewski, K.; Sheiko, S. S. *Journal of the American Chemical Society* **2013**.

(183) Zhang, L.; Eisenberg, A. *Macromolecules* **1999**, *32*, 2239–2249.

(184) Yu, Y.; Zhang, L.; Eisenberg, A. *Macromolecules* **1998**, *31*, 1144–1154.

(185) Gast, A. P.; Vinson, P. K.; Cogan-Farinas, K. A. *Macromolecules* **1993**, *26*, 1774–1776.

(186) Zhang, L.; Barlow, R. J.; Eisenberg, A. *Macromolecules* **1995**, *28*, 6055–6066.

(187) Antonietti, M.; Heinz, S.; Schmidt, M.; Rosenauer, C. *Macromolecules* **1994**, *27*, 3276–3281.

(188) Won, Y. Y.; Davis, H. T.; Bates, F. S.; Agamalian, M.; Wignall, G. D. *J. Phys. Chem. B* **2000**, *104*, 7134–7143.

(189) Gao, Z.; Varshney, S. K.; Wong, S.; Eisenberg, A. *Macromolecules* **1994**, *27*, 7923–7927.

(190) Jain, S.; Bates, F. S. *Science* **2003**, *300*, 460–464.

(191) Zhang, L.; Shen, H.; Eisenberg, A. *Macromolecules* **1997**, *30*, 1001–1011.

(192) Lim Soo, P.; Eisenberg, A. *Journal of Polymer Science Part B: Polymer Physics* **2004**, *42*, 923–938.

(193) Shen, H.; Eisenberg, A. *The Journal of Physical Chemistry B* **1999**, *103*, 9473–9487.

(194) Zupancich, J. A.; Bates, F. S.; Hillmyer, M. A. *Macromolecules* **2006**, *39*, 4286–4288.

(195) Jain, S.; Dyrdahl, M. H. E.; Gong, X.; Scriven, L. E.; Bates, F. S. *Macromolecules* **2008**, *41*, 3305–3316.

(196) Aniansson, E. A. G.; Wall, S. N.; Almgren, M.; Hoffmann, H.; Kielmann, I.; Ulbricht, W.; Zana, R.; Lang, J.; Tondre, C. *The Journal of Physical Chemistry* **1976**, *80*, 905–922.

(197) Halperin, A.; Alexander, S. *Macromolecules* **1989**, *22*, 2403–2412.

(198) Lund, R.; Willner, L.; Richter, D.; Dormidontova, E. E. *Macromolecules* **2006**, *39*, 4566–4575.

(199) Bermudez, H.; Brannan, A. K.; Hammer, D. A.; Bates, F. S.; Discher, D. E. *Macromolecules* **2002**, *35*, 8203–8208.

(200) Creutz, S.; Van Stam, J.; Antoun, S.; De Schryver, F. C.; Jérôme, R. *Macromolecules* **1997**, *30*, 4078–4083.

(201) Won, Y. Y.; Davis, H. T.; Bates, F. S. *Macromolecules* **2003**, *36*, 953–955.

(202) Davis, K. P.; Lodge, T. P.; Bates, F. S. *Macromolecules* **2008**, *41*, 8289–8291.

(203) Terreau, O.; Luo, L.; Eisenberg, A. *Langmuir* **2003**, *19*, 5601–5607.

(204) Larsen, A. L.; Terentjev, E. M. *Macromolecules* **2006**, *39*, 9508–9518.

(205) Ghoroghchian, P. P.; Lin, J. J.; Brannan, A. K.; Frail, P. R.; Bates, F.; Therien, M. J.; Hammer, D. A. *Soft Matter* **2006**, *2*, 973–980.

(206) Lee, J. C. M.; Santore, M.; Bates, F. S.; Discher, D. E. *Macromolecules* **2002**, *35*, 323–326.

(207) Cai, S.; Vijayan, K.; Cheng, D.; Lima, E.; Discher, D. *Pharmaceutical Research* **2007**, *24*, 2099–2109.

(208) Allen, C.; Maysinger, D.; Eisenberg, A. *Colloids and Surfaces B: Biointerfaces* **1999**, *16*, 3–27.

(209) Kumar, V.; Prud'homme, R. K. *Journal of Pharmaceutical Sciences* **2008**, *97*, 4904–4914.

(210) Park, J. H.; Lee, S.; Kim, J.-H.; Park, K.; Kim, K.; Kwon, I. C. *Progress in Polymer Science* **2008**, *33*, 113–137.

(211) Sethuraman, V.; Lee, M.; Bae, Y. *Pharmaceutical Research* **2008**, *25*, 657–666.

(212) Wang, Y.-C.; Tang, L.-Y.; Sun, T.-M.; Li, C.-H.; Xiong, M.-H.; Wang, J. *Biomacromolecules* **2008**, *9*, 388–395.

(213) Sutton, D.; Nasongkla, N.; Blanco, E.; Gao, J. *Pharmaceutical Research* **2007**, *24*, 1029–1046.

(214) Tong, R.; Cheng, J. *Polymer Reviews* **2007**, *47*, 345–381.

(215) Dalhaimer, P.; Engler, A. J.; Parthasarathy, R.; Discher, D. E. *Biomacromolecules* **2004**, *5*, 1714–1719.

(216) Geng, Y.; Discher, D. E. *Polymer* **2006**, *47*, 2519–2525.

(217) Kim, Y.; Dalhaimer, P.; Christian, D. A.; Discher, D. E. *Nanotechnology* **2005**, *16*, S484–S491.

(218) Geng, Y.; Dalhaimer, P.; Cai, S.; Tsai, R.; Tewari, M.; Minko, T.; Discher, D. E. *Nature Nanotechnology* **2007**, *2*, 249–255.

(219) Discher, B. M.; Won, Y. Y.; Ege, D. S.; Lee, J. C. M.; Bates, F. S.; Discher, D. E.; Hammer, D. A. *Science* **1999**, *284*, 1143–1146.

(220) Ahmed, F.; Pakunlu, R. I.; Brannan, A.; Bates, F.; Minko, T.; Discher, D. E. *Journal of Controlled Release* **2006**, *116*, 150–158.

(221) Mueller, W.; Koynov, K.; Fischer, K.; Hartmann, S.; Pierrat, S.; BascheÌ• , T.; Maskos, M. *Macromolecules* **2009**, *42*, 357–361.

(222) Lee, J. C.-M.; Bermudez, H.; Discher, B. M.; Sheehan, M. A.; Won, Y.-Y.; Bates, F. S.; Discher, D. E. *Biotechnology and Bioengineering* **2001**, *73*, 135–145.

(223) Woodle, M. C.; Lasic, D. D. *Biochimica et Biophysica Acta - Reviews on Biomembranes* **1992**, *1113*, 171–199.

(224) Parr, M. J.; Ansell, S. M.; Choi, L. S.; Cullis, P. R. *Biochimica et Biophysica Acta (BBA) - Biomembranes* **1994**, *1195*, 21–30.

(225) Kenworthy, A. K.; Simon, S. A.; McIntosh, T. J. *Biophysical journal1* **1995**, *68*, 1903–1920.

(226) Photos, P. J.; Bacakova, L.; Discher, B.; Bates, F. S.; Discher, D. E. *Journal of Controlled Release* **2003**, *90*, 323–334.

(227) Mather, B. D.; Viswanathan, K.; Miller, K. M.; Long, T. E. *Prog Polym Sci* **2006**, *31*, 487–531.

(228) Binder, W. H.; Sachsenhofer, R. *Macromolecular Rapid Communications* **2007**, *28*, 15–54.

(229) Hoyle, C. E.; Bowman, C. N. *Angewandte Chemie International Edition* **2010**, *49*, 1540–1573.

(230) Golas, P. L.; Matyjaszewski, K. *Chemical Society Reviews* **2010**, *39*, 1338–1354.

(231) Hoyle, C. E.; Lowe, A. B.; Bowman, C. N. *Chemical Society Reviews* **2010**, *39*, 1355–1387.

(232) Discher, B. M.; Bermudez, H.; Hammer, D. A.; Discher, D. E.; Won, Y.-Y.; Bates, F. S. *The Journal of Physical Chemistry B* **2002**, *106*, 2848–2854.

(233) Katz, J. S.; Levine, D. H.; Davis, K. P.; Bates, F. S.; Hammer, D. A.; Burdick, J. A. *Langmuir* **2009**, *25*, 4429–4434.

(234) Discher, D. E.; Ahmed, F. *Annual Review of Biomedical Engineering* **2006**, *8*, 323–341.

(235) Dorr, R. T. *The Annals of Pharmacotherapy* **1994**, *28* , 11–14.

(236) Park, J. W. *Breast Cancer Research* **2002**, *4*, 95–99.

(237) Immordino, M. L.; Brusa, P.; Arpicco, S.; Stella, B.; Dosio, F.; Cattel, L. *Journal of Controlled Release* **2003**, *91*, 417–429.

(238) Hillmyer, M. A.; Bates, F. S. *Macromolecules* **1996**, *29*, 6994–7002.

(239) Meng, F.; Hiemstra, C.; Engbers, G. H. M.; Feijen, J. *Macromolecules* **2003**, *36*, 3004–3006.

(240) Ahmed, F.; Discher, D. E. *Journal of Controlled Release* **2004**, *96*, 37–53.

(241) Ghoroghchian, P. P.; Li, G.; Levine, D. H.; Davis, K. P.; Bates, F. S.; Hammer, D. A.; Therien, M. J. *Macromolecules* **2006**, *39*, 1673–1675.

(242) Sinha, V. R.; Bansal, K.; Kaushik, R.; Kumria, R.; Trehan, A. *International Journal of Pharmaceutics* **2004**, *278*, 1–23.

(243) Geng, Y.; Discher, D. E. *Journal of the American Chemical Society* **2005**, *127*, 12780–12781.

(244) Ahmed, F.; Pakunlu, R. I.; Srinivas, G.; Brannan, A.; Bates, F.; Klein, M. L.; Minko, T.; Discher, D. E. *Molecular Pharmaceutics* **2006**, *3*, 340–350.

(245) Moghimi, S. M.; Hunter, A. C.; Murray, J. C.; Szewczyk, A. *Science* **2004**, *303* , 626–628.

(246) Savić, R.; Luo, L.; Eisenberg, A.; Maysinger, D. *Science* **2003**, *300* , 615–618.

(247) Vangeyte, P.; Gautier, S.; Jerome, R. *Colloids and Surfaces A: Physicochemical and Engineering Aspects1* **2004**, *242*, 203–211.

(248) Aliabadi, H. M.; Elhasi, S.; Mahmud, A.; Gulamhusein, R.; Mahdipoor, P.; Lavasanifar, A. *International Journal of Pharmaceutics* **2007**, *329*, 158–165.

(249) Vangeyte, P.; Leyh, B.; Heinrich, M.; Grandjean, J.; Bourgaux, C.; Jerome, R. *Langmuir* **2004**, *20*, 8442–8451.

(250) Lin, J. J.; Ghoroghchian, P. P.; Zhang, Y.; Hammer, D. A. *Langmuir* **2006**, *22*, 3975–3979.

(251) Trollsås, M.; Kelly, M. A.; Claesson, H.; Siemens, R.; Hedrick, J. L. *Macromolecules* **1999**, *32*, 4917–4924.

(252) Vangeyte, P.; Jérôme, R. *Journal of Polymer Science Part A: Polymer Chemistry* **2004**, *42*, 1132–1142.

(253) Ghoroghchian, P. P.; Frail, P. R.; Li, G.; Zupancich, J. A.; Bates, F. S.; Hammer, D. A.; Therien, M. J. *Chem. Mater.* **2007**, *2007*, 1309–1318.

(254) Ghoroghchian, P. P.; Frail, P. R.; Susumu, K.; Blessington, D.; Brannan, A. K.; Bates, F. S.; Chance, B.; Hammer, D. A.; Therien, M. J. *Proceedings of the National Academy of Sciences* **2005**, *102*, 2922–2927.

(255) Zupancich, J. A.; Bates, F. S.; Hillmyer, M. A. *Biomacromolecules* **2009**, *10*, 1554–1563.

(256) Kolb, H. C.; Finn, M. G.; Sharpless, K. B. *Angewandte Chemie International Edition* **2001**, *40*, 2004–2021.

(257) Finn, M. G.; Fokin, V. V *Chemical Society Reviews* **2010**, *39*, 1231–1232.

(258) Bouzide, A.; Sauvé, G. *Organic Letters* **2002**, *4*, 2329–2332.

(259) Bae, J. W.; Lee, E.; Park, K. M.; Park, K. D. *Macromolecules* **2009**, *42*, 3437–3442.

(260) Y., D.; H., B.-P.; S., S.; B., F. G.; B., M. J.; M., T.; Dori, Y.; Bianco–Peled, H.; Satija, S. K.; Fields, G. B.; McCarthy, J. B.; Tirrell, M. *Journal of Biomedical Materials Research* **2000**, *50*, 75–81.

(261) Mardilovich, A.; Kokkoli, E. *Biomacromolecules* **2004**, *5*, 950–957.

(262) Haxton, K. J.; Burt, H. M. *Journal of Pharmaceutical Sciences* **2009**, *98*, 2299–2316.

(263) Sanchez-Cano, C.; Hannon, M. J. *Dalton Transactions* **2009**, *48*, 10702–10711.

(264) Peleg-Shulman, T.; Gibson, D.; Cohen, R.; Abra, R.; Barenholz, Y. *Biochimica et Biophysica Acta - Biomembranes* **2001**, *1510*, 278–291.

(265) Working, P. K.; Newman, M. S.; Sullivan, T.; Brunner, M.; Podell, M.; Sahenk, Z.; Turner, N. *Toxicological Sciences* **1998**, *46*, 155–165.

(266) Zamboni, W. C.; Gervais, A. C.; Egorin, M. J.; Schellens, J. H. M.; Zuhowski, E. G.; Pluim, D.; Joseph, E.; Hamburger, D. R.; Working, P. K.; Colbern, G. *Cancer Chemotherapy and Pharmacology* **2004**, *53*, 329–336.

(267) Newman, M. S.; Colbern, G. T.; Working, P. K.; Engbers, C.; Amantea, M. A. *Cancer Chemotherapy and Pharmacology* **1999**, *43*, 1–7.

(268) Bandak, S.; Goren, D.; Horowitz, A.; Tzemach, D.; Gabizon, A. *Anti-Cancer Drugs* **1999**, *10*, 911–920.

(269) Rosenthal, D. I.; Yom, S. S.; Liu, L.; Machtay, M.; Algazy, K.; Weber, R. S.; Weinstein, G. S.; Chalian, A. A.; Miller, L. K.; Rockwell, K.; Tonda, M.; Schnipper, E.; Hershock, D. *Investigational New Drugs* **2002**, *20*, 343–349.

(270) White, S. C.; Lorigan, P.; Margison, G. P.; Margison, J. M.; Martin, F.; Thatcher, N.; Anderson, H.; Ranson, M. *British Journal of Cancer* **2006**, *95*, 822–828.

(271) Harrington, K. J.; Lewanski, C. R.; Northcote, A. D.; Whittaker, J.; Wellbank, H.; Vile, R. G.; Peters, A. M.; Stewart, J. S. W. *Annals of Oncology* **2001**, *12*, 493–496.

(272) Seetharamu, N.; Kim, E.; Hochster, H.; Martin, F.; Muggia, F. *Anticancer research* **2010**, *30*, 541.

(273) Kuwada, S. K.; Li, X. *Molecular Biology of the Cell* **2000**, *11*, 2485–2496.

(274) Honoré, S.; Pichard, V.; Penel, C.; Rigot, V.; Prévôt, C.; Marvaldi, J.; Briand, C.; Rognoni, J.-B. *Histochemistry and Cell Biology* **2000**, *114*, 323–335.

(275) Croyle, M. A.; Walter, E.; Janich, S.; Roessler, B. J.; Amidon, G. L. *Human Gene Therapy* **1998**, *9*, 561–572.

(276) Kozlova, N. I.; Morozevich, G. E.; Chubukina, A. N.; Berman, A. E. *Oncogene* **2001**, *20*, 4710–4717.

(277) Hidalgo, I. J.; Raub, T. J.; Borchardt, R. T. *Gastroenterology* **1989**, *96*, 736–49.

(278) Press, B.; Di Grandi, D. *Current Drug Metabolism* **2008**, *9*, 893–900.

(279) Birtwistle, M. R.; Kholodenko, B. N. *Molecular Oncology* **2009**, *3*, 308–320.

(280) Petersen, M. A.; Yin, L.; Kokkoli, E.; Hillmyer, M. A. *Polymer Chemistry* **2010**, *1*, 1281–1290.

(281) Golla, E. D. *Talanta* **1973**, *20*, 199–210.

(282) Onaca, O.; Nallani, M.; Ihle, S.; Schenk, A.; Schwaneberg, U. *Biotechnology Journal* **2006**, *1*, 795–805.

(283) Avgoustakis, K.; Beletsi, A.; Panagi, Z.; Klepetsanis, P.; Karydas, A. G.; Ithakissios, D. S. *Journal of Controlled Release* **2002**, *79*, 123–135.

(284) Rexeisen, E. L.; Fan, W.; Pangburn, T. O.; Taribagil, R. R.; Bates, F. S.; Lodge, T. P.; Tsapatsis, M.; Kokkoli, E. *Langmuir* **2009**, *26*, 1953–1959.

(285) Greenspan, P.; Mayer, E. P.; Fowler, S. D. *The Journal of Cell Biology* **1985**, *100* , 965–973.

(286) Fowler, S. D.; Greenspan, P. *Journal of Histochemistry & Cytochemistry* **1985**, *33* , 833–836.

(287) Manders, E. M. M.; Verbeek, F. J.; Aten, J. A. *Journal of Microscopy* **1993**, *169*, 375–382.

(288) Costes, S. V; Daelemans, D.; Cho, E. H.; Dobbin, Z.; Pavlakis, G.; Lockett, S. *Biophysical journal* **2004**, *86*, 3993–4003.

(289) Nair, L. S.; Laurencin, C. T. *Progress in Polymer Science* **2007**, *32*, 762–798.

(290) Sun, H.; Mei, L.; Song, C.; Cui, X.; Wang, P. *Biomaterials* **2006**, *27*, 1735–1740.

(291) Juliano, R. L.; Ming, X.; Nakagawa, O. *Bioconjugate Chemistry* **2011**, *23*, 147–157.

(292) Mayor, S.; Pagano, R. E. *Nature Reviews Molecular and Cellular Biology* **2007**, *8*, 603–612.

(293) Sottile, J.; Chandler, J. *Molecular Biology of the Cell* **2005**, *16*, 757–768.

(294) Shi, F.; Sottile, J. *Journal of Cell Science* **2008**, *121*, 2360–2371.

(295) Chunhua Shen Chengfei Lu,, S. G. *Polymers for Advanced Technologies* **2008**, *19*, 66–72.

(296) Jung, J. H.; Ree, M.; Kim, H. *Catalysis Today* **2006**, *115*, 283–287.

(297) Gan, Z.; Jim, T. F.; Li, M.; Yuer, Z.; Wang, S.; Wu, C. *Macromolecules* **1999**, *32*, 590–594.

(298) Carstens, M. G.; Van Nostrum, C. F.; Verrijk, R.; De Leede, L. G. J.; Crommelin, D. J. A.; Hennink, W. E. *Journal of Pharmaceutical Sciences* **2008**, *97*, 506–518.

(299) Lam, C. X. F.; Savalani, M. M.; Teoh, S.-H.; Hutmacher, D. W. *Biomedical Materials* **2008**, *3*, 34108.

(300) Geisow, M. J.; D'Arcy Hart, P.; Young, M. R. *The Journal of Cell Biology* **1981**, *89*, 645–652.

(301) Brown, M. S.; Dana, S. E.; Goldstein, J. L. *Proceedings of the National Academy of Sciences U.S.A.* **1975**, *72*, 2925–2929.

(302) Goldstein, J. L.; Brunschede, G. Y.; Brown, M. S. *Journal of Biological Chemistry* **1975**, *250*, 7854–7862.

(303) Wagner, E.; Zatloukal, K.; Cotten, M.; Kirlappos, H.; Mechtler, K.; Curiel, D. T.; Birnstiel, M. L. *Proceedings of the National Academy of Sciences U.S.A.* **1992**, *89*, 6099–6103.

(304) Bareford, L. M.; Swaan, P. W. *Advanced Drug Delivery Reviews* **2007**, *59*, 748–758.

(305) Hostetter, A. A.; Osborn, M. F.; DeRose, V. J. *ACS Chemical Biology* **2012**, *7*, 218–225.

(306) Reedijk, J.; Lohman, P. *Pharmacy World & Science* **1985**, *7*, 173–180.

(307) Larsen, A. K.; Escargueil, A. E.; Skladanowski, A. *Pharmacology & Therapeutics* **2000**, *85*, 217–229.

(308) Akaboshi, M.; Kawai, K.; Maki, H.; Akuta, K.; Ujeno, Y.; Miyahara, T. *Cancer Science* **1992**, *83*, 522–526.

(309) Zhang, J.; Whan, R.; Hambley, T.; Begley, T. P. In *Wiley Encyclopedia of Chemical Biology*; John Wiley & Sons, Inc., 2007; pp. 1–10.

(310) Klein, A. V; Hambley, T. W. *Chemical Reviews* **2009**, *109*, 4911–4920.

(311) Huck, W. T. S. *Materials Today* **2008**, *11*, 24–32.

(312) Liu, F.; Urban, M. W. *Progress in Polymer Science* **2010**, *35*, 3–23.

(313) Hu, J.; Liu, S. *Macromolecules* **2010**, *43*, 8315–8330.

(314) Hoffman, A. S. *Advanced Drug Delivery Reviews* **2013**, *65*, 10–16.

(315) Meng, H.; Jinlian Hu *Journal of Intelligent Material Systems and Structures* **2010**, *21* , 859–885.

(316) Roy, D.; Cambre, J. N.; Sumerlin, B. S. *Progress in Polymer Science* **2010**, *35*, 278–301.

(317) Esser-Kahn, A. P.; Odom, S. A.; Sottos, N. R.; White, S. R.; Moore, J. S. *Macromolecules* **2011**, *44*, 5539–5553.

(318) Doane, T. L.; Burda, C. *Chemical Society Reviews* **2012**, *41*, 2885–2911.

(319) Faraji, A. H.; Wipf, P. *Bioorganic & Medicinal Chemistry* **2009**, *17*, 2950–2962.

(320) Geisow, M. J.; Evans, W. H. *Experimental Cell Research* **1984**, *150*, 36–46.

(321) Tannock, I. F.; Rotin, D. *Cancer Research* **1989**, *49*, 4373–4384.

(322) Schmaljohann, D. *Advanced Drug Delivery Reviews* **2006**, *58*, 1655–1670.

(323) Dai, S.; Ravi, P.; Tam, K. C. *Soft Matter* **2008**, *4*, 435–449.

(324) Binauld, S.; Stenzel, M. H. *Chemical Communications* **2013**, *49*, 2082–2102.

(325) Panyam, J.; Labhasetwar, V. *Advanced Drug Delivery Reviews* **2012**, *64, Supple*, 61–71.

(326) Mora-Huertas, C. E.; Fessi, H.; Elaissari, A. *International Journal of Pharmaceutics* **2010**, *385*, 113–142.

(327) Ma, X.; Zhou, Z.; Jin, E.; Sun, Q.; Zhang, B.; Tang, J.; Shen, Y. *Macromolecules* **2012**, *46*, 37–42.

(328) Petersen, M. A.; Hillmyer, M. A.; Kokkoli, E. *Bioconjugate Chemistry* **2013**.

(329) Falco, E.; Patel, M.; Fisher, J. *Pharmaceutical Research* **2008**, *25*, 2348–2356.

(330) Fife, T. H.; Jao, L. K. *The Journal of Organic Chemistry* **1965**, *30*, 1492–1495.

(331) Pchelintsev, V. V.; Sokolov, A. Y. *Polymer Degradation and Stability* **1988**, *21*, 285–310.

(332) Cheng, J.; Ji, R.; Gao, S.-J.; Du, F.-S.; Li, Z.-C. *Biomacromolecules* **2011**, *13*, 173–179.

(333) Morinaga, H.; Morikawa, H.; Wang, Y.; Sudo, A.; Endo, T. *Macromolecules* **2009**, *42*, 2229–2235.

(334) Paramonov, S. E.; Bachelder, E. M.; Beaudette, T. T.; Standley, S. M.; Lee, C. C.; Dashe, J.; Frechet, J. M. J. *Bioconjugate Chemistry* **2008**, *19*, 911–919.

(335) Heffernan, M. J.; Murthy, N. *Bioconjugate Chemistry* **2005**, *16*, 1340–1342.

(336) Gillies, E. R.; Frechet, J. M. J. *Chemical Communications* **2003**, *0*, 1640–1641.

(337) Khaja, S. D.; Lee, S.; Murthy, N. *Biomacromolecules2* **2007**, *8*, 1391–1395.

(338) Pemba, A. G.; Flores, J. A.; Miller, S. A. *Green Chemistry* **2013**, *15*, 325–329.

(339) Penczek, S. *Journal of Polymer Science Part A: Polymer Chemistry* **2000**, *38*, 1919–1933.

(340) Szymanski, R.; Kubisa, P.; Penczek, S. *Macromolecules* **1983**, *16*, 1000–1008.

(341) Odian, G. *Principles of Polymerization*; 4th ed.; John Wiley & Sons, Inc.: Hoboken, NJ, 2004.

(342) Heller, J.; Penhale, D. W. H.; Helwing, R. F. *Journal of Polymer Science: Polymer Letters Edition* **1980**, *18*, 293–297.

(343) Tomlinson, R.; Klee, M.; Garrett, S.; Heller, J.; Duncan, R.; Brocchini, S. *Macromolecules* **2002**, *35*, 473–480.

(344) Schacht, E.; Toncheva, V.; Vandertaelen, K.; Heller, J. *Journal of Controlled Release* **2006**, *116*, 219–225.

(345) Jain, R.; Standley, S. M.; Fréchet, J. M. J. *Macromolecules* **2007**, *40*, 452–457.

(346) Heller, J.; Barr, J.; Ng, S. Y.; Abdellauoi, K. S.; Gurny, R. *Advanced Drug Delivery Reviews* **2002**, *54*, 1015–1039.

(347) Murthy, N.; Thng, Y. X.; Schuck, S.; Xu, M. C.; Frechet, J. M. J. *Journal of the American Chemical Society* **2002**, *124*, 12398–12399.

(348) Zhang, L.; Bernard, J.; Davis, T. P.; Barner-Kowollik, C.; Stenzel, M. H. *Macromolecular Rapid Communications* **2008**, *29*, 123–129.

(349) Lee, S. J.; Min, K. H.; Lee, H. J.; Koo, A. N.; Rim, H. P.; Jeon, B. J.; Jeong, S. Y.; Heo, J. S.; Lee, S. C. *Biomacromolecules* **2011**, *12*, 1224–1233.

(350) Wolfe, P. S.; Wagener, K. B. *Macromolecular Rapid Communications* **1998**, *19*, 305–308.

(351) Yamashita, M.; Nishida, H. Process for Preparation of 1,3-Dioxane-4-one Compounds by Cyclization **1997**.

(352) Juge, S.; Genet, J.-P.; Mallart, S. Preparation of 1,3-dioxan-4-one Derivatives as Intermediates for Beta-Hydroxy-Alpha-Amino Acids **1989**.

(353) Lowe, J. R.; Martello, M. T.; Tolman, W. B.; Hillmyer, M. A. *Polymer Chemistry* **2011**, *2*, 702–708.

(354) Tsuruta, T.; Matsuura, K.; Inoue, S. *Die Makromolekulare Chemie* **1964**, *75*, 211–214.

(355) Le Hellaye, M.; Fortin, N.; Guilloteau, J.; Soum, A.; Lecommandoux, S.; Guillaume, S. M. *Biomacromolecules* **2008**, *9*, 1924–1933.

(356) Zhang, D.; Hillmyer, M. A.; Tolman, W. B. *Macromolecules* **2004**, *37*, 8198–8200.

(357) Kricheldorf, H. R. Polypeptides and 100 Years of Chemistry of α-Amino Acid N-Carboxyanhydrides. *Angewandte Chemie International Edition* **2006**, *45*, 5752–5784.

(358) Deming, T. J. *Journal of Polymer Science Part A: Polymer Chemistry* **2000**, *38*, 3011–3018.

(359) Kricheldorf, H. R.; Berl, M.; Scharnagl, N. *Macromolecules* **1988**, *21*, 286–293.

(360) Barakat, I.; Dubois, P.; Jerome, R.; Teyssie, P. *Macromolecules* **1991**, *24*, 6542–6545.

(361) Cao, A.; Kasuya, K.; Abe, H.; Doi, Y.; Inoue, Y. *Polymer* **1998**, *39*, 4801–4816.

(362) Nanba, T.; Ito, H.; Kobayashi, H.; Hayashi, T. No Title **1994**.

(363) Andreeßen, B.; Steinbüchel, A. *Applied and Environmental Microbiology 76* , 4919–4925.

(364) Doi, Y. *Macromolecular Symposia* **1995**, *98*, 585–599.

(365) Gresham, T. L.; Jansen, J. E.; Shaver, F. W. *Journal of the American Chemical Society* **1948**, *70*, 998–999.

(366) Ouhadi, T.; Heuschen, J. M. *Journal of Macromolecular Science: Part A - Chemistry* **1975**, *9*, 1183–1193.

(367) Yamashita, M.; Takemoto, Y.; Ihara, E.; Yasuda, H. *Macromolecules* **1996**, *29*, 1798–1806.

(368) Jedliński, Z.; Kurcok, P.; Kowalczuk, M. *Polymer International* **1995**, *37*, 187–190.

(369) Miyake, A.; Stockmayer, W. H. *Die Makromolekulare Chemie* **1965**, *88*, 90–116.

(370) Greer, S. C. *Annual Review of Physical Chemistry* **2002**, *53*, 173–200.

(371) Das, S. S.; Andrews, A. P.; Greer *Journal of Chemical Physics1* **1995**, *102*, 2951.

(372) Zhuang, J.; Das, S. S.; Nowakowski, M. D.; Greer, S. C. *Physica A* **1997**, *244*, 522–535.

(373) Poland, D. *Journal of Chemical Physics* **1999**, *111*, 8214.

(374) Save, M.; Schappacher, M.; Soum, A. *Macromolecular Chemistry and Physics* **2002**, *203*, 889–899.

(375) Martello, M. T.; Burns, A.; Hillmyer, M. *ACS Macro Letters* **2011**, *1*, 131–135.

(376) Wanamaker, C. L.; Tolman, W. B.; Hillmyer, M. A. *Biomacromolecules* **2009**, *10*, 443–448.

(377) Zhang, D.; Hillmyer, M. A.; Tolman, W. B. *Biomacromolecules* **2005**, *6*, 2091–2095.

(378) Lowe, J. R.; Tolman, W. B.; Hillmyer, M. A. *Biomacromolecules* **2009**, *10*, 2003–2008.